DISS. ETH NO.26352

Developments in balloon-borne water vapour measurements with frost point hygrometers

A thesis submitted to attain the degree of

DOCTOR OF SCIENCES of ETH ZURICH

(Dr. sc. ETH Zurich)

presented by
TERESA FILIPA PATO BARRADAS DA SILVA JORGE
MSc. in Energy Technologies
KIT - Karlsruhe Institute of Technology
born on 11. 04. 1990
citizen of Portugal

accepted on the recommendation of
Prof. Dr. Thomas Peter, examiner
Dr. Frank G. Wienhold, co-examiner
Dr. Holger Vömel, co-examiner

2019

Tudo vale a pena, quando a alma não é pequena.
Fernando Pessoa

Foreword

This was no common PhD Work. Yet again, I am still to discover what a common PhD Work is. What I am sure is that the a few important lessons I learnt in the last four years were neither as a scientist nor as an engineer. Do not get me wrong, in my opinion, as climate and atmospheric scientists we are concerned with some of the most crucial questions and tasks facing society and our planet. However, my personal development by far surmounts any other outcome of this time, and I would like to leave it documented here.

When I started this PhD in October 2015, the idea of a Peltier cooled frost point hygrometer was just that, an idea. And a lot of the electronics development work was still to be done. So, fast, I got diverted to the next pressing exciting project happening right there: the StratoClim balloon campaigns. And what a ride that was ... If anything was worth something in these four years, it was the relation me and Simone built organizing and living these campaigns. When people talk about PhD siblings, they mean us. Simone taught me what tolerance is and how to look on the bright side, although I still struggle with both. His spirit helped us through 8 weeks in Nainital, India and 7 weeks in Nepal.

The campaign preparations brought us to the 'Workshop on dynamics, transport and chemistry of the UT/LS Asian Monsoon' in March 2016 in Colorado, USA, where we met an inspiring community of scientists and to the GRUAN Lead Center in Lindenberg Germany in April 2016 where we met our biggest allies in these adventures, Peter Oelsner and Susanne Meier. In July 2016, we started our Indian adventure hosted by Manish Naja at ARIES in Nainital and supported by Survana Fadavnish from IMTT in Pune. There we met amazing colleagues such as Bhupendra Sing and Harsha Hanumanthu. It took some time, persistence and overcoming adversity to go from 'us' and 'them' to a team: from custom delays to a truck crossing India from Mumbai to Naintal arriving one hour before the first launch; from lack of trust to having the campaign start with radiosondes flown in Tom's luggage and driven nine hours across muddy roads from Delhi to Nainital; from communication problems to capacity building and a full week of post-monsoon launches entirely operated by the Indian colleagues themselves. A book could be written on what happened, many words were of what seemed like world-shattering events. However, the human brain has a way of forgetting the bad and remembering the good.

It felt amazing to come back home with a one-of-a-kind dataset and to enjoy being a beacon of hope for the StratoClim aircraft campaign. All the promise and excitement of new science waiting to happen, what an exhilarating feeling. Besides the fresh memory of all the hardship of an 8-week campaign, we started preparing the 2017 campaign, which ended up not being in Nainital but in Dhulikhel Nepal, 20 km from Kathmandu, where the StratoClim campaign managed to bring the Geophysica aircraft. In the middle of a EUFAR aircraft summer school in Ireland, where we flew as science crew in an

aircraft 60 ft from the Atlantic Ocean surface, me and Simone were summoned to Zürich to change the location of the entire campaign. In 15 days, we were in Kathmandu, with the instruments on the way, no balloon launch permissions and no host location.

After countless official meetings with the Nepalese authorities of the meteorological services, the civil aviation and the airport management; after crossing the country to Pokhara and back by van because you wouldn't catch me dead in a Nepalese airline aircraft; after being inappropriately treated by the campaign liaison; we found a host in Dhulikhel: Rijan Kayastha at the Kathmandu University and we got permissions for night time launches during airport closing times. Nepal made India look like child's play. Thirty 120 kg hydrogen bottles and only 20 kg out of the ton of dry ice we ordered arrived after baking for five days under the Indian sun. Unfortunately, half the instruments (the COBALDs) never arrived, they were lost forever in Switzerland. We also learned how unsettling internal conflicts in the team can be. Nevertheless, we returned home with 1 ppmv water vapour observations in the tropopause, an isothermal tropopause and a priceless dataset to join that of the Indian campaign. Publishing with this dataset has been a challenge on its own, which for now I have only experienced second hand. But soon ...

Being part of the StratoClim project, participating in excellent science discussions at home in ETH and abroad in all the annual Stratoclim meetings in Madrid 2016, Rome 2017 and Potsdam 2019, getting to know the inspiring UTLS European science community and being able to share all of it with Simone was the best experience I could have hoped for in my PhD time.

Meanwhile the PCFH development was running in parallel. In May 2018, I co-wrote a proposal for the 'Development, Validation and Implementation of a GRUAN-Worthy Plug-and-Play Balloon Borne Hygrometer' submitted to the GAW-CH Call 2018-2021, which was accepted for funding by MeteoSwiss. It has been an informative experience to be part of the 'GAW-CH Landesausschuss' meetings, a community concerned with keeping Switzerland in the forefront of atmospheric research, giving relevance to sometimes less sexy science as is instrument development and supporting the World Meteorological Organization (WMO).

Managing the development of the PCFH has been challenging work, especially as a very independent PhD student with a dead-line managing other team members with different time constraints. Furthermore, in the beginning of 2018, Uwe Weers, our engineer stopped working on the project due to health problems. Nevertheless, I persisted and with the help of Guillaume Cesbron, an intern, who I supervised in the PCFH project, I assembled the first two PCFH instruments flown in July 2018. In November 2018, I assembled three more instruments flown later in December 2018. I had the privilege of presenting my work concerning the PCFH at the SPARC workshop 'The UT/LS current status and emerging challenges' in Mainz, the GRUAN ICM10 meeting in Potsdam and at the SPARC General Assembly in Kyoto, Japan.

At the end of the year 2018, I suffered a ski accident and ruptured my left knee anterior cross ligament for which I got re-constructive surgery in March 2019. Since then I have been doing physiotherapy and finishing up my PhD work and Thesis. By writing this Foreword, I intend to illustrate that much more has happened in these four years than what is reported in this Thesis. A lot of work goes on in the background, and most of the learning is personal.

How do you measure the worth of a (wo)man?

Abstract

Water vapour is the fourth most abundant gas in the global atmosphere. In gaseous form it is the most important greenhouse gas, in condensed form–liquid or ice clouds–it strongly affects the radiative balance, and therefore climate. Furthermore, it plays a fundamental role in cleansing our atmosphere through the washout of soluble chemical species, hence determining atmospheric chemistry and air quality. However, its variability in abundance, phase and vertical distribution in the troposphere and stratosphere, make the science and engineering of its observation challenging. Measurements in the upper troposphere and lower stratosphere are particularly challenging because of the low H_2O concentrations and the sticky character of the H_2O molecule covering any solid structure. Yet, accurate measurements are important, because of the climatic and hydrological effects of H_2O even at high altitudes.

We acquired extensive experience with balloon-borne frost point hygrometers during the 2016-2017 StratoClim balloon campaigns on the southern slopes of the Himalayas and launched 63 radiosondes equipped with dedicated instrumentation from the dripping wet monsoon into the very dry tropopause region and stratosphere. This campaign revealed systematic patterns of contamination in stratospheric H_2O measurements. From there, we started addressing long standing questions and new challenges of measurement contamination in frost point hygrometers. Nine of the 43 water vapour profiles were measured with the Cryogenic Frost point Hygrometer (CFH) and showed contamination rendering stratospheric H_2O measurements impossible. Three of the nine contaminated soundings carried the COmpact Backscatter AerosoL Detector (COBALD), providing information on the clouds the sondes traversed in the troposphere. The most likely cause of the measurement contamination are supercooled liquid droplets in mixed-phase clouds freezing on the CFH intake tube and subsequently sublimating in the dry and warm stratosphere. Modelling of the Wegener-Bergeron-Findeisen process of droplet evaporation and ice crystal growth confirms the likelihood of supercooled liquid and ice co-existence in the clouds. The oscillatory motion of the balloon-borne payload and the prevalence of large supercooled droplets in glaciating clouds facilitate the accumulation of an ice layer at the top of the intake tube. This educated conjecture is quantified by the analysis of the payload motion by means of GPS data and by Computational Fluid Dynamic (CFD) simulations of droplet trajectories inside the intake tube. Through CFD calculations with a commercial software (FLUENT in the ANSYS Workbench), we match the contaminated water vapour observations to the water vapour sublimating from an icy intake tube top. Two of the contaminated soundings show recovery of instrument operation, i.e. non-contaminated water vapour measurements were established before balloon burst. From these observations, we can quantify the amount of sublimated water in the stratosphere and estimate the Liquid Water Content (LWC) in the observed mixed-phase clouds. We find that even cold mixed-phase

clouds with little LWC can affect the operation of the CFH.

Using CFD we are able to differentiate between contamination from evaporation of ice in the intake tube and outgassing moisture from the balloon skin; since the magnitude of of these two types of contamination are considerably different. The balloon contamination is a prevalent feature in all flights above the 20-hPa level. With CFD simulations we can confirm the effectiveness of the intake tube in preventing contamination of sampled stratospheric air by outgassing moisture from the instrument package.

The StratoClim balloon campaigns represent a unique dataset of CFH measurements at the extremely cold tropopause of the Asian Monsoon Anticyclone with a very moist troposphere below. With experience of the operation of frost point hygrometers under such conditions together with the recent international ban of the cryogenic liquid R23 used by the leading reference instruments CFH and FPH, we started the in-house development of a new balloon-borne hygrometer, the 'Peltier Cooled Frost point Hygrometer' (PCFH). The new implementation is fundamentally different in its design: twin instrument construction, double stage Peltier element, detection scheme with a reference surface, air as only cooling agent, and a state-of-the-art approach to controlling the frost or dew layer in quasi-equilibrium with the gas phase, where it is neither growing nor evaporating. The controller of a frost point hygrometer is its biggest source of uncertainty. In the PCFH, we strive for the implementation of optimal control i.e. optimized as a function of controller effort and error accuracy and optimal controller law, which takes into consideration the dynamic behaviour of the system. The instrument is designed with this goal in mind and subsequently modelled according to its construction and specifically its thermal reservoirs.

Five PCFH prototypes have been assembled and tested in the lab with and without air flow, which is a critical aspect for the Peltier element because of the thermal load, which the flow represents. The prototypes have flown in mid-latitudes under summer and winter conditions, for instrument characterization but not yet aiming at reliable water vapour measurements. Since each prototype is composed of two sub-units, testing possibilities per prototype double and allow testing the performance of alternative components such as single and double stage Peltier elements and heavier and lighter heat sinks with different number of cooling fins. The goal of the initial flights was a proof of concept and to validate the system's model. For this purpose, a sequence of different Pulse Width Modulator (PWM) duty cycles are used to evaluate the system's transfer function. This type of characterization is particularly relevant for the modelling of the thermal reservoirs of the PCFH in flight and to evaluate the cooling range of the Peltier elements.

After comparing the performance of double and single stage Peltier elements, we decided to use double stage Peltier elements. Nevertheless, the cooling range of the instrument design remains critical. We demonstrated the accessibility to stratospheric frost point temperatures reaching T_{frost} = -85 °C at p_{air} = 40 hPa and T_{air} = -60 °C, but only for one instrument out of the five. While this is an important step in the proof-of-concept, there is so far no proof of reproducibility and optimal control has not yet been implemented. The assembled double Peltier element has reached a maximum temperature depression between the hot and cold side of ΔT_{max} = 40 K at T_{air} = -60 °C and registered ΔT_{max} = 65 K during the lab tests without air flow, while the Peltier element datasheet advertises a ΔT_{max} = 86 K at ground conditions (T_{air} = 27 °C and $p_{\mathrm{air}} \sim$ 1000 hPa). We attribute the loss of ΔT from the datasheet

specifications to the tests in the lab without air flow to the assembly of the Peltier element into the PCFH. The reduction by 20 K is the best assembly so far. Once air flow of ~ 5 m s^{-1} is added, the ΔT reduction becomes significant. Luckily, the flow effect decreases as the atmospheric air becomes less dense, which partially compensates the ΔT reduction at colder operating temperatures of the Peltier element in the stratosphere. Furthermore, $\Delta T_{\mathrm{max}} = 40$ K at $T_{\mathrm{air}} = -60$ °C correspond to about 20 K between cold side and ambient temperature due to losses between the Peltier hot side, heat sink, and ambient air.

The reflectance of the ice/dew layer on the mirror responds to the temperature difference between the mirror temperature and the actual frost point temperature, which we tested by equipping two out of the ten flown sub-units with an alternating set-point proportional-integral-derivative controller (PID). Unfortunately, the collected reflectance data was so far insufficient to estimate the water vapour diffusivity, a parameter required for the PCFH mathematical model. Nevertheless, we optimized the thermodynamic part of the model for the first prototype version and validated it with in-flight data. The agreement of the simulated variables after optimization with the measured thermal reservoirs temperatures was within ±1 °C for slow changing thermal reservoirs (e.g. heat sink) and within ±5 °C for the fast changing variables (e.g. Peltier cold side). This means that the accuracy of the model after optimization is fairly good, although the Peltier cold side temperature prediction is not yet within an acceptable range. The development of the PCFH is ongoing and we are looking forward to a first test campaign with controller and comparison with CFH under Arctic conditions at Ny Ålesund, Svalbard, in February 2020.

Zusammenfassung

Wasserdampf ist das vierthäufigste Gas in der globalen Atmosphäre. In gasförmiger Form ist es das wichtigste Treibhausgas, in kondensierter Form - Flüssigkeits- oder Eiswolken - beeinflusst es stark das Strahlungsgleichgewicht und damit das Klima. Darüber hinaus spielt es eine grundlegende Rolle bei der Reinigung unserer Atmosphäre durch das Auswaschen von löslichen chemischen Spezies und bestimmt damit die Luftchemie und die Luftqualität. Seine Variabilität in Vorkommen, Aggregatzustand und vertikaler Verteilung in der Troposphäre und Stratosphäre machen Wissenschaft und Technik der Wasserdampfmessungen zur Herausforderung. Messungen in der oberen Troposphäre und der unteren Stratosphäre sind aufgrund der niedrigen H_2O-Konzentrationen und des adhäsiven Charakters des H_2O-Moleküls, das jede feste Struktur bedeckt, besonders schwierig. Dennoch sind genaue Messungen aufgrund der klimatischen und hydrologischen Auswirkungen von H_2O auch in großen Höhen wichtig.

Wir haben während der StratoClim-Ballonkampagnen 2016-2017 an den Südhängen des Himalaya umfangreiche Erfahrungen mit ballongestützten Frostpunkt-Hygrometern gesammelt und 63 speziell instrumentierte Radiosonden vom tropfnassen Monsun in die sehr trockene Tropopausenregion und Stratosphäre geflogen. Diese Kampagne zeigte systematische Kontaminationsmuster bei stratosphärischen H_2O-Messungen. Von dort aus begannen wir, uns mit langjährigen Fragen und neuen Herausforderungen der Kontaminationsmessung bei Frostpunkt-Hygrometern zu befassen. Neun der 43 mit dem Cryogenen Frostpunkt-Hygrometer (CFH) gemessenen Wasserdampfprofile zeigten Kontaminationen, die stratosphärische H_2O-Messungen unmöglich machten. Drei der neun kontaminierten Sondierungen trugen den COmpact Backscatter AerosoL Detector (COBALD), der Informationen über die Wolken liefert, durch die die Sonden in der Troposphäre flogen. Die wahrscheinlichste Ursache für die Messkontamination sind unterkühlte Flüssigkeitströpfchen in Mischphasenwolken, die auf dem CFH-Einlassrohr gefrieren und anschließend in der trockenen und warmen Stratosphäre sublimieren. Die Modellierung des Wegener-Bergeron-Findeisen-Prozesses der Tröpfchenverdunstung und des Eiskristallwachstums bestätigt die Wahrscheinlichkeit der Koexistenz von unterkühlter Flüssigkeit und Eis in diesen Wolken. Die oszillierende Bewegung der ballongestützten Nutzlast und die Existenz größerer unterkühlter Tröpfchen ermöglichen den Aufbau einer Eisschicht an der Spitze des Einlassrohres. Die wird durch die Analyse der Nutzlastbewegung mittels GPS-Daten und durch Computational Fluid Dynamics (CFD)-Simulationen von Tropfentrajektorien im Ansaugrohr quantifiziert. Durch CFD-Berechnungen mit der Software FLUENT (in der ANSYS Workbench) gleichen wir die Beobachtungen der kontaminierten Wasserdämpfe mit dem Wasserdampf ab, der von einer eisigen Oberseite des Einlassrohrs sublimiert. Zwei der kontaminierten Sondierungen zeigen eine Erholung des Instrumentenbetriebs, d.h. es wurden wieder unkontaminierte Wasserdampfmessungen durchgeführt, bevor der Ballon platzt. Aus diesen Beobachtungen können wir die Menge an sublimiertem Wasser in

der Stratosphäre quantifizieren und den Flüssigwassergehalt (LWC) in den beobachteten Mischphasenwolken schätzen. Wir stellen fest, dass selbst kalte Mischphasenwolken mit wenig LWC den Betrieb der CFH beeinträchtigen können.

Mit Hilfe von CFD können wir zwischen Kontaminationen durch Verdunstung von Eis im Einlassrohr und ausgasender Feuchtigkeit aus der Ballonhaut unterscheiden: Die Größenordnung dieser beiden Arten von Kontaminationen ist sehr unterschiedlich. Die Ballonkontamination wird bei allen Flügen oberhalb des 20-hPa-Niveaus zu einem weit verbreiteten Merkmal. Mit CFD-Simulationen können wir die Wirksamkeit des Einlassrohres bei der Vermeidung einer Kontamination der beprobten stratosphärischen Luft durch Ausgasung von Feuchtigkeit aus dem Instrumentenpaket bestätigen.

Die StratoClim Ballonkampagnen stellen einen einzigartigen Datensatz von CFH-Messungen in der extrem kalten Tropopause des asiatischen Monsunantizyklons mit einer sehr feuchten Troposphäre dar. Aufgrund der Erfahrung im Betrieb von Frostpunkt-Hygrometern unter solchen Bedingungen und dem jüngsten internationalen Verbot der kryogenen Flüssigkeit R23, die von den führenden Referenzgeräten CFH und FPH verwendet wird, haben wir mit der Eigenentwicklung eines neuen ballonbasierten Hygrometers begonnen, des 'Peltier Cooled Frost Point Hygrometer' (PCFH). Die neue Implementierung unterscheidet sich grundlegend in ihrer Gestaltung: zweistufiger Instrumentenaufbau, zweistufiges Peltierelement, Detektionsschema mit Referenzfläche, Luft als einziges Kältemittel. Vor allem unterscheidet sie sich durch ihren modernen Ansatz zur Steuerung der Frost- oder Tauschicht, die im stabilen Zustand, d.h. weder wachsend noch verdunstend, im Gleichgewicht mit dem durchströmenden Wasserdampfgehalt der Luft steht. Die Steuerung eines Frostpunkt-Hygrometers ist die größte Unsicherheitsquelle. In PCFH streben wir die Umsetzung einer optimalen Steuerung an, wie optimalen Parametern, z.B. optimiert als Funktion des Steuerungsaufwands und der Fehlergenauigkeit, und/oder im optimalen Steuerungsgesetz, das das dynamische Verhalten des Systems berücksichtigt. Das Instrument wurde unter Berücksichtigung dieses Ziels entwickelt und anschließend entsprechend seiner Konstruktion und insbesondere seiner thermischen Speicher modelliert.

Wir haben Fünf Prototypen von PCFH montiert und im Labor mit und ohne Luftstrom getestet, was für das Peltierelement aufgrund der thermischen Belastung, die die Strömung darstellt, ein kritischer Aspekt ist. Die Prototypen sind unter Sommer- und Winterbedingungen in den mittleren Breitengraden geflogen, allerdings bisher nur zum Zwecke der Gerätecharakterisierung und noch nicht mit dem Ziel, zuverlässige Wasserdampfmessungen zu erhalten. Da jeder Prototyp aus zwei Untereinheiten besteht, verdoppeln sich die Testmöglichkeiten pro Prototyp, z.B. Test der Leistung alternativer Komponenten wie ein- und zweistufige Peltierelemente, oder schwerere und leichtere Kühlkörper mit unterschiedlicher Anzahl von Kühlrippen. Ziel der ersten Flüge war es, den Nachweis der Machbarkeit zu erbringen und das Systemmodell zu validieren, das für die Umsetzung einer optimalen Steuerung unerlässlich ist. Zu diesem Zweck wurde eine Abfolge von Schritten mit unterschiedlichen Pulsbreitenmodulator-(PWM)-Tastzyklen, die das Gerät als Peltierstrom wahrnimmt, als Input für das System genutzt, um die Übertragungsfunktion des Systems zu erhalten. Diese Art der Charakterisierung ist besonders relevant für die Modellierung der thermischen Speicher des PCFH im Flug und für die Bewertung des Kühlbereichs des Peltierelements nach der Montage in das PCFH.

Nachdem wir die Leistung von zwei- und einstufigen Peltierelementen in der PCFH-Montage verglichen hatten, entschieden wir uns, zweistufige Peltier-Elemente in allen zukünftigen Prototypen

einzusetzen. Dennoch bleibt der Kühlbereich des Gerätedesigns kritisch. Wir demonstrierten die Erreichbarkeit von stratosphärischen Frostpunkttemperaturen, d.h. T_{frost} = -85 °C bei p_{air} = 40 hPa und T_{air} = -60 °C, aber nur für eines der fünf Instrumente. Dies ist zwar ein wichtiger Schritt im Rahmen der Machbarkeitsstudie, aber es gibt bisher keinen Nachweis der Reproduzierbarkeit und eine optimale Kontrolle ist noch nicht implementiert. Das montierte doppelte Peltierelement hat eine maximale Temperatursenkung zwischen der heißen und der kalten Seite von ΔT_{max} = 40 K bei T_{air} = -60 °C erreicht und während der Labortests ohne Luftstrom ΔT_{max} = 65 K, während das Peltier-Elementdatenblatt ein ΔT_{max} = 86 K bei Bodenverhältnissen verspricht (T_{air} = 27 °C und $p_{\mathrm{air}} \sim$ 1000 hPa). Wir führen den Verlust von ΔT in den Labortests ohne Luftstrom gegenüber den Datenblattangaben zurück auf die Montage des Peltierelements in die PCFH. Die Reduzierung um 20 K ist die bisher beste Baugruppe. Sobald ein Luftstrom von $\sim$ 5 m s^{-1} wie bei einem Instrument unter Feldbedingungen hinzugefügt wird, gewinnt die ΔT-Reduktion noch mehr an Bedeutung. Glücklicherweise verringert sich der Strömungseffekt, wenn die Luftdichte mit der Höhe sinkt, was den Reduktionseffekt in ΔT teilweise kompensiert der kältere Betriebstemperaturen des Peltierelements. Darüber hinaus entspricht ΔT_{max} = 40 K bei T_{air} = -60 °C etwa 20 K zwischen Kaltseite und Umgebungstemperatur aufgrund von Verlusten zwischen der Peltier-Heißseite, dem Kühlkörper und der Umgebungsluft.

Die Reflexion der Eis-/Tauschicht auf dem Spiegel reagiert auf die Temperaturdifferenz zwischen der Spiegeltemperatur und der tatsächlichen Frostpunkttemperatur, die wir getestet haben, indem wir zwei der zehn geflogenen Untereinheiten mit einem alternierenden, auf Sollwerte optimierten, proportional-integral-derivativen Regler (PID) ausgestattet haben. Leider waren die gesammelten Reflexionsdaten bisher nicht ausreichend, um die Wasserdampfdiffusionsfähigkeit abzuschätzen, ein Parameter, der für das mathematische Modell der PCFH erforderlich ist. Dennoch haben wir den thermodynamischen Teil des Modells für die erste Prototypenversion optimiert und mit Daten aus dem Flugzeug validiert. Die Übereinstimmung der simulierten Variablen nach der Optimierung mit den gemessenen Temperaturwerten der thermischen Speicher lag innerhalb von ±1 °C für langsam wechselnde thermische Speicher (z.B. Kühlkörper) und innerhalb von ±5 °C für die schnell wechselnden Variablen (z.B. Peltier-Kaltseite). Das bedeutet, dass die Genauigkeit des Modells nach der Optimierung ziemlich gut ist, obwohl die Peltier-Vorhersage der Kaltseite noch nicht in einem akzeptablen Bereich liegt, wenn man bedenkt, dass wir T_{frost} mit einer Genauigkeit von ± 0.25 K messen müssen. Die Weiterentwicklung der PCFH ist im Gange, während wir uns auf eine erste Testkampagne mit Controller und Vergleich mit CFH unter arktischen Bedingungen von Ny Ålesund, Svalbard, im Februar 2020 freuen.

Contents

Chapter 1

Introduction

1.1 Scientific background: water vapour in the atmosphere

1.1.1 Troposphere and Stratosphere

The atmosphere is the gaseous mass that surrounds the Earth. For this work we are interested in the lower part of the atmosphere, which comprises the troposphere and the stratosphere. The troposphere extends form the Earth's surface to the tropopause and is characterized by decreasing temperature with height and strong vertical mixing. The stratosphere starts at the tropopause and extends to the stratopause at about 50 km height and is characterised by increasing temperature with height, high stability and slow vertical mixing.

The WMO (1957) (World Meteorological Organization) tropopause definition is 'the lowest level at which the temperature lapse rate decreases to -2 K km^{-1} or less, provided also the average lapse rate between this level and all higher levels within 2 km does not exceed -2 K km^{-1}'. The height of the tropopause depends on latitude and season: in the tropics it can be as high as 18 km and over the poles as low as 8 km. The temperature in the troposphere decreases almost linearly with height. The troposphere's main heat source is the earth's surface, which in turn is warmed by solar radiation. As air ascends, it cools adiabatically in response to the lower pressure region above. The rate of dry adiabatic cooling is -9.8 K km^{-1} (when no condensation occurs). The air parcel's temperature in relation to its new environment after the expansion process will determine its further ascent.

More than 2/3 of Earth's surface is covered by water. A small fraction of this water (10^{-5}) exists in the atmosphere, almost all of it in the troposphere in the form of water vapour. As air temperature decreases with height so does the ability of air to sustain water vapour, due to the strong dependence of saturation vapour pressure with temperature. After an air parcel has reached saturation (RH = 100%, relative humidity), very small supersaturations suffice to trigger a phase transition and the formation of liquid clouds. The formation of clouds releases latent heat, which counteracts the air parcel cooling and sustains the temperature disequilibrium with surrounding air parcels, propelling the air parcel higher and allowing for more condensation. The resulting moist adiabatic lapse rate in the lower troposphere is -5.5 K km^{-1}. This mechanism generates convective cumulus clouds, which can transport air from the Earth's surface to the upper troposphere within a few hours (Vaughan et al., 2008). The higher reaching convective outflows are in the tropics due to warmer surface temperatures and higher water

content. They might reach up to 17 km height (Vaughan et al., 2008), with overshooting updrafts up to 18 - 19 km (Corti et al., 2008; Dauhut et al., 2015). From this point on, air is radiatively heated under all sky conditions. Below, air is radiatively cooling (subsiding) (Fueglistaler et al., 2009). The tropics is, hence, the gate way of tropospheric air into the stratosphere. Furthermore, this air can then stay in the tropics and rise towards the stratopause or move poleward, a phenomenon known as the tropical pipe. The tropical pipe starts at approximately 20 - 21 km.

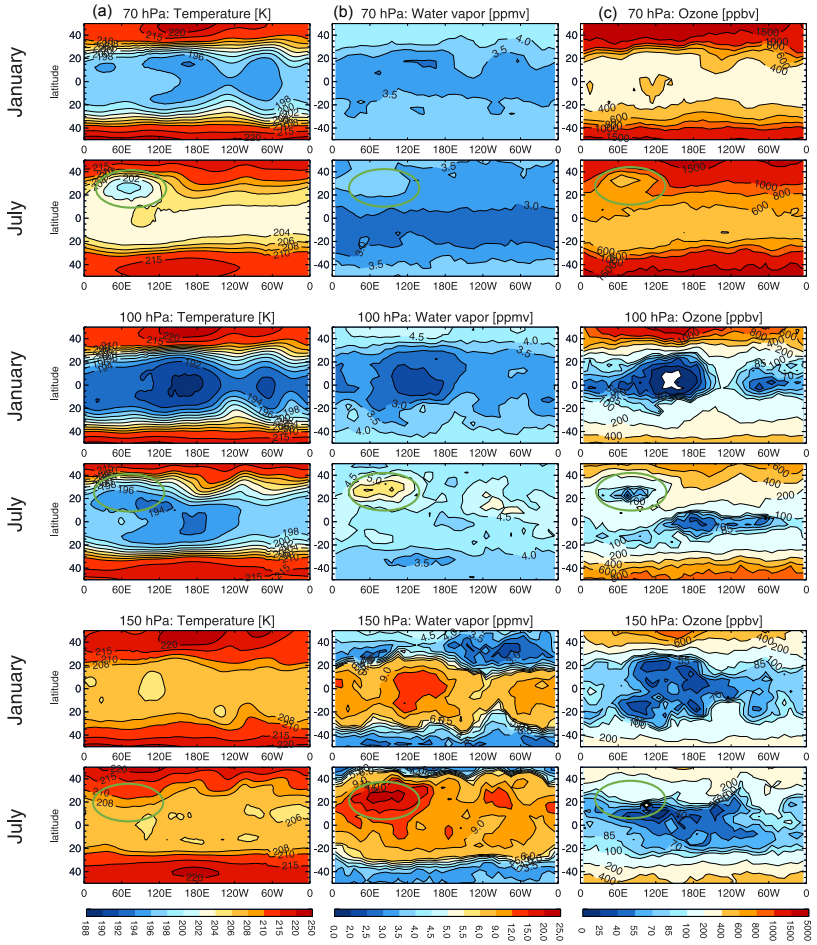

Figure 1.1: Temperature (left), water vapour mixing ratio (center) and ozone (right) at tropopause levels (adapted from Fueglistaler et al. (2009)). The green ovals indicate the region of the Asian Summer Monsoon Anticyclone, which was sampled during the 2016-2017 StratoClim balloon campaigns.

The tropopause region in the tropics extends over several kilometres in thickness, representing a transition layer between the troposphere and the stratosphere, where characteristics of both regimes can be observed. It is referred in the literature as tropical tropopause layer (TTL, sometimes also as tropical transition layer)(Fueglistaler et al., 2009). Together with the midlatitudinal lowermost stratosphere and upper troposphere, the region is referred to as upper troposphere lower stratosphere (UTLS). With such high reaching convective outflows, air temperatures in the TTL may be well below -80 °C; see Figure 1.1 adapted from Fueglistaler et al. (2009). Ice formation and gravitational settling dehydrates the air on average to a water vapour mixing ratio (χ_{H_2O}) of 4 parts per million volume

of air (ppmv). In the deep tropics, the 100 hPa panels for the temperature shows the tropopause to be colder in boreal winter than in boreal summer, and as a consequence in the neighbouring panels we can see more water vapour associated with the warmer conditions than with the colder conditions. The tropical pipe brings this very dry air into the stratosphere. When we look into the water vapour 70 hPa panels in Figure 1.1, we can see the inverse of the panels at 100 hPa: the winter season is wetter than the summer season, a phenomenon known as the tape recorder (Mote et al., 1996; Glanville and Birner, 2017). The panels for July, i.e. boreal summer, provide evidence for the Asian Summer Monsoon (ASM, marked by a green oval), in particular the high water vapour at 150 hPa (∼13 km altitude) indicates the deep monsoon convection. This is still clearly visible at the level of the Asian Monsoon Anticyclone (ASMA) at 100 hPa (∼ 16 km), together with low temperatures and a pronounced minimum in ozone. The maximum in H_2O and the minima in T and O_3 extend all the way to the 70 hPa level (∼ 18 km).

Neither the tropical pipe nor the ASMA are perfectly isolated and a part of the lifted air mixes horizontally with lower stratospheric air of the extra-tropics. Following the principle of mass conservation, air leaving the troposphere to the stratosphere, needs to be replenished. This happens through subsidence of stratospheric air in the mid-latitudes and polar regions. This global circulation is known as the Brewer-Dobson circulation (Brewer, 1949), which is driven by planetary waves propagating from the upper stratosphere to the lower stratosphere and breaking there (Holton et al., 1995).

During its transport through the stratosphere, which takes months to years before returning to the troposphere, the air undergoes chemical reactions. Notably, there is a significant stratospheric in situ source for water vapour from the slow oxidation of methane:

$$CH_4 + OH \longrightarrow CH_3 + H_2O \tag{R1}$$

The methyl radical continues to react readily, eventually leading to complete oxidation via formaldehyde and carbon monoxide to CO_2. The net reaction is:

$$CH_4 + 2\,O_2 \longrightarrow CO_2 + 2\,H_2O \tag{R2}$$

Since the air entering the stratosphere has originally about 1850 ppbv methane, air masses that spend several years in the stratosphere may be moistened by 1-3 ppm due to CH_4 oxidation (depending on the residence times, altitudes and latitudes the air parcel experienced).

1.1.2 Clouds

When moist air masses cool through adiabatic lifting or radiative heat loss and eventually supersaturate sufficiently with respect to liquid water or ice, cloud formation sets in. Clouds play a major role in the Earth's radiation budget. They cool the planet by reflecting sunlight back to space when optically thick at low altitudes and warm the planet by trapping infrared radiation emitted by Earth's surface and reemitting it backwards in the case of optically thin high level clouds (Lohmann et al., 2016). Clouds also redistribute water over the Earth's surface, being a key element in the hydrological cycle. They clean the atmosphere from gaseous and particulate matter through wet deposition and provide a medium for aqueous-phase chemical reaction and production of secondary species. Clouds also

redistribute trace species in the atmosphere through updrafts and downdrafts. Despite much progress in recent years towards a better understanding of cloud formation, much is still uncertain.

In particle-free air, supersaturations of several hundred percent are necessary to form water droplets, as can be shown in laboratory experiments. In the natural atmosphere, pre-existing aerosol particles enable the formation of clouds at much lower saturation ratios. Particles that can activate at a given supersaturation are defined as cloud condensation nuclei (CCN). The resulting supersaturation is typically less than 2%. The CCN may be for example, aerosol particles of soluble salts that dissociate completely as RH exceeds 100%. When they exceed a certain size by water uptake, they are considered activated and the diluted droplets grow freely. CCN may also be water insoluble substances such as dust and combustion products. In the atmosphere it has been observed that liquid clouds can exist at atmospheric temperatures well below 0 °C. These supercooled clouds are quite common, especially with cloud top temperatures down to -10 °C as can be seen in Figure 1.2.

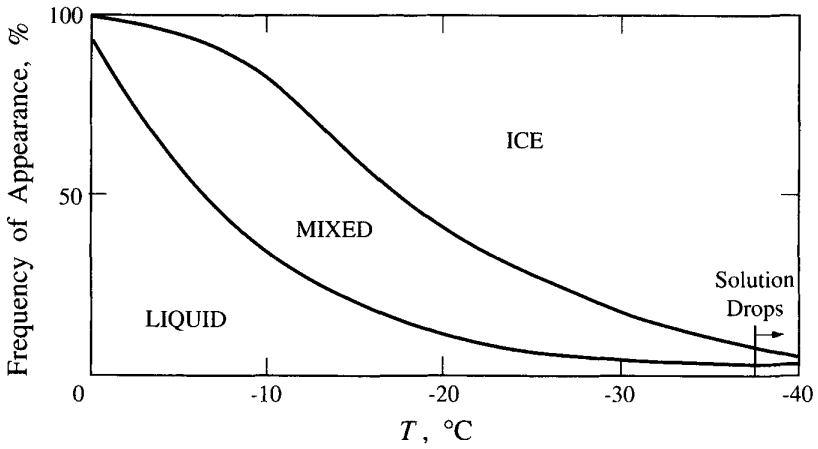

Figure 1.2: Mixed phase clouds frequency of occurrence (from Seinfeld and Pandis (2006)).

The formation of ice particles at temperature above -40 °C requires the existence of Ice Nucleating Particles (INP), and the process is referred to as heterogeneous ice nucleation. Different mechanisms have been explored for ice cloud formation such as immersion freezing, condensation freezing or contact freezing, usually starting with a liquid droplet. INP are usually at much lower concentrations than CCN; they are insoluble and have a chemical affinity and a crystallographic structure similar to ice. With decreasing temperature the percentage of particles that become active INP increases. In this cloud regime between 0 °C and -40 °C, liquid droplets and ice crystal can co-exist, commonly known as mixed-phase clouds, see Figure 1.2. The equilibrium of the three water phases in these clouds–vapour, liquid and solid–exists in four regimes known as the Wegener-Bergeron-Findeisen (WBF) regimes controlled by the vapour pressure over liquid water (saturation ratio S_{liq}) and over ice (S_{ice}) (Korolev et al., 2017).

At temperatures lower than -40 °C, ice can form spontaneously by homogeneous freezing at high supersaturation over ice. This can happen either in (deep) convection, when cooling is very rapid, or at low temperatures in the upper troposphere, leading to clouds that are generally refereed to as in-situ cirrus clouds, and the majority of clouds in the TTL may form homogeneously (Peter et al., 2006). Sometimes the presence of INP in these clouds can be ruled out due to transport constraints of dust or

combustion particles. However, during our StratoClim balloon campaigns we observed extremely thin ice clouds, evidence that many of the cirrus in ASMA must have formed by heterogeneous freezing (Brunamonti et al., 2018). Glassy organic aerosols and meteoritic dust has suggested as potential INP for these clouds.

Clouds are mainly associated with the troposphere; however, in special occasions they can also occur in the stratosphere as is the case in Polar Stratospheric Clouds (PSCs)and may consist of ice crystals, nitric acid trihydrate (NAT) crystals, supercooled solution droplets of $H_2O/H_2SO_4/HNO_3$, or combinations of any of these (Pitts et al., 2009). They can form only under very cold conditions during polar stratospheric winter. PSCs play an important role in activating anthropogenic emissions of ozone depleting substances (ODS) such as chlorofluorocarbons (CFCs), leading to the annual development of the Antarctic ozone hole (Solomon et al., 1986).

1.1.3 Climate change

Water vapour is the strongest greenhouse gas in the atmosphere, trapping long wave infrared radiation emitted by the Earth's surface. However, because emissions of water vapour in the troposphere do not accumulate as is the case for other GHGs, and will rain out with the next rain event, there is–fortunately–no enhanced greenhouse effect from H_2O emissions. Correspondingly, its contribution to radiative forcing (RF) is estimated to be only $+0.07$ W m^2 due to changes in stratospheric methane, see (R1-R2) and the CH_4-bar in Figure 1.3. Its contributions through aerosols and clouds adjustments, however, is vastly uncertain, see Figure 1.3 (IPCC, 2013).

Observations show that stratospheric water vapour concentration increased by approximately 1% per year in the period 1954 to 2000 (Rosenlof et al., 2001), which can also be seen in Figure 1.4. Even though the contribution to the radiative forcing relative to 1750 is small (Figure 1.3), the stratospheric water vapour increase between 1980-2000 is estimated to be responsible for 30% of the rate of global surface warming compared to that resulting from carbon dioxide and other greenhouse gases (Solomon et al., 2010). During the decade of 2000-2009 stratospheric water vapour decreased by 10%, which was shown to slow down the rate of global surface warming by about 25% compared to estimates neglecting this effect (Solomon et al., 2010). Only 25% to 50% of stratospheric water vapour increase in the last decades can be justified by the increase of stratospheric methane. The remaining may be due to transport changes (Rosenlof et al., 2001; Hurst et al., 2011).

Not all climate feedbacks associated with water vapour are well understood. However, it is clear that water vapour plays an important role in the atmosphere and climate systems and further research and monitoring are necessary. This PhD thesis wants to contribute to work on this task.

1.2 State-of-the-art: challenges of water vapour measurements

In the atmosphere, water is neither the most abundant nor the least, but the science and engineering of its measurement has always been challenging. With temperatures in the troposphere as low as -80 °C at the tropical tropopause the range of water vapour measurements is from 30000 ppmv at the surface to 4 ppmv at the tropopause, sometimes even 1 ppmv. Many approaches exist for this measurement.

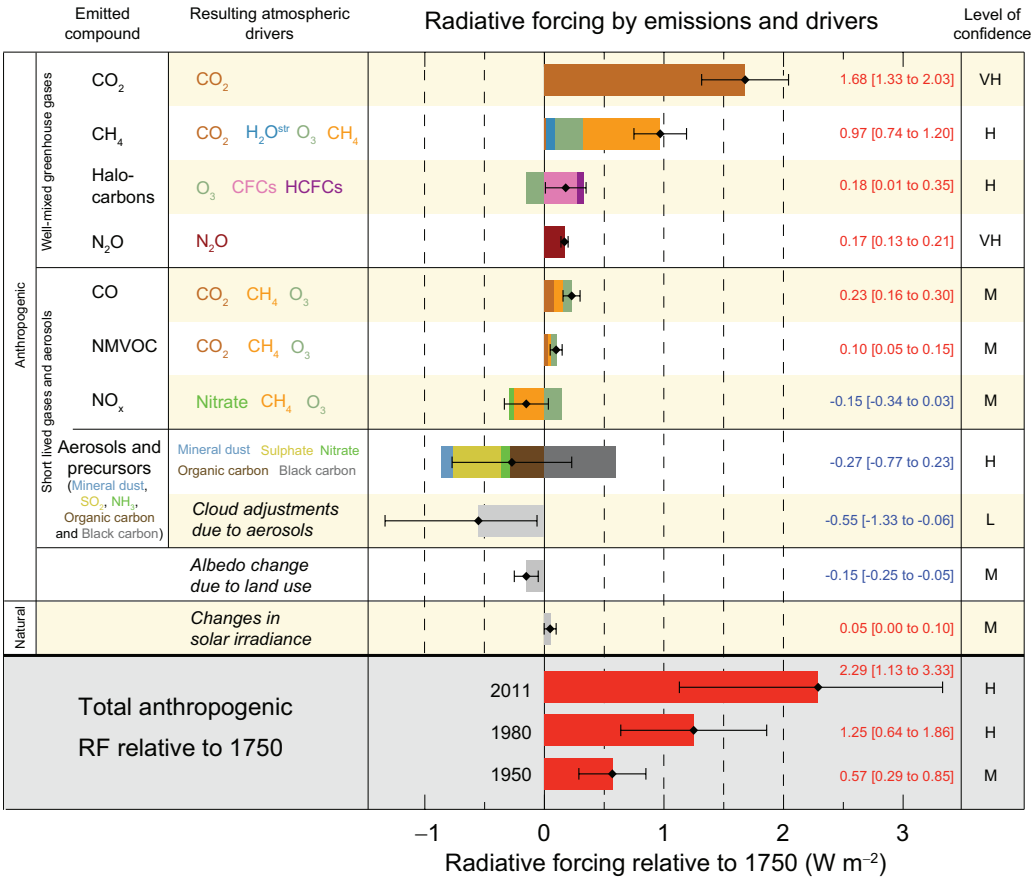

Figure 1.3: Radiative Forcing , i.e. change in the difference between insolation absorbed by the Earth and energy radiated back to space between 2011 and 1750 (from IPCC (2013)

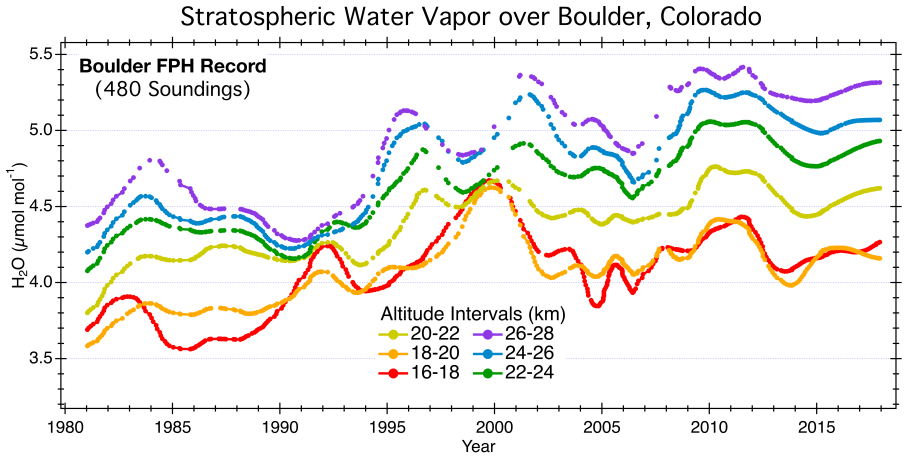

Figure 1.4: Stratospheric water vapour mixing ratios measured by the balloon-borne NOAA Frost Point Hygrometer (FPH) over Boulder, Colorado. Data are averaged in 2-km altitude bins. The long-term net increase through 2013 is approximately 20%. Continued from Hurst et al. (2011) (https://www.esrl.noaa.gov/gmd/ozwv/wvap/, accessed on 2019-09-09).

1.2.1 Technologies for water vapour measurement in the atmosphere

Upper troposphere and lower stratosphere (UTLS) water vapour measurements have been performed on board of various platforms, the most common being balloon (Vömel et al., 2002; Hurst et al., 2011; Dirksen et al., 2014) research aircraft (Vaughan et al., 2008; von Hobe et al., 2013) and passenger aircraft (Petzold et al., 2017) and satellites (Randel et al., 2001; Rosenlof et al., 2001) and ground based remote sensing (Brocard et al., 2013), all of which present their pros and cons. Besides the different platforms also different principles of detection are employed, such as chilled mirrors (Vömel et al., 2007b), tunable diode lasers (TDL) (May, 1998), and Lyman α hygrometers (Vömel et al., 2007c). These are employed mainly as balloon and aircraft-borne instruments for in-situ measurements. In addition, satellite-borne and ground-based remote sensing technology, such as LIDAR (Brocard et al., 2013), is employed. In-situ measurements are essential for the microphysical understanding of physical phenomena, while remote sensing allow for a better understanding of atmospheric humidity on a larger scale. Both methods are intrinsically connected, in-situ validates remote sensing and remote sensing usually sets a larger context for in-situ measurements (Vömel et al., 2007a). The different measurement principles are implemented with different techniques for different instruments. The instruments that are most interesting for this PhD work are balloon-borne chilled mirror hygrometers, for which SnowWhite, CFH, and FPH are the main examples.

When talking about water vapour measurements in the atmosphere it is essential to also mention radiosondes. The instrument principles mentioned above are mainly used for research applications. Since the alternate development of the thin film polymer technique, trade marked as Humicap sensors by Vaisala and followed suit by others, it has been possible to incorporate relative humidity measurements into operational radiosondes. The thin film polymer sensors are widely used and its results are fairly accurate, especially the Humicap by Vaisala, in the lower troposphere region making them ideal as routine meteorological observation instruments (Vaisala, 2013). However, their accuracy is seriously impaired for upper troposphere and stratospheric water vapour measurement, although improvements are made every year, mainly in the course of extensive comparison work with some of the scientific instruments (Survo et al., 2015; Brunamonti et al., 2019).

1.2.2 Water vapour measurements UTLS reference

In 2007, the AquaVIT-1 intercomparison campaign of atmospheric water vapour measurement techniques tested state-of-the-art and prototype atmospheric hygrometers in the aerosol and cloud chamber AIDA at the Karlsruhe Institute of Technology, Germany (Fahey et al., 2014). Still lacking a reliable reference instrument for UTLS conditions (low pressure, low temperatures, and very low water concentrations), the absolute accuracy of the instruments could not be firmly established. Instead, the intercomparison reference value was taken as the ensemble mean of a subset of so-called 'core instruments', which – based on various metrics – were believed to be most reliable. For the tested instruments, the agreement between nominal mixing ratios of 10 and 150 ppmv H_2O is considered good, with variations around the reference of $\pm 10\%$. In the region most interesting for the UTLS, i.e. at H_2O mixing ratios between 1 and 10 ppmv, the agreement between the core instruments was fair, with variations around the reference of $\pm 20\%$. For Fahey et al. (2014), the implication of the AquaVIT-1 campaign for atmospheric measurements was that the large differences observed during

in-flight comparison stem also from the moving platforms and the non-laboratory environments. A second AquaVIT comparison was held in 2014, whose publication is still pending. Without a consensus of the community on a humidity reference for the UTLS, studying some of the outstanding questions such as supersaturations in the tropopause region remains difficult (Fahey et al., 2014).

1.2.3 Ice clouds microphysics

Upper tropospheric observations in clear sky and inside cirrus clouds have shown water vapour mixing ratios exceeding ice saturation values and sometimes even saturation with respect to supercooled liquid water. Relative humidity over ice of more than 200% has been reported from balloon and aircraft measurements in recent years (with uncertainties up to 17%) (Krämer et al., 2009). These observations suggest either a lack of understanding of ice cloud microphysics or that the water measurements are not reliable but suffer from large uncertainties (Krämer et al., 2009). Some of the microphysical explanations offered for the unexpected saturation values are related to a hindrance of equilibration of the supersaturated water vapour: either suppressed nucleation or suppressed growth of nucleated ice crystals due to various potential reasons (Peter et al., 2006). Either way, without more consistent and reliable water vapour measurements in the UTLS, it will be very hard to improve the understanding of the formation and evolution of cirrus clouds.

1.2.4 Frost point hygrometry: a thermodynamic reference?

For balloon-borne measurements in the UTLS, frost-point hygrometers such as the CFH are considered the closest to a reference based on the thermodynamic standard–namely the frost point temperature– used as physical principle of detection. Their use and development dates back to 1940s and the discovery of the stratosphere (Brewer et al., 1948).

The principle of measurement consists of creating and mantaining a condensate, either liquid water or ice, on a chilled mirror. In the absence of growth or evaporation of the condensate, the temperature of the mirror is equal to the dew point or frost point temperature. This is the temperature at which both the vapour and condensed water phases are in thermodynamic equilibrium. By means of the relationship between vapour pressure and temperature, known as Clausius-Clapeyron Equation, it is possible to determine the water vapour partial pressure:

$$\frac{d \ln p_{\mathrm{sta,i}}}{dT} = -\frac{\Delta H_s}{T\,(v_v - v_i)} \tag{1.1}$$

where $p_{\mathrm{sta,i}}$ is the saturation vapour pressure of water over ice, ΔH_s is the molar enthalpy for ice sublimation, and v_i and v_v are the molar volumes of the ice and water vapour (Seinfeld and Pandis, 2006); The parameterisation of this relationship accepted as the most accurate is the parameterisation provided by Murphy and Koop (2005). The classification of this method as a thermodynamic reference can be challenged due to the difficulty of assuring the measured temperature is the actual frost point temperature, due to controlling instabilities, inhomogeneity of deposit phase (liquid or ice) or temperature gradients in the mirror.

1.3 Frost point hygrometer - different implementations

Cryogenic-cooled Frost point Hygrometer (CFH)

Vömel et al. (2007b) developed a new cryogenic frost point hygrometer, which was named CFH. The new instrument's design heavily relies on a previously developed frost point instrument no longer in use referred to as NOAA/CMDL instrument (Mastenbrook and Dinger, 1961; Mastenbrook, 1968; Mastenbrook and Oltmans, 1983; Vömel et al., 1995). The CFH was designed to overcome limitations of its predecessor including a reduction of power consumption, weight (400 g now), cost, and handling skills. The chilled mirror is cooled with a cryogenic liquid, trifluoromethane (R23 - CHF_3). A thermistor is used to measure the mirror temperature. The mirror and cold finger piece are machined from an OFCH (oxygen free high conductivity) copper and gold plated. An infrared LED and a photodiode are used in the configuration shown in Figure 1.5 for control of the condensed substrate. An extra pair of a photodiode and an LED face each other for device temperature deviation tracking and compensation. A phase sensitive detector is implemented to eliminate the spurious solar light contribution in the photodiode. The feedback controller is a proportional-integral-derivative controller (PID), which is implemented digitally with a microprocessor instead of the previously used simple analogue electronics. The tuning of the PID is optimized for measurements during balloon ascent. The PID parameters are frequently updated during the entire flight. However, the controller is still the largest source of uncertainty in the instrument and regulator oscillations in the stratosphere are unavoidable, being only mitigated by averaging (Vömel et al., 2007b, 2016; Kämpfer, 2013).

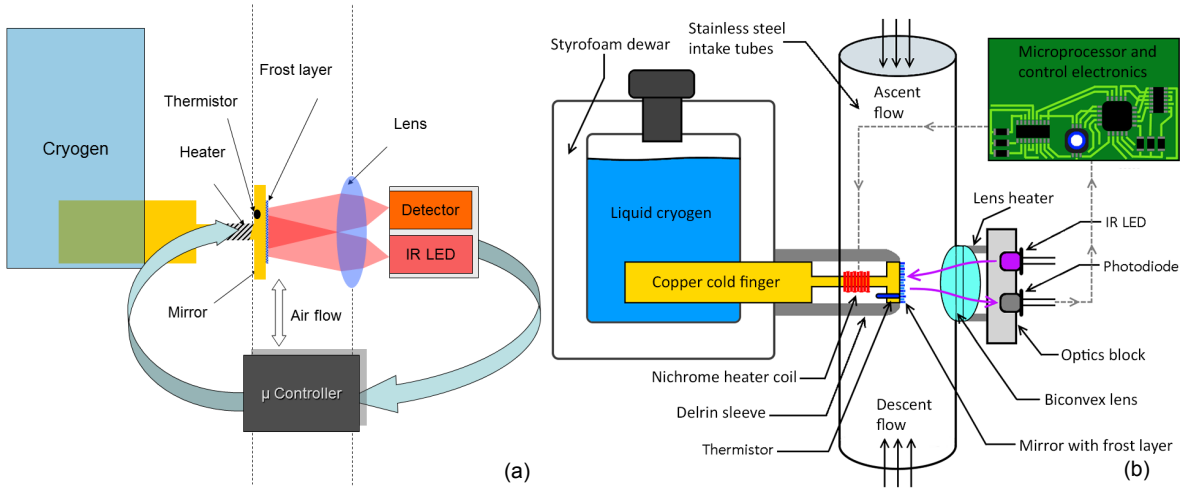

Figure 1.5: (a) Schematic of the CFH sonde. The vertical dashed lines represent the intake and outlet tube (from Fahey et al. (2014)). (b) Schematic of the FPH sonde (from Hall et al. (2016))

Frost Point Hygrometer (FPH)

The FPH construction is very similar to the CFH construction, since both evolved from the NOAA/CMDL instrument. The main differences are an integrated pressure sensor for the implementation of the mirror cleaning cycles, while the cleaning cycles in CFH are activated by temperature of the condensate; the PID schedule parameters and the thermistor calibration process (Hall et al., 2016). The FPH

can be used through a scientific collaboration with NOAA, while the CFH is a commercially available instrument (ENSCI, 2019).

SnowWhite

In 1997, Meteolabor AG Switzerland designed a novel chilled mirror hygrometer named SnowWhite. It uses a single stage Peltier device to cool the mirror. The largest differences between ambient and frost point temperatures obtained by the Peltier cooler are 50 K at +20 °C, 32 K at -30 °C and 22 K at -80 °C (Fujiwara et al., 2003). The temperature on the cold side is measured by a 3 mm×3 mm copper-constantan wire thermocouple plated with gold, which acts also as mirror. The thickness of the condensate is monitored with a lamp, optical fiber, and phototransistor. The electric feedback circuit implements a PID, which automatically controls the power of the Peltier cooler. A large aluminium radiator is essential to cool the hot side of the Peltier. SnowWhite has two versions: a 'day' type and a 'night' type. In the day type version, the sensor housing and radiator are enclosed in Styrofoam to prevent solar heating and stray light contamination. Air is conducted through a duct to the sensor housing. In the night type version, the sensor housing and radiator are directly exposed to the ambient conditions in order to minimize water contamination and outgassing problems. Conversely, the day type has been found to suffer frequently from hydrometers impacting the inlet duct and sublimating causing contamination of the water vapour measurements (Vömel et al., 2003; Vaughan et al., 2005).

SkyDew

Since 2009, SkyDew, a two-stage Peltier-based chilled mirror hygrometer has been under development. The instrument uses the sensor probe of FINEDEW, which is a commercially available chilled mirror developed for industrial purposes with associated U.S. patents (Kanai, 2008b,a, 2010, 2007). A PT100 sensor is located between the mirror and cold side of the Peltier device for frost point temperature measurements. The achieved temperature difference is 55 K at 25 °C and 30 K in the lower stratosphere region. The hot side of the Peltier is cooled by evaporation of ethanol. The intensity of the scattered light is used to monitor the condensate on the mirror. The light is electrically modulated to prevent light contaminations. The main innovation beyond SnowWhite is the implementation of a digital PID controller with a microprocessor to maintain the equilibrium of the condensate. The tuning of the PID followed the 'Ultimate Tuning Method' of Ziegler and Nichols (1942) and some empirical tuning during the test phase (Sugidachi, 2014), a method also used in the CFH and FPH. In 2014 the instrument was taken over by Meisei, the Japanese radiosonde producer. Since 2018, the instrument has had several successful flights with good agreement with CFH and MLS (Microwave Limb Sounder - water vapour measuring satellite) up to 25 km during the night and 15 km height during the day (Sugidachi and Fujiwara, 2018; Sugidachi, 2019).

1.4 Long term stratospheric water vapour monitoring

Balloon borne hygrometers have been flown since 1980 from Boulder, Colorado, USA. First the the NOAA/CMDL instrumen was flown and more recently the FPH. Between 1964 and 1980, the program existed in Washington (D.C.) (Mastenbrook and Oltmans, 1983). Executed for the past 39 years,

these observations are the longest stratospheric water vapour monitoring record (see Fig. 1.4). Similar measurement series with FPH's have been initiated at Lauder, New Zealand, in 2004 and at Hilo, Hawaii, in 2010, i.e. monitoring records of stratospheric water vapour in the southern mid-latitudes and tropics, respectively (Hall et al., 2016).

The GRUAN (GCOS Reference Upper-Air Network) program has been established to provide long-term, highly accurate measurements of the atmospheric profile complemented by ground-based state of the art instrumentation, to constrain spatially comprehensive global observing systems (Immler et al., 2010). The frost-point hygrometer CFH plays an important role in the atmospheric profile measurements in the GRUAN program. Stratospheric water vapour records with the CFH exist at Sodankylä, Finland, since 2002; San José, Costa Rica, since 2005; Lindenberg, Germany, since 2009 and Ny-Ålesund, Svalbard, since 2012. The scientists responsible for both programs agree that a main concern for the consistency and legitimacy of the programs is the intense study of instrumental uncertainties and the traceability of the references (Hall et al., 2016; Vömel et al., 2016).

1.4.1 HFC cryogenic liquid ban

Both the CFH and FPH rely on the CHF_3 cryogenic liquid, a hydrofluorocarbon (HFC). The usage of this liquid is extremely regulated and only allowed for scientific purposes. It is used as an alternative to the even more problematic cryogenic liquids based on CFCs since their ban with the Montreal Protocol. CHF_3 is not an Ozone-Depleting Substance (ODS) but it is a gas with strong Greenhouse Gas Potential (GHGP). In the Kigali Amendments of the Montreal Protocol in October 2016, a deal was reached on a timetable that will mandate countries to phase down the production and usage of HFCs (Kigali, 2016). This poses a serious problem for the research questions introduced above with the instruments available at the moment and makes the need for an alternative approach a very pressing issue.

1.5 PCFH - A new solution

The PCFH is the main outcome of this PhD work. It is an optimally controlled Peltier-cooled frost point hygrometer for water vapour measurements in the UTLS. For its development, we considered what has been accomplished so far in dew/frost point hygrometry. Lessons learnt from SnowWhite, CFH and FPH and new approaches to the open problems are used to implement a more reliable water vapour measurements in the UTLS, hopefully suited as a long term solution.

The development of SnowWhite addressed the described problems of the cryogenically cooled frost point hygrometers by replacing the inconvenient logistics of their handling and insecure perspective of the future use of HFCs for a Peltier element. For a new solution, we maximize the cooling range of an off-the-shelf Peltier element by a careful study of its limitations, behaviour and response to its environment. A good development of SnowWhite was the use of thermocouples. Thermocouples are a more demanding technique in terms of electronics implementation than thermistors but they provide better accuracy and versatility, and they only need to be calibrated once. The PCFH uses thermocouples.

The points where SnowWhite definitely needed improvement was the feedback control loop, which tended to instabilities, and the instrument housing, which was prone to self-pollution (Vaughan et al.,

2005; Cirisan et al., 2014). For these two key design features, we based our design on the CFH, but the goal is to push for improvements beyond CFH for which stratospheric contaminated water vapour measurements are common under tropical and monsoon wet conditions (Brunamonti et al., 2018). In spite of the PID parameters tuned to different water vapour abundance affecting the time response of the system under control, and therefore updated regularly during a flight, the instrument still shows instabilities that are only being addressed by a statistical treatment (Vömel et al., 2016). Substantial progress is expected from replacing the Ziegler and Nichols methods (Ziegler and Nichols, 1942) by a state of the art optimal control scheme (Lewis et al., 2012). Unambiguous identification of self-contamination interferences is targeted by a systematic design of the instrument as double instrument – with two independent sensor heads and intakes and by optimization of the intake tube.

SkyDew followed a very different development direction, by re-using established technology from FINEDEW, implementing a dew/ice detection scheme based on scattered light instead of reflectivity. This allows their design to work without intake tubes. SkyDew does not use cryogenic cooling, but the cooling of the hot side relies on ethanol. This solution is passively implemented, the dispensed flow increases with decreasing pressure (Sugidachi, 2019). For the PCFH implementation we hope to accomplish hot side cooling just with ambient air. We believe this will make the instrument also suited for implementation in long duration balloon flights.

The real challenge

In Figure 1.6, we show air and frost point temperatures obtained by the RS41 and CFH at three different locations: at Nainital, India, (29.38°N, 79.46°E) on the 17 August 2016, a subtropical site during the monsoon season, showing the characteristics of a tropical convective profile; at Lindenberg, Germany, (52.15°N, 14.15°E) on the 25 July 2018 and the 12 December 2018, a mid-latitude summer and winter profiles; and at Ny-Ålesund, Svalbard, (78.92°N, 11.91°E) on 15 November 2018, a polar winter profile. These four profiles give an interesting perspective of the spatial and temporal variability of the temperature and water vapour content in the troposphere, stratosphere, and their transition layer: the tropopause. The highest and coldest tropopause is observed in the tropics on top of the wettest troposphere and below the steepest temperature increase in the stratosphere (Fig 1.6a). The further from the tropics the lower and warmer the tropopause and the smoother the temperature increase in the stratosphere. In mid-latitudes and during polar winter, the temperature does not increase in the stratosphere, but decreases in the lowermost stratosphere due to reduced solar irradiation.

On average, we see from Figure 1.6 that the PCFH should be able to provide 20 to 40 K mirror temperature reduction at any given air temperature at any given pressure to fulfil operational requirements anywhere and whenever in the troposphere and lower stratosphere. These temperature differences are already demanding for Peltier elements. Furthermore, we must consider that for there to be heat transfer from the hot side to the ambient air there will be an additional temperature difference between the two. A big part of this work was optimizing the thermal balance of the PCFH so operation might be possible for all conditions. However, at the time of the reporting of this PhD work the development of the PCFH is not complete. We have flown a total of 5 prototypes and achieved proof-of-concept with one of the implementation which reached temperatures in the range of the frost point temperature up to 40 hPa level.

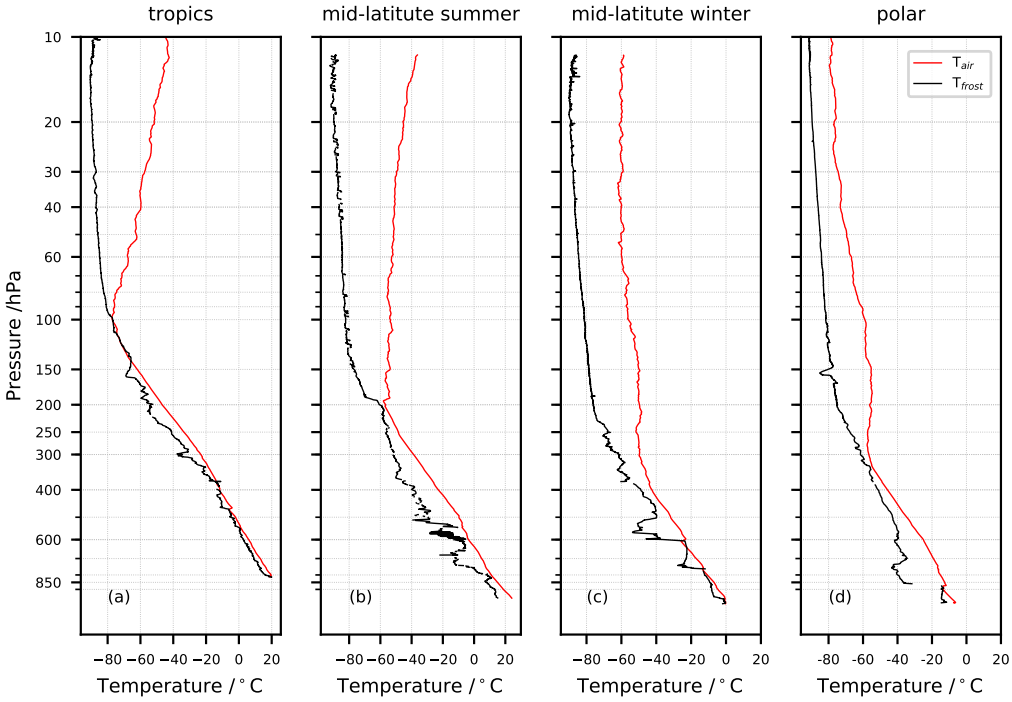

Figure 1.6: Air (T_{air}) and frost point temperature (T_{frost}) from RS41 and CFH at different locations and seasons. (a) 17 August 2016, Nainital India; (b) 25 July 2018, Lindenberg Germany; (c) 12 December 2018, Lindenberg Germany; (d) 15 November 2018, Ny-Ålesund Svalbard.

1.6 Thesis Outline

This thesis is structured as follows. Chapter 2 presents a study for the understanding of contaminated water vapour measurement by frost point hygrometers. The study is based on observations with the CFH during the 2016-2017 StratoClim balloon campaigns at the southern slopes of the Himalayas (Brunamonti et al., 2018) and simulations using computational fluid dynamics (CFD). Chapter 3 contains an instrument description of the PCFH. In this chapter, we provide information on the different components of the instrument and justify their design towards the completion of the instrument objectives. The instrument development was a team effort. In Chapter 4, we present the efforts so far for the implementation of the optimal control of the instrument and introduce the PCFH model. Chapter 5 and 6 present results from first flights, laboratory experiments, and steps towards the optimization and validation of the PCFH model. At the end of this thesis we present a summary of the work so far and an outlook.

Chapter 2

Understanding water vapour concentrations measured by cryogenic frost point hygrometers after contamination by mixed-phase clouds

Teresa Jorge, Simone Brunamonti, Yann Poltera, Frank G. Wienhold, Bei P. Luo and Thomas Peter,
to be submitted to *Atmos. Meas. Tech.*

Abstract

Balloon-borne water vapour measurements in the (sub)tropical upper troposphere and lower stratosphere (UTLS) by means of frost point hygrometers provide important information on air chemistry and climate. However, low in-situ H_2O concentrations and the risk of contamination from evaporating water droplets collected by the intake tube render these measurements difficult, particularly after crossing low clouds containing supercooled droplets. A large set of measurements during the 2016-2017 StratoClim balloon campaigns at the southern slopes of the Himalayas allows us to perform an in-depth analysis of this type of contamination. We investigate the efficiency of wall-contact and freezing of supercooled droplets in the intake tube and the subsequent sublimation in the UTLS using Computational Fluid Dynamics (CFD). We find that the airflow can enter the intake tubes with angles up to 60°, owing to the pendulum motion of the payload. Supercooled droplets with radii > 70 μm, as they frequently occur in mid-tropospheric clouds, typically undergo contact freezing when entering the intake tube, whereas only about 50% of droplets with 10 μm radius freeze, and droplets < 5 μm radius mostly avoid contact. According to CFD, sublimation of water from an icy intake can account for the occasionally observed high water vapour mixing ratios ($\chi_{H_2O} > 100$ ppmv) in the stratosphere. Furthermore, we use CFD to differentiate between stratospheric water vapour contamination by an icy intake tube and contamination caused by outgassing from the balloon and payload, revealing that the latter starts playing a role only at high altitudes ($p < 20$ hPa).

2.1 Introduction

Sources of contamination for cryogenic frost point hygrometers are water vapour outgassing from the balloon envelope, the parachute, the nylon cord, or evaporation of hydrometeors collected in the intake tube of the instrument (Hall et al., 2016; Vömel et al., 2016). These are contamination sources common to all balloon-borne water vapour measurement techniques (Goodman and Chleck, 1971; Vömel et al., 2007c; Khaykin et al., 2013). Contamination can be severe in the stratosphere where the environmental water vapour mixing ratios are 2 - 3 orders of magnitude smaller than in the troposphere. Over time this type of contamination has been reduced by increasing the length of the cord by means of an unwinder and by giving preference to descent over ascent data (Mastenbrook and Dinger, 1961; Mastenbrook, 1965, 1968; Mastenbrook and Oltmans, 1983; Oltmans and Hofmann, 1995; Vömel et al., 1995; Oltmans et al., 2000; Hall et al., 2016). Standard lengths presently used are of the order of 50 to 60 m (Vömel et al., 2016; Brunamonti et al., 2018). The World Meteorological Organization recommends ropes longer than 40 m (WMO, 2008; Immler et al., 2010). Nevertheless, the balloon wake in combination with the swinging motion of the payload has been shown to leave a quasi-periodic signal even in the temperature measurements (Kräuchi et al., 2016). Descent data is not always an option because some instruments intake and control systems are optimized for ascent (Kämpfer, 2013).

The first water vapour measurements in the stratosphere by balloon borne instruments reported a frost point temperature of about -70 °C at 15 hPa (Barret et al., 1949, 1950; Suomi and Barrett, 1952), corresponding to unrealistically high H_2O mixing ratios ($>$ 100 ppmv). Later, Mastenbrook and Dinger (1961) used a new light-weight dew point instrument for frost point measurements in the stratosphere. For the first time, measures to minimize contamination of the air sample with moisture carried aloft by the the balloon were mentioned. The instrument was carried 900 ft, about 275 m, below the balloon assembly and the ascent data was accepted only if validated by the descent data. The descent was achieved by two methods: the use of a big parachute or the use of a tandem balloon assembly. Mastenbrook (1965, 1968) identified contamination of the instrument package as a source of the higher and more variable concentrations of water vapour at stratospheric levels. The surfaces of the sensing cavities and intake ducts were considered as a potential contamination source and redesigned using stainless steel and allowing higher flow rates. These improvements enabled to measure typical stratospheric H_2O mixing ratios of about 4 ppmv. The instruments started being built as absolutely symmetrical for ascent and descent (Mastenbrook, 1966). Mastenbrook and Oltmans (1983) paid particular attention to the intake tubes of the frost point hygrometer. These tubes, until today, are 2.5 cm in diameter, made of stainless steel and need to be thoroughly cleaned before flight. They extend above and below the instrument package by more than 15 cm, shielding the air against the contamination by water outgassing from the instrument's Styrofoam containment.

New designs of frost point hygrometers such as the SnowWhite sonde from Meteolabor, steered away from the intake tube design (Fujiwara et al., 2003; Vömel et al., 2003). However, this design was shown to be susceptible to the ingress of hydrometeors in the intake (Cirisan et al., 2014). The intake duct was actively heated in the troposphere under supersaturation conditions, with the intention to measure the total water content (TWC), i.e. gaseous plus particulate H_2O, instead of just gaseous H_2O mixing ratio, as claimed by the manufacturer (Vaughan et al., 2005). The SnowWhite sonde was also reported to measure saturation over ice (S_{ice}, sometimes also termed $\mathrm{RH}_{\mathrm{ice}}$) in the troposphere

of 120-140% which could not be modelled irrespective of the assumed scenario, leading Cirisan et al. (2014) to conclude the measurement was erroneous and likely created by contamination.

With the increasing miniaturization and ease of use, balloon-borne frost point hygrometers started to be used more systematically at an increasing number of locations and under a wide range of meteorological conditions (Vömel et al., 2002, 2007b; Bian et al., 2012; Hall et al., 2016; Brunamonti et al., 2018), creating new challenges for the instrument. When passing through mixed-phase clouds with supercooled liquid droplets, the balloon and payload surfaces can easily accumulate ice which will sublimate in the dry and warm environment of the stratosphere. Intake tubes might represent a preferential surface for this type of contamination (Vömel et al., 2016).

During the 2016-2017 StratoClim balloon campaigns on the southern slopes of the Himalayas, 43 out of a total of 63 soundings carried water vapour measurements by means of the Cryogenic Frost point Hygrometer (CFH; see Vömel et al. (2007b, 2016)) and of these 9 showed strongly contaminated water vapour measurements in the stratosphere. These 9 soundings are shown in Figure 2.1 (see also grey points in Fig. 2 of Brunamonti et al. (2019)). This is not exceptional, but a normal occurrence when the troposphere is very moist, such as during tropical deep convection [Holger Vömel, personal communication, 2016]. It requires a careful quality check of the CFH data before their use in scientific studies, representing a source of uncertainty, especially in the lower stratosphere. This artifact can also lead to systematic biases, as it causes the operators to give preference to dryer launching conditions which can affect satellite validation procedures and climatological records (Vömel et al., 2007a).

Here, we perform a thorough analysis of this type of contamination. In Section 2.2, we present the data of the 9 contaminated cases, select cases with suitable cloud information from the COmpact Backscatter AerosoL Detector (COBALD) (Brabec et al., 2012; Brunamonti et al., 2018), and analyse mixed-phase cloud conditions (Korolev et al., 2017). In Section 2.3, we describe cloud-traversing balloon trajectories and estimate the payload oscillatory movement and impingement angles of super cooled droplets with the top of the intake tubes. Section 2.4 introduces the Computational Fluid Dynamic (CFD) tool FLUENT by ANSYS (2012). In Section 2.5, we present the results of the different CFD studies, namely: Section 2.5.1 for the freezing efficiency of supercooled droplets in the intake tube based on the oscillatory movement of the payload; Section 2.5.2 for the CFD-based description of the sublimation process causing the exaggerated H_2O mixing ratios, and the evolution of the ice layer as it sublimates; Section 2.5.3 for the implications for the measurements in the upper troposphere between the mixed-phase cloud and the tropopause; and Section 2.5.4 for the simulation of the contamination stemming from the balloon envelope and instrument packaging. Finally in Section 2.6, we provide design and operation recommendations to decrease the effect of contamination.

2.2 StratoClim Balloon Campaigns

Brunamonti et al. (2018) offered an overview of the instrumentation and dataset collected during the 2016 - 2017 StratoClim balloon campaigns on the southern slopes of the Himalayas, deriving a comprehensive understanding of the morphology and large-scale dynamics of the Asian Summer Monsoon Anticyclone (ASMA). Here, we focus on humidity measurements in the cold upper troposphere and tropopause region, including the measurement of mixed-phase clouds and ice clouds, providing brief instrument descriptions.

2.2.1 CFH and RS41 Water Vapour Measurements

The two instruments measuring water vapour content in this study are the radiosonde RS41-SGP (herein after referred to as 'RS41') manufactured by Vaisala (2013), Finland, and the Cryogenic Frost point Hygrometer, CFH (Vömel et al., 2007c, 2016) manufactured by ENSCI. The RS41 measures relative humidity (RH) by means of a thin film capacitive sensor. The RS41 has a nominal uncertainty in soundings of 4% for temperature warmer than -60 °C (Vaisala, 2013). In this study, we use the 'RH corrected data', which Vaisala offers by implementing an empirical time lag correction, accounting for the operation of the capacitive sensor under heated conditions by $\Delta T = 5$ K above ambient temperature and correcting for irregularities determined by the automatized ground check. In contrast to RS41, CFH measures the frost point temperature (T_{frost}). It controls the thickness of a dew or frost layer on a mirror by heating the mirror against a cold sink - a reservoir of cryogenic refrigerant liquid. When the dew or frost layer is in thermal equilibrium with the air mass water content, i.e. neither growing nor evaporating, the dew point or frost point temperature is a direct measure of the H_2O partial pressure in the gas phase. The uncertainty of CFH has been estimated to be smaller than 10% in water vapour mixing ratio up to approximately 28 km altitude (Vömel et al., 2007c, 2016).

The performance of the two instruments during the 2016 - 2017 StratoClim balloon campaigns has been thoroughly compared and a dry bias of 3-6% (0.1-0.5 ppmv) for 80-120 hPa, and 9% (0.4 ppmv) for 60-80 hPa of the RS41 compared to the CFH was found (Brunamonti et al., 2019). These are campaign mean results, whereas flight by flight discrepancies as large as 50% can occur. In previous publications of this dataset (Brunamonti et al., 2018, 2019), contaminated measurements in the stratosphere were discarded using an empirical threshold. In particular, all data above the cold-point tropopause (CPT) were flagged as contaminated, if H_2O mixing ratio exceeds 10 ppmv at any altitude in the stratosphere. In addition, all data at pressures below 20 hPa were also discarded, due to suspected contamination by the balloon or payload train. With decreasing pressures in the 20-60 hPa range, all RS41 measurements show an unrealistic increase in H_2O mixing ratios up to several tens of ppmv (Brunamonti et al., 2019). We do not consider this behaviour to be due to contamination. The capacitive sensor of RS41 is constantly heated to 5 °C warmer than ambient air preventing icing of the sensor in supercooled clouds and supersaturation conditions. Rather, the operation of capacitive sensors is limited at very low relative humidity (Vaisala, 2013).

In contrast to (Brunamonti et al., 2018, 2019), we do not remove CFH clearing and freezing cycles (Vömel et al., 2016), which occur twice per flight at approximately -15 °C and -53 °C frost point temperature, because this gives us confidence that the phase of the deposit in the mirror after the clearing cycle is ice. The ice saturation ratio S_{ice}, i.e. relative humidity with respect to ice, is calculated using the frost point temperature measured by CFH, the air temperature measured by RS41, and the parameterisation for saturation vapour pressure over ice by Murphy and Koop (2005). While relative humidity with respect to liquid water ($\text{RH} = S_{\text{liq RS41}}$) is a direct measurement from RS41, we also present relative humidity (S_{liq}) computed from CFH frost point temperature, RS41 air temperature and the parameterisation for saturation vapour pressure over water by Murphy and Koop (2005). $S_{\text{liq,d}}$ considers the deposit on the CHF mirror to be dew, i.e. liquid water, and $S_{\text{liq,f}}$ considers the deposit to be frost, i.e. ice. Water vapour mixing ratio ($\chi_{\text{H}_2\text{O CFH}}$) in ppmv from the CFH is calculated from the frost (or dew) point temperature, the air pressure from RS41 and the parameterisation for saturation vapour pressure over ice (or liquid water) by Murphy and Koop (2005). Water vapour mixing ratio

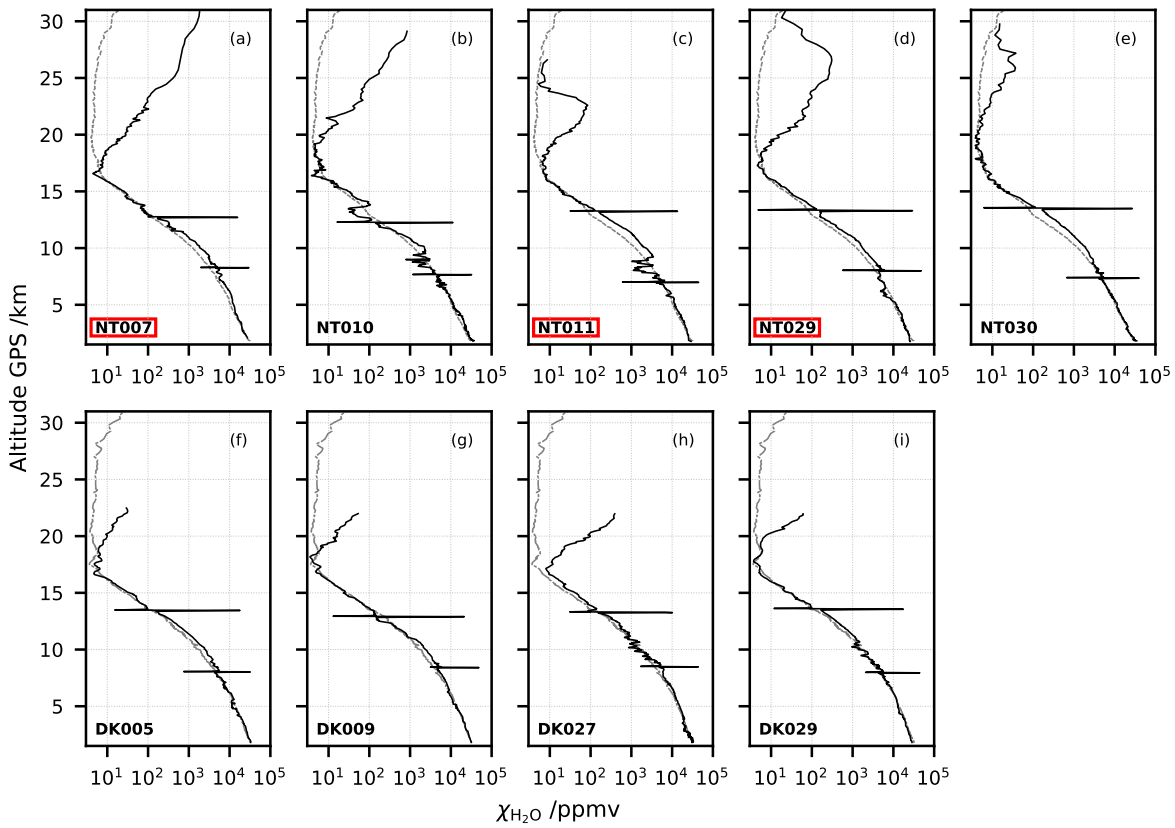

Figure 2.1: Nine water vapour mixing ratio profiles from CFH showing contaminated values in the stratosphere out of 43 profiles taken during the 2016 - 2017 StratoClim balloon campaigns at the southern slopes of the Himalayas. (a-e) Campaign in Naintal (NT), India, summer 2016. (f-i) Campaign in Dhulikel (DK), Nepal, summer 2017. Black lines: individual profiles with identifier in the respective panel. Grey lines: respective campaign season average (mean of 22 (NT) or 7 (DK) uncontaminated profiles) as shown in Brunamonti et al. (2018). Two spikes per profile: instrumental freezing and clearing cycles. Highlighted in red: three night time launches with CFH and COBALD, which are further investigated in this study.

in ppmv for the RS41 ($\chi_{H_2O\,RS41}$) uses the relative humidity, air temperature, and air pressure from RS41 and the parameterisation for saturation vapour pressure over water by Hardy (1998) as used by Vaisala (2013).

In this work, we average the atmospheric data in 1 hPa intervals (bins) from the ground to the burst altitude. All data presented were taken during balloon ascent, because this is the part of the flight affected by contamination. The downward looking intake does not get contaminated by hydrometeors during mixed-phase cloud traverses. For the analysis of the payload pendulum oscillation, we use 1 s GPS data retrieved from RS41. We also use GPS altitude as the main vertical coordinate for all instruments. The ascent velocity (w) in m s^{-1} and latitude and longitude in $^\circ$ are taken directly from the RS41 GPS product.

During the 2016 - 2017 StratoClim balloon campaigns we performed a total of 63 balloon soundings, namely 35 in 2016 from Nainital (NT), India, and 28 in 2017 from Dhulikhel (DK). Of these soundings,

43 carried CFH, of which 20 were performed at night, also carrying COBALD, so that liquid and ice clouds in the lower and middle troposphere can be detected. Figure 2.1 shows those 9 out of 43 CFH soundings, which display contamination in the lower stratosphere (black lines) in comparison to the mean uncontaminated profile (gray lines). Three of the 9 contaminated CFH soundings are with COBALD, namely NT007, NT011 and NT029. We will analyse these three soundings in more detail.

In addition, DK027, a contaminated day time flight, shows very anomalous behaviour, likely because the payload flew through a liquid cloud from above 0 °C into the mixed-phase regime glaciating the wet surface on the interior of the intake tube. Since the flight was during the day, in the upper troposphere and stratosphere, radiation heats the intake tube above ambient air temperature and the sublimated water from the intake wall supersaturates the sampled air. This explains the observation of supersaturation in the stratosphere.

2.2.2 COBALD Backscatter measurements

COBALD data are expressed as backscatter ratio (BSR), i.e., the ratio of the total-to-molecular backscatter coefficient. This is calculated by dividing the total measured signal by its molecular contribution, which is computed from the atmospheric extinction according to Bucholtz (1995), and using air density derived from the measurements of temperature and pressure (Cirisan et al., 2014). The COBALD BSR uncertainty as inferred by this technique is estimated to be around 5% (Vernier et al., 2015). For the backscatter data analysis, we present also the Colour Index (CI). CI is defined as the 940-to-455 nm ratio of the aerosol component of BSR, i.e., $CI = (BSR_{940} - 1)/(BSR_{455} - 1)$. CI is independent of the number density; therefore, it is a useful indicator of particle size as long as particles are sufficiently small, so that Mie scattering oscillations can be avoided ($CI < 15$ for aerosol and $CI > 15$ for cloud particles) (Cirisan et al., 2014; Brunamonti et al., 2018).

The CFH / COBALD combination is a powerful tool to investigate cirrus clouds. Although it is impossible to translate the BSR measurements from COBALD with just 2 wavelengths–455 nm and 940 nm–to ice water content (IWC) without additional information about the ice crystal size or distribution, IWC can be constrained for thin cirrus clouds (Brabec et al., 2012). The retrieval of information about droplet size is a matter of size distribution complexity: if it is simple, as in the stratosphere (for aerosols), the mode radius can be estimated from the color index.

In this work; however, we are interested in relatively thick mixed-phase clouds as observed in tropical convection (Wendisch et al., 2016; Cecchini et al., 2017). The backscatter (BS) from dense mixed-phase clouds may saturate COBALD. The saturation can be instrumental or geometric. The two types are hard to differentiate: instrumental can be detected when the raw data signal strength exceeds certain limits - but geometric is the attenuation of the LED light with distance where correction is possible in principle but does not work out in practice. In this context, it is hard to retrieve more information from COBALD than the vertical thickness of these clouds and the indication if they are purely glaciated ($CI \sim 20$) or not.

2.2.3 Flight NT011

We discuss results of the analysis for sounding NT011 in the main body of this paper and the results for NT029 and NT007 in Appendix A.1 and A.2. Figure 2.2 shows the vertical profile of NT011 on 15

August 2016 in Nainital. Figure 2.2a displays the air temperature from RS41 (green), $S_{\text{liq RS41}}$ from RS41 (pink), calculated ice saturation ratio S_{ice} from CFH (blue) and calculated water saturation ratio $S_{\text{liq,d}}$ and $S_{\text{liq,f}}$ from CFH (purple and violet, respectively); note that the condensate on the CFH mirror is forced to turn from dew to frost after the freezing cycle, at T_{frost} = -15 °C. Figure 2.2b shows the H_2O mixing ratio, χ_{H_2O} (red) and the Nainital campaign mean excluding the contaminated CFH measurements (thin black line). Both panels (a) and (b) show 1-s data to illustrate the signal-to-noise ratio (S/N) of the CFH water vapour measurements. Figure 2.2c shows COBALD BSR at 940 nm (red line), BSR at 450 nm (blue) and CI (green).

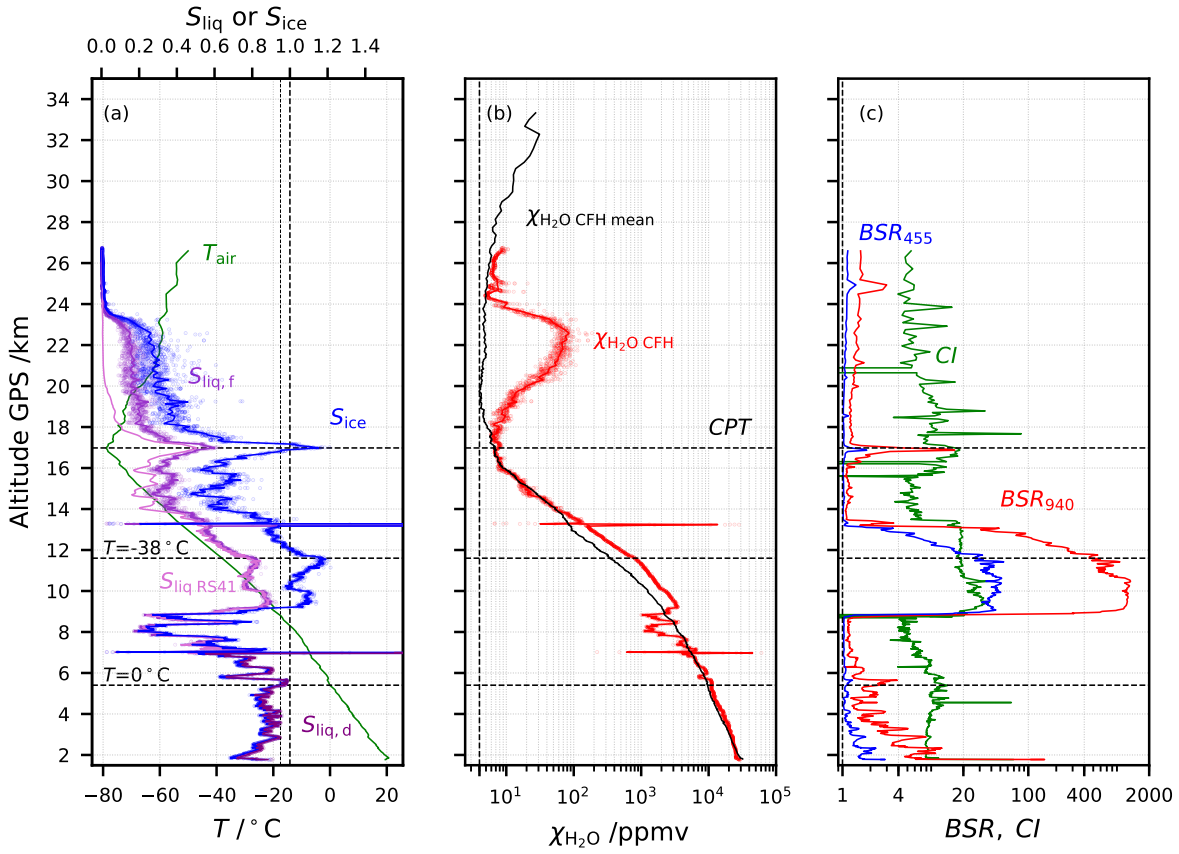

Figure 2.2: Flight NT011 in Nainital, India, on 15 August 2016. Lines: 1 hPa interval averaged values. Dots: 1 s data. (a) Green: air temperature from Vaisala RS41; pink: saturation over water ($S_{\text{liq RS41}}$) measured by RS41; blue: ice saturation (S_{ice}) from CFH, purple: saturation over water ($S_{\text{liq,d}}$) from CFH considering the deposit on the mirror to be dew; violet: saturation over water ($S_{\text{liq,f}}$) from CFH considering the deposit on the mirror to be frost. (b) Red: H_2O mixing ratio from CFH in ppmv; black: average H_2O mixing ratio from uncontaminated CFH for the Nainital 2016 summer campaign (Brunamonti et al., 2018); 'CPT' marks the cold point tropopause. (c) Red: 940-nm backscatter ratio from COBALD; blue: same for 455 nm; green: color index (CI) from COBALD.

In this flight, the lower stratospheric water vapour mixing ratios are unrealistically large, most likely due to contamination, becoming visible right above the CPT, but returning to reasonable stratospheric values below the balloon bursts at 27 km height. COBALD identifies two clouds, one very thin cirrus cloud directly below the CPT (-78 °C) and another geometrically and optically thick cloud in the

range 9 km to 13 km and -20 °C to -50 °C. The lower cloud is sufficiently cold to make a high degree of glaciation likely (Korolev et al., 2003a). However, the CI observed between 9 km and 10 km altitude supports the existence of liquid in this cloud at these altitudes (T = -17...-25 °C). Fully developed ice clouds are characterized by a very regular CI of about 20 with large ice particles, as evidenced in this cloud above 11 km altitude. CI around 30 stems from the Mie oscillations in the transition regime and thus from the presence of smaller and more monodisperse scatterers, most likely supercooled cloud droplets. Additionally, the 940 nm $BSR \sim 1000$ is about as high as can be observed with COBALD before the instrument goes into electronic saturation. As indicated in Figure 2.2, only the lowermost 750 m of the cloud provides evidence for the existence of supercooled droplets at temperatures $T = -17... - 25$ °C. Table 2.1 provides an overview of supercooled or mixed-phase cloud appearances in the three analysed soundings

Table 2.1: Start altitude, length, and estimation of liquid water content (LWC) in mixed-phase clouds for flights NT011, NT029 and NT007.

flights	in cloud			
	start altitude (km)	thickness (m)	LWC (g m^{-3})	
			lower limit	upper limit
NT011	9.25	750	0.011	0.016
NT029	8.1	1000	0.032	0.160
NT007	6.25 and 9.2	750 + 600	0.080 + 0.020	0.137 + 0.034

2.2.4 Modelling of mixed-phase clouds

Supercooled liquid droplets might lead to icing of the balloon and the payload during the passage through mixed-phase clouds, because they freeze upon contact with cold surfaces and may lead to an icy surface coating. In contrast, passages through fully glaciated cirrus are less critical, because the ice crystals likely bounce off the surface. Subsequently, our aim is to learn whether or not the Wegener-Bergeron-Findeisen process provides enough time for NT011 to encounter supercooled liquid droplets at these high altitudes ($>$ 9 km) and low temperatures ($\sim$ -20 °C).

Figure 2.3 shows the air temperature, the balloon ascent velocity, the saturation ratios S_{ice} and $S_{\mathrm{liq,f}}$ relative to ice and supercooled water from the CFH, respectively, and the S_{liq} from RS41, as well as the 940-nm backscatter ratio and the 940-to-455 colour index. The lower part of the cloud (9.25 – 10 km) shows 5 – 10% ice supersaturation but 10% to 15% subsaturation over water. This represents an unstable situation as the ice crystals grow at the expense of the liquid droplets, eventually resulting in a fully glaciated cloud with $S_{\mathrm{ice}} = 1$ (Korolev et al., 2017). At altitudes above 10 km, the balloon encountered $S_{\mathrm{liq}} < 0.8$, i.e. liquid droplets cannot survive for long.

In order to estimate the glaciation time (τ_g) we apply a simple evaporation model based on the solution of the diffusion equation for diffusive particle growth or evaporation

$$\frac{dr^2}{dt} = 2\, V_{\mathrm{H_2O}}\, D_g\, n_g\, (S-1)\,, \tag{2.1}$$

where r is the droplet or ice particle radius, $V_{\mathrm{H_2O}}$ is the volume of a H_2O molecule in the condensed phase (liquid or ice), D_g is the diffusivity of H_2O molecules in air, n_g is the number density of H_2O

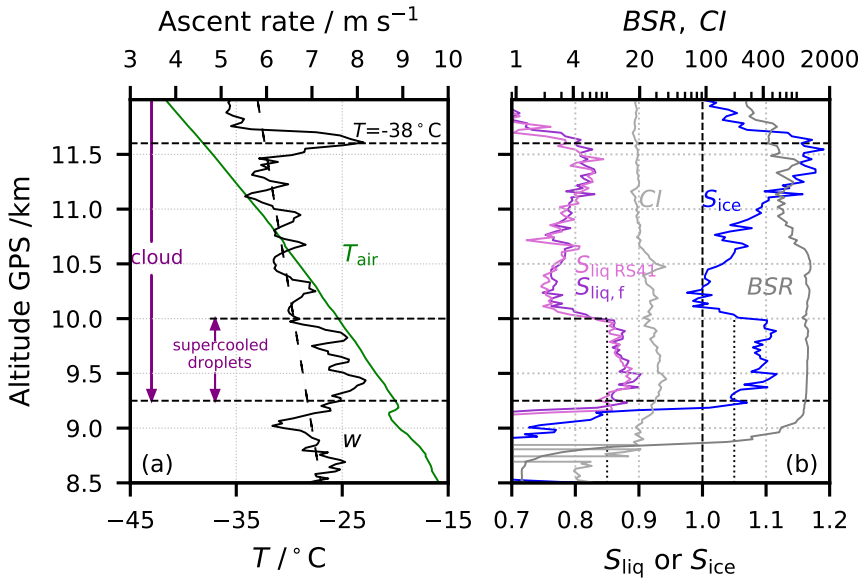

Figure 2.3: Mixed-phase cloud detail of flight NT011. Lines: 1 hPa interval averaged values. (a) Green: air temperature; black: ascent velocity measured by RS41 in m s^{-1}. (b) Pink: saturation over water ($S_{\mathrm{liq\,RS41}}$) measured by RS41; violet: saturation over water ($S_{\mathrm{liq,f}}$) from CFH considering the deposit on the mirror to be frost; blue: ice saturation (S_{ice}) from CFH; dark grey: 940-nm backscatter ratio from COBALD; light grey: color index (CI) from COBALD. Horizontal dashed lines mark supercooled droplet region and T_{air}= -38 °C.

molecules in the gas phase, and S is the saturation ratio of water vapour over liquid water or ice. Equation 2.1 is a simplified form of Eq. 13-21 of Pruppacher and Klett (1997).

We model the Bergeron-Findeisen process in these clouds by applying Eq. (2.1) to both the evaporating droplets ($S_{\mathrm{liq}} < 1$) and the growing ice crystals ($S_{\mathrm{ice}} > 1$). We chose the size distribution of the liquid droplets to be bimodal, to approximate in-situ observations of broad droplet spectra in mixed-phase clouds (Korolev et al., 2017), with small liquid droplets $r_{\mathrm{liq,1}} = 10$ μm, $n_{\mathrm{liq,1}} = 10$ cm^{-3} and big liquid droplets $r_{\mathrm{liq,2}} = 100$ μm, $n_{\mathrm{liq,2}} = 0.003$ cm^{-3}. We considered the number density of ice crystals to be consistent with ice nucleation particles (INP) at about 0.02 cm^{-3} (DeMott et al., 2010), neglecting secondary ice production processes, which may enhance ice number densities (Lawson et al., 2017), but are highly uncertain. During the evolution of the mixed-phase under the conditions characteristic for the lower end of the cloud in NT011 (9.25 – 10 km), the many small liquid droplets evaporate first, providing favourable conditions for the fewer large droplets, which need about 20 minutes to finally evaporate, see Figure 2.4.

The low concentration of ice crystals and the bimodality of the liquid droplet distribution allows the bigger droplets to exist for a relative long period of time in a mildly subsaturated environment ($S_{\mathrm{liq}} \sim 0.90 - 0.85$). For the simulation, we assumed two different initial distributions: a lower and an upper limit of liquid water content (LWC), see Table 2.1. The lower limit is constrained by the amount of water required to sublimate in the stratosphere from the CFH intake tube in order to explain the observed contamination as determined by the Computational Fluid Dynamics simulations discussed in the next sections. The upper limit was determined such that it would provide the sum of the amount

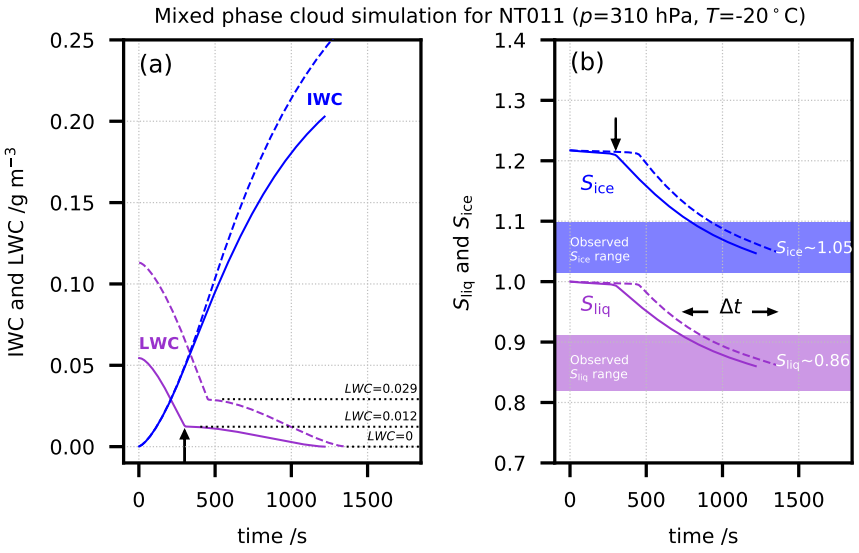

Figure 2.4: Modelling of the Wegener-Bergeron-Findeisen process in mixed-phase cloud demonstrating that flight NT011 likely flew through supercooled liquid droplets. Solid lines: lower limit of liquid water content (LWC). Dashed lines: upper limit (see text). Initial size distributions for lower limit simulation: $n_{\mathrm{ice}} = 0.02$ cm^{-3}, $r_{\mathrm{ice}} = 10$ μm; $n_{\mathrm{liq},1} = 10$ cm^{-3}, $r_{\mathrm{liq},1} = 10$ μm; $n_{\mathrm{liq},2} = 0.003$ cm^{-3}, $r_{\mathrm{liq},2} = 100$ μm. Initial size distributions for upper limit simulation are identical but with 50 % larger $n_{\mathrm{liq},1}$ and $n_{\mathrm{liq},2}$. (a) Blue lines: ice water content (IWC); purple lines: liquid water content (LWC); (b) Blue lines: ice saturation ratio (S_{ice}); purple lines: liquid water saturation ratio (S_{liq}) for lower and upper limits. Glaciation times of small droplets $\tau_{g,1} \sim 6$ minutes, of big droplets $\tau_{g,2} \sim 17$ minutes. Shaded saturated ratios: observed ranges from Figure 2.3. Vertical arrows: time when smaller liquid droplets fully evaporated. The computed time interval with S_{ice} and S_{liq} matching flight observations is $\Delta t \sim 7$ minutes.

of water sublimated in the stratosphere plus the amount sublimated in the upper troposphere, the latter computed from the difference between $\chi_{\mathrm{H_2O}}$ from RS41 and $\chi_{\mathrm{H_2O}}$ from CFH. These limits will be discussed more thoroughly in Sections 2.5.2 and 2.5.3.

Figure 2.4 shows the results of this simulation. Both, the simulation with lower (solid lines) and upper (dashed) limits show glaciation times of smaller droplet mode of $\tau_g \sim 6$ minutes, of the bigger droplet mode of $\tau_g \sim 17$ minutes. The overlap with the range of observed S_{liq} and S_{ice} (shaded purple and blue, from Figure 2.3) lasts for some 7 minutes, demonstrating that the cloud at 9.25 – 10 km in NT011 may have contained sufficient supercooled liquid to explain the contamination.

While these simulations support a causal relationship between the mixed-phase cloud and the CFH intake contamination, the necessary assumptions on the cloud properties make them hypothetical. However, the updraft cores of the colder clouds observed by Lawson et al. (2017) over the Colorado and Wyoming high plains support these assumptions, as these clouds did not experience the secondary ice process and significant concentrations of supercooled liquid in the form of small drops have survived temperatures as low as -37.5 °C. Observed ice crystal number densities were lower than 4 cm^{-3} in clouds warmer than -23 °C, increasing to 77 cm^{-3} at -25 °C and to several hundred per cm^{-3} at even lower temperatures. Thus, some of the clouds described by Lawson et al. (2017) contain fewer ice

particles and more supercooled droplets than in the exemplary case treated here.

2.3 Balloon pendulum movement

As we will show below by means of computational fluid dynamics (CFD) simulations, the passage through clouds containing supercooled water leads to hardly any collisions of the droplets with the walls of the intake tube, if the airflow is parallel to the walls. Under these conditions, only the mirror extrusion causes collisions of larger droplets. Below the mirror extrusion, a recirculation cell may also cause some of the smaller droplets to collide, however this hardly affects the humidity measurement on the mirror. The situation changes dramatically when the air enters the intake tube at an angle, which happens when pendulum oscillations of the balloon payload induce a component of the payload motion perpendicular to the tube walls. Such swinging or rotational motion has been documented in the literature (e.g., Kräuchi et al., 2016). Subsequently, we approximate the balloon plus payload by a two body system connected by a weightless nylon cord, and quantify the oscillations in terms of the instantaneous displacement of the payload from the balloon path. We then use the displacement angle and the associated horizontal velocity of the payload to quantitatively estimate the internal icing of the intake tube.

2.3.1 Pendulum oscillations derived from GPS data

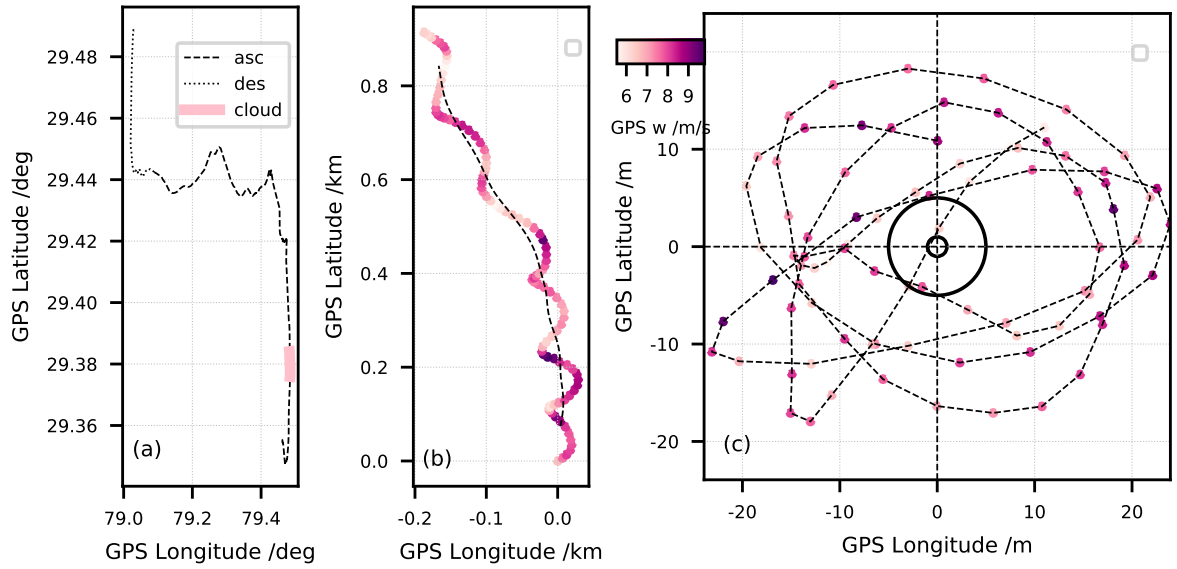

Figure 2.5: Pendulum analysis for this section of flight NT011 traversing the mixed-phase cloud. (a) Payload trajectory for entire flight: ascent (dashed), descent (dotted) and mixed-phase cloud between 9.25 and 10 km height (thick rose line). (b) Zoom in on the mixed-phase cloud with 1-second GPS data of payload trajectory (symbols) and derived balloon trajectory (dashed). (c) Detrended payload oscillations; approximate balloon sizes on the ground (r = 1 m) and at burst (r = 5 m) are shown by two circles. Colour code in (b) and (c): balloon ascent velocity.

We isolate the payload oscillations in relation to the balloon by removing the averaged trajectory

of the payload. Figure 2.5a shows the horizontally projected trajectory of NT011, travelling first about 10 km northward in the troposphere and then about 40 km westward in the stratosphere before the balloon burst. The thick rose line shows the part of the trajectory, where the sonde flew through the cloud containing supercooled droplets, between 9.25 and 10 km height (see Figure 2.3). The contamination happens most likely in this segment of the flight (see below). The coordinates have been transformed from degrees lat/long to distances in km using the geographical distance equation from a spherical earth to a plane , $d = R_e \left[(\Delta\phi)^2 + (\cos(\phi_m)\,\Delta\lambda)^2 \right]^{1/2}$ (Wikipedia, 2018), where the bottom of the cloud (λ_0, ϕ_0) is taken as the origin (0,0) of this new coordinate system. Differences in longitude and latitude are calculated in radians as $\Delta\lambda(t) = \lambda(t) - \lambda_0$ and $\Delta\phi(t) = \phi(t) - \phi_0$, respectively. Distances d are given in km, R_e is the Earth radius (6371 km), and the mean latitude ϕ_m is taken as ϕ_0.

Figure 2.5b zooms in on this cloudy section, showing the 1-s GPS data colour-coded by the ascent velocity in m s^{-1}. Figure 2.5c shows the residual payload motion relative to the balloon after 'detrending', i.e. subtracting the average trajectory of the payload (black dashed line in Figure 2.5b). We obtained the average payload trajectory or balloon trajectory by smoothing the payload trajectory with a moving average corresponding to the pendulum oscillation period, which we evaluated by two independent methods. First by considering the ideal pendulum oscillation frequency, $\omega = (g/L)^{1/2}$ where L is the length of the pendulum, in our case 55 m and $g = 9.81$ m s^{-2}. This yields the oscillation period $\tau = 2\pi/\omega$ =15 s. Second, we confirmed this result by means of a Fast Fourier Transform (FFT) analysis on the latitude and longitude detrended time series, see Appendix A.3. We conclude that independently of the moving average used to detrend the longitude and latitude used in the FFT, the oscillation period is $\tau \sim 16.6$ s.

Figure 2.5c shows the residual motion of the payload after detrending. We see that the radial displacement R of the payload in relation to the balloon position is typically larger than 5 m (only 4% of the measurements have $R < 5$ m). The corresponding displacement angle α (see Figure 2.6) is

$$\alpha(t) = \sin^{-1}\left(\frac{R(t)}{L}\right) > 5^\circ \tag{2.2}$$

The maximum displacement is $R_{\max} \sim 23$ m, corresponding to a displacement angle $\alpha_{\max} \sim 25^\circ$. On average, $\langle R \rangle \sim 15$ m and $\langle \alpha \rangle \sim 16^\circ$, which presents a significant deviation from an ideal flow through the tube. The impingement angle of droplets onto the CFH intake tube is partly determined by α. Moreover, the associated horizontal swinging or rotating motion leads to additional sideways impingement, which we will show to be even more important (see next section).

Figure 2.5c also provides information on the degree to which the rubber balloon itself might contribute to the contamination. The approximate balloon sizes at launch and burst are depicted as circles with 1 m and 5 m radius, respectively. The oscillatory movement places the payload typically far outside the balloon wake only sporadically penetrating the wake. The lack of periodic signs of contamination, renders it unlikely that H_2O collected by the rubber skin of the balloon contributes to the observed contamination. However, this behaviour changes above ~27 km, where the H_2O partial pressure becomes sufficiently low and also the swing and rotation of the payload is weaker, so that the balloon outgassing starts to dominate over the natural signal, leading to a systematic contamination in virtually every sounding (see Section 2.5.4).

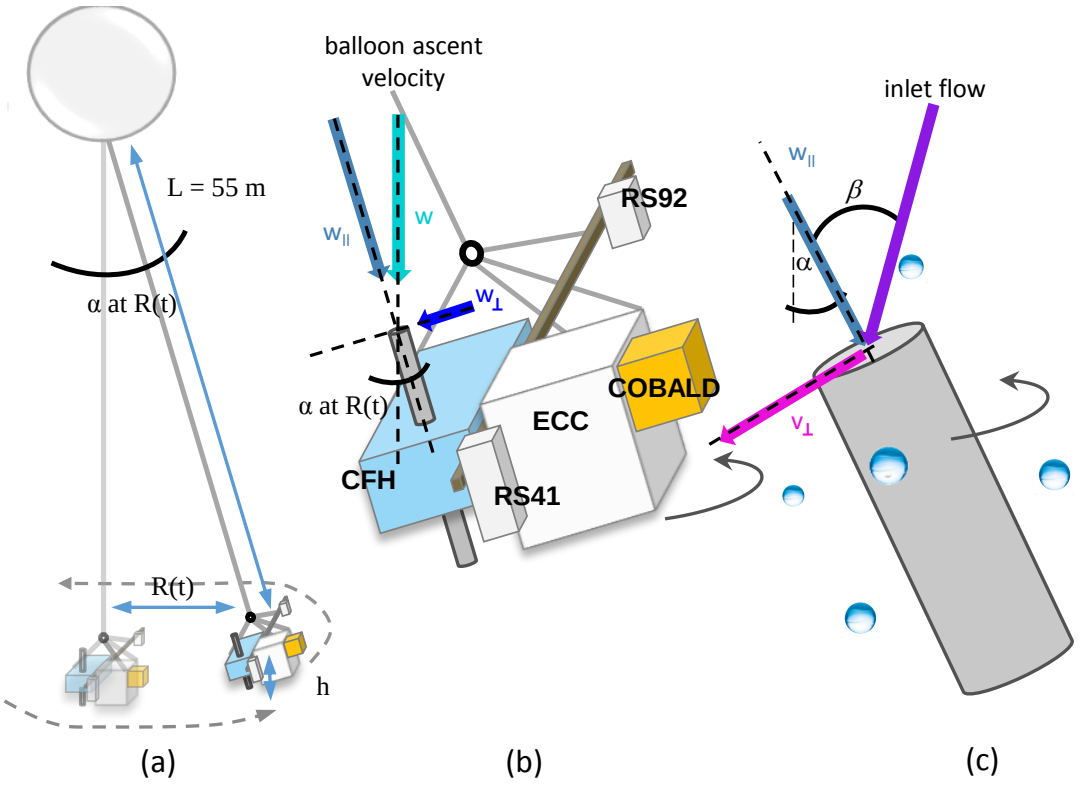

Figure 2.6: (a) Schematic of balloon and payload (not to scale). Payload is connected to the balloon by a 55 m long light-weight nylon cord. Payload oscillates with angles α up to 25°, while balloon ascends. (b) Schematic of payload with the 2 radiosondes (RS41 and RS92), and the 3 instruments (CFH, ECC Ozone and COBALD). The ascent velocity of the payload (w) has a component parallel to the intake tube ($w_{||}$) and a component perpendicular to the tube walls ($w_{\perp}$). (c) From the rotational speed and the tilt of the tube, the horizontal (perpendicular) velocity $v_{\perp}$ of the inlet flow can be determined as well as the impingement angle β.

2.3.2 Impingement angles derived from payload motion

Impingement of droplets onto the walls of the intake tube is forced by two effects:

(i) the tube is tilted relative to the ascent flow, leading to a velocity component $w_{\perp} = v_{\perp,\,\mathrm{tilt}}$;

(ii) the tube itself has a horizontal velocity $v_{\perp,\,\mathrm{rot}}$ caused by the swinging or rotational motion of the payload;

(iii) the combined effect of (i) and (ii) is given by the the vector sum, $v_{\perp} = v_{\perp,\,\mathrm{tilt}} + v_{\perp,\,\mathrm{rot}}$.

In addition, we must take into account the possibility of droplet impingement on the mirror holder in the center of the tube, even when the flow is perfectly aligned to the tube, but compared to (i)-(iii) this is a smaller contribution (because larger droplets will impinge already at the beginning of the tube and many of the smaller ones, which make it to the middle of the tube, will be able to curve around the mirror holder and avoid contact).

Figure 2.5c shows that the residual motion of the payload resembles a circular motion with radius $R = 15$ m. Here, we will treat only this simplified case, but provide a full treatment in Appendix D.

The horizontal velocity component $w_\perp = v_{\perp,\,\mathrm{tilt}} = w \sin\alpha$ can be determined from the tilt angle α and the ascent velocity $w \sim 7.5$ m s^{-1} (Figure 2.3a). From Eq. 2.2 with $R(t) = 15$ m and $L = 55$ m yields $\alpha = 16°$ and $v_{\perp,\,\mathrm{tilt}} = 2.1$ m s^{-1}.

The horizontal velocity component $v_{\perp,\,\mathrm{rot}}$ can be calculated from the distance between consecutive measurements after detrending. Measurements are received every second. Figure 2.5c shows that $v_{\mathrm{h,\,rot}}$ can be as small as 2 m s^{-1} far from the equilibrium point straight below the balloon or as big as 10 m s^{-1} when the payload traverses the equilibrium point. The horizontal motion of the payload leads to generally more impingement than the tilt of the tube.

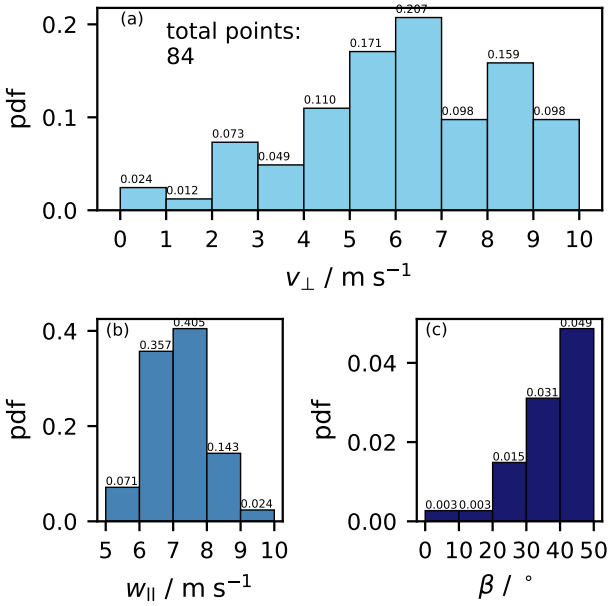

Figure 2.7: Probability density functions (pdf) of impingement parameters at the top end of the CFH intake tube during the passage through the mixed-phase cloud of flight NT011. (a) Velocity $v_\perp$ perpendicular to the tube walls; (b) velocity $w_{||}$ parallel to the axis of the tube; (c) impingement angle (β).

Combining tilt and rotation effects needs to take into account the direction of movement since the oscillation is not linear as a pendulum. As the horizontal impingement speed can be as high as 10 m s^{-1}, this corresponds to a maximum impingement angle $\beta = 53°$ (see Figure 2.6c). This angle might seem surprisingly large, but this is the reason why CFH flying through mixed-phase clouds encounters a large risk of droplet collisions and freezing, accumulating potentially thick ice layers inside the intake tube, which render further measurements in the stratosphere either impossible or possible only after a long recovery period of the instrument. As result from the full numerical treatment of the impingement in Appendix A.4, Figure 2.7 shows the probability density functions (pdf) of the perpendicular velocity ($v_\perp$) to the intake tube walls, parallel component of the ascent velocity ($w_{||}$) and the impingement angle (β) as derived for the intake tube in the 9.25-10.0 km cloud section in flight NT011.

2.4 Computational fluid dynamic simulations

Computational Fluid Dynamics (CFD) tools have become commonly used in environmental studies, e.g. for error estimation of lidar and sodar Doppler beam swinging measurements in wakes of wind turbines (Lundquist et al., 2015), in new designs of photooxidation flow tube reactors (Huang et al., 2017), or to improve vehicle-based wind measurements (Hanlon and Risk, 2018). In our study we use CFD to estimate collision efficiencies of liquid droplets with different sizes encountering the CFH intake tube under various impingement angles in order to understand first the ice build-up and second its sublimation from the icy intake wall to the passing air flow. We use the academic version of FLUENT and ANSYS Workbench 14.5 Release (ANSYS, 2012).

2.4.1 Geometry and mesh

By means of ANSYS Workbench software, a mesh was developed mapping the intake tube geometry and providing the optimal geometric coverage. The geometry is as described by Vömel et al. (2007c) for the CFH intake tubes: a 2.5 cm diameter cylinder that extends for 34 cm. The walls of the intake tube have a thickness of 0.025 mm, but in the modelling are assumed to have no thickness. At the center of the tube the mirror head is mapped by a cylinder extruding from the intake tube wall. The mirror is 7 mm in diameter, 1.25 cm from the wall, perpendicular to the flow.

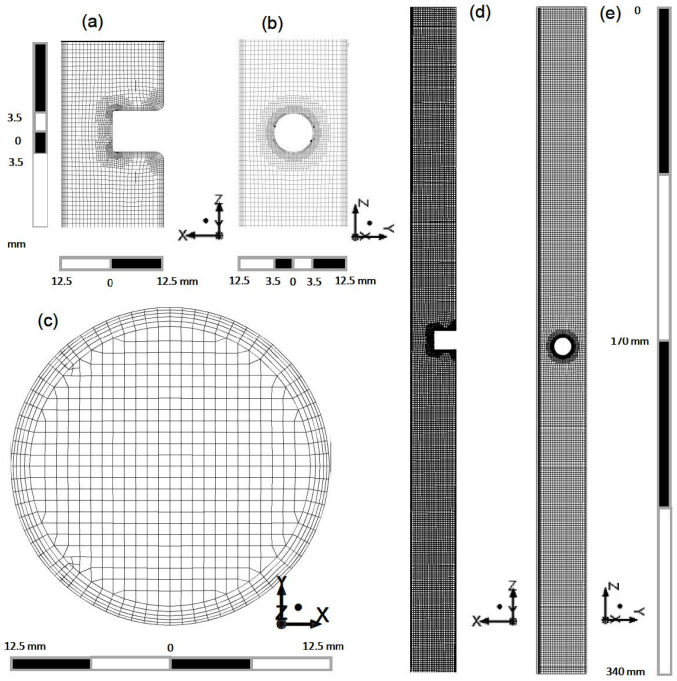

Figure 2.8: Cryogenic frost point hygrometer (CFH) intake tube mesh and geometry. The coordinate origin is located at the top center of the intake tube. (a,b) Detailed views of mirror extrusion on y = 0 and x = 0 planes. (c) Intake tube cross-section. (d,e) Intake tube on y = 0 and x = 0 planes.

The mesh is designed specific for CFD simulations, see Figure 2.8. The mesh assembly method is 'cutcell', which provides organized elements in the flow direction. Simulations have to cover conditions from the lower troposphere, where liquid and mixed-phase clouds occur, to the lower stratosphere

where the sublimation of ice from the intake walls takes place. This requires coping with Reynolds numbers (Re) of the order of 5000 in the cloud to 300 in the stratosphere, accompanied by transitions from turbulent to laminar regimes:

$$Re = \frac{\rho\, v\, L}{\mu}, \tag{2.3}$$

where ρ is the fluid's density in kg m^{-3}, v is the fluid's velocity in m s^{-1}, L is a characteristic linear dimension in m, which in a cylinder is its diameter, and μ is the fluid's dynamic viscosity in kg m^{-1} s^{-1}. We are especially interested in the near wall effects, since the sublimation and the collision efficiency are evaluated near the wall. To enhance the mesh description near the wall, the first layer thickness is 0.2 mm. The subsequent layers grow in thickness at a rate of 1.2 for a total of 5 layers, before the scheme changes from radial to Cartesian coordinates with grid spacing of 1.5 mm.

2.4.2 FLUENT computational fluid dynamics software

We use a 3D steady state pressure-based solver. As recommended for wall-affected flow with small Reynolds numbers, where turbulent resolution near the wall is important, we use a SST (shear stress transport) $k-\omega$ model (CFDWiki, 2011; ANSYS, 2012), including the activation of the energy equation. The fluid material, air, is treated as a three substance mixture of N_2, O_2 and H_2O. We specified how FLUENT computes the material properties, namely calculating density (ρ) using an incompressible ideal gas law

$$\rho = \frac{p_{op}}{RT\sum_i \frac{m_i}{M_i}}, \tag{2.4}$$

where p_{op} is the simulation-defined operating pressure in Pa, R is the ideal gas constant, T is the absolute temperature, m_i and M_i are the mass fraction and molar mass of species i, respectively. Heat capacity (c_p) is calculated using a FLUENT-defined mixing law (ANSYS, 2012):

$$c_p = \sum_i m_i c_{p,i}. \tag{2.5}$$

In the dilute approximation scheme, the mass diffusion flux of a chemical species in a mixture is calculated according to Fick's law (ANSYS, 2012):

$$J_i = \rho D_i \frac{\partial m_i}{\partial x}, \tag{2.6}$$

where D_i is the diffusion coefficient of species i in the mixture. This relation is strictly valid when the mixture composition stays approximately constant and the mass fraction m_i of a species is much smaller than 1. The amount of water expected in the simulations is less than 1000 ppmv, therefore the dilute approximation for the diffusion of water vapour in air, $i = H_2O$, is an accurate description.

The temperature and pressure dependencies of the diffusion coefficient of H_2O in air are given by Pruppacher and Klett (1997)

$$D = 0.211 \frac{\mathrm{cm}^2}{\mathrm{s}} \left(\frac{T}{T_0}\right)^{1.96} \left(\frac{p_0}{p}\right), \tag{2.7}$$

where $T_0 = 273.15$ K and $p_0 = 1013.25$ hPa. For the viscosity and thermal conductivity no mixture laws were considered. The values of viscosity and thermal conductivity were derived from a linear

fit to air viscosity and thermal conductivity of dry air (EngineeringToolbox, 2005). Air viscosity is $\mu_a(T) = (0.0545 \times (T/K) + 2.203) \times 10^{-6}$ in kg m^{-1} s^{-1} and air thermal conductivity is $k_a = 8.06 \times 10^{-5} \times (T/K) + 2.02 \times 10^{-3}$ in W m^{-1} K^{-1} both for $T \in$ (193 K, 300 K), with both properties being only weakly pressure-dependent.

A velocity-inlet and a pressure-outlet boundary condition are defined for the intake tube. For the velocity-inlet boundary conditions, it is possible to define the velocity magnitude and direction, turbulence intensity and temperature.

2.4.2.1 Velocity and flow profiles

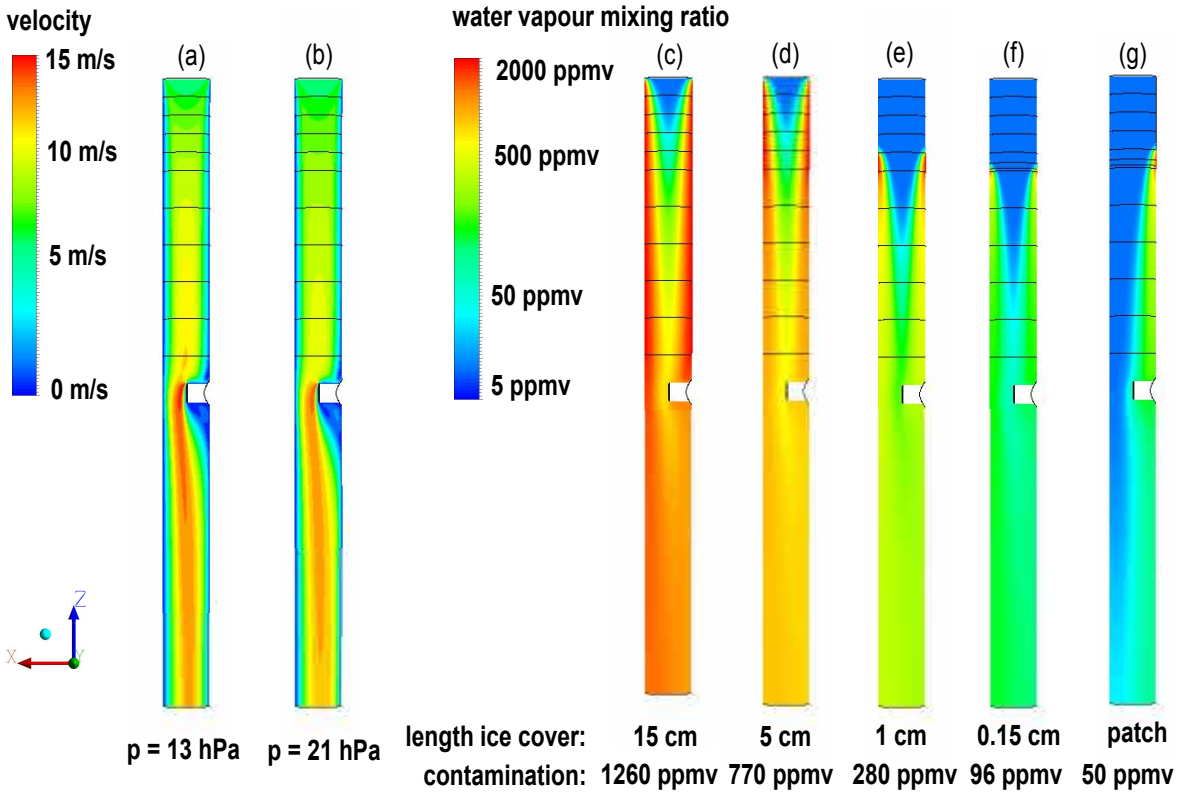

Figure 2.9: FLUENT simulation results for air flow velocity and water vapour sublimation analysis in the stratosphere (plane x = 0, i.e. centre cut through mirror extrusion). (a,b) Air flow velocity contours. (a) p = 13 hPa and T = -48.5 °C and (b) p = 21 hPa and T = -52.8 °C simulations. (c-g) H_2O mixing ratio contour for p = 15 hPa and T = -51.4 °C with different ice coverage of the intake tube: (c) 15 cm with $\langle \chi_{H_2O} \rangle_{Vol}$ = 1260 ppmv averaged over the tube volume, (d) 5 cm with $\langle \chi_{H_2O} \rangle_{Vol}$ = 770 ppmv, (e) 1 cm with $\langle \chi_{H_2O} \rangle_{Vol}$ = 280 ppmv, (f) 0.15 cm with $\langle \chi_{H_2O} \rangle_{Vol}$ = 96 ppmv and (g) rotationally asymmetric patch of 1/8 intake tube circumference and 1 cm length with $\langle \chi_{H_2O} \rangle_{Vol}$ = 50 ppmv.

Panels (a) and (b) of Figure 2.9 show two examples of velocity profiles computed by FLUENT CFD for two pairs of stratospheric pressures and temperatures, p = 13 hPa and T = -48.5 °C and p = 21 hPa and T = -52.8 °C. The two examples have the same inlet velocity of 6.6 m s^{-1}. Under these conditions, we are at low Reynold numbers and the flow is laminar. As expected for the flow in a cylindrical tube, the flow velocity decreases towards the tube walls, becomes zero at the wall and in

return accelerates at the center of the tube, thus conserving mass flux. Vömel et al. (2007c) estimated the flow through the intake tube to be 50 % of the balloon velocity. From simulations including the entire CFH package and prescribing an in flow velocity equivalent to the balloon ascending velocity, we find that the flow velocity at the inlet of the intake tube is about 70% of the balloon ascending velocity (see Figure 2.15c below) which is a better estimated than the 50% provided in Vömel et al. (2007c). For our simulations we take the balloon ascent velocity as the velocity of the flow entering the intake tube. In the simulations considering only the tube geometry, the flow becomes fully developed within the length of the tube (Wikipedia, 2019b).

Initially, we considered using a tube geometry without the mirror extrusion for simplicity and better computational times. However, the influence of the mirror geometry in the flow is unavoidable. The presence of the mirror support slows the flow down on one side of the intake tube, creating a recirculation region below the mirror extrusion and accelerating the flow on the opposing side. The flow accelerates in front of the mirror by up to 50% of the maximum fully developed flow velocity. The acceleration observed in front of the mirror intensifies for simulations with lower pressure and higher temperatures. As the pressure decreases and the temperature increases, the flow becomes fully developed earlier inside the tube. This is a direct consequence of the smaller Reynolds number (Eq. 2.3) observed in more viscous (warmer) and less dense (lower pressure, warmer) flows.

2.4.2.2 Discrete phase model

We used FLUENT's discrete phase module to compute the collision efficiency for water droplets entering the tube together with the air at some angle. The droplets will be accelerated in the direction of the air flow and either manage to avoid a collision with the wall or hit it at some distance down the tube. We inject one particle from each of the cells in the top inlet plane. We treat the injected particles as inert water droplets with uniform diameter distribution. For each of the mixed-phase cloud simulations, we defined the droplet diameter, inlet angle and velocity magnitude. The inlet angle and velocity magnitude are assumed to be the same as for the air flow. The discrete phase module runs on top of the solved flow case.

The simulation in Figure 2.10 was run with NT011 cloud conditions, p = 310 hPa and T = -20 °C. The velocity at the intake tube inlet surface is -7.5 m s^{-1} in the normal component (z direction) and 6 m s^{-1} in the parallel component (x direction), which corresponds to an inlet angle of about 39°. For clarity, only one every six droplet's trajectory is shown in Figure 2.10. Only the first 7 cm of the intake tube are shown. As expected the air flow affects different size droplets differently. Smaller droplets have less inertia, hence tend to stay within the air flow, avoiding the tube's wall while bigger droplets (with higher inertia) are deflected from the streamlines and collide with the walls. Most 20 μm diameter droplets will avoid collision, only the droplets entering close to the intake tube wall will collide. The bigger diameter droplets, to some extend also re-adjust with the flow, but most of them will collide within the first 5 cm of the intake tube.

Considering how the injection of liquid droplets is set up in FLUENT, with one droplet per cell in the top inlet plane, we have to account for the mesh cell surface density. As discussed above, the cell surface density is higher closer to the intake tube wall (see Figure 2.8c). Therefore, we normalize all collision efficiency results to the top inlet plane cell surface density, removing the effect of the mesh density from the results (see in Figures 2.11, A.6, A.14 and A.15 below).

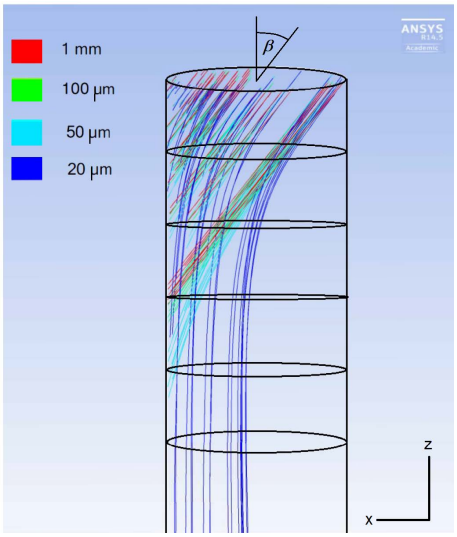

Figure 2.10: Collision efficiency analysis based on FLUENT simulation results for particle tracks of hydrometeors with diameters between 20 μm and 1 mm (colour-coding). The figure shows the top 7 cm of the intake tube. Flow simulations are for the mixed-phase cloud of flight NT011, p = 310 hPa and T = -20 °C. Inlet velocity is -7.5 m s^{-1} in z direction (largely due to the balloon's ascent velocity) and 6 m s^{-1} in x direction (largely due to the swinging motion of the payload), which results in an inlet angle β of about 39°.

2.4.2.3 Species transport

Figure 2.9 panels (c) to (g) show FLUENT flow simulations of the water vapour mixing inside the tube resulting from different degrees of icing of the intake tube induced by the collisions calculated in Section 2.4.2.2. The species transport module of FLUENT was used for the lower stratospheric and upper tropospheric sublimation simulations further discussed in Sections 2.5.2 and 2.5.3. This module allows for the definition of a mixture, the transport and change of species concentration within the mixture. For the simulations, we define a background water vapour mixing ratio for the inlet flow. We apply a user defined function (UDF) developed by Lüönd (2009), which takes the saturation water vapour pressure parameterisation from Murphy and Koop (2005) and the simulation's pressure and temperature to implement the saturation water vapour mixing ratio in the cells closest to the icy intake tube wall to mimic the effect of sublimating water vapour. The tubes are considered to be in thermal equilibrium with the inlet flow (Vömel et al., 2007b). If the cell already contains water vapour, the program adds only enough water vapour for the the cell to be saturated with respect to ice. The intake tube wall has been divided in layers and each can be controlled separately. FLUENT calculates the distribution of this water vapour through the intake tube with a combination of molecular diffusivity (Eq. 2.6) and eddy diffusivity (Massie and Hunten, 1981). Simulation results are compared through volume averaged water vapour mixing ratio in the lower 30 cm of the intake tube ($\langle\chi_{H_2O}\rangle_{Vol}$) and area averaged water vapour mixing ratio at the mirror surface ($\langle\chi_{H_2O}\rangle_{Area}$). $\langle\chi_{H_2O}\rangle_{Area}$ is evaluated at the mesh cells closest to the mirror surface.

Figure 2.9 panels (c) to (g) show the water vapour mixing ratio contours for different ice configurations of the same FLUENT flow simulation. For this simulations we took stratospheric conditions with p = 15 hPa and T = -51.4 °C. The flow speed is 7.2 m s^{-1} normal to the inlet surface. For cases

(c)-(f), the ice covers the tube all around its circumference and extends for 15 cm, 5 cm, 1 cm and 1.5 mm in the flow direction. Ice of 15 cm and 5 cm starts at the inlet of the intake tube, while ice of 1 cm and 1.5 mm starts 4 cm into the intake tube, mimicking different phases of sublimation from the tube (which is fastest at the top of the tube). Further explanation on this configuration follows in Section 2.5.2.2. Panel (g) shows a rotationally asymmetric patch, which covers one eight of the intake circumference and extends for 1 cm. The contamination values $\langle \chi_{H_2O} \rangle_{Vol}$ are presented for each case (panels (c) to (g)). Larger icy wall extent will result in higher contamination. However, the relation between tube ice coverage and contamination is not linear. As humidity increases in the inlet air, less water vapour sublimates from the tube. In dry stratospheric air, a 15 cm long ice cover achieves $S_{ice} \sim 0.6$, while a 1 cm long ice cover achieves $S_{ice} \sim 0.15$ at the position of the mirror. We performed steady state FLUENT calculations, so the results are snapshots along the balloon flight.

Figure 2.9 shows how contamination diffuses from the tube walls towards the center of the tube; and within the length of the tube (34 cm) the contamination homogenises. At the mirror location, 17 cm from the top of the tube, the flow is not yet homogeneous. We believe this gradient within the tube to be real. The payload moves at 7.2 m s^{-1}, which means the air within the 34 cm long tube has a residency time of $\tau \sim 0.05$ s. Within this time and with a molecular diffusivity of 2.6 cm^2 s^{-1} calculated from Eq. (2.7), the H_2O molecules are expected to travel a distance $(\tau D)^{1/2} \sim 0.4$ cm towards the inner part of the tube. This boundary layer is well visible in the upper parts of the tubes shown in Figure 2.9c-f. Any further diffusion can be attributed to eddy diffusivity, which the turbulence scheme of FLUENT is designed to properly determine. In this range of the stratosphere, eddy diffusivity is about 0.5 m^2 s^{-1} (Massie and Hunten, 1981); however, this value applies to the large-scale stratospheric dimensions, not to the small dimensions inside the tube. Therefore, the effective diffusivity is somewhere between the molecular and the free stratospheric value, as calculated by FLUENT.

We investigated the influence of an air flow inlet angle different than the normal (0°) to the inlet surface. Although a different inlet angle than 0° disturbs the flow in the first centimetres of the tube, the flow recovers. The uptake of water vapour from the icy wall into the air flow in these first disturbed few centimetres is radially asymmetric. However, over the length of the tube it homogenises and on average we obtain the same level of contamination independent of the inlet angle. Therefore, for the stratospheric and upper tropospheric ice sublimation simulations in Section 2.5.2 and 2.5.3 respectively, we only consider normal inlet angles.

2.5 Results

2.5.1 Hydrometeors freezing efficiency derived from inlet flow angles

To estimate the collision efficiency of supercooled droplets during the cloud passage in flight NT011, we performed 10 FLUENT simulations as described in Section 2.4.2.2, using $w_n = 7.5$ m s^{-1} for the velocity component normal to the inlet surface (see Figure 2.7b). For each of the ten FLUENT simulations we took a different horizontal velocity v_h as shown in Figure 2.7a.

In Figure 2.11 (a-i), we show collision efficiency results for each horizontal velocity. The panels are also identified with the corresponding inlet angle (β). For each of the different horizontal inlet velocities, we considered droplet sizes of 100 μm and 50 μm radius. We consider the smaller liquid droplets size, 50 μm radius, to account for the expected evaporation of the super cooled droplets in the

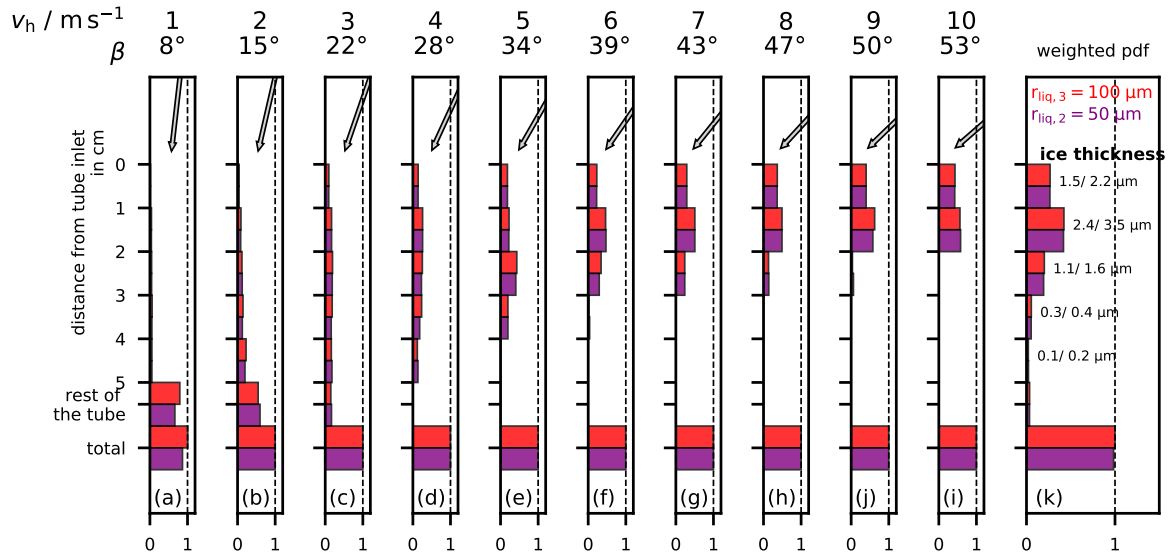

Figure 2.11: Collision/freezing efficiency of hydrometeors in the intake tube for the flight NT011 mixed-phase cloud with vertical inlet velocity $\langle w_n \rangle = 7.5$ m s^{-1}. $r_{\mathrm{liq},3} = 100$ μm (red), $r_{\mathrm{liq},2} = 50$ μm (purple). (a-i) Freezing efficiency for various horizontal inlet velocities: (a) 1 m s^{-1}, 8°; (b) 2 m s^{-1}, 15°; (c) 3 m s^{-1}, 22°; (d) 4 m s^{-1}, 28°; (e) 5 m s^{-1}, 34°; (f) 6 m s^{-1}, 39°; (g) 7 m s^{-1}, 47°; (h) 8 m s^{-1}, 47°; (i) 9 m s^{-1}, 50°; (i) 10 m s^{-1}, 53°. The 'rest of the tube' takes account of all collisions occurring deeper than 5 cm inside the tube, including the mirror holder. (k) Weighted sum of the efficiencies from panels (a-i) by the horizontal velocity pdf of Figure 2.7a, in front of each bar we write the thickness of the subsequent ice layer considering radially homogeneous cover of the intake tube and the lower (left) and upper (right) LWC limit for the cloud.

sub-saturated in relation to water ($S_{liq} < 1$) environment observed in the cloud of NT011 (see Section 2.2.4). In all panels of Figure 2.11, the first 5 horizontal bars represent the first 5 cm of the tube, the 6$^{\mathrm{th}}$ bar represents the rest of the tube (including the mirror holder) and the 7$^{\mathrm{th}}$ bar is the sum of all the above, representing the probability of the droplet hitting the tube at all. Differences to 100% represent droplet percentage that escaped the intake tube wall. Figure 2.11k shows the collision efficiencies weighted sum by the occurrence probability (pdf) of each horizontal velocity as calculated for the NT011 cloud and shown in Figure 2.11a.

For the droplet sizes and inlet angles considered, 100% of the droplets collide with the intake tube wall and more than 90% of these collide within the first 4 cm. For the relatively big droplet sizes considered there appears to not be dependence of the efficiency on the droplet size, possibly due to similar inertia of the droplets. In Figure 2.11k we calculated the thickness of the ice layer in the first 5 cm of the intake tube after passing the cloud, assuming an even coverage of the intake tube inner surface and taking into consideration the simulated collision efficiencies and the upper and lower limit of liquid water content (LWC) that we have used in Section 2.2.4. The first value per horizontal bar in Figure 2.11k refers to the lower LWC limit and the second to the upper LWC limit.

Figure 2.11 shows that the combination of high inlet angles and big droplet sizes causes an ice layer to accumulate at the top of the intake tube. Smaller inlet angles, up to 15° cause a more even coverage of the entire length of the intake tube. However, the layer remains quite thin, in the range

of 1 to 6 μm, which represents less than 1‰ of the intake tube radius. Therefore, the ice layer will not affect the inlet flow, but it has a catastrophic influence on the water vapour measurement in the stratosphere.

2.5.2 Contaminated water vapour measurements in the stratosphere

2.5.2.1 Sublimation and sublimated water estimation

For the stratospheric sublimation simulations we use the FLUENT configuration as described in Section 2.4.2.3. We defined three scenarios of ice coverage of the intake tube wall as shown in panels (c) to (e) of Figure 2.9: coatings of 15 cm, 5 cm and 1 cm depth. We ran simulations approximately every km in the stratosphere with 1 km interval averaged measurements of temperature, pressure, ascent velocity, and background water vapour mixing ratio. In Figure 2.12, we show flight NT011 stratospheric measurements, the values used in the FLUENT simulations and results. Figure 2.12a displays the air temperature (green), the average Naintial 2016 summer campaign air temperature (dashed black) and the ascent velocity (black). The green triangles and grey dots represent the averaged temperature and ascent velocity used in the FLUENT simulations.

In this flight there was a lot of variability in ascent velocity, so we calculated the standard deviation for each averaged point, shown in the graph as grey x-error bars and performed FLUENT simulations to investigate the influence of the ascent velocity variability. We concluded that ± 2 m s^{-1} has no significant impact on the volume averaged water vapour mixing ratio in the lower 30 cm of the intake tube ($\langle \chi_{H_2O} \rangle_{Vol}$).

In Figure 2.12b, we show χ_{H_2O} from CFH (red), the average χ_{H_2O} for the Nainital 2016 summer campaign (dashed black). For both lines, we show the 1 km interval averaged values used for the FLUENT simulations in red diamonds and black circles, respectively. We also show the saturation χ_{H_2O} for the flights temperature (dashed red). $\langle \chi_{H_2O} \rangle_{Vol}$ for the 15 cm intake tube wall ice coverage is shown as left facing triangles, for the 5 cm intake tube wall ice coverage $\langle \chi_{H_2O} \rangle_{Vol}$ as right facing triangles, and $\langle \chi_{H_2O} \rangle_{Vol}$ for the 1 cm intake tube wall ice coverage are shown as down facing triangles and $\langle \chi_{H_2O} \rangle_{Vol}$ for the 0.45 cm intake tube wall ice is represented by a star. The values used for the simulation and results are presented in Table 2.2.

In Table 2.2, we also present the area averaged water vapour mixing ratio at the mirror surface ($\langle \chi_{H_2O} \rangle_{Area}$) for the 5 cm intake tube ice wall coverage. They show water vapour mixing ratio 60% to 50% smaller than $\langle \chi_{H_2O} \rangle_{Vol}$ for the same simulation. We do not believe these simulated values to be an accurate description of the air mass experienced by the mirror in real flight conditions. The cell closest to the mirror surface in the simulation is 0.2 mm thick and the area averaged velocity for these cells is 0 m s^{-1}. We believe the mirror to experience a better mixed and larger amount of the passing air flow. For this reason, for further analysis of the simulation results we take $\langle \chi_{H_2O} \rangle_{Vol}$.

From the comparison of the simulation results for χ_{H_2O} in Figure 2.12b, we conclude that the 5 cm intake tube ice covered wall simulations describes the observations better. This result is consistent with the collision efficiency results of Section 2.5.1. As the observed χ_{H_2O} decreases, higher in the stratosphere, the 5 cm simulation starts to overestimate χ_{H_2O}. As the ice coverage decreases, the inlet air flow is exposed to a smaller ice surface and is less hydrated, until, finally, no ice surface is left and the instrument observes ambient χ_{H_2O}. The transition from 5 cm ice wall coverage is very fast. At

Table 2.2: FLUENT stratospheric and upper tropospheric simulations input data and results for flight NT011.

Measurements						Simulations			
						1 cm	5 cm		10 cm
h (km)	p (hPa)	T (°C)	w_n (m s^{-1})	χ_{H_2O} (ppmv)	$\chi_{H_2O\ mean}$ (ppmv)	$\langle\chi_{H_2O}\rangle_{Vol}$ (ppmv)	$\langle\chi_{H_2O}\rangle_{Vol}$ (ppmv)	$\langle\chi_{H_2O}\rangle_{Area}$ (ppmv)	$\langle\chi_{H_2O}\rangle_{Vol}$ (ppmv)
26.1	22	-52.8	5.2	7	6	155	429	288	701
24.8	27	-55.5	4.6	7	5	87	238	152	390
23.6	33	-58.7	4.7	27	5	44	116	67	192
22.4	40	-59.6	5.0	71	5	30	77	40	128
21.1	49	-61.5	4.4	53	5	20	48	25	79
19.9	59	-67.6	4.4	21	4	9	17	10	27
18.7	73	-72.4	4.8	10	5	6	9	7	12
17.5	90	-76.2	5.0	7	6	6	7	7	7
15.9	118	-71.9	3.7	9	6 [1]	7	8	7	10
15.2	132	-67.9	3.8	16	16 [1]	17	18	17	20
14.6	146	-63.0	3.4	31	18 [1]	20	24	21	28
14.0	160	-58.0	6.0	52	33 [1]	36	42	39	48

[1] X_{H_2O} RS41

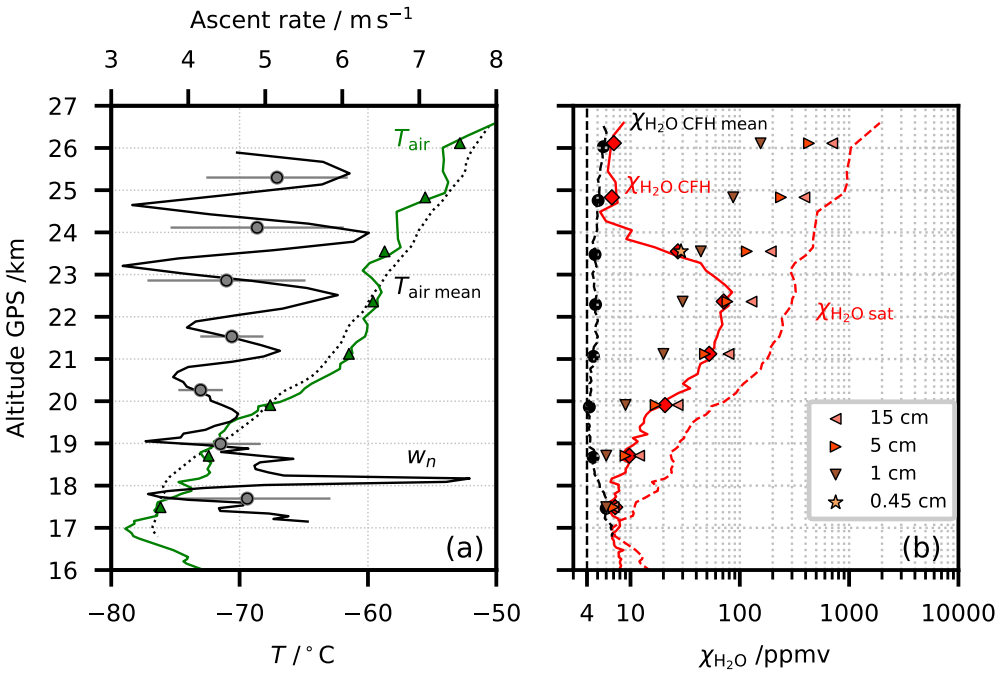

Figure 2.12: Stratospheric part of flight NT011 and FLUENT simulation results for the stratospheric sublimation. (a) Green: air temperature; green triangles: 1 km interval averaged air temperature; dotted black: average air temperature for the 2016 Nainital summer campaign; black: ascent velocity; grey circles: 1 km interval averaged ascent velocity; horizontal grey lines: 1 km interval averaged ascent velocity standard deviation. (b) Red: H_2O mixing ratio from the CFH; red diamonds: 1 km interval averaged H_2O mixing ratio from the CFH; dashed black: average H_2O mixing ratio for the uncontaminated soundings during the 2016 Nainital summer campaign; black dots: 1 km interval averaged χ_{H_2O} 2016 Nainital summer campaign; dashed red; saturation H_2O mixing ratio for the air temperature; other markers: FLUENT simulation results for the tube average mixing ratios $\langle \chi_{H_2O} \rangle_{Vol}$ in tubes with different ice coating depths d (full circumference): ◀ $d = 15$ cm; ▶ $d = 5$ cm; ▼ $d = 1$ cm; ★ $d = 0.45$ cm.

22 km, the 5 cm simulation still matches the observation, while one km higher at 23 km, we were able to match the observation to the 0.45 cm simulation. At 25 km height we consider the measurement to be recovered.

Considering, the water vapour to be well mixed within the intake tube and knowing the pressure and temperature, it is possible to estimate the total water evaporated in the stratosphere. Since flight NT011 recovers to normal operation before burst, we also know the excess integrated water vapour to be that which was frozen in the intake tube during the traverse of the mixed-phase cloud in the troposphere. Using the ideal gas law and assuming the uncontaminated profile to be equal to the season average profile, we can calculate the number of extra molecules in the intake tube, which have caused the observed contamination. Integrating from the CPT (h_{CPT}) to balloon burst (h_{burst}) altitude we recover the total sublimated water in the stratosphere.

Table 2.3: Integrated water vapour in the stratosphere and upper troposphere for flights NT011, NT029 and NT007.

flights	after the cloud passage		
	Excess integrated Water Vapour (mg)		
	troposphere	stratosphere	total
NT011	1.45	4.35	5.80
NT029	3.5 + 60.5	15.7	79.7
NT007	4.4 + 43.5	65.5	113

$$\sum_{i}^{N} \frac{p_{\mathrm{air_i}}\ 100\ V_{\mathrm{tube}}}{R\ T_{\mathrm{air_i}}} \left(\chi_{\mathrm{H_2O\ CFH_i}} - \chi_{\mathrm{H_2O\ CFH\ mean_i}}\right) \tag{2.8a}$$

$$N = \frac{h_{\mathrm{burst}} - h_{\mathrm{CPT}}}{340} \tag{2.8b}$$

Results for the stratospheric integration of water vapour for NT011, NT029 and NT007 are shown in Table 2.3. 4.35 mg of water have sublimated from the intake tube in the stratosphere in flight NT011. We consider this the lower limit of water that would have frozen in the intake tube during the ascent through the mixed-phase cloud. Since we know the cloud extend (750 m) and since we have estimated the collision and freezing efficiency of the hydrometeors in the cloud to be 100%, we calculate the lower limit of liquid water content (LWC) in the cloud to have been 0.011 g m^{-3}. This is very little LWC for a mixed-phase cloud, so we conclude that it was an almost completely glaciated mixed-phase cloud. This was the value used to set the lower limit for LWC limit for the cloud simulation in Section 2.2.4.

2.5.2.2 Ice layer evolution

The ice wall coverage of the intake tube is not homogeneous, as we saw from the collision efficiency results in Figure 2.11k. From these assumptions, we tried to understand how this inhomogeneity influences the sublimation and the life time of the ice in the intake tube. For this, we did several FLUENT simulations with different intake tube ice wall coverages. We run simulations with increasing length of the ice wall layer, from covering the top 1 cm of the tube, to covering the top 2 cm and so on until the the first 5 cm of the tube are covered. We chose three different stratospheric scenarios to investigate if the contribution from each ice layer in percentage of saturation was independent of pressure and temperature: p = 15 hPa and T = -51.4 °C, and p = 25 hPa and T = -53.6 °C and p = 39 hPa and T = -59.2 °C. The inlet flow velocity is the same for the three scenarios: normal to the intake tube inlet surface and 6.5 m s^{-1} to remove any inlet velocity effect from the comparison. The results are presented in Table 2.4. For one of the cases (p = 25 hPa) we also investigated the contribution of a longer ice layer extending further than the first 5 cm of the tube. From 5 cm, we increased the ice wall in 2 cm steps until the the top 15 cm of the intake tube are covered. The results are presented in Table 2.6.

Then, we did FLUENT simulations for each 1 cm and 2 cm layer individually: for the top 1 cm, 2^{nd} cm until the 5^{th} and then for 2 cm layers, from 5 cm to 7 cm and so on until the last layer from

13 cm to 15 cm. We consider that the hydration contribution from an ice layer below 15 cm will not affect the measurement. The results are presented in Table 2.4 and 2.6 as $\langle \chi_{H_2O} \rangle_{Vol}$. The results for the simulations with the individual layers are presented in the 'isolated' columns. In the 'in group' columns, we present the influence of the single ice layer in a longer ice layer simulation as the difference of $\langle \chi_{H_2O} \rangle_{Vol}$ of two simulations: one with all the ice layer active from the top until the identified layer and a second with all the ice layers active from the top including the identified layer. For example, the contribution of layer 3 - 4 cm is calculated by subtracting $\langle \chi_{H_2O} \rangle_{Vol}$ of the simulation with ice wall from the top to 3 cm length from $\langle \chi_{H_2O} \rangle_{Vol}$ of the simulation with ice wall from top to 4 cm length.

Table 2.4: Results for ice layer evolution in the stratosphere due to sublimation for three cases of flight NT029 stratosphere.

	p = 39 hPa, T = -59.2 °C				p = 25 hPa, T = -53.6 °C			
saturation	210 ppmv				1000 ppmv			
	isolated		in group		isolated		in group	
walls	(ppmv)	(%)	(ppmv)	(%)	(ppmv)	(%)	(ppmv)	(%)
0 - 1 cm	36	17%	–	–	135	13%	–	–
1 - 2 cm	30	14%	12	6%	110	11%	50	5%
2 - 3 cm	28	13%	10	5%	103	10%	38	4%
3 - 4 cm	27	13%	8	4%	98	10%	31	3%
4 - 5 cm	26	12%	7	3%	94	9%	27	3%

Table 2.5: Results for ice layer evolution in the stratosphere due to sublimation for three cases of flight NT029 stratosphere - continuation 2.

	p = 15 hPa, T = -51.4 °C			
saturation	2200 ppmv			
	isolated		in group	
walls	(ppmv)	(%)	(ppmv)	(%)
0 - 1 cm	370	17%	–	–
1 - 2 cm	300	14%	136	6%
2 - 3 cm	279	13%	103	5%
3 - 4 cm	266	12%	86	4%
4 - 5 cm	255	12%	74	3%

From this analysis, we confirm that the hydration contribution of the ice wall depends on the level of saturation of the passing air and on its ability to sustain water vapour. The first cm of the intake tube is the most efficient at hydrating the passing air comparing to other isolated ice layers lower inside the intake tube - probably due to the inlet flow not being fully developed at the start of the intake tube. We can expect this layer to be the first to sublimate.

If the passing air has already contacted with an icy surface, the hydration efficiency of the following ice layers is seriously reduced. The lower layers from 5 to 15 cm inside the tube have the least contribution to the air hydration if other ice layers exist above. Note, however, that in Table 2.6, the contribution of these layers to the inlet flow hydration is given for 2 cm layers while for the layers from 0 to 5 cm, these are given for 1 cm layers. To compare these values, we should also take into consideration that the first cm of this 2 cm layer would also be more efficient at hydrating the air than

Table 2.6: Results for ice layer evolution in the stratosphere due to sublimation for three cases of flight NT029 stratosphere - continuation 3.

	p = 25 hPa, T = -53.6 °C			
saturation	1000 ppmv			
	isolated		in group	
walls[1]	(ppmv)	(%)	(ppmv)	(%)
5 - 7 cm	134	13%	48	5 %
7 - 9 cm	124	12%	39	4 %
9 - 11 cm	115	11%	32	3 %
11 - 13 cm	106	11%	27	3 %
13 - 15 cm	97	10%	22	2 %

[1] note that these walls are 2 cm long instead of 1 cm

the second cm. Despite the small contributions from these layers we believe they sublimate relatively early in the flight because the ice deposition from the hydrometeor collision was also small, see Figure 2.11k. Hence, our 5 cm simulations include the first 5 cm of the intake tube.

After the first cm of the intake-tube ice-layer would sublimate, the biggest contribution would come from the next layer between 1 cm and 2 cm. However, this is also the thickest layer as we saw in Figure 2.11k, it would have an extended lifetime. The layers below are thinner but they also contribute with some water vapour for the flow hydration. With these assumptions it is harder to estimate the evolution of the ice layer. However, as seen in Table 2.4, once isolated, the contribution from any layer in this region is comparable, each contributing: 14% to 12% of saturation. So, we have set our 1 cm layer to start at 4 cm deep into the intake tube. The patch ice coverage and thinner layers (0.45 or 0.15 cm) that have been used for some simulations (Figures 2.12, A.7 and A.16) are conceivable since we do not expect sublimation to be a uniform and homogeneous process.

From the comparison of the different stratospheric cases in Table 2.4, we can say that the sublimations at p = 39 hPa and p = 15 hPa are equivalent in percentage of saturation, while the sublimation at p = 25 hPa is weaker. We do not have an explanation for this difference, but also do not consider it to be significant for the overall picture of the study.

As a summary, we expect the lower regions of the ice layer covering the inner wall of the intake tube to be the first to sublimate, because only a thin layer of ice was deposited there when traversing the cloud. Then, we expect the ice layer to sublimate from the top down, because hydration is more efficient if the air is at stratospheric dryness.

2.5.3 Considerations for the upper troposphere

The contamination in the stratosphere is a remarkable feature and is relatively easy to spot since the expected values are in a well defined range 4-8 ppmv. However, it is also expected that the sublimation is not only happening in the stratosphere. If an ice layer is present in the intake tube of CFH after the mixed-phase cloud, it will sublimate when the conditions are favourable. This is, when the ambient air is not saturated. For the stratospheric contamination we have a clear background water vapour from which to calculate the contamination water vapour: the mean water vapour mixing ratio of the season. Water vapour in the stratosphere is known to not be very variable. However, tropospheric water

vapour is extremely variable. Luckily, we had a second measurement of water vapour on the flight, via the RS41 RH measurement. In Brunamonti et al. (2019), the RS41 was found to have a dry bias in comparison with CFH in the upper troposphere. The comparison includes the upper troposphere of these three flights: NT007, NT011 and NT029, that we consider contaminated and 24 others, which should make the overall contribution of the 3 contaminated flights less significant. Irrespective of the observed mean bias, we take the RS41 water vapour measurement as background for the analysis of the CFH contamination in the upper troposphere.

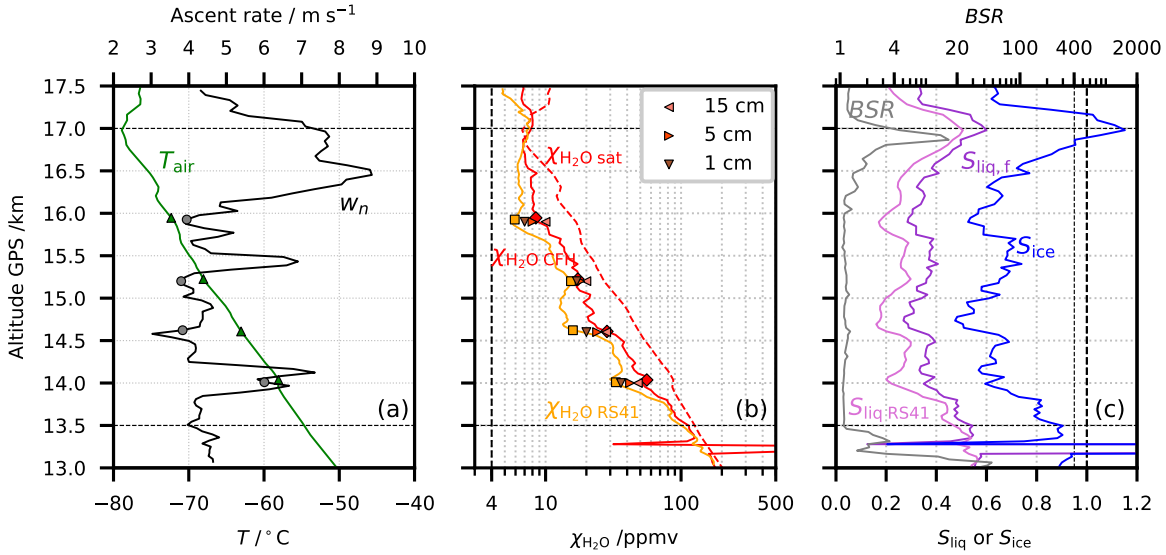

Figure 2.13: Upper tropospheric part of flight NT011 and FLUENT simulation results for the upper tropospheric sublimation. (a) Green: air temperature; green triangles: air temperature simulation input; black: ascent velocity; grey circles: ascent velocity simulation input. (b) Red and red diamonds: H_2O mixing ratio by the CFH; orange: H_2O mixing ratio RS41; orange squares: H_2O mixing ratio RS41 simulation input; dashed red: saturation H_2O mixing ratio for the air temperature; other markers: FLUENT simulation results for the tube average mixing ratios $\langle\chi_{H_2O}\rangle_{Vol}$ in tubes with different ice coating depths d (full circumference): ◀ d = 15 cm; ▶ d = 5 cm; ▼ d = 1 cm; (c) Pink: saturation over water ($S_{liq\,RS41}$) by RS41; violet: saturation over water ($S_{liq\,f}$) from CFH considering the deposit on the mirror to be frost; blue: ice saturation (S_{ice}) from CFH; grey: 940-nm backscatter ratio from COBALD. Horizontal dashed lines limit the integration interval used for estimating the sublimated water in the upper troposphere.

In Figure 2.2, we see that between the top of the lower cloud and the cirrus cloud at the tropopause there is a sub-saturated layer. In Figure 2.13, we provide a detailed view of this region of the flight, between 13 and 17.5 km height. In panel (a) and (b) of Figure 2.13 we show the same variables as panel (a) and (b) of Figure 2.12 with the exception that in panel (b) we do not show $\chi_{H_2O\,CFH\,mean}$, but $\chi_{H_2O\,RS41}$ (orange). In Figure 2.13c, we show the same variables as in panel (b) of Figure 2.3. The dry bias of RS41 in comparison to CFH is noticeable in the region between 13.5 km and 17 km, right until the CPT. To understand if the proposed mechanism of water vapour sublimation from an ice layer at the top of the intake tube can explain the dry/wet bias observed, we run FLUENT simulations at four chosen locations. At three of these locations there is a significant difference between CFH and

RS41 measured χ_{H_2O}. Observed S_{liq} is below 30% for RS41 and S_{ice} for CFH is below 70%. A fourth location is chosen where observed χ_{H_2O} is the same for RS41 and CFH, S_{liq} from RS41 is 30% and S_{ice} for CFH is 70%. The pressure, temperature, inlet velocity and background water vapour from RS41 used for the FLUENT simulations are presented in Table 2.2. For these simulations, the results are once again presented as $\langle \chi_{H_2O} \rangle_{Vol}$.

For the lower two locations at approximately 14 and 14.6 km height, the three simulations for the three different ice wall coverage of the intake tube: 15 cm, 5 cm and 1 cm, can account for the extra water vapour measured by the CFH. At the 14 km height, the CFH observes even more water vapour than that that can be explained by the 15 cm ice wall coverage simulation. The CFH observation at 15.9 km height could be due to the presence of a 5 cm ice layer at the top of the intake tube. The lower 10 cm of the ice layer cloud have evaporated between the lower observation at 14.5 km height and the observation at 15.9 km. However, it is good to remember that this is all a speculative study. The fourth location at 15.2 km height does not support this hypothesis. In this simulation all three ice coverages considered over-estimate the CFH observation, mainly because the CFH and RS41 observation at this location is identical although we are not at ice saturation. It is worth to notice that the spread of $\langle \chi_{H_2O} \rangle_{Vol}$ for the three simulations at these S_{liq} and S_{ice} is much smaller than that at the other locations. It could also be, that for such high water vapour concentrations, the dilute approximation used in the FLUENT simulation is no longer valid.

We did the same integration for this interval as for the stratosphere using Equation (2.8a) in the interval between 13.5 and 17 km height. CFH measured more 1.45 mg of water in this interval than the RS41. This could be water that had accumulated during the mixed-phase cloud and sublimated in the upper-troposphere. Adding this water to the water sublimated in the stratosphere, we have a total of 5.8 mg of water sublimated in flight NT011, which would indicated a upper limit of LWC for the observed mixed-phase cloud of 0.016 g m^{-3}. This values are all shown in Table 2.3 together with upper and lower limit of LWC estimations for the mixed-phase clouds of NT029 and NT007.

2.5.4 Other types of contamination

To complete the study of contaminated water vapour measurements for cryogenic frost point hygrometers, we did two extra related studies with FLUENT simulations but with a different focus and hence different geometries and meshes. The principle of the implemented simulations is identical to what was described in Section 2.4.2.

2.5.4.1 Balloon envelope

When addressing contamination of water vapour measurements, there is usually some uncertainty about the source of the contamination. For all water vapour measurements from a balloon platform, the balloon envelope is the main source of contamination. However, for cryogenic frost point hygrometers, the intake tube also plays a significant role in contamination. Here, we conclusively differentiate the contamination from both sources.

We run FLUENT simulations with idealized tropospheric and stratospheric conditions which are shown in Table 2.7. We designed a new mesh, where the balloons radius changes with atmospheric conditions. We considered an initial balloon size of 1 m radius at 800 hPa and 25 °C, approximately

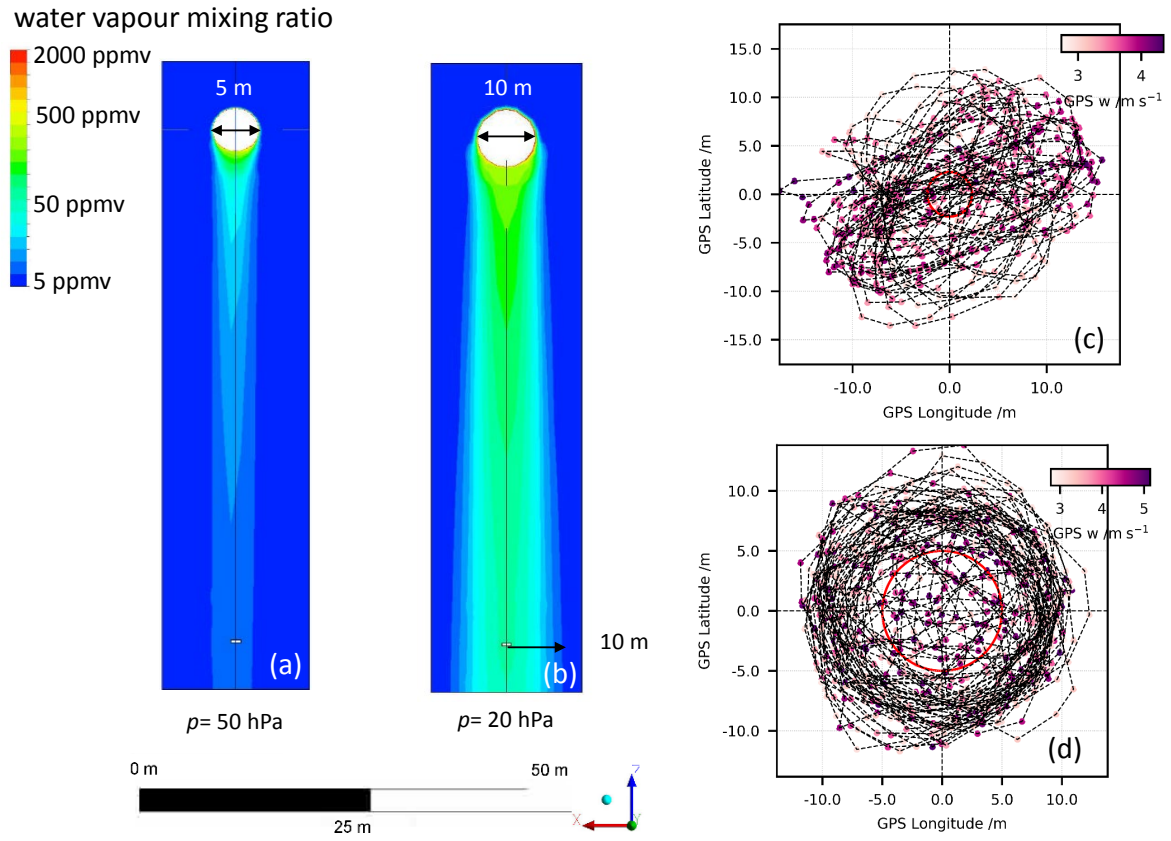

Figure 2.14: Balloon contamination contours: (a) H_2O mixing ratio contour (y = 0) for 50 hPa and (b) for 20 hPa; (c) balloon oscillation at 50-hPa and (d) above 20-hPa level for flight NT007. Red circle: typical balloon cross-section at respective pressure level.

corresponding to the launching conditions at Nainital during the summer season. As the payload ascends, the balloon volume increases, and hence its radius. The balloon radius for each simulation is also shown in Table 2.7. In the simulation, we place the CFH package 55 m below the balloon center. For the simulations, we considered two different ascent velocities: 4 and 7 m s^{-1}, both oriented along the z direction of the geometry, and the entire surface of the balloon to be covered with an ice layer implemented similarly as the ice covered intake tube wall. The simulation domain extends 5 m from the balloon surface in every direction and 5 m below the CFH package.

In Figure 2.14 panel (a) and (b), we see the water vapour mixing ratio contours for the balloon and payload ascending at 7 m s^{-1} at 50-hPa and 20-hPa levels, respectively. At the 50-hPa level, the excess water vapour due to balloon contamination is not significant. The total water vapour observed 55 m below the balloon at the payload level is within the stratosphere natural variability (4-8 ppmv). At the 20-hPa, the effect of contamination by the balloon is more significant. The water vapour perturbations in the wake of the balloon extend by 10 m in radius at the payload level and is up to 100 ppmv. It is also worth mentioning the balloon oscillation, for flight NT007 at the 50-hPa level the payload shows a displacement from under the balloon wake far greater than the balloon dimension at this level, which reduces the amount of time spent within the wake of the balloon (see Figure 2.14c). At the

Table 2.7: Balloon envelope and instrument package contamination FLUENT simulation input values and results.

p	T	w	$r_{balloon}$	background χ_{H_2O}	$\langle\chi_{H_2O}\rangle_{Area\ CFH}$	
(hPa)	(°C)	(m s^{-1})	(m)	(ppmv)	(ppmv)	
10	-40	4, 7	4.0	5	498, 428	(233* + 189**)
20	-50	4, 7	3.1	5	53, 48	
50	-60	4, 7	2.3	5	7.6, 7.3	
100	-70	4, 7	1.8	5	5.5, 5.5	
200	-40	4, 7	1.5	100	112, 111	
800	25	4, 7	1.0	20000	–	

Results for 10 hPa simulation with $w = 7$ m s^{-1} considering the:
* top half of the balloon to be icy or the
** bottom half of the balloon to be icy

20-hPa level, the payload oscillation shows a perfect circular movement around the balloon, with a displacement between 5 and 10 m (see Figure 2.14d). The CFH consistently probes the edge of the balloon wake.

In Table 2.7, we compare the contamination caused by the balloon at different levels through the averaged water vapour mixing at the CFH package surfaces ($\langle\chi_{H_2O}\rangle_{Area\ CFH}$). From the balloon wake at 100 hPa we expect 0.5 ppmv contamination, at 50 hPa we expect about 2.5 ppmv contamination, at 20 hPa 50 ppmv contamination and at 10 hPa 500 ppmv. The magnitude of the contamination from the balloon envelope is very different from the contamination we investigate in this paper which we attribute to the sublimation of ice accumulated in the CFH intake tube. Hence, we can exclude that the balloon envelope is responsible for the contaminated measurements shown in Figure 2.1. The balloon envelope can be the source of the contamination we observe from 20 hPa onwards in all flights, see Figure 1 panel (b) of Brunamonti et al. (2018). In the average profile of water vapour mixing ratio for 2016 Nainital summer campaign, we observe between 6 and 20 ppmv between 20 and 10 hPa, which are too high compared to the expected stratospheric background water vapour mixing ratio.

The contamination values presented in Table 2.7 are for a full coverage of the balloon skin with ice and at the center of the balloon wake. For the 10 hPa stratospheric conditions, we also present results for two simulations: one considering the top half of the balloon to be covered in ice, which causes a $\langle\chi_{H_2O}\rangle_{Area\ CFH}$ of 233 ppmv; and a second simulation considering the bottom half of the balloon to be covered in ice, which causes a contamination up to 189 ppmv.

We also investigate if the balloon can cause contamination in the upper troposphere. We run a simulation for 200 hPa with background water vapour of 100 ppmv. At this level and temperature of -40 °C, water vapour saturation is 600 ppmv.55 m below the balloon, we can expect an extra 12 ppmv. The contamination is not negligible, but it is comparable to the instrumental uncertainty of CFH (10%) and it would also be seen by the radiosonde, hence it cannot be uniquely identified.

2.5.4.2 Instrument package

To exclude possible contributions from the instrument package to the observed contamination, we run simulations for the atmospheric conditions as summarized in Table 2.7 and using an instrument package

geometry and mesh with intake and outlet tube. The CFH package extends for 12 cm in the vertical direction and has a rectangular horizontal shape of 17 cm × 31 cm. However, the CFH package is not symmetric. The intake tube is not located at the center of the package. It is centred along the shortest direction (Figure 2.15a) and 13.5 cm from the edge along the longest direction (Figure 2.15d). The simulation domain extends 25 cm from the top of the intake tube, 30 to 35 cm from CFH package sides, and 150 cm from below the outlet tube.

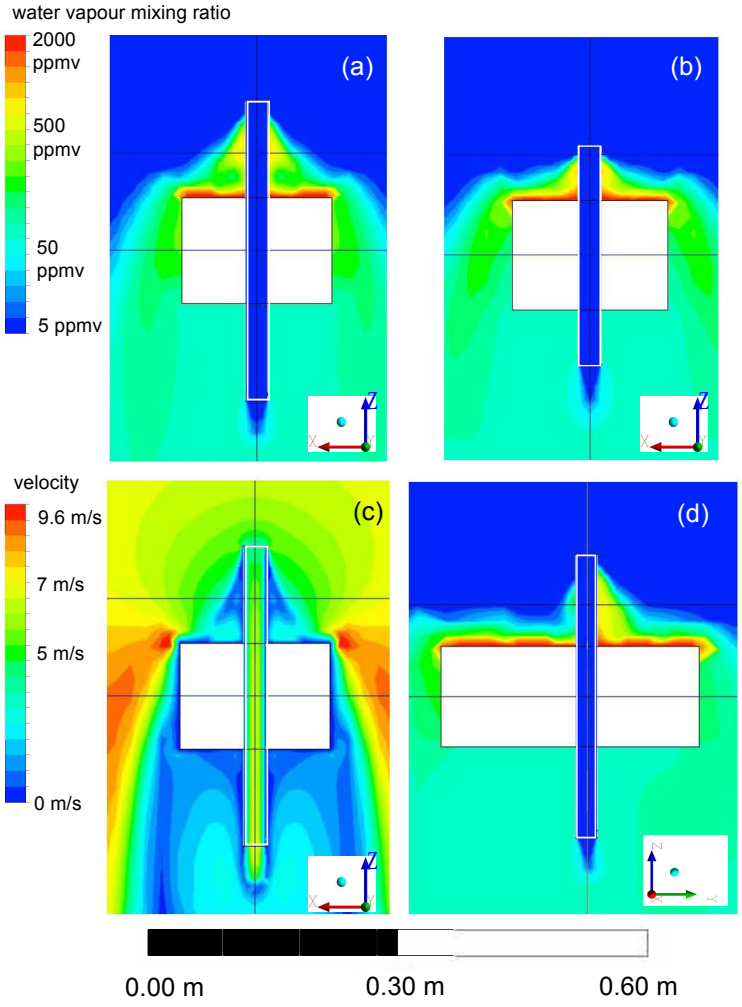

Figure 2.15: Package contamination contours for 20 hPa and balloon ascent velocity of 7 ms^{-1}. (a) H_2O mixing ratio contour (y = 0) for CFH intake tube 11 cm from the package; (b) same for intake extending 6 cm from the package; (c) velocity contour (y = 0) extending 11 cm from the package. (d) H_2O mixing ratio contour (x = 0) for CFH intake tubes extending 11 cm from the package.

In Figure 2.15, we show results for CFH package contamination at 20 hPa with 7 $m\,s^{-1}$ ascent velocity along the z direction. We have considered the top surface of the CFH to be covered in ice. Panel (a) shows water vapour mixing ratio at y = 0. Panel (b) shows the same but we altered the length of CFH intake tube, in this simulation it is 12 cm long, and extends only 6 cm above the package. Panel (c) shows the velocity profile at y = 0. And Panel (d) shows the water vapour mixing ratio at x = 0.

For the four stratospheric pressure and temperature cases (Table 2.7), we observe the magnitude of the contamination in the wake of the payload increase with decreasing pressure and increasing temperature. Recurrent in all simulations is the flow deceleration above and below the package (Figure 2.15c), creating a recirculation in these areas, and a flow acceleration on the sides. Note that in this simulation, the flow is also simulated inside the intake tube, and it becomes developed inside the tube. In the developed region, the inlet flow velocity is equivalent to the velocity seen outside of the payload influence.

The recirculation effect above the CFH package is able to pull water vapour from the package surface and increase the water vapour mixing ratio of the air surrounding the intake tube. In this case, the intake tube prevents water vapour from the package to contaminate the sampled air. Air is non-contaminated in the layer 2 cm below the intake tube inlet. However, the intake tube causes and enhances the re-circulation effect above the CFH package. From the simulation with the shorter intake tube (Figure 2.15b), we see the contaminated area starting lower than for the longer intake tube (Figure 2.15a). However, the shorter intake tube does not seem to be a good option to prevent water vapour from the package to contaminate sampled air. Figure 2.15d shows the recirculation to be more intense on the shorter side of the package and χ_{H_2O} to be higher in this region. We have performed simulations with a symmetric package, where the asymmetry in the results is eliminated. As conclusion, the intake tube is effective at preventing contamination from the instrument package. A reduction of its length is not recommended.

2.6 Conclusion

In this study, we looked into contaminated water vapour measurements by means of cryogenic frost point hygrometers during the 2016-2017 StratoClim balloon campaigns on the southern slopes of the Himalayas. We analysed extensively three distinct cases, where contaminated values were observed. In these cases, we encountered mixed-phase clouds in the troposphere and by means of observation and modelling we proved liquid water could be present in all of them. By novel interpretation of the GPS data we quantified the balloon pendulum movement. By means of computational fluid dynamic (CFD) simulations we estimated the impact of the pendulum motion on the collision efficiency of supercooled liquid droplets on the inner wall of the intake tube. We clarified that the inlet flow angles in the intake tube are bigger than the pendulum oscillation angles due to horizontal velocity of the payload induced by the pendulum and rotating movements. We also compared the impact of different size droplets: big droplets have higher collision efficiency rates than smaller droplets, with some dependence on the flow inlet angle. For example, less than 50% of liquid droplets with $r \sim 10$ μm freeze in the intake tube at inlet angles of around 50°, while 100% of droplets with $r > 70$ μm will freeze already at angles $> 5°$.

We matched the contaminated water vapour measurements in the stratosphere to simulation results for a 5 cm deep icy wall coverage at the top of the intake tube for most of the simulations. We showed the recovery of contaminated water vapour measurements can be explained in terms of smaller surface ice coverages eventually leading to uncontaminated water vapour observation in the stratosphere after all ice in the intake tube sublimated. We provided a clear picture on the evolution of the ice layer inside of the intake tube during the sublimation process. Ice layers closer to the top of the intake tube will sublimated more efficiently than layers closer to the center. However, because the collisions are

less efficient closer to the center of the tube, they generate a thinner ice layer and sublimate first. The last layers to sublimate will be those around 4 to 5 cm from the top of the intake tube. By comparison with RS41 we have also concluded that water vapour measurements in the upper troposphere after passing through the mixed-phase cloud from a flight presenting contaminated water vapour values in the stratosphere could also be contaminated, especially at S_{ice} lower than 0.7.

The three cases can be grouped into two categories. Characteristics common to flights NT011 and NT029 are the presence of cold mixed-phase clouds, at air temperature lower than -20 °C; fast ascent balloon velocity 6 to 7.5 m s^{-1}; and the total sublimation of any ice coverage of the intake tube within the flight time, before balloon burst. These characteristics contrast to those of flight NT007 where a warm mixed-phase cloud was also present at air temperatures between 0 and -5 °C; a slow balloon ascent through the entire flight between 3 and 4 m s^{-1}; and the persistent contamination water vapour measurements in the stratosphere until burst. It was known that liquid clouds and mixed-phase clouds could irreversibly contaminate water vapour observations by cryogenic frost point hygrometers [Holger Vömel, personal communication, 2016]. Our results show that even cold mixed-phase clouds with very low LWC, can affect the operation of the CFH.

We also show that neither the balloon envelope nor the instrument package are likely to cause the water vapour values observed in these cases. However, the balloon may cause the enhanced and contaminated water vapour values observed between the 20-hPa level and balloon burst (as shown in Figure 1b in Brunamonti et al. (2018)). The intake tube successfully shields sampled air from package contamination.

2.6.1 Design and operation recommendations

For operational purposes, to reduce the pendulum oscillation of the payload, we recommend investigating to fly a two balloon tandem separated by a rigid triangle as described by Kräuchi et al. (2016). It would need further investigation to confirm that by reducing the oscillation we would be reducing the contamination. The payload would fly more often in the wake of the balloons and hence be subject to contamination by the balloon. Furthermore, the oscillatory movement would not be completely avoided, but smaller oscillations might result in faster sublimation, shorter contamination in the stratosphere and faster recovery of the instrument. However, variability in LWC will be a much larger effect that cannot be controlled.

We recommend trying to widen the intake tubes to increase inlet flow (Mastenbrook, 1965, 1968) and the placement of the measurement head as far from any of the intake tubes walls as possible. As seen in Figure 2.9, ambient air can enter the tube and remain unperturbed in terms of water vapour for a few centimetres. The wider the tubes the longer the air can remain unperturbed and the closer the measurement is to the inlet the better. However, the tubes are effective at protecting the measurement from contamination from the instrument package, so we do not recommend shortening or removing them.

Heating of the intake tubes has been suggested; however, this would perturb the measurement of water vapour (Kämpfer, 2013). Heated tubes could evaporate liquid or ice water present in the air and contaminate the entire measurement of water vapour turning it into a total water measurement and make it more difficult to assess supersaturations in cloud. We suggest performing one heating cycle of the inlet tubes after the region of mixed-phase cloud, at air temperatures colder than -38 °C, similar

to what is done in the mirror with a clearing and a freezing cycle (Vömel et al., 2007b) but for the tube. The measurement would be perturbed in the upper troposphere for a few seconds or minutes, but a clean stratospheric water vapour profile might be the reward.

Many assumptions had to be made throughout this study due to the lack of information of the observed clouds, because the backscatter measurements from COBALD do not suffice to derive cloud drop sizes and physical states. One instrument that could provide useful additional information is a hot-wire probe to measure liquid water content (LWC) and total water content (TWC) in mixed-phase clouds. The instrument is mainly used in aircraft and we are not aware of its use for balloon sounding. The principle is really simple and detection limits are of the order of 0.003 to 0.005 g m^{-3} (Korolev et al., 2003a). However, a limitation for implementation in balloon sounding could be the power availability. In Serke et al. (2014) a new vibrating wire sonde based of the design of Hill and Woffinden (1980) is use to measure SLWP (Supercooled Liquid Water Content) from a balloon platform with interesting results, but no information on droplet size distribution.

Acknowledgements

The research leading to these results received funding from the European Community's Seventh Framework Programme (FP7/2007–2013) under grant agreement no. 603557 and from GAW-CH under the 'Development, Validation and Implementation of a GRUAN-Worthy Plug-and-Play Balloon-Borne Hygrometer' project.

The authors would like to acknowledge the contributions from: Peter Oelsner, Susanne Meier and Ruud Dirksen from the 'Deutscher Wetterdienst' (DWD) / GCOS Reference Upper Air Network (GRUAN) Lead Center, Lindenberg, Germany; Suvarna Fadnavis, Bhupendra B. Singh, Sreeharsha Hanumanthu, K. Ravi Kumar and Sunil Sonbawne from the Indian Institute of Tropical Meteorology (IITM), Pune, India; Manish Naja and Deepak Singh from the Aryabhatta Research Institute of Observational Sciences (ARIES), Nainital, India; Maxi Boettcher from Institute for Atmospheric and Climate Science (IAC), Swiss Federal Institute of Technology (ETH), Zürich, Switzerland; Hannu Jauhiainen from Vaisala Oyj, Vantaa, Finland; Rijan Kayastha from the Kathmandu University (KU), Dhulikhel, Nepal; Jagadishwor Karmacharya from the Department of Hydrology and Meteorology (DHM), Meteorological Forecasting Division, Kathmandu, Nepal and Markus Rex from Alfred Wegener Institute (AWI) for Polar and Marine Research, Potsdam, Germany.

Peltier Cooled Frost point Hygrometer (PCFH)

Chapter 3

Instrument description

Teresa Jorge, Frank G. Wienhold, Thomas Brossi, Uwe Weers, Marco Vicellio, Uli Krieger, Michael Rösch, Tatjana Naebert and Thomas Peter.

Disclaimer The PCFH has been a team development. Individual authors contributions. Teresa Jorge: Peltier element, heat sink, intake tube, multiblock and reference surface re-design, gluing aids, housing, heat sink radiation protection and instrument assembly; Frank G. Wienhold: detection scheme, mirror design, reflection electronics, reflection and controller board integration and multiblock re-design; Thomas Brossi: thermocouple module, controller and communications electronics, communication protocols and firmware; Uwe Weers: multiblock design; Marco Vicellio: housing, intake tubes, multiblock re-design and gluing aids; Uli Krieger: copper insert; Michael Rösch: bottom ring and gluing aids; Tatjana Naebert: heat sink radiation protection; Thomas Peter: double unit design.

The PCFH was developed for the purpose of measuring frost point temperatures in the troposphere and stratosphere. A region of special interest is the upper troposphere and lower stratosphere (UTLS). For a Peltier cooled frost point hygrometer this transition region is particularly critical because both the water vapour and the temperature regime change. Water vapour, in general, decreases up to the UTLS and then stays approximately constant at 4 to 8 ppmv. The temperature also decreases constantly up to the UTLS, however it starts increasing in the stratosphere, depending on the latitude, the change can be more or less sharp.

The PCFH is set up as a redundant instrument with two identical sub-units. Each sub-unit is comprised of one gold coated aluminium mirror attached using heat conductive glue to a double stage Peltier element. The Peltier element is in turn attached with heat conductive glue to a copper finger inserted in a 3D printed aluminium block (multiblock). This block is designed such that the mirror sits approximately at the center of a 40 mm Ø inlet tube exposed to passing ambient air. The operation principle of the instrument is to keep the mirror at the frost point temperature with a constant ice/dew coverage. The Peltier element controls the mirror at the desired temperature.

The multiblock has a cuboid shape with a cylindrical cut-out in the middle. Inside the cut-out there is a protruding bridge which holds the main mirror and Peltier element construction. The face of the multiblock behind the Peltier element is screwed to a 8-fin heat-sink exposed to ambient air.

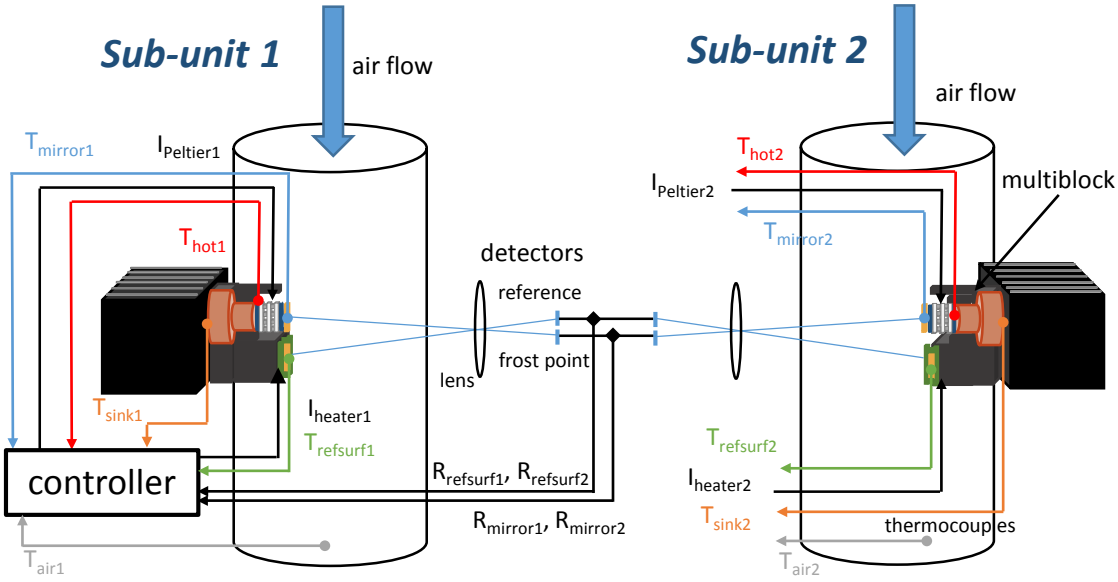

Figure 3.1: PCFH Schematics

The face opposing the bridge contains two circular cut-outs. The third multiblock's face neighbours the instrument current drivers and the fourth touches the instrument Styrofoam housing. The internal circular face of the block is part of the intake tube and is exposed to passing ambient air.

The circular cut-outs in the multiblock allow passing light from an LED source to the mirror and from the mirror to the detector. The cut-outs normal form a 26° angle with each other and a 13° angle with the normal of the bridge. The detection scheme is designed in a way that it uses the reference reflectance from a clean reference surface to evaluate the ice coverage of the frost mirror. This reference surface is located below the mirror. It is gold plated and integrated into an aluminium core PCB.

Temperature is measured in relevant positions with thermocouples: inside the main mirror (T_{mirror}), between the hot-side of the Peltier element and the copper finger (T_{hot}), between the multiblock and the heat-sink (T_{sink}), in the reference surface PCB ($T_{\text{ref surf}}$) and outside the PCFH housing to measure the passing air temperature (T_{air}). Figure 3.1 is a schematics of the PCFH. The specific locations at which each temperature is measured are shown in Figure 3.1, as well as the reflectance signals (R_{mirror} and $R_{\text{ref surf}}$) and input currents of the Peltier element (I_{Peltier}) and reference surface heaters (I_{heater}) for both sub-units. Throughout this chapter we will look in more detail to each of the PCFH's components.

3.1 Peltier element

The Peltier element (PE) is the crucial component of the PCFH and at the same time a limiting component. The Peltier element is a thermo electric device, which when provided electrical current–I_{P}–can generate a temperature difference–ΔT–between its surfaces and/or transport heat from the cold to the hot side ($\dot{Q}_{\text{c}}$). The Peltier cooling ($\dot{Q}_{\alpha_P}$) is due to Seebeck effect. The temperature difference

attainable for a certain input current is offset by the heat the PE transports from the cold to the hot side: to reach $\Delta T_{\max}$, the PE can not transport any external heat ($\dot{Q}_{\mathrm{c}} = 0$ W); to transport the maximum heat across the PE ($\dot{Q}_{\mathrm{c\,max}}$), $\Delta T = 0$ K. Spurious heat contributions come from Joule heating ($\dot{Q}_{R_P}$) generated in the PE by the input current (I_P) and its internal electrical resistance (R_P) and the heat flow that is created by having a temperature difference across the PE itself ($\dot{Q}_{K_P}$). The different heat contributions are shown in Figure 3.2. More information on the thermoelectric effect can be found in Appendix B.1.

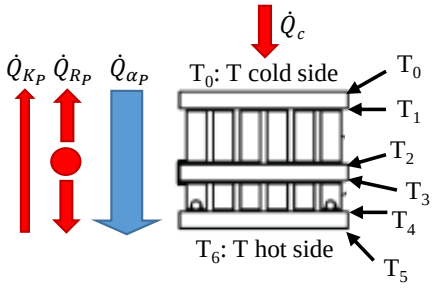

Figure 3.2: Peltier element schematic with heat contribution and different layer temperatures.

For the PCFH we looked for a Peltier element which could provide the following characteristics:

- Small size: approximately 5×5 mm^2;
- Large ΔT at low operating temperatures: $\Delta T \approx 35$ K @ $T_{\mathrm{amb}} = 198$ K;
- Small amount of heat to be removed from the hot side of the PE: $\dot{Q}_{\mathrm{h}} < 1$ W.

We decided to take an off-shelf solution from RMT Thermoelectric cooling solutions (RMT, 2019). RMT provides an in-house software, which allows to search the characteristics at different operation temperatures and heat loads of the Peltier elements they provide.

3.1.1 Single vs double stage

During the development phase of the PCFH we have considered two different Peltier elements from RMT: a single stage (1MC04-017-05) and a double stage (2MDX04-022-0510). In Table 3.1, we show the geometry of the two Peltier elements and in Table 3.2 the datasheet values for operation at a hot side temperature (T_{h}) of 27 °C in air. In Figure 3.3, Panels (a) and (b), we show a side and top view of PE 1MC04-017-05, respectively. In Panels (c) and (d), we show a side and top view of PE 2MDX04-022-0510. The single stage PE has a bigger surface area than the double stage, and it is thinner than the double stage.

The advantage of double stage PE in relation to a single stage is that double stage can provide higher temperature differences between PE cold and hot side. For the considered Peltier elments, the double stage provides a maximum temperature difference ($\Delta T_{\max}$), when the transferred heat is 0 W, of 86 K compared to 67 K that the single stage can provide. The disadvantage of a double stage PE in relation to single stage is that it can transfer less heat from the cold to the hot side. When there is no temperature difference between the hot and cold side in the two considered Peltier elements, the

Table 3.1: Peltier element 1MC04-017-05 and 2MDX04-022-0510 datasheet geometrical information

	Peltier element			pellets		ceramic[1]	# pellets	
	cold side (mm^2)	hot side (mm^2)	height (mm)	area (mm^2)	height (mm)	height (mm)	1^{th} stage	2^{nd} stage
1MC04-017-05	4.8×4.8	4.8×4.8	1.59	0.4×0.4	0.5	0.5	34	
2MDX04-022-0510	3.8×3.8	3.8×3.8	2.64	0.4×0.4	0.5	0.5	12	32

[1] material above, below and between stages

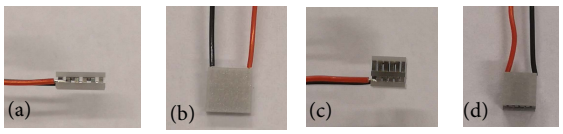

Figure 3.3: Single and double stage Peltier element. (a and b) single stage Peltier element 1MC04-017-05 side and top view respectively. (c and d) double stage Peltier element 2MDX04-022-0510. Pictures at comparable scale.

double stage PE can transfer the maximum heat ($\dot{Q}_{max}$) of 0.72 W compared to 1.89 W for the single stage.

Table 3.2: Peltier element 1MC04-017-05 and 2MDX04-022-0510 datasheet values for operation at 300 K (27 °C) in air.

Peltier element	ΔT_{max} (K)	I_{max} (A)	$\dot{Q}_{max}$ (W)	U_{max} (V)	R_P (Ω)
1MC04-017-05	67	1.5	1.89	2.11	1.07
2MDX04-022-0510	86	1.2	0.72	2.00	1.39

In Figure 3.4a, we see how the maximum temperature difference (ΔT_{max}) of the two considered Peltier elmenent's is affected by the operating hot side temperature (T_h). For the two, we can see that the colder T_h, the smaller ΔT_{max} is. Figure 3.4b shows how the transport of heat from the cold side to the hot side ($\dot{Q}_c$) of the PE affects ΔT at different T_h. When the application requires higher heat transfer, a single stage PE performs better than a double stage, and it is capable of keeping a higher ΔT. We call this ability of the PE stiffness. At T_h= 27 °C, for $\dot{Q}_c$<0.2 W, the double stage can keep higher ΔT than the single stage. As T_h decreases, so does the maximum $\dot{Q}_c$ that the double stage PE can transfer at a ΔT higher than the single stage. For the PCFH application, we flew in the same instrument, for the different sub-units, a double and a single stage Peltier element and confirmed that the double stage PE can attain larger ΔT than the single stage through the entire flight for the observed heat loads, making it a better option. We suspect, that for the PCFH application, we do not observe larger cold side heat loads than 0.05 W. In Figure 3.4c, we see how the temperature difference across the two Peltier elements relates to the input current at T_h= 27 °C in air (ΔT vs I_P). The curves

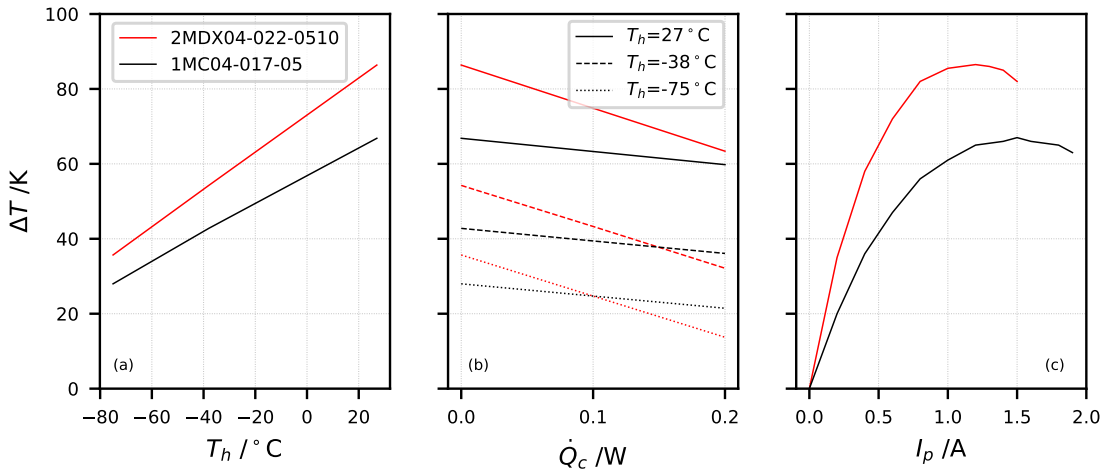

Figure 3.4: Datasheet values for Peltier elements 2MDX04-022-0510 (red) and 1MC04-017-05 (black) from RMT (RMT, 2019). (a) $\Delta T_{\max}$ for different hot side temperatures (T_{h}) in air; (b) ΔT for different cold side heat loads ($\dot{Q}_{\mathrm{c}}$) in W at different T_{h}: 27 °C (solid line), -38 °C (dashed line), -75 °C (dotted line); (c) ΔT for different input current (I_{P}) in A at T_{h} 27 °C in air.

have a parabolic shape due to the counteraction of linear heat transport ($\dot{Q}_{\alpha_{\mathrm{P}}}$) versus quadratic Joule heating ($\dot{Q}_{\mathrm{R_P}}$). ΔT peaks at 1.2 A and 1.5 A, for the double and single stage respectively.

3.2 Thermocouples

Thermocouples are another implementation of the thermoelectric effect. Their main application is for temperature measurements. For the implementation of thermocouples in PCFH we partnered with mylab elektronik GmbH (http://www.mylab.ch/), a Swiss company specializing in thermocouples.

Thermocouples for temperature measurements consist of two wires of different metals. In the PCFH, the two metals are copper (Cu) and constantan (Ko), a copper alloy. mylab elektronik GmbH purchased high quality cooper and constantan and turned them into several meters of different thickness wire: 0.05 mm. 0.1 mm and 0.3 mm. Wires obtained from the same melt lead to identical thermocouple characteristics. Thus just a single calibration of the lot is sufficient; individual calibration of each sensor is not required. To perform the temperature measurement, two wires of the same thickness and of different metals are connected at both ends, either by soldering or by welding (more information regarding these two methods in Appendix 3.2). One of the joints is kept at a known temperature. In the PCFH, this joint is kept at a reference thermometer on the thermocouple module board. This thermometer has been calibrated for temperatures down to -20 °C. The other joint of the thermocouple is placed where the temperature is to be measured. The temperature difference between the two joints, creates a voltage difference across the two wires. This voltage is measured by the application specific ADC (analog to digital converter) of the thermocouple module board designed by mylab elektronik GmbH. In Figure 3.5 Panels (a) and (b), we show a picture of the tip of a Ø 0.1 mm soldered thermocouple and the thermocouple module board where all 14 channels of the ADC are in use by different thickness thermocouples, respectively.

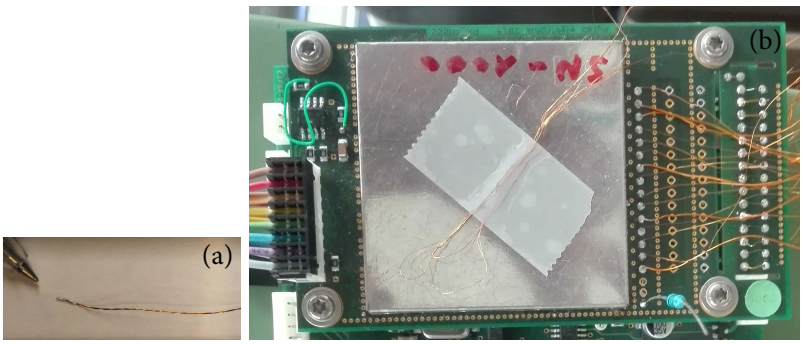

Figure 3.5: (a) Soldered Cu and Ko Ø 0.1 mm thermocouple. (b) PCFH Thermocouple module board with different thickness thermocouples soldered.

3.2.1 Thermocouple calibration: voltage to temperature

The thermocouples have been calibrated to Swiss national standards to ensure traceability. The calibration certificates are available on-line (Roth+Co.Ag, 2016).

The voltage to temperature calibration is approximated as fourth order polynomial as shown in Equation (3.1). The calibration coefficients are given in Table 3.3. Figure 3.6 shows the difference from the measured temperature used for the calibration and the temperature calculated from the measured voltage using the calibration of Table 3.3. In the region of interest for the PCFH, between +40 °C and -100 °C, the calculated temperature agrees with the measured temperature within 0.05 K. The temperature to voltage calibration is given in Appendix 3.2.

$$T = b_0 + U\ (a_1 + U\ (b_2 + U\ (b_3 + U\ b_4))) \tag{3.1}$$

Table 3.3: Voltage to temperature calibration coefficients

mm	b_4	b_3	b_2	b_1	b_0
Ø 0.3	-6.736950×10^{-15}	7.726287×10^{-11}	-7.785970×10^{-7}	2.579393×10^{-2}	1.793765×10^{-2}
Ø 0.1	-6.431381×10^{-15}	7.617175×10^{-11}	-7.784069×10^{-7}	2.577527×10^{-2}	3.481059×10^{-2}
Ø 0.05	-6.279936×10^{-15}	7.612948×10^{-11}	-7.852761×10^{-7}	2.576808×10^{-2}	3.010441×10^{-2}

3.2.2 ADC testing

We evaluated uncertainties of the PCFH temperature measurements. First we compared the performance of the PCFH thermocouple module ADC to a very accurate nano-voltmeter (Keysight 34420A, SN My42006584, Agilent (2019)) for different reference voltages: short-circuit, 1 mV, 5 mV and 10 mV, at different operating temperatures: 25 °C, 5 °C, 0 °C, -5 °C and -15 °C. We found that the channel's voltage agreed with each other to within a ±0.25 μV range; this corresponds to a temperature error smaller than ±0.01 K. The standard deviation for each channel is also on average within a ±1.5 μV range, which is a ±0.04 K uncertainty. There were differences between the nano-voltmeter reference measurement and the PCFH-ADC measurements as small as ±0.5 μV and as big as ±3 μV depending

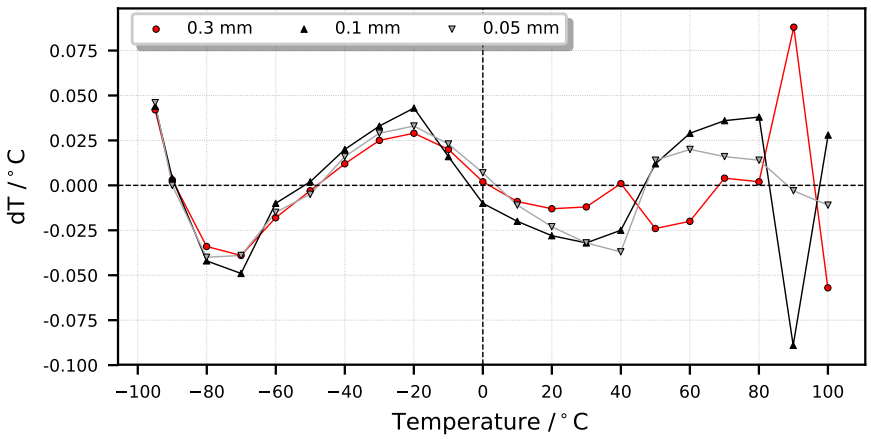

Figure 3.6: Difference between measured and calculated values for voltage to temperature calibration of thermocouples. Circle: Ø 0.3 mm, up triangle: Ø 0.1 mm, down triangle: Ø 0.05 mm.

on the tested voltage and temperature, which translates to an accuracy better than ±0.1 K. There is no clear dependence in temperature for all measured voltages. The linearity of the measurement was especially good for the 1 mV test. Table 3.4 provides a coarse conversion from voltage to temperature according to the thermocouples calibration.

Table 3.4: Rule of thumb thermocouple calibration conversion between voltage and temperature.

4 mV	400 μV	40 μV	4 μV	0.4 μV
100 K	10 K	1 K	0.1 K	0.01 K

3.2.3 Validation of thermal board and thermocouple calibration

Second, we compared the performance of the PCFH thermal-module ADC with thermocouples to a reference thermometer 1502A by Fluke (2019), calibration certificate number 19774 on the 20/01/2017 by ELCAL (https://www.elcal.ch/). Very long thermocouples, 1.5 m, of different thickness (0.05, 0.1 and 0.3 mm; each thermocouple is assembled with same thickness wires) were attached, electrically insulated but with thermal contact, to an aluminium block involving the reference thermometer. The temperature of the entire set-up was equilibrated to 0 °C and -20 °C using a portable cooling chamber and to -80 °C using dry ice in a dewar.

These tests revealed that with decreasing thermocouple thickness, there is an increase of temperature measured by the thermocouples in relation to the reference thermometer. This increase is attributed to decreasing cross section hence increasing resistance of the wires. On the positive side, there is no significant difference between thermocouples of similar thickness, except for the tests at -80 °C. For these tests, since the cooling was done with dry ice and the temperature difference reached was very high, we believe the aluminium block temperature was not homogeneous, and there was residual heat being transported through the thermocouple wires, especially the thicker ones. See the average temperature difference between thermocouples and reference thermometer for the different thickness thermocouples in Table 3.5.

Table 3.5: Average temperature difference in K between thermocouples of different thickness and reference thermometer.

temperature tests	thermocouple thickness and numbers		
	Ø 0.3 mm	Ø 0.1 mm	Ø 0.05 mm
	5	6	1
	(K)	(K)	(K)
0 °C	0.046±0.008	0.290±0.010	1.043
-20 °C	0.073±0.014	0.335±0.005	1.104
-80 °C	0.007±0.075	0.301±0.067	1.206

For each temperature and each thermocouple, we chose a time interval of 3 hours to evaluate the linearity of the thermocouple calibration. On average the standard deviation for these intervals is ±0.035 K, which corresponds to the observed voltage ADC precision. In Table 3.6, we present the average result of a linear fit to the three average temperatures of each test (0 °C, -20 °C and -80 °C) for the thermocouples of different thickness versus the average temperature measured by the reference thermometer during the same time interval. On average the linearity of the measurement is independent of thickness, with a different offset for each thermocouple thickness. The offset is consistent with the difference between channels and reference thermometer observed in Table 3.5.

Table 3.6: Linear relation between different thickness thermocouple and reference thermometer

$y = a \cdot x + b$	thermocouple thickness		
	Ø 0.3 mm	Ø 0.1 mm	Ø 0.05 mm
a ()	1.001±0.001	1.000±0.001	0.998
b (K)	0.063±0.013	0.311±0.002	1.053

In Appendix 3.2, we estimate the resistance of thermocouples of different thickness with 1.5±0.1 m length. The constantan wire represents the biggest contribution for the wire resistance. Its resistance is barely influenced by the temperature change of the material, unlike copper, which resistance in the temperature interval observed can change by 37%. However, this represents a 1% change of the thermocouple resistance. If we consider a 1 μA current to flow through the thermocouple, the voltage drop due to the wire's resistance is sufficient to cause the observed temperature difference to the reference for the different thickness thermocouples. Following this discovery, the thermcouple board was altered to include a voltage buffer in the ADC channels to prevent current to be drawn through the thermocouple. Theoretically this addition the the thermocouple board fixes the problem, but the tests were not repeated with the new boards.

In these tests, we also compared thermocouples built with different techniques: soldering and welding, and found there to be no difference in terms of accuracy nor precision. For the PCFH application we decided to use soldered Ø 0.1 mm thermocouples. The instrument is designed as a double instrument, and since the thermocouple module board is not placed symmetrically in relation to the two sub-units (see Figure 3.13), the thermocouples have different lengths. For sub-unit 1, closer to the ADC soldering pads the thermocouples are 25 cm long (Cu: 25 cm and Ko: 20 cm) and for sub-unit 2 the thermocouples are 35 cm long (Cu: 35 cm and Ko: 30 cm).

3.2.4 Housekeeping data

For each sub-unit we measure five temperatures, two are relevant to evaluate the water vapour content, relative humidity and ice saturation of the air parcel:

1. Mirror temperature ($T_{\text{mirror}_{1/2}}$);
2. Air temperature ($T_{\text{air}_{1/2}}$);

And three are considered house-keeping data, and help evaluate whether the instrument is performing according to expectation.

3. Peltier hot side temperature ($T_{\text{hot}_{1/2}}$);
4. Heat sink temperature ($T_{\text{sink}_{1/2}}$);
5. Reference surface temperature ($T_{\text{ref surf}_{1/2}}$).

3.3 Mirror

The mirror is the measurement surface which is cooled by the Peltier element and on which the deposit (dew or frost) forms. The thickness of the deposit is then object of monitoring by the detection scheme and object of control through growth or evaporation by cooling or warming respectively by the Peltier element.

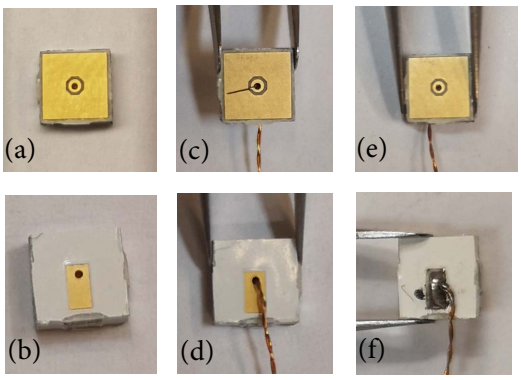

Figure 3.7: PCFH mirror. (a) Front and and (b) back view of the PCFH mirror respectively. (c) Front and (d) back view of the PCFH mirror with mirror thermocouple.(e) Front and (f) back view of the PCFH mirror with soldered thermocouple.

The mirror is a custom made double layer metal(Al) PCB element. It has 4×4 mm^2 surface and it is 1 mm thick. Its top surface is covered by a 3.9×3.9 mm^2 gold plating. The top and bottom surface of the mirror are connected by a Ø 0.3 mm^2 hole. On the bottom surface, the hole is also connected to a gold solder pad, see panel (a) and (b) Figure 3.7. Through the hole we insert a non soldered but connected thermocouple joint as seen in Panels (c) and (d) of Figure 3.7. The hole and thermocouple are then sealed with solder as seen in Panel (e) and (f) of Figure 3.7. On the top surface the hole is circled by Ø 0.5 mm gap, which prevents the solder to spread across the entire surface. This

thermocouple is the 'mirror thermocouple'. Through this assembly method, the thermocouple has a good thermal contact to the entire mirror and the temperature is the true mirror temperature. We assume the mirror temperature to be the dew/frost temperature when the dew/frost layer deposited in the mirror is in equilibrium with its environment.

Following the indication of the U.S. patent 7,393,135 B2 (Kanai, 2008a), we do not oppose the irregularities created in the mirror surface by the tip of the thermocouple, solder or circular dent. They might enhance the condensation of water vapour, serving as cores for the deposit growth.

3.3.1 Thermal glue

After mounting the thermocouple, the mirror is connected to the cold side of the Peltier element. Since the cold surface of the Peltier element is made of ceramics it is not possible to solder the two parts together.Following the Peltier element manufacturer's advice we resorted to a thermal glue (Wärmeleitkleber, 2019), used mainly for electronic cooling purposes, see Panel (f) Figure 3.9, the blue layer behind the mirror. The specific thermal resistance of this glue is 1.2 m K W^{-1}. Passing 0.01 W through a 4×4 mm^2 surface of 0.2 mm thickness corresponding to the thermocouple in the back of the mirror causes a 0.15 K temperature increase across the layer. When gluing the mirror and Peltier element together, we ensure the alignment of the two square shapes and the homogeneous thickness of the glue, to ensure the best possible thermal contact between the two elements. For this, we use in-house machined gluing aids made of Teflon with the desired tolerances.

3.4 Detection scheme and reference surface

The PCFH optical detection works by comparing light reflected from the mirror with light reflected from a reference surface. LED light intensity is very sensitive to temperature variations of the device. There are different ways to track the stability of the LED, such as monitoring LED brightness or ensuring operation at constant temperature throughout the flight, both strategies are employed by the CFH and FPH, respectively. (Vömel et al., 2007b, 2016; Hall et al., 2016). By using the reference surface, we aim to account for temperature drifts and other disturbances to the light path. For this purpose, it is essential that at all times the reference mirror is clear of ice or dew. For this we keep it 3 °C warmer than ambient air up to slightly above the tropopause, while supersaturation may be expected, and relax the difference in the stratosphere, where ambient cooling of the Peltier hot side becomes critical.

The LED light is incident at an angle of 13° and reflected at the same angle into an optical path, into a photo-detector pair. The reference surface is a 4×4 mm^2 golden plated metal core PCB surface located in the same plane 1 cm below the PCFH mirror. The LED light is reflected of both surfaces, passes through a solar filter and an imaging lens, which inverts the light paths as shown in Figure 3.1 and focuses them into two identical photo detectors. The clean mirror to reference surface brightness ratio is calibrated before flight. The outputs of the detection scheme are the mirror reflectance and the reference surface reflectance for the two sub-units: $R_{\mathrm{mirror}_{1/2}}$ and $R_{\mathrm{ref\ surf}_{1/2}}$ (Figure 3.1).

In Figure 3.9f, we can see two resistors that warm the entire PCB, into which the reference surface is integrated. The warmer reference mirror is below the Peltier mirror to reduce the possibility of measurement contamination from evaporation of liquid water or sublimation of ice. As can be seen in

Figure 3.9f, the PCB board of the reference surface has four electric pads at the bottom and two at the top. The two pads at the top serve to power the Peltier element. The four bottom pads connect the reference surface PCB board to the main PCFH board Peltier element drivers and reference surface heater drivers. We refer to the currents powering the Peltier elements and warming the reference surfaces of the two sub-units as $I_{\mathrm{Peltier}_{1/2}}$ and $I_{\mathrm{heater}_{1/2}}$ as shown in Figure 3.1 and throughout the rest of this thesis as I_{P} and I_{H}.

The reference surface PCB has been subject to some alterations after the PCFH first flights. The opening for the Peltier element and mirror has been enlarged to decrease heat coupling between the heated reference surface PCB and the Peltier element cold side mirror. For a picture of a previous version please refer to Appendix B.3. The heating scheme of the reference surface PCB, has also been altered. Now, it incorporates a capacitor and an inductor smoothing the current driving the resistors to reduce interferences on the delicate thermocouple voltage measurement. The pad between the Peltier element mirror opening and the reference surface, is for soldering of the 'reference surface thermocouple'.

3.5 Intake tube

To bring atmospheric air to the sensor head we decided to pursue a design similar to the CFH and FPH. Since the detection scheme based of reflected light requires the optics to face the mirror and Peltier element, and both these components need to be connected to the main board, housing is needed, which accepts an intake and outlet tube.

The tubes are made of 0.05 mm thick 150×140 mm^2 stainless steel sheet metal. The sheet metal is rolled into a cylinder and point welded along the long edge. For stability a 30 mm long aluminium ring with inner Ø 39.2 mm and outer Ø 40 mm is added around and at the bottom of the tube. This ring makes the contact between the intake tube and the multiblock and the outlet tube and the multiblock lower ring. Figure 3.8 shows one intake tube. Figure 3.14 shows an intake and outlet tube assembled into the PCFH.

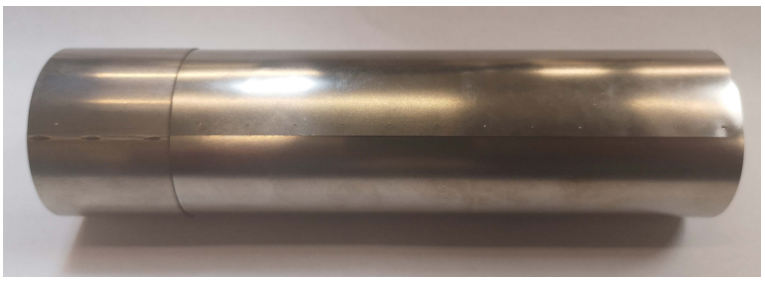

Figure 3.8: PCFH intake tube

The intake tubes are wider and slightly shorter than the intake tubes of the CFH: Ø 40 mm and 150 mm length in comparison to Ø 25 mm and 170 mm length of the CFH. However, they still extend 120 mm above the instrument housing as the CFH intake tubes. From recommendations of the computational fluid dynamics study of water vapour contamination (Section 2), we decided to increase the intake tubes cross section. Future changes to the design of the intake tubes are not excluded. We

also expect the double design of the instrument to allow for the exploration of different intake tubes designs.

3.6 Multiblock and component assembly

The multiblock was designed to integrate all the components of the PCFH sensor head: Peltier element, mirror, reference surface board and its electric connections, thermocouples, optical detection elements, intake and outlet tubes, heat sink and to connect all of these to the PCFH main board.

Figure 3.9: Multiblock

Peltier element and reference surface

After the study of water vapour contamination in frost point hygrometers (Chapter 2), we consider the placement of the detection mirror away from the intake tube wall as an advantage. So, for the PCFH design we wanted to have the Peltier element and mirror moved into the center of the intake tube. For this purpose the multiblock is designed with an arm or bridge extension as seen in Figure

3.9 Panels (a), (b) and (d). At the same time, the reference surface and the mirror glued in the Peltier element should be at the same level for optical purposes, so the bridge is equipped with a hole of the right depth to fit the Peltier element, so the mirror and reference surface are in the same plane.

The Peltier element hot side is also made of ceramics, so it is not possible to solder it to the multiblock. As an alternative we have resorted to thermal glue as for the connection of the mirror to the Peltier cold side. To improve the controlling of the Peltier element, we introduce the 'Peltier hot side' thermocouple into the thermal glue between the Peltier hot side and the multiblock. This design might require revision, because with the thermocouple between the PE hot side and the copper finger, we expect the glue layer to be 0.2 mm thick which causes a temperature increase of the order of 10 K for a 1 W heat across.

The multiblock arm has a rectangular shape to fit the reference surface PCB and a small edge around the entire surface to determine its place, as can be seen in Panel (d) and (f) of Figure 3.9. At the top there is a small dent to pass the Peltier element supply wires, which are soldered to the reference surface PCB above the Peltier element. This design feature coming from previous iterations of the multiblock may be changed in the future. The arm of the multiblock has a carved path, running the length of the reference surface board behind it, to fit the mirror, reference surface and Peltier hot side thermocouple wires.

Detection scheme

The multiblock also accommodates the detection scheme elements: the infra-red LED, optical tube and detectors to their right alignment. The opening for the LED is identified with number 1 in Panel (e) of Figure 3.9 and the opening for the optical tube with number 2. In Figure 3.10, we show all the components of the optical path and detection scheme. The optical tube (g) is 3D printed in plastic. It fits an acrylic focusing lens (f). An aluminium spacer (e) keeps the lens in place. The optical tube is then screwed into the multiblock and together with the aluminium spacer presses the sun filter (d) against the multiblock opening. An o-ring (c) is placed between the filter and the multiblock to prevent contamination of the outside air with air from inside the housing. The photo detectors (h) are screwed into place on the other extremity of the optical tube. The photo detectors and LED are assembled in small PCB boards, which are connected vertically to the PCFH main board as seen in Figure 3.13. An acrylic collimator is glued to the LED PCB board (a) and the entire construction is screwed into the multiblock. An o-ring (b) is placed between the lens and the multiblock to seal the outer atmosphere from housing air.

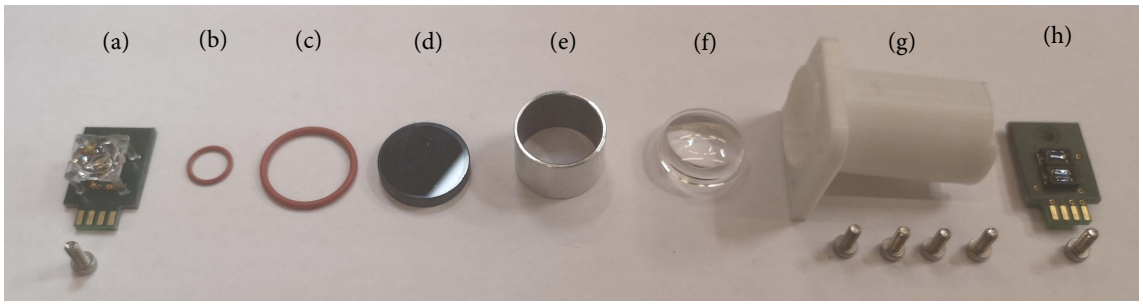

Figure 3.10: PCFH detection scheme components

Connection to PCFH main board and intake tubes

As mentioned, the PCFH is a double instrument, so the PCFH main board is designed with 2 openings to hold 2 multiblocks. The two multiblocks are placed in diagonally opposing corners of the main board for stability and weight symmetry as can be seen in Figure 3.13a. Each multiblock is screwed into position with a plastic 3D printed bottom part as seen in Figure 3.9b and 3.13b. The PCFH main board stays between the two pieces. O-rings are used on each side of the main board for sealing.

The intake tube is then mechanically forced into the top opening of the multiblock up to the small dent made visible in Figure 3.9 by the dashed white lines. The outlet tube is also mechanically forced into the bottom ring until it reaches the PCB or the multiblock. So far we have taped the intake tube and outlet tube in place as can be seen in Figure 3.14. We consider the use of an epoxy for future flights, not for robustness purposes, but for sealing and contamination prevention.

Material and production

Considering all details required for the multiblock, it had to be 3D printed. However, a good thermal conductivity for the multiblock is a requirement, considering we need to remove heat from the hot side of the Peltier element with the least possible additional temperature gradient to ensure a good performance of the Peltier element. For this reason, it is printed in an aluminium alloy: $AlSi_{10}Mg$ (Aluminium, 2019). The heat conductivity of this alloy when printed represents a significant improvement from a plastic (for example: ABS) printed multiblock and it can be further improved with heat treatment for 2 hours at 300 °C. However, the thermal conductivity of the printed alloy is still 25% less than pure aluminium (Al) and 60% less than copper (Cu) as can be seen in Table 3.7. The multiblock after printing is heat treated, sand polished and anodized. The anodization darkens it for optical purposes.

Table 3.7: Multiblock material's thermal properties

material property	ABS[1]	$AlSi_{10}Mg$[2]		Al[3]	Cu[3]
		As built	heat treated		
thermal conductivity k (W m^{-1} K^{-1})	0.24	103±5	173±10	235	401
heat capacity c_p (J kg^{-1} K^{-1})	1260-1675	920±50	890±50	910	390

[1] (Trhlíková et al., 2016; Weiss et al., 2015)
[2] (Aluminium, 2019) from here on we will refer to the material as Al 3 D.
[3] (EngineeringToolbox, 2019a,b) at 0 °C

After some initial testing with Peltier elements glued directly to the multiblock, we realized the thermal conductivity of the material to be too small for the desired performance of the Peltier element. For new multiblock designs, a hole is drilled from the back of the multiblock to the location of the Peltier element and a copper finger is pressed and hammered into position. During the development phase different configurations of copper fingers have been investigated. At the moment, the copper finger has two diameters, on the side where the Peltier element is glued the Ø is 7 mm. On the side that contacts the heat sink the Ø is 15 mm. The thermal conduction is proportional to the cross

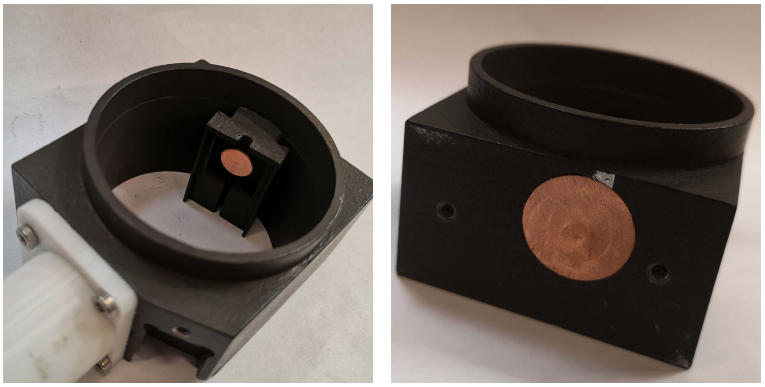

Figure 3.11: PCFH multiblock copper insert

section of the finger. The change in diameter also helps control the depth of the cooper finger in the multiblock, hence the position of the Peltier element and mirror. Refer to Appendix B.3 for a picture of the multiblock previous version.

3.7 Heat sink

The purpose of the heat sink is to increase the contact area of the Peltier element hot side with the ambient air which is the cooling agent of the PCFH. For the PCFH we chose an off-the-shelf heat sink (Panasonic, 2019). We decided on an anodized aluminium heat sink with 8-fins 8 mm apart. The fin geometry is standard for cooling electronics, hence more available, and also easier to simulate. The fins have a contact surface of 27×25 mm^2 on each side and are 2 mm thick. The fins are 27 mm long in the flow direction and they have texture to improve convective heat transfer. The heat sink is screwed into the back of the multiblock. Between the two we spread a thermal paste to improve the thermal contact (DOWSIL, 2019).

The heat transferred by the heat sink into the ambient air depends on the difference of its temperature to the ambient air, the contact surface of the heat sink with ambient air and the convective heat transfer coefficient (h) of air. The convective heat transfer of air depends on the thermodynamic and fluid dynamic properties of air as well as the geometry of the heat sink. Appendix 4.3 presents a study of air thermodynamic and fluid dynamic properties with the purpose of estimating convective heat transfer coefficients. We saw that a heat sink with a similar geometry (design used in PCFH's first flights, see Figure B.14 in Appendix B.3) would be able to provide up to 5 W of cooling potential with a temperature increase from ambient smaller than 2 °C. This is an acceptable performance, a loss of 1 to 2 °C from ambient should always be expected, there is no heat transfer (cooling) without temperature difference. However, at lower pressure levels of the stratosphere, below 20 hPa, we can expect temperature differences up to 10 °C from the ambient, for a cooling potential of less than 5 W. At these pressure levels, we are anyway out of the operating range of the PCFH, due to Peltier element limitations, so the heat sink is not the only limiting factor in this region.

3.8 Radiation protection and housing

The PCFH housing is a Styrofoam box with lid, with four openings for the two intake and outlet tubes. The housing exposes the heat sinks as much as possible to maximize their contact surface with ambient air. For safety reasons we add a cylindrical protection around the heat sinks, to prevent any damage in case the instrument should land with the heat sinks first into a car, for example, see Figure 3.12. The cylindrical protection has a second purpose: it shields the heat sink from radiation from the sun, during the day, if this is not directly above the payload, and from the universe at night.

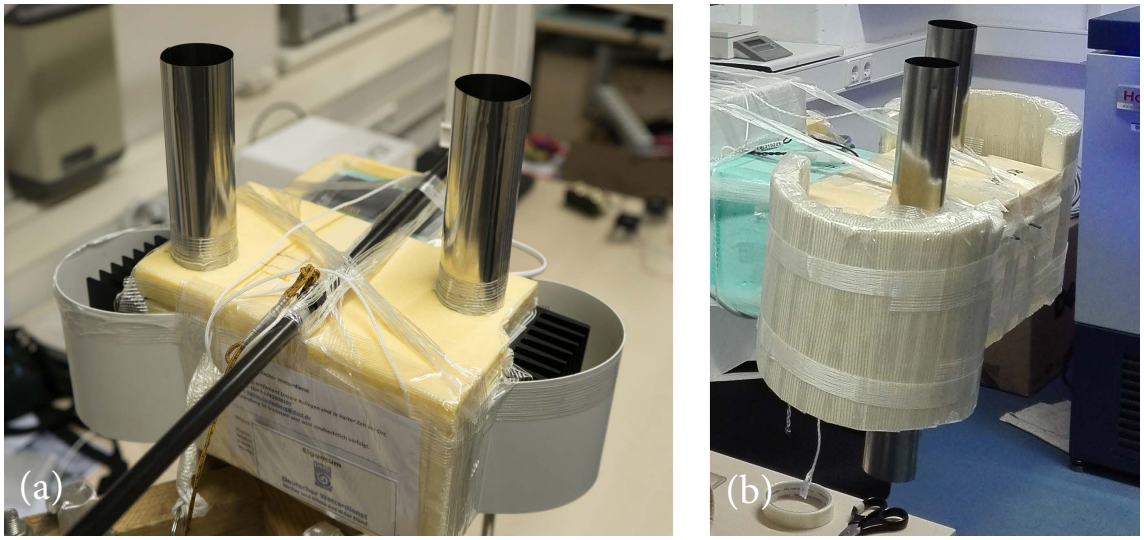

Figure 3.12: PCFH housing and radiation protection. (a) PCFH flown on the 25 July 2018. (b) PCFH flown on the 13 December 2018.

3.9 Instrument integration and power supply

The PCFH has three independent power supplies two at 4.5 V and one at 6 V. The 6 V power supply composed of 4×1.5 V AAA lithium batteries powers the analogue electronics of the optical detection scheme. Initially the 4.5 V power supply composed of 3×1.5 V AA lithium batteries powered all the digital electronics, current drivers for the Peltier elements and reference surface heaters and the thermocouple module board. After the first flights, we realized the PCFH had higher power requirements and the drivers caused peaks of current drainage which were affecting the power supply of the thermocouple module and disturbing the temperature measurements. Now the thermocouple module has its own power supply of 3×1.5 V AA lithium batteries shared only with the digital electronics and separated from the current drivers which are powered by two packs of 3×1.5 V AA lithium batteries. The batteries are connected to the PCFH main board from below as can be seen in Figure 3.13b. In Table 3.8 we summarize the PCFH's power requirements.

The PCFH was developed modularly. The thermocouple module board and the board with the communication, controller and drivers of the Peltier element, and heaters were developed by mylab elektronik GmbH. The board with the detection scheme was developed at ETH. The two later boards have now been integrated. Figure 3.14 shows the partially exposed instrument with intake and outlet

Table 3.8: Power supply

9	AA lithium batteries
4	AAA lithium batteries

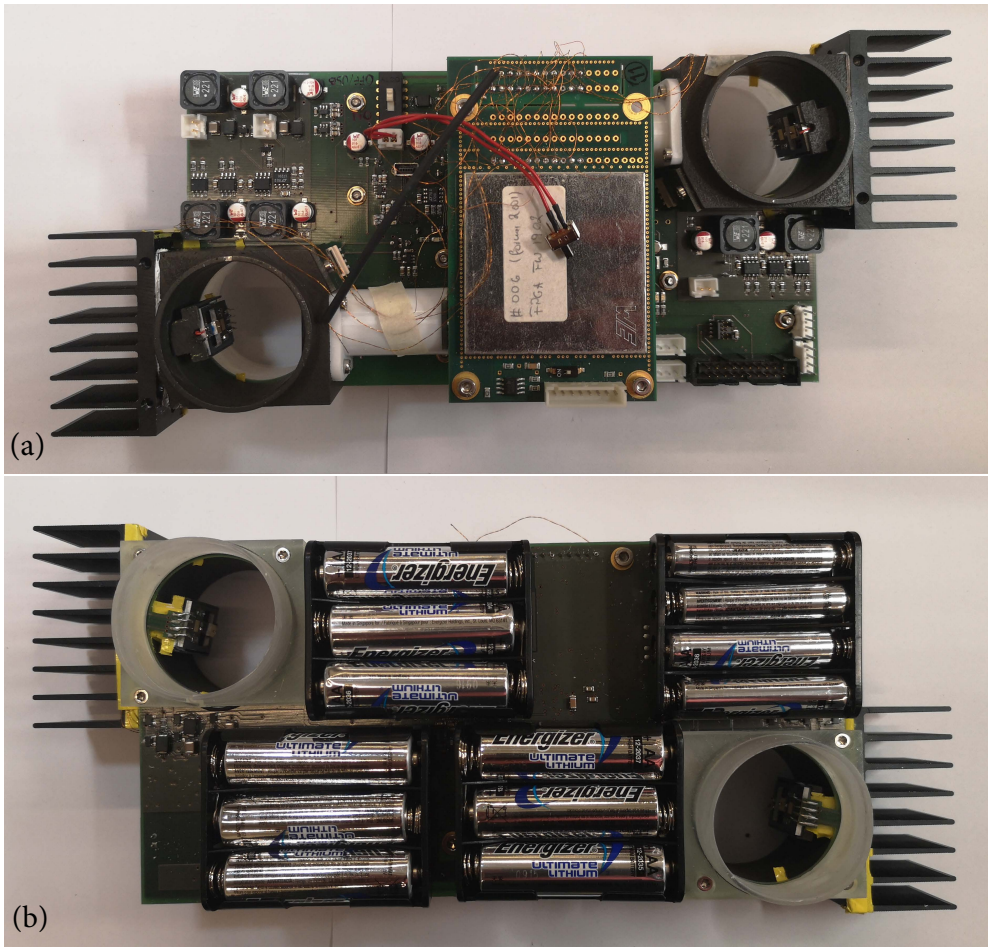

Figure 3.13: PCFH (a) top view; (b) bottom view

tubes. For a picture of a previous version, refer to Figure B.15, Appendix B.3.

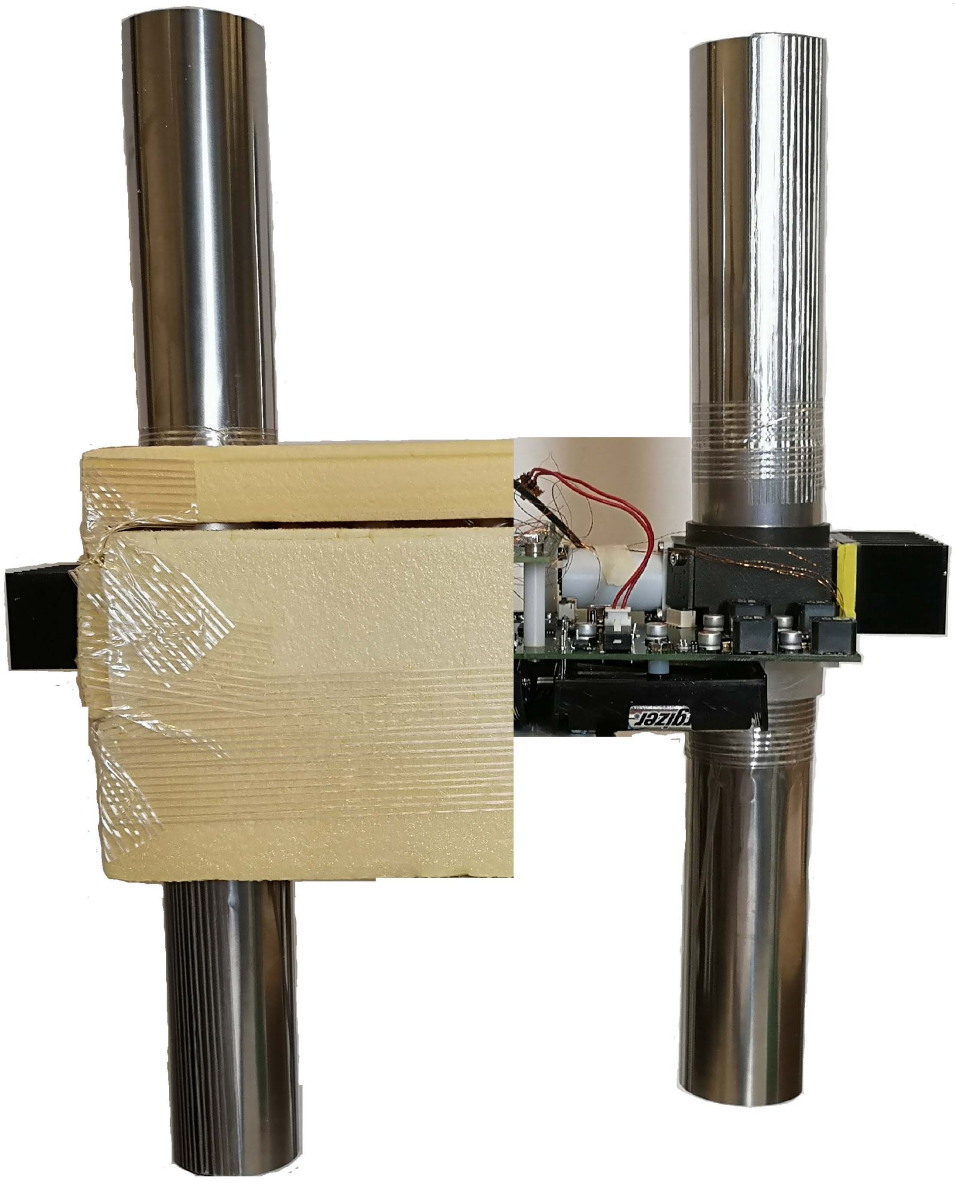

Figure 3.14: PCFH instrument with partially exposed circuit board

3.10 Communication

The PCFH has three main types of communication: for operation, two serial ports (i.e. logic level RS-232) 'radiosonde' and 'instrument' according to the X-DATA specifications (Wendell and Jordan, 2016), and a third serial port for lab setup and testing. The PCFH has additional ports for firmware programming. Telemetry is used when the PCFH is operating in the atmosphere as a balloon borne instrument. In laboratory and development environments, we use serial communication via a USB port. Before flight, the PCFH is configured via serial communication.

During flight the PCFH communicates 4 regular independent telemetry packets: two packets every 1 second for communication of fast changing measurements from each of the sub-units, one packet every 5 seconds with slow changing measurements from the two sub-units and one packet every 10 seconds with instrument configuration data. PCFH also has the option of activating further experimental packets. In Table 3.9 we show the composition of the regular packets. The telemetry encoding is available on-line (Jorge and Wienhold, 2019).

Table 3.9: Regular telemetry packets

sub-unit 1	sub-unit 2	slow
Instrument ID (II)		
Daisy Chain index (DI)		
Packet ID (PI)		
Time stamp (TS)		
T_{mirror1}	T_{mirror2}	T_{sink1}
T_{hot1}	T_{hot2}	$T_{\text{ref surf1}}$
T_{air1}	T_{air2}	T_{sink2}
T_{target1}	T_{target2}	$T_{\text{ref surf2}}$
R_{mirror1}	R_{mirror2}	T_{ref} [1]
$R_{\text{ref surf1}}$	$R_{\text{ref surf2}}$	T_{res} [2]
I_{heater1}	I_{heater2}	U_{bat60}
I_{Peltier1}	I_{Peltier2}	U_{bat45}
1 s	1 s	5 s
16 bytes	16 bytes	15 bytes

[1] Temperature of the reference thermometer in the thermocouple module board
[2] not in use

Chapter 4

System modelling for control implementation

In this chapter, we report on the developments so far towards the implementation of optimal control in the PCFH. First, we give a brief introduction to dynamic systems, control, feedback, feedforward a and how these concepts apply to PCFH. We also provide some information regarding different control implementations such as PID and optimal control. Then we look at how to create a model for a thermodynamic system such as the PCFH and present the PCFH model. The model implementation in Simulink will be presented in Chapter 6 as well as first steps towards model optimization and validation. We have not achieved a stable PCFH design, which can fulfil the operation requirements for water vapour measurements in the stratosphere. We will proceed with the controller implementation once the instrument design, and model are stable.

4.1 Dynamic systems, control, feedback and feedforward

Feedback implies the modification of a dynamical system. Feedback may be implemented for a number of reasons: to regulate a physical variable, such as temperature or pressure; to speed up a sluggish system or slow down a jumpy one; to stabilize an otherwise unstable dynamics. Whatever the reason, one always starts from a given dynamical system and creates a 'better' one.

4.1.1 Dynamic systems: time and frequency domain

Concepts of control, feedback and feedforward are usually approached in the frequency domain because it is easier to deal with algebraic expressions than with linear differential equations. However, control, feedback and feedforward apply to dynamic systems which exist and are perceived by humans in the time domain. Dynamic systems can be described as:

$$\dot{\vec{x}} = \vec{f}\,(\vec{x}, \vec{u}) \tag{4.1a}$$

$$\vec{y} = \vec{g}\,(\vec{x}, \vec{u}) \tag{4.1b}$$

where the vector $\vec{x}$ represents n independent 'states' of a system, $\vec{u}$ represents m independent inputs (driving terms), and $\vec{y}$ represents p independent outputs. The vector-valued function $\vec{f}$ represents the (non-linear) dynamics and $\vec{g}$ translates the state $\vec{x}$ and 'feeds' the input $\vec{u}$ directly to the output $\vec{y}$. The role of Equation (4.1b) is to translate the perhaps unobservable state variables $\vec{x}$ into output variables $\vec{y}$.

Simpler systems may not require this general notation. A linear system can be written as:

$$\dot{\vec{x}} = \tilde{A}\vec{x} + \tilde{B}\vec{u} \tag{4.2a}$$

$$\vec{y} = \tilde{C}\vec{x} + \tilde{D}\vec{u} \tag{4.2b}$$

where the dynamics $\tilde{A}$ are represented as an $n \times n$ matrix, the input coupling $\tilde{B}$ as an $n \times m$ matrix, the output coupling $\tilde{C}$ as a $p \times n$ matrix, and $\tilde{D}$ is a $p \times m$ matrix. $\tilde{D}$ describes the direct feed-through and is frequently set to 0 (Bechhoefer, 2005).

We look at the example of a damped harmonic oscillator which models the typical behaviour of many systems when slightly perturbed from equilibrium:

$$m\ddot{q} + 2\gamma\dot{q} + kq = kq_0(t) \tag{4.3}$$

we can scale time by $\omega_0^2 = k/m$, the undamped resonant frequency, and by defining $\zeta = (\gamma/m)\sqrt{m/k} = \gamma/\sqrt{mk}$ as a dimensionless damping parameter, with $0<\zeta<1$ for an underdamped oscillator and $\zeta>1$ for an overdamped system.

$$\ddot{q} + 2\zeta\dot{q} + q = q_0(t) \tag{4.4}$$

To bring this into the form of Equations 4.2, we let $x_1 = q$, $x_2 = \dot{q}$. Then $n = 2$ (second-order system) and $m = p = 1$ (one input, $u = q_0$, and one output, q), and we have:

$$\frac{d}{dt}\begin{pmatrix} x_1 \\ x_2 \end{pmatrix} = \begin{pmatrix} 0 & 1 \\ -1 & -2\zeta \end{pmatrix}\begin{pmatrix} x_1 \\ x_2 \end{pmatrix} + \begin{pmatrix} 0 \\ 1 \end{pmatrix} \cdot u(t) \tag{4.5}$$

with

$$y = \begin{pmatrix} 1 & 0 \end{pmatrix}\begin{pmatrix} x_1 \\ x_2 \end{pmatrix} + 0 \cdot u(t) \tag{4.6}$$

where the matrices $\tilde{A}$, $\tilde{B}$, $\tilde{C}$ and $\tilde{D}$ are all written explicitly. In this example, there is little reason to distinguish between x_1 and y, except to emphasize that one observes only the position, not the velocity.

To transform time domain systems to frequency domain system, one usually resorts to Laplace transforms. Laplace transforms are preferred over Fourier transforms, because their transformable function space vastly exceed that of the Fourier transform. They handle initial conditions better, which are explicitly specified in the transform, as well as non decaying functions such as step functions. The Laplace transform of $y(t)$ can be defined as:

$$\mathcal{L}[y(t)] \equiv y(s) = \int_0^\infty y(t)\, e^{-st} dt \tag{4.7}$$

For zero initial conditions, $\mathcal{L}[d^n y/dt^n] = s^n y(s)$ and $\mathcal{L}\left[\int y(t)\, dt\right] = (1/s)\, y(s)$. Note that we use

the same symbol y for the time and transform domains, which are quite different functions of the arguments t and s.

An nth-order linear differential equation in t transforms to an nth-order algebraic equation in s. For example, the first-order system:

$$\dot{y}(t) = -\omega_0 y(t) + \omega_0 u(t) \tag{4.8}$$

becomes

$$sy(s) = \omega_0 [-y(s) + u(s)] \tag{4.9}$$

leading to

$$G(s) \equiv \frac{y(s)}{u(s)} = \frac{1}{1 + s/\omega_0} \tag{4.10}$$

where the transfer function $G(s)$ is the ratio of output to input, in the transform (frequency) space (Bechhoefer, 2005).

4.1.2 Control, feedback and feedforward

Consider a system whose dynamics is described by $G(s)$. The goal of control is to have the system's output $y(s)$ follow a control signal $r(s)$ as faithfully as possible. Note, $r(s)$ is the **control signal** . The general strategy consists of two parts: first, we measure the actual output $y(s)$ and determine the difference between it and the desired control signal $r(s)$, i.e. we define $e(s) = r(s) - y(s)$, which is known as the error signal. Then we apply a **control law** K to the error signal to try to minimize its magnitude, as seen in Figure 4.1. The new input signal to the system becomes $u(s) = K(s)e(s)$ and the new output signal is $y(s) = K(s)G(s)e(s)$ or as in

$$y(s) = \frac{K(s)G(s)}{1 + K(s)G(s)} r(s) \tag{4.11}$$

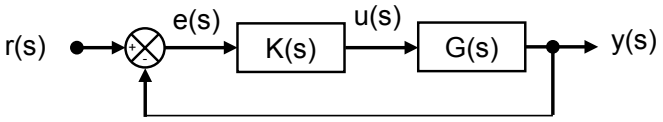

Figure 4.1: Close-loop control. Adapted from Bechhoefer (2005).

Another basic idea of control theory is the notion of feedforward, which is a useful complement to feedback. Say that one wants a step change in the reference function. For example, in a loop controlling the PCFH reflectance of the ice layer, one can suddenly change the desired set-point from 90% to 80%. The feedback loop may work satisfactorily in response to frost point perturbations, but if one knows ahead of time that one is making a sudden change, one can do better than to just let the feedback loop respond. Because it is usually impossible to implement perfect feedforward and because disturbances are usually unknown, one generally combines feedforward with feedback as in Figure 4.2 where $d(s)$

represent disturbances and $\xi(s)$ measurement noise. The control signal $r(s)$ is assumed to be noise free. The block $F(s)$ adds feedforward dynamics. The output $y(s)$ then becomes as in equation 4.12.

$$y(s) = \frac{KG}{1+KG}\left[F(s)r(s) - \xi(s)\right] + \frac{1}{1+KG}d(s) \tag{4.12}$$

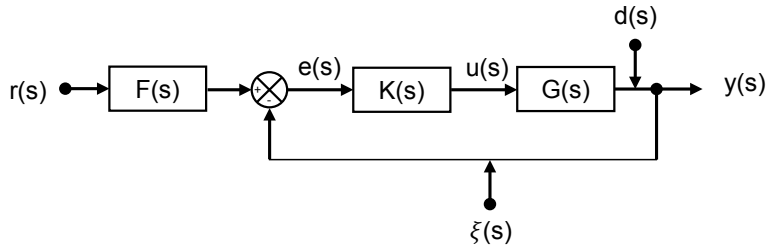

Figure 4.2: Close-loop control with feedforward. Adapted from Bechhoefer (2005).

We can now better appreciate the distinction between 'control' and 'feedback'. The former refers to the general problem of how to make a system behave as desired. The latter is one technique for doing so. What we have seen so far is that feedback, or closed-loop control, is useful for dealing with uncertainty, in particular by reducing the effects of unknown disturbances. On the other hand, feedforward, or open-loop control, is useful for making desired (i.e., known) changes. One usually wants to combine both control techniques.

Time domain

The previous discussion focuses on feedback in the frequency domain, but it is sometimes preferable to use the time domain, working directly with Equation 4.2. State-space approaches are particularly useful for cases where one has multiple inputs and multiple outputs (MIMO). Here we provide an example for single input, single output (SISO). With the introduction of feedback the new system equations look like:

$$\begin{aligned} &\dot{\vec{x}} = \tilde{A}\vec{x} + \tilde{B}\vec{u},\ u = -\vec{k}^T\vec{x}, \\ &y = \vec{c}^T\vec{x} \end{aligned} \tag{4.13}$$

In Equation 4.13, row vectors are represented, for example, as $\vec{c}^T = (c_1\ c_2)$. The problem is then one of choosing the feedback vector $\vec{k}^T = (k_1\ k_2)$ so that the eigenvalues of the new dynamical system, $\dot{\vec{x}} = \tilde{A}'\vec{x}$ with $\tilde{A}' = \tilde{A} - \vec{b}\,\vec{k}^T$, have the desired properties.

Important concepts for states are 'controllability' and 'observability'. If an element of $\vec{b}$, for example b_1 is zero, then clearly, there is no way that $u(t)$ can influence the state $x_1(t)$. We say the system state is not 'controllable'. Similarly, if an element of $\vec{c}$ is zero, then $y(t)$ will not be influenced at all by the corresponding element of $\vec{x}(t)$, and we say that that state is not 'observable'. The important question here is if the 'uncontrollable' or 'unobservable' states are stable.

4.1.3 Different control implementations: PID and optimal control

Probably the most common form for control $K(s)$ is the PID controller, which is a combination of proportional, integral and differential control:

$$K(s) = K_p + \frac{K_i}{s} + K_d s \tag{4.14}$$

where K_p, K_i, and K_d are gain parameters to be tuned for a particular application.

Proportional: The simplest control law is $K(s) = K_p$, a constant. This is a proportional feedback, since the feedback signal is proportional to the error signal $u(t) = K_p e(t)$. If we take a simple system of a first-order, low-pass filter as described in Equation 4.15, after proportional control, the closed-loop transfer function has the form as in Equation 4.16. It is a low-pass filter with modified DC gain and cut-off frequency.

$$G(s) = \frac{G_0}{1 + s/\omega_0} \tag{4.15}$$

$$\begin{aligned} T(s) &= \frac{K_p G_0}{K_p G_0 + 1 + s/\omega_0} \\ &= \left(\frac{K_p G_0}{K_p G_0 + 1}\right) \frac{1}{1 + s/\omega_0(1 + K_p G_0)} \end{aligned} \tag{4.16}$$

Integral: All systems with proportional control feedback suffer from "proportional droop': i.e., the long term response to a steady-state input differs from the desired set point. Thus if the (static) control input to a low-pass filter is r, the system settles to a solution $y_\infty = [K_p/(1+K_p)]r_\infty$. Only for an infinite gain will $y_\infty = r_\infty$, but in practice, the gain cannot be infinite. The difference between the desired signal r_∞ and the actual signal equals $[1/(1+K_p)]r_\infty$.

With integral control, one applies a control $K_i \int_{-\infty}^{t} e(t')dt'$ in addition to the proportional control term $K_p\, e(t)$. The integral will build up as long as $e(t) \neq 0$. In other words, the integral term eliminates the steady-state error. We can see this easily in the time domain, where

$$\dot{y}(t) = -\frac{1}{\tau} y(t) + \frac{K_i}{\tau} \int_{-\infty}^{t} [r_\infty - y(t')]dt' \tag{4.17}$$

where K_i is rescaled to be dimensionless. Differentiating:

$$\ddot{y}(t) = -\frac{1}{\tau}\dot{y}(t) + \frac{K_i}{\tau^2}[r_\infty - y(t)] \tag{4.18}$$

which has the steady state solution $y_\infty = r_\infty$. The K_i/s term in Equation (4.14) provides the infinite feedback required steady state response (i.e. $s \to 0$).

Derivative: The intuitive justification for derivative control is that if one sees the system moving at high 'velocity', one knows that the system state will change rapidly. One can thus speed the feedback response greatly by anticipating this state excursion and taking counteraction immediately. However, if the sensor is noisy, random fluctuations can lead to large spurious rates of change and to inappropriate controller response. Thus many experimentalists trying derivative control find that it

makes the system noisier and then give up (Bechhoefer, 2005). One obvious response is to limit the action of the derivative term by adding one or more low-pass elements. The control equation becomes

$$K(s) = \frac{K_p + K_i/s + K_d s}{(1 + s/\omega_0)^n} \tag{4.19}$$

where we have added n low-pass filters with cut off frequencies all at ω_0.

Ziegler Nichols method - empirical parameter estimation

Ziegler and Nichols (1942) presented an empirical method to determine optimal PID parameters for a system. It consists of determining the ultimate sensitivity (S_u) of the system and its period (P_u). Sensitivity is the measure of proportional response, and the ultimate sensitivity is the oscillation above which any oscillation will increase to a maximum amplitude and below which an oscillation of any size will diminish to straight line control.

Another method involves analysing the system lag and reaction curves. The reaction curve can be determined by the response of the system to a step without any control implemented. The 'reaction rate' (R) is the maximum rate at which the signal changes, which occurs at the point of inflection in the reaction curve. By drawing a line to the point where it intersects the initial state some time after the initial step, we get the lag (L).

Table 4.1 provides the empirical values determined by Ziegler and Nichols (1942).

Table 4.1: Ziegler and Nichols (1942) PID parameters

Proportional			
K_p	Sensitivity	$= 0.5S_u$	$= 1/(R \cdot L)$
Proportional plus reset (plus integral)			
K_p	Sensitivity	$= 0.45S_u$	$= 0.9/(R \cdot L)$
K_i	Reset rate	$= 1.2/P_u$	$= 0.3/L$
Proportional plus reset plus pre-act (plus integral plus derivative)			
K_p	Sensitivity	$= 0.6S_u$	$= 1.2/(R \cdot L)$
K_i	Reset rate	$= 2.0/P_u$	$= 0.5/L$
K_d	Pre-act time	$= P_u/8$	$= 0.5L$

Control optimization

A fundamentally different approach is to formalize the tuning process by defining a scalar 'performance index', which is a quantity that is minimized for the 'best' choice of parameters. This is the basis of 'optimal control'. The standard performance indices are of the form:

$$J = \int_0^\infty V\left[x(t), u(t)\right] dt = \int_0^\infty \left[e^2(t)Q + u^2(t)R\right] dt \tag{4.20}$$

where the general function $V[x, u]$ commonly has a quadratic form and where Q and R are positive constants that balance the relative 'costs' of errors $e(t)$ and control efforts $u(t)$ (Bechhoefer, 2005). Implicit in Equation 4.20 is the choice of a control signal $r(t)$ and a disturbance $d(t)$. Frequently, one assumes a step function input $r(t) = \theta(t)$, with $d(t) = 0$. Alternatively, one can keep $r(t)$ constant and add a step disturbance for $d(t)$.

As an example, we consider the one dimensional system $\dot{x} = -\alpha x(t) + u(t)$ with proportional control $u(t) = -K_p e(t)$ and reference signal $r(t) = 0$ (Skogestad and Postlethwaite, 1996; Bechhoefer, 2005). The proportional control gives a motion $x(t) = x_0 e^{-(\alpha + K_p)t}$, which, when inserted into the cost function, Equation 4.20, gives (with $Q = 1$):

$$J(K_p) = \left(1 + RK_p^2\right) \frac{x_0^2}{2\left(\alpha + K_p\right)} \tag{4.21}$$

Minimizing J with respect to K_p gives an optimal

$$K_p^* = -\alpha + \sqrt{\alpha^2 + 1/R} \tag{4.22}$$

From this simple example, one can see the advantages and disadvantages of optimal control. First of all, optimal control does not eliminate the problem of tuning a parameter. Rather, in this case, it replaces the problem of choosing the proportional gain K_p with that of choosing the weight R. The advantage, however, is making trade-offs in the design process more transparent. However, 'optimal' does not mean 'good', for a poor choice of weights will lead to a poor controller.

Optimal control

One can be more ambitious and ask for more than an optimal set of parameters, given a particular control law. Indeed, why not look for the best of all possible control laws? For example, we can interpret the minimization of the performance index J in Equation 4.20 as a problem belonging to the calculus of variations, which is to find the optimal control $u(t)$ that minimizes J, under the constraint that the equation of motion $\dot{x} = f(x, u)$ is obeyed. One can solve this problem by using Lagrange multipliers and minimizing $\mathcal{L} = \int_0^\infty L dt$, where $L(x, \dot{x}, u, \lambda) = \lambda_0 V\left(x, u\right) - \lambda(f - \dot{x})$ through variation of x, u, and the Lagrange multiplier λ. Setting the variation of J with respect to x, u, and λ equal to

zero leads to three sets of Euler-Lagrange equations:

$$\frac{d}{dt}\frac{\partial L}{\partial \dot{x}} - \frac{\partial L}{\partial x} = 0 \tag{4.23a}$$

$$\frac{\partial L}{\partial u} = 0 \tag{4.23b}$$

$$\frac{\partial L}{\partial \lambda} = 0 \tag{4.23c}$$

Equations 4.23a and 4.23b are obeyed by the performance index V; Equation 4.23c is the equation of motion. The Hamiltonian formulation is usually preferred. There, one defines a Hamiltonian $H = L + \lambda\dot{x} = V + \lambda f$. The Euler-Lagrange equations can then be transformed into the control theory version of Hamilton's equations:

$$\dot{x} = \frac{\partial U}{\partial \lambda} \tag{4.24a}$$

$$\dot{\lambda} = \frac{\partial U}{\partial x} \tag{4.24b}$$

$$\frac{\partial U}{\partial u} = 0 \tag{4.24c}$$

4.2 System modelling

The optimal control approach demands a state system description of the plant and hence a numerical model of the instrument's behaviour to derive the control law. Before we can start implementing a controller, we need to build an instrument that meets our operation requirements, and then we need to measure and model the system transfer function or system dynamics, $G(s)$. This is a step usually overlooked by hurried experimentalists. This is not a simple task, it implies four separate steps: first, determine experimentally the transfer function; second, fit the model transfer function based on physical laws; third, approximate a high-order system accurately by a lower-order system, because a full description of the experimental transfer function usually leads to very high-order systems; and fourth, determine whether the system can be 'improved' to make control easier and more effective (Bechhoefer, 2005).

We measured the PCFH transfer function in-flight, as opposed to in a climate chamber. Results for the PCFH flight and the fit to the model transfer function will be described in Chapter 5 and 6. For the rest of this chapter we introduce the PCFH transfer function model.

4.2.1 Modelling methodology: reservoir-based approach

There are three types of models: 'black-box' models, derived from experiments only; 'grey-box' models, model based but experiments are needed for parameter identification and model validation, and 'white-box' models, no experiments are needed at all. Model system description is based on physical first principles, which has two major benefits when compared to experimental methods: the model obtained is able to extrapolate the system behaviour, valid beyond the operating condition used in model validation, and it is useful when the real system is not available, still in planning phase or if experiments

cannot be run too often as is the case of balloon launches. When modelling systems for control, there are two main classes of objects to take into account:
Reservoirs: accumulative elements, for example of thermal or kinetic energy, of mass, or of information;
Flows: for instance heat, mass, etc. flowing between reservoirs.
The notion of reservoirs is fundamental, only systems including one of more reservoirs exhibit dynamic behaviour. To each reservoir there is an associated 'level' variable, which is a function of the reservoir's content (in control literature: 'state variable'). Flows are typically driven by the differences in the reservoir level.

To write a physical model, we first define the system boundaries (inputs, outputs). Second, we identify the relevant 'reservoirs' – for mass, energy, information - and corresponding 'level variables' (or state variables). Third, we formulate the differential equations ('conservation laws') for all relevant reservoirs, which will allow us to write the model in the form of:

$$\frac{d}{dt}\left(\text{reservoir content}\right) = \sum \text{inflows} - \sum \text{outflows} \tag{4.25}$$

reminiscent of Eq. (4.2). Then, we formulate the algebraic relations, which express the 'flows' between reservoirs as function of the level variables and resolve implicit algebraic loops, if possible, and simplify the resulting mathematical relations as much as possible. Lastly, we identify the unknown system parameters using some experiments and validate the model with experiments that have not been used to identify the system parameters.

4.2.2 Thermodynamic systems

Now we introduce a few thermodynamic concepts, which are important for thermodynamic system modelling.

Internal energy U: For a closed system, i.e. without mass transfer, during an arbitrary process, the variation of U is the sum of the work of external forces plus thermal energy (heat) transferred by/to the system.

$$dU = \delta W + \delta Q \tag{4.26}$$

- Adiabatic process: no heat transfer, $\delta Q = 0$: $dU = \delta W$.
- Isochoric process: no volume change, $\delta W = 0$: $dU = \delta Q$.
- Isolated system: $dU = 0$.
- Work of external forces $\delta W = P_{ext}\, dV$.
- The heat transfer is as described by Equation 4.27. For processes with no change in volume: c_v is the specific heat at constant volume (J K^{-1} kg^{-1}). For processes with no change in pressure: c_p is specific heat at constant pressure (J K^{-1} kg^{-1}).

$$\delta Q = m\, c_v\, dT \tag{4.27a}$$

$$\delta Q = m\, c_p\, dT \tag{4.27b}$$

· In incompressible systems (solid and fluids)

$$U(T) = m\, c\, T \tag{4.28}$$

where $c = c_v = c_p$ is independent of temperature.

Enthalpy H: In many industrial applications, there is a continuous flow of fluid through the thermodynamic system (transfer of mass). This is no longer a closed system, and we talk about 'open systems' (valve, turbine, compressor, etc.). For open systems, we use Enthalpy defined as

$$H = U + P\, V \tag{4.29}$$

where the term $P\, V$ takes into account the work (energy) of fluid transport. Enthalpy is not relevant for the PCFH, since there is no significant mass transfer involved in its operation. Ideal gases behave according to the two laws of Joule: their internal energy U and enthalpy H only depend on temperature T.

Heat Transfer $\dot{Q}$: is the movement of heat across the boundary of the system due to temperature difference between the system and the surroundings. Heat is the vibration energy of the molecules.

· Conduction: heat is transferred through molecular vibration in W or J s^{-1}. **Fourier's law**: one-dimensional case, for example a thin cylinder of cross section area A and length l, k is the thermal conductivity in W K^{-1} m^{-1}.

$$\dot{Q} = \frac{k\, A}{l}\,(T_1 - T_2) \tag{4.30}$$

· Convection: heat is transferred through transport of mass, in W or J s^{-1}. **Newton's law**: heat (thermal energy) is transfered between a solid body with contact surface A and the surrounding fluid, h is the convective heat transfer coefficient, depending on the surface and fluid flow properties in W K^{-1} m^{-2}. More on convective heat transfer in Appendix 4.3.

$$\dot{Q} = h\, A\ (T_1 - T_2) \tag{4.31}$$

· Radiation: heat is transferred through electromagnetic radiation. It can go through vacuum, there is no transport of mass. An example is heat transfer from the Sun to Earth in W or J s^{-1}. **Stefan-Boltzmann's law**: heat radiation from a body of surface A at temperature T_1 and its surroundings at T_2. Emissivity ϵ: dimensionless, $\leq$1 (black body ϵ =1), depends on the material and surface structure. Stefan-Boltzmann constant: $\sigma = 5.67036710{\times}10^{-8}$ W m^{-2} K^{-4}.

$$\dot{Q} = \epsilon\, \sigma\, A\ \left(T_1^4 - T_2^4\right) \tag{4.32}$$

4.3 Convective heat transfer

A crucial step in the designing of the PCFH was to establish if the cooling capabilities of tropospheric and stratospheric air would be enough for the PCFH requirements. We decided to increase the heat

transfer potential of the hot side by including a heat sink. In this section, we present the theoretical considerations to confirm said requirements could be met. First, we present stratospheric and tropospheric air thermodynamic properties and the derivation of convective heat transfer from a finned surface. From the derived air fluid dynamic properties considering a heat sink geometry, we calculate the forced convection heat transfer coefficient for the heat sink. We also investigate the forced convective heat transfer inside the intake, tube which affects the mirror, reference surface, and multiblock. Lastly, we examine the convective heat transfer inside the instrument housing due to natural convection.

4.3.1 Air thermodynamic properties

Density (kg m^{-3})

$$\text{Ideal gas law: } \rho = \frac{P}{T}\,\frac{M}{R} \tag{4.33}$$

molar mass $M = 0.0289$ kg mol^{-1}, ideal gas constant $R = 8.31432$ m^3 Pa K^{-1} mol^{-1}

Thermal conductivity (W m^{-1} K^{-1})

$$k = 8.06 \times 10^{-5}\ (T/K) + 2.02 \times 10^{-3},\ \text{for } 193K < T < 300K,\ R^2 = 0.998 \tag{4.34}$$

Specific heat (kJ kg^{-1} K^{-1})

$$c_p = -8.94 \times 10^{-9}\ (T/K)^3 + 7.02 \times 10^{-6}\ (T/K)^2 + -1.82 \times 10^{-3}\ (T/K) + 1.16,$$
$$\text{for } 193K < T < 300K,\ R^2 = 0.999 \tag{4.35}$$

Dynamic viscosity (N s m^{-2})

$$\mu = (0.0545\ (T/K) + 2.203) \times 10^6,\ \text{for } 193K < T < 300K,\ R^2 = 0.9975 \tag{4.36}$$

In Figure 4.3, we use the temperature profile (panel (a)) of the balloon sounding NT015 from Nainital, India, on the 17 August 2016 to compute the air thermodynamic properties. In Panel (b), (c), (d), and (e), we show density (ρ), thermal conductivity (k), specific heat (c_p), and dynamic viscosity (μ) according to Equations 4.33, 4.34, 4.35, and 4.36, respectively, which were fitted from data found in EngineeringToolbox (2005).

4.3.2 Heat transfer from finned surface

Convection heat transfer

$$\dot{Q}_{conv} = h\ A_s\ (T_s - T_\infty)\,, \tag{4.37}$$

where A_s is the heat transfer surface (m^2), h is the convective heat transfer coefficient (W K^{-1} m^{-2}), T_s is the temperature at the surface (K), and T_∞ is the temperature of surrounding medium (K).

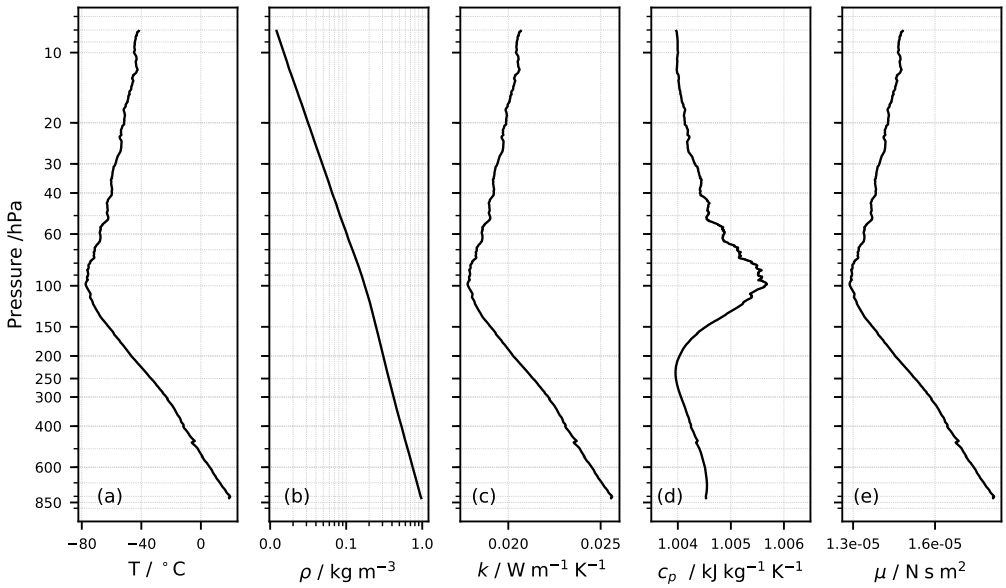

Figure 4.3: Air thermodynamic properties based of the temperature profile of flight NT015 on the 17 August 2016 in Nainital, India during the 2016-2017 Stratoclim balloon campaigns. (a) Temperature profile; (b) density profile; (c) thermal conductivity profile; (d) heat capacity profile; (e) dynamic viscosity.

Steady state equation:

$$\begin{pmatrix} \text{rate of heat} \\ \text{conduction} \\ \text{into the element} \\ \text{at } x \end{pmatrix} = \begin{pmatrix} \text{rate of heat} \\ \text{conduction} \\ \text{into the element} \\ \text{at } x + \Delta x \end{pmatrix} + \begin{pmatrix} \text{rate of heat} \\ \text{convection} \\ \text{from the} \\ \text{element} \end{pmatrix}$$

$$\dot{Q}_{cond_x} = \dot{Q}_{cond_{x+\Delta x}} + \dot{Q}_{conv} \tag{4.38}$$

equation 4.37 can be written as:

$$\dot{Q}_{conv} = h\ (p\ \Delta x)\ (T_s - T_\infty) \tag{4.39}$$

substituting and dividing by Δx:

$$\frac{\dot{Q}_{cond_{x+\Delta x}} - \dot{Q}_{cond_x}}{\Delta x} + h\ p\ (T_s - T_\infty) = 0 \tag{4.40}$$

$\Delta x \to 0$

$$\frac{d\dot{Q}_{cond}}{dx} + h\ p\ (T_s - T_\infty) = 0 \tag{4.41}$$

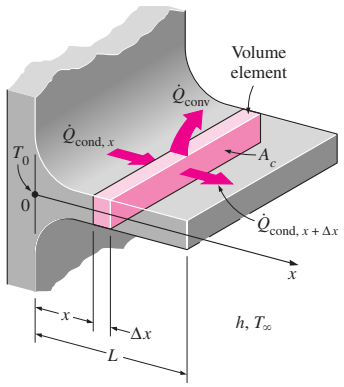

Figure 4.4: Heat transfer finned surface. Volume element of a fin at location x having a length of Δx, cross-sectional area of A_c, and perimeter of $p = 2 \times L_f + 2 \times t$. The perimeter accounts for the fin's length in the flow direction (L_f) and the fin thickness (t) (from Çengel (1998)).

From Fourier law of heat conduction $\dot{Q}_{cond} = -k\ A_c\ \frac{dT}{dx}$

$$\frac{d}{dx}\left(k\ A_c\ \frac{dT}{dx}\right) - h\ p\ (T_s - T_\infty) = 0 \tag{4.42}$$

where usually A_c and p change with x for a fin, which makes Equation 4.42 hard to solve. Assuming constant cross section (A_c) and constant thermal conductivity (k), Equation 4.42 is of the form

$$\frac{d^2\theta}{dx^2} - a^2\theta = 0,\ a = \frac{h\ p}{k\ tA_c} \text{ and } \theta = T - T_\infty. \tag{4.43}$$

The temperature profile in the fin is

$$\theta(x) = C_1\ e^{a\ x} + C_2\ e^{-a\ x}, \tag{4.44}$$

where C_1 and C_2 are determined by the boundary conditions at the base and tip of the fin. We only need two boundary conditions (BC) for this determination.

Boundary condition at fin base:

$$\theta(0) = \theta_b = T_b - T_\infty \tag{4.45}$$

where T_b is the temperature at the fin base.

Boundary condition at fin tip:

1. Infinitely long fin ($T_{\text{fin tip}} = T_\infty$)
   A sufficiently long tip of constant cross section will approach ambient temperature T_∞ at tip, thus $\theta = 0$. $\theta(L) = T(L) - T_\infty = 0$ as $L \to \infty$. In this case, $e^{-a\ x}$ satisfies the condition, but not $e^{a\ x}$: as $x \to \infty$, $\theta \to \infty$. So:
   $$\theta(x) = C_1\ e^{-a\ x},\ C_2 = 0 \tag{4.46}$$

where C_1 is determined by the other boundary condition $\theta(0)$.

$$\theta(0) = \theta_b \Rightarrow C_1\, e^{-a\,0} = \theta_b,\; C_1 = \theta_b \tag{4.47}$$

$$\theta(x) = \theta_b\, e^{-a\,x} \Rightarrow \frac{T(x) - T_\infty}{T_b - T_\infty} = e^{-x\sqrt{h\,p/(k\,A_c)}} \tag{4.48}$$

The steady rate of heat transfer from the entire fin can be determined from Fourier's law of heat conduction:

$$\dot{Q}_{\text{long fin}} = -k\,A_c \frac{dT}{dx}\,|_{x=0} = \sqrt{h\,p\,k\,A_c}\,(T_b - T_\infty) \tag{4.49}$$

2. Negligible heat loss from the fin tip ($\dot{Q}_{\text{fin tip}} = 0$)
It is usually not realistic nor efficient,at least in weight terms, to have a fin long enough that $T_{\text{fin tip}} = T_\infty$. A more realistic approach is to consider the heat transfer from the tip to be negligible, because the tip surface can be considered negligible compared to the entire fin area. The boundary condition at the fin tip is:

$$\begin{cases} \frac{d\theta}{dx}\,|_{x=L} = 0 \Rightarrow a\,C_1\,e^{a\,L} - a\,C_2\,e^{-a\,L} = 0 \\ \theta(0) = \theta_b = T_b - T_\infty \Rightarrow C_1 + C_2 = \theta_b \end{cases} \tag{4.50}$$

$$\cosh(x) = \frac{1}{2}\left(e^{-x} + e^{x}\right);\; \sinh(x) = \frac{1}{2}\left(e^{x} - e^{-x}\right)$$

$$\theta(x) = \theta_b\,\frac{\cosh a(L-x)}{\cosh aL} \Rightarrow \frac{T(x) - T_\infty}{T_b - T_\infty} = \frac{\cosh a(L-x)}{\cosh aL} \tag{4.51}$$

The steady rate of heat transfer from the entire fin can be determined from Fourier's law of heat conduction:

$$\dot{Q}_{\text{insulated tip}} = -k\,A_c \frac{dT}{dx}\,|_{x=0} = \sqrt{h\,p\,k\,A_c}\,(T_b - T_\infty)\tanh aL \tag{4.52}$$

3. Convection from fin tip
This is the realistic boundary condition. However, the complexity involved in solving the equations do not account for an actual accuracy improvement. A practical way to account for the heat loss from the fin tip is to replace the fin length in the relation for the insulted tip case by a corrected length

$$L_c = L + \frac{A_c}{p} \tag{4.53}$$

where A_c is the cross section area and p the perimeter. This replacement provides good results, when the temperature variation near the fin tip is small ($aL \gg 1$) and the heat transfer coefficient is the same at the lateral as at the tip. For rectangular fins $L_c = L + t/2$, where t is the thickness. For cylindrical fin $L_c = L + D/4$, where D is the diameter. The steady rate of heat transfer from

the entire fin can be determined from Fourier's law of heat conduction:

$$\dot{Q}_{\text{convection from tip}} = -k\ A_c \frac{dT}{dx}\,|_{x=0} = \sqrt{h\ p\ k\ A_c}\,(T_b - T_\infty)\tanh aL_c, \tag{4.54a}$$

$$a = \frac{h\ p}{k\ A_c},\ L_{c_{\text{rectangular}}} = L + t/2, \tag{4.54b}$$

where h is the convective heat transfer coefficient (W K^{-1} m^{-2}), p is the fin perimeter (m), k is the fin thermal conductivity (W m^{-1} K^{-1}), A_c is the fin cross sectional area (m^2), t is the fin thickness (m), T_b is the temperature at fin base (K), and T_∞ is the ambient temperature (K).

4.3.3 Air fluid dynamic properties and forced convection coefficient

There are two types of convective heat transfer: natural and forced. In natural convective heat transfer, the fluid's movement is caused by natural warming and expansion of the fluid due to contact with a warmer surface. In forced heat convection, the fluid is forced over the surface by a fan, or in the PCFH case by the balloon ascent. The fluid properties relevant to estimate forced convective heat transfer coefficients are:

Nusselt Number

$$Nu = \frac{h\ D}{k} \tag{4.55}$$

where h is the convective heat transfer coefficient (W m^{-2} K^{-1}), D is the characteristic length parameter (m), and k is the thermal conductivity (W m^{-1} K^{-1}) of the fluid.

Prandtl Number

$$Pr = \frac{\mu\ c_P}{k} \tag{4.56}$$

where μ is the dynamic viscosity (N s m^{-2}),($\mu = \nu\ \rho$), c_p is the specific heat (kJ kg^{-1} K^{-1}), and k is the thermal conductivity (W m^{-1} K^{-1}).

Reynolds number

$$Re = \frac{D\ v\ \rho}{\mu} \tag{4.57}$$

where D is the characteristic length (m) of a certain geometry, v is the characteristic velocity (m s^{-1}), i.e., average velocity for pipe flow, ρ is the fluid's density (kg m^{-3}), and μ its dynamic viscosity (N m^2 s^{-1}).

Depending on the geometry of the surface subject to convective heat transfer and the regime of the flow, laminar or turbulent, these fluid properties will correlate differently to estimate a Nusselt number (Nu) from which we can estimate the convective heat transfer coefficient.

$$h = \frac{Nu\ k}{D} \tag{4.58}$$

Heat sink

For the heat sink, we consider the heat transfer as forced convection for flow parallel to a flat plate. The boundary layer development is as in Figure 4.5. When the flow starts to go over the flat plate, it forms a laminar boundary layer. At x_{cr} from the leading edge of the flat plate, the flow enters the transition region, until a turbulent boundary layer is developed. For laminar flow, the fluid properties relation is

$$Nu_{L_f} = \frac{h\,L_f}{k} = 0.664\,Re_{L_f}^{0.5}\,Pr^{1/3},\ Re < 5\times10^5 \tag{4.59}$$

and for turbulent flow, it is

$$Nu_{L_f} = \frac{h\,L_f}{k} = 0.037\,Re_{L_f}^{0.8}\,Pr^{1/3},\ 0.6 \le Pr \le 60,\ 5\times10^5 \le Re_{L_f} \le 10^7 \tag{4.60}$$

where L_f, the flat plate length, is the characteristic dimension D in Equations 4.55 and 4.57 for the parallel flow over the flat plate.

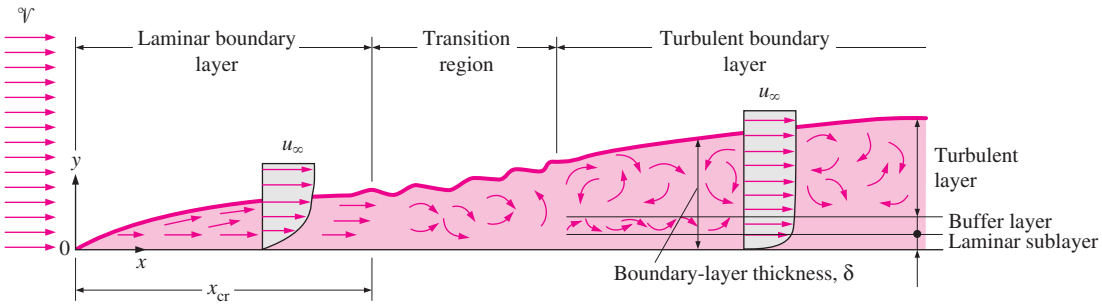

Figure 4.5: The development of the boundary layer for flow over a flat plate, and the different flow regimes (from Çengel (1998)).

Considering again the balloon sounding NT015 from Nainital, India, on the 17 August 2016, and the thermodynamic air properties calculated in Figure 4.3, we calculate air fluid dynamic properties: Reynolds (Re_{L_f}), Prandtl (Pr), and Nusselt (Nu_{L_f}) numbers according to Equations 4.57, 4.56, and 4.59, respectively. The results are shown in Figure 4.6. For the calculations, we considered the geometrical characteristics of the PCFH first heat sink shown in Figure 4.7 which is 50 mm long in the flow direction, which means the characteristic length of Equation 4.57 is $D{=}L_f = 50$ mm. For Re_{L_f}, we consider 4 different mean flow velocities: 3, 4, 5, and 6 m s^{-1}. All $Re_{L_f} < 5\times10^5$, i.e. laminar flow, which justifies the usage of Equation 4.59 for the Nu_{L_f} number. In Figure 4.6d, we present the convective heat transfer coefficient (h) calculated using Equation 4.58. Above the 60-hPa level, all h are lower than 10 W m^{-2} K^{-1}, and above the 20-hPa level, all h are lower than 5 W m^{-2} K^{-1}. Figure 4.6e translates h into temperature differences (ΔT), for different amounts of heat ($\dot{Q}$) transferred across the heat sink into the environment.

In Figure 4.7, we provide a schematics for the PCFH first heat sink. The fin length is $L = 40$ mm-10 mm=30 mm. We have 7 equally thin and spaced fins: the fin thickness is $t = 66$ mm/13=5 mm. The corrected fin length is $L_c = 30$ mm+5 mm/2=32.5 mm. The fin is 50 mm long in the flow direction, which makes the fin cross sectional area equal to $A_c = 50$ mm×5 mm = 250 mm^2 and the fin perimeter

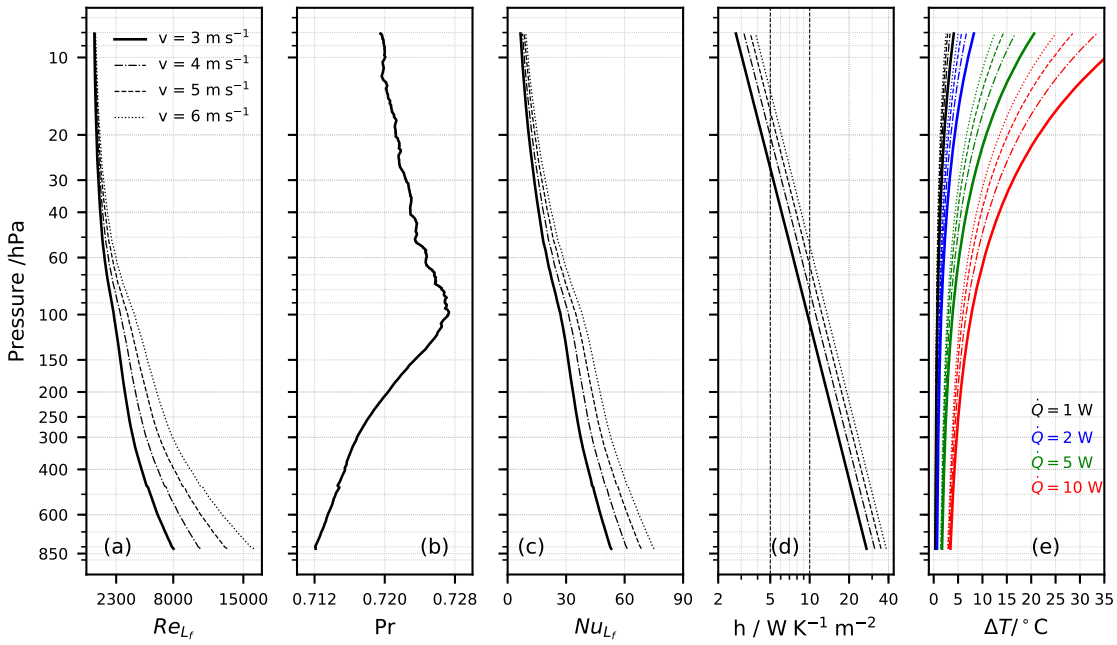

Figure 4.6: Air fluid dynamic properties for laminar flow over a flat plate for the temperature profile of flight NT015 on the 17 August 2016 in Naintal, India during the 2016-2017 StratoClim balloon campaigns. (a) Reynolds number, solid: mean flow velocity 3 m s^{-1}, dashed-dotted: 4 m s^{-1}, dashed: 5 m s^{-1}, dotted: 6 m s^{-1}; (b) Prandtl number; (c) Nusselt number, lines same as in panel (a); (d) convective heat transfer coefficient, lines same as in panel (a); (e) temperature difference for different heat transfers ($\dot{Q}$), black: 1 W, blue: 2 W, green: 5 W; red: 10 W, lines same as in panel (a).

equal to p = 2×50 mm+2×5 mm=110 mm. In Figure 4.6e, we can see that the heat sink with this geometry would be able to provide up to 5 W of cooling potential with a temperature increase from ambient smaller than 2 °C. This is an acceptable performance, a loss of 1 to 2 °C from ambient should always be expected. There is no heat transfer (cooling) without temperature difference. However, at lower pressure levels of the stratosphere, above the 20-hPa level, we can expect temperature differences up to 10 °C from the ambient, for a cooling potential of less than 5 W. At these pressure levels, we are anyway out of the operating range of the PCFH, due to Peltier element limitations, so the heat sink is not the only limiting factor in this region.

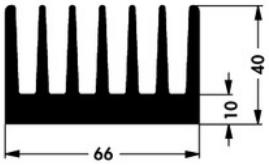

Figure 4.7: PCFH heat sink previous design schematics

Intake tube: mirror, reference surface and multiblock

For the intake tube, we consider the heat transfer as forced convection inside a circular tube. Flow in a tube can be laminar or turbulent. Fluid flow is laminar at low velocities, but turns turbulent as the velocity is increased beyond a critical value. Transition from laminar to turbulent flow does not occur suddenly; rather, it occurs over some range of velocity. Most pipe flows encountered in practice are turbulent. The usual Reynolds number for transition inside a circular tube are provided below:

$$\begin{array}{rlll} & Re_D & < 2300 & \text{laminar flow} \\ 2300 \leq & Re_D & \leq 10000 & \text{transitional flow} \\ & Re_D & > 10000 & \text{turbulent flow} \end{array}$$

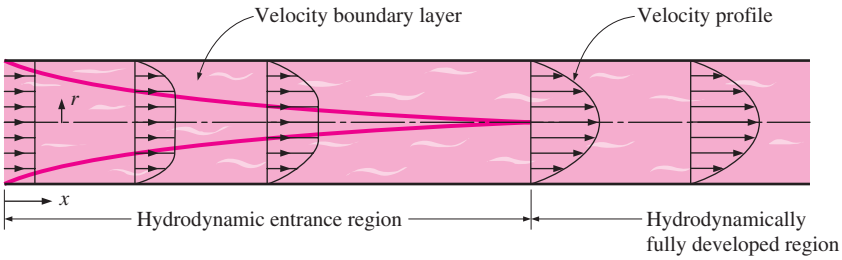

Figure 4.8: The development of the velocity boundary layer in a tube. The developed mean velocity profile will be parabolic in laminar flow, as shown, but somewhat blunt in turbulent flow (from Çengel (1998)).

The boundary layer development is as in Figure 4.8 for laminar flow. As the flow enters the tube, the fluid particles close to the surfaces start to slow down, the particles directly above them feel the slow down effect. To make up for this velocity reduction, the velocity of the fluid at the midsection of the tube will have to increase to keep the mass flow rate through the tube constant. Until the boundary layers meet at the center of the tube, the flow is considered to be in the hydrodynamic entrance region, pass this point the flow is considered fully developed. This effect happens in both laminar and turbulent flows. For heating of a flow, there is a similar effect, but with a thermal entrance region. In fluids with $Pr \approx 1$, the hydrodynamic and thermal region are equivalent, this is usually the case for gases. The length of this region can be determined as

$$L_{h,\,\text{laminar}} \approx 0.05\, Re_D \cdot D \tag{4.61a}$$

$$L_{h,\,\text{turbulent}} = 1.359\, Re_D^{1/4} \tag{4.61b}$$

Considering the geometry of the PCFH intake tube: Ø 40 mm and length 150 mm, we can say that the multiblock will only experience fully developed flow at $Re_D < 75$, which for our tropospheric and stratospheric conditions happen only at pressures lower than 20 hPa.

For a not fully developed laminar flow, Nu_D can be determined as

$$\text{Entry region, laminar: } Nu_D = 3.66 + \frac{0.065\ (D/L)\ Re_D\ Pr}{1 + 0.04\ [(D/L)\ Re_D\ Pr]^{2/3}}, \tag{4.62}$$

where D is the tubes diameter, and L is the tubes length, respectively 40 mm and 150 mm. For turbulent flows, the fully developed flow Nu is considered to represent accurately enough the entry region.

$$Nu = \frac{(f/8)\,(Re_D - 1000)\,Pr}{1 + 12.7\,(f/8)^{0.5}\,(Pr^{2/3} - 1)} \quad \begin{pmatrix} 0.5 \leq Pr \leq 2000 \\ 3 \times 10^3 < Re_D < 5 \times 10^6 \end{pmatrix} \tag{4.63}$$

$$\text{first Petukhov equation: } f = (0.790 \ln Re_D - 1.64)^{-2} \tag{4.64}$$

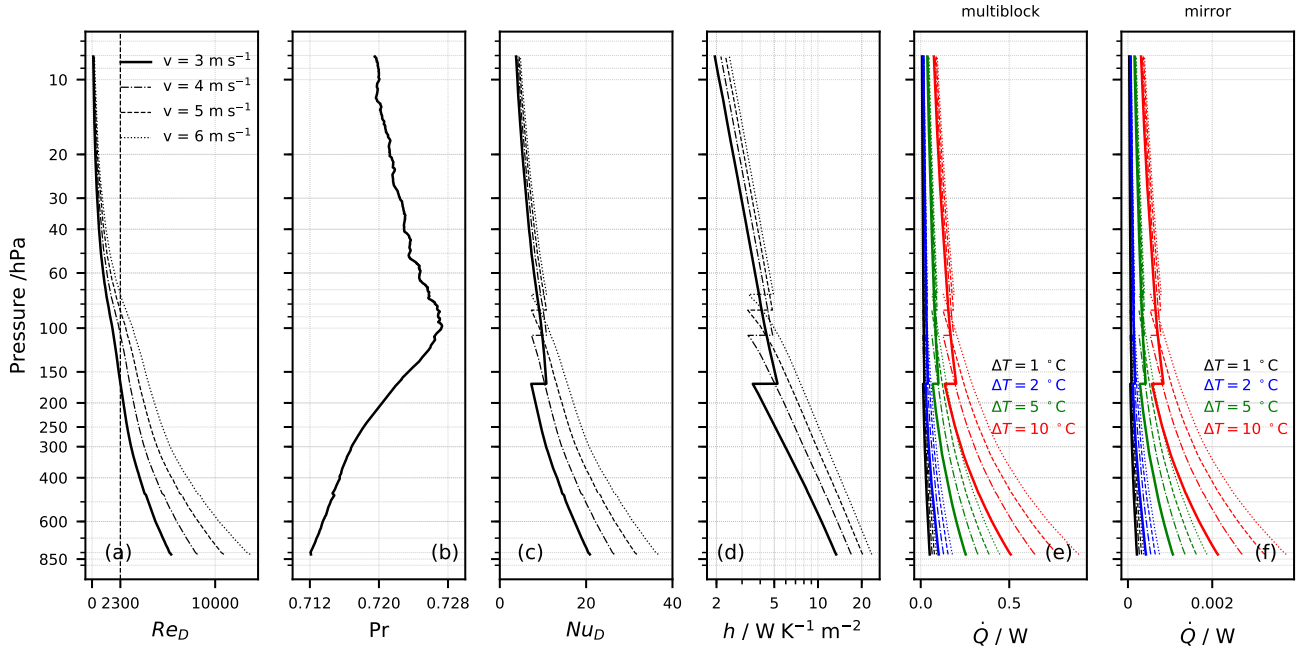

Figure 4.9: Air fluid dynamic properties for flow inside a circular tube for the temperature profile of flight NT015 on the 17 August 2016 in Nainital, India, during the 2016-2017 StratoClim balloon campaigns. (a) Reynolds number, solid: mean flow velocity 3 m s^{-1}, dashed-dotted: 4 m s^{-1}, dashed: 5 m s^{-1}, and dotted: 6 m s^{-1}, transition to laminar flow marked with a vertical line at $Re_D = 2300$; (b) Prandtl number; (c) Nusselt number, lines same as in panel (a), discrete transition to laminar flow above 200-hPa level; (d) convective heat transfer coefficient, lines same as in panel (a); (e) transferred heat ($\dot{Q}$) for different temperature differences (ΔT) for the multiblock surface inside the intake tube, black: 1 °C, blue: 2 °C, green: 5 °C, and red: 10 °C, lines same as in panel (a); (f) same as (e) for the Peltier element mirror.

Considering again the balloon sounding NT015 from Nainital, India, on the 17 August 2016, and the thermodynamic air properties calculated in Figure 4.3, we calculate air fluid dynamic properties: Reynolds (Re_D), Prandtl (Pr) and Nusselt (Nu_D) numbers according to Equations 4.57, 4.56 and 4.62 or 4.63, respectively depending on $Re_D < 2300$ (laminar flow). The results are shown in Figure 4.9. In

Figure 4.9d, we present the convective heat transfer coefficient (h) calculated using Equation 4.58. h inside the intake tube is almost always half of the h for the heat sink, as shown in Figure 4.6. In Panel (e) and (f) of Figure 4.9 we translate h into transferred heat ($\dot{Q}$) for different temperature differences (ΔT) for the multiblock inner surface and the mirror, respectively. The difference between the two panels is the surface area scaling from 3810 mm^2 to 16 mm^2.

4.3.4 Natural convection coefficient: inside PCFH housing

Inside the PCFH housing, the air is stationary. It is not affected by the ascent speed of the balloon. Due to the instrument operation, the temperature inside the housing is warmer than the exterior, multiblock, and heat sink. Heat is transferred from the interior of the housing to the multiblock by natural convection.

Heat transfer by forced convection occurs because a fluid is forced over a surface. In natural convection, all motion occurs due to natural means such as buoyancy, which usually involve very low velocities. Since convective heat transfer is a strong function of velocity, natural convective heat transfer coefficients are much smaller than force convective heat transfer coefficients.

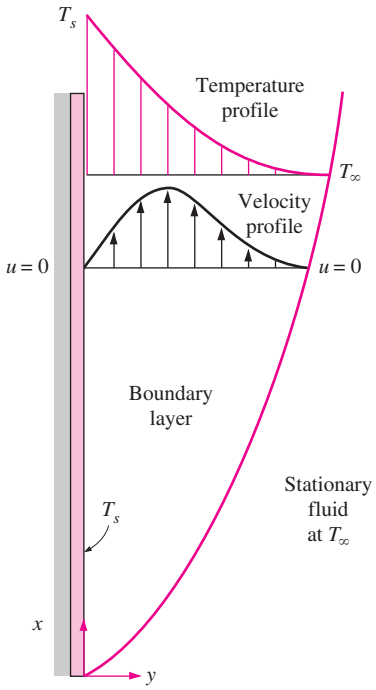

Figure 4.10: Typical velocity and temperature profiles for natural convection flow over a hot vertical plate at temperature T_s inserted in a fluid at temperature T_∞ (from Çengel (1998)).

For natural convection heat transfer, we need to consider a fifth thermodynamic parameter: thermal expansion (K^{-1}),

$$\text{Ideal gas: } \beta = \frac{1}{T} \tag{4.65}$$

besides density, thermal conductivity, specific heat, and viscosity, whose parameterisations are shown

in Equations 4.34, 4.35 and 4.36, respectively.

Since natural convection is controlled by buoyancy effects, the Reynolds number (Re) is no longer a good dimensionless parameter. The Grashof Number Gr_L is a better suited dimensionless parameter. Grashof number

$$Gr_L = \frac{g\,\beta\,(T_s - T_\infty)\,L_c^3}{\nu^2}, \tag{4.66}$$

where g is the gravitational acceleration (m s^{-2}), β is the coefficient of volume expansion (K^{-1}), T_s is the temperature of the surface (K), T_∞ is the temperature of the fluid sufficiently far from the surface (K), L_c is the characteristic length of the geometry (m), and ν is the kinematic viscosity of the fluid (m^2 s^{-1}).

We consider the multiblock contact surface inside the PCFH housing as a vertical plate of characteristic length $L = 25$ mm and constant temperature. The Nusselt number empirical correlation is:

$$Nu_L = \left\{ 0.825 + \frac{0.387\,Ra_L^{1/6}}{\left[1 + (0.492/Pr)^{9/16}\right]^{8/27}} \right\}^2 \;;\; \text{valid for all } Ra_L \tag{4.67}$$

Rayleigh number

$$Ra_L = Gr_L\,Pr \tag{4.68}$$

All fluid properties are to be evaluated at film temperature $T_{\text{film}} = (T_s + T_\infty)/2$.

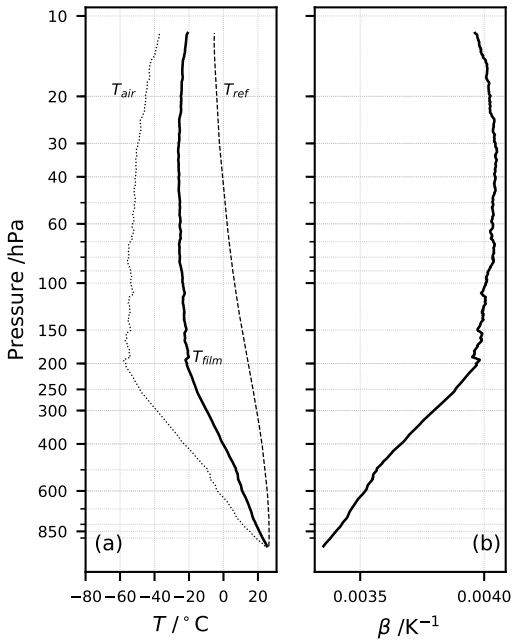

Figure 4.11: Convective heat transfer: natural convection thermodynamic parameters evaluated for PCFH flight 02 on the 25 July 2018 in Lindenberg, Germany. (a) Dotted: air temperature (T_{air}), dashed: thermocouple module reference temperature (T_{ref}), and solid: film temperature (T_{film}); (b) air thermal expansion coefficient considering T_{film}.

In Figure 4.11a, we show the air temperature profile for PCFH flight 02 on the 25 July 2018 in Lindenberg, Germany. We also show the temperature inside the PCFH housing for which the thermal board reference temperature is a proxy. For natural convection consideration, T_{air} becomes T_s and T_{ref} becomes T_∞. In Panel (a), we also show T_{film}, evaluated as $(T_{\text{air}} + T_{\text{ref}})/2$. In Figure 4.11b, we show the thermal expansion coefficient evaluated at T_{film}.

In Figure 4.12, we show air fluid properties for natural convection: Prandtl number (Pr), Grashof number (Gr_L), and Nusselt number (Nu_L), calculated with the respective Equations 4.56, 4.66, and 4.67. In Figure 4.12d, we show the convective heat transfer coefficient derived from Equation 4.58 and considering Nu_L as shown in Panel (c). In Panel (d), we show the heat transfer we can expect from the interior of the PCFH housing at T_{ref} into the multiblock considering $\Delta T = T_{\text{air}} - T_{\text{ref}}$. The maximum heat load we can expect from the PCFH housing is 1 W, at the tropopause level.

So far, we do not consider the PCFH housing to provide adequate insulation. The thermocouple board should operate with a reference temperature warmer than -20 °C, i.e. within calibration. Once the housing provides better insulation and the temperature inside is higher, we can not neglect it as a heat source of the multiblock and heat sink complex.

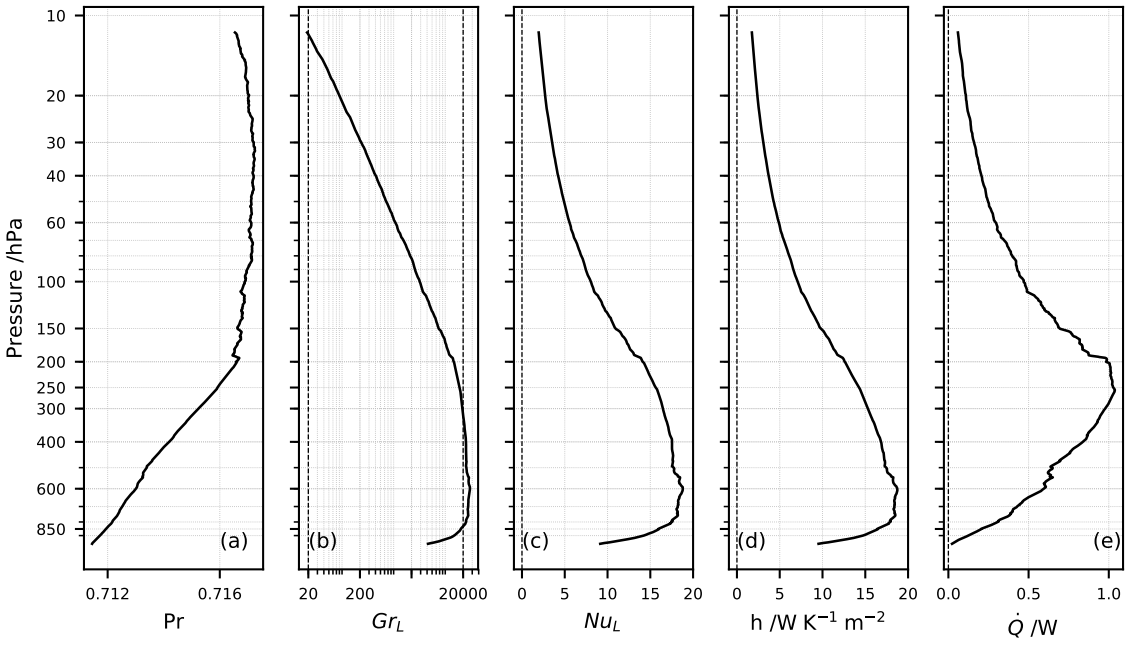

Figure 4.12: Convective heat transfer: natural convection air fluid properties evaluated at T_{film} for PCFH flight 02 on the 25 July 2018 in Lindenberg, Germany. (a) Prandtl number, (b) Grashof number, (c) Nusselt number, (d) natural convection heat transfer coefficient (h), and (e) transferred heat from inside PCFH housing at T_{ref} to multiblock at T_{air}.

4.4 PCFH System modelling

4.4.1 Problem definition

The description of the instrument in Chapter 3, identifies several controllable inputs: the Peltier current ($I_{\text{Peltier}} = I_P = u_1(t)$) and the squared Peltier current ($I_P^2 = u_2(t)$), which are considered as two different inputs in an attempt to linearise the system, and the squared reference surface heater current ($I_{\text{Heater}}^2 = I_H^2 = u_3(t)$). Additionally, three other variables can be considered as non-controllable inputs. These are the air temperature (T_{air}), the instrument internal temperature which is given by the thermocouple module reference temperature (T_{ref}), and the frost point temperature (T_{frost}).

The control signals will be applied to the mirror reflectance (R), which is controlled to be constant within a certain reflectance interval ($r_1(t)$), and to the reference surface temperature (T_{RS}), which is controlled to be 3 °C warmer than air temperature ($r_2(t)$).

From the PCFH sub-unit construction, it is possible to identify three important thermodynamic reservoirs, which identify with three state variables: the ice layer and mirror temperature $T_C = x_1(t)$, which is measured on the PE cold side by the mirror thermocouple T_{mirror}; the multiblock and heat sink temperature $T_{HS} = x_2(t)$, which is measured between the multiblock and heat sink by the heat sink thermocouple T_{sink}; and the reference surface board temperature $T_{RS} = x_3(t)$, which is measured at the reference surface board by $T_{\text{ref surf}}$ thermocouple. We identify a fourth state variable, which is also the system output: the mirror/ ice layer reflectance $R = x_4(t) = y(t)$. We summarize these in Table 4.2. In the next sections, each of the state variable equations and control signals ($r_1(t)$ and $r_2(t)$) are defined.

Table 4.2: System modelling summary table

State variables (Equations)	4	T_C, T_{HS}, T_{RS} and R (4.77), (4.79), (4.85), (4.89)
Outputs	1+1	R, T_{RS}
Controllable inputs	2 + 1	I_P, I_P^2 and I_H^2
Non-controllable inputs	3	T_{ref}, T_{air} and T_{frost}

The assumption of a closed system for the multiblock and reference surface board is well justified, since there is no mass transfer. The recommended thermodynamic description is internal energy U. To respect the form of Equation 4.2 we take the derivative of Equation 4.28, the internal energy change dU.

For the mirror and ice layer, this is not such a good assumption. The system operation requires the ice layer to grow and shrink implying mass transfer. However, the growth and shrinkage is residual and controlled to a minimum, therefore we neglect mass transfer and assume a closed system. The use of enthalpy dH for the description would not be justified because we are not concerned with a continuous flow (of ice) from one medium to the next. For the reflectance, we resort to a 'grey-box' description.

4.4.2 Mirror - cold side heat balance

The mirror is a relevant reservoir to consider. It has the same temperature as the ice layer. The difference between this temperature and the actual frost point temperature drives the growth or evaporation of the ice/dew layer on the mirror.

We assume $T_{\text{ice}} = T_C$ because the mass of ice is just about 0.01 μg and the thermal conductivity of aluminium is high (k_{Al}=235 W K^{-1} m^{-1}, see Table 3.7) rendering the temperature difference between the mirror and the Peltier cold side residual, although the glue layer may add 0.15 K for 0.01 W transferred from the cold side. The ice layer is a negligible heat reservoir due to its residual mass contribution. The ice layer is treated as the ideal observer not disturbing the system in terms of heat, but signalling change in frost point temperature. Equation (4.69) is built from the heat transfer contributions of the mirror. On the left-hand side is the derivation of Equation (4.28) considering the ice layer mass changes and the masses of the ice layer and mirror. On the right hand side there are heat flow contributions.

$$\frac{d\left(m\ c_p\ T\right)}{dt} = \dot{m_{\text{ice}}}\ c_{p_{\text{ice}}} + \left(m_{\text{ice}}\ c_{p_{\text{ice}}} + m_{\text{Al}}\ c_{p_{\text{Al}}}\right)\ \frac{dT_{\text{C}}}{dt} = +\dot{Q}_{Pc} + \dot{Q}_{PE-air} + \dot{Q}_{mb} + \dot{Q}_L \tag{4.69}$$

The PE cold side heat ($\dot{Q}_{Pc}$) is given in Equation 4.70

$$\dot{Q}_{Pc} = \dot{Q}_{\alpha_P} + \dot{Q}_{R_P} + \dot{Q}_{K_P} \tag{4.70}$$

$\dot{Q}_{\alpha_P}$: Seebeck effect PE cold side. $\alpha_P\left(T_C, T_H\right)$ is the Seebeck coefficient at the PE operating temperature in W K^{-1} A^{-1}. I_P is the Peltier current in A and for cooling it is negative.

$$\dot{Q}_{\alpha_P} = \alpha_P\left(T_C, T_H\right)\ T_C\ I_P \tag{4.71}$$

$\dot{Q}_{R_P}$: Joule heating due to PE internal resistance (R_P) in Ω and Peltier current (I_P). We consider the PE Joule heating to be added at the center of the PE (see Figure 3.2), so only half of it contributes to the heat balance of the PE cold side, while the other half contributes to the heat balance of the hot side.

$$\dot{Q}_{R_P} = \frac{1}{2}\ R_P\left(T_C, T_H\right)\ I_P^2 \tag{4.72}$$

$\dot{Q}_{K_P}$: is the hot to cold side heat transfer through the PE due to the temperature difference between the cold and hot side. K_P is PE internal thermal conductance in W K^{-1}.

$$\dot{Q}_{K_P} = K_P\left(T_C, T_H\right)\ \left(T_H - T_C\right) \tag{4.73}$$

$\alpha_P\left(T_C, T_H\right)$, $R_P\left(T_C, T_H\right)$, and $K_P\left(T_C, T_H\right)$ are a function of the PE internal temperature and can be calculated from the PE geometry and material properties, but usually they are calculated from operation values given in the datasheet. $\alpha_P\left(T_C, T_H\right)$, $R_P\left(T_C, T_H\right)$, and $K_P\left(T_C, T_H\right)$ for the PE 2MDX04-022-0510 are presented in Table C.3 in Appendix C.1.

$\dot{Q}_{PE-air}$: is the heat removed from or added to the ambient air flow by the PE. h_{IT} is the intake tube convective heat transfer coefficient (see Section 4.3) and the mirror/cold side surface is

$A_m = 4 \times 4\ \text{mm}^2$.

$$\dot{Q}_{PE-air} = A_m\ h_{IT}\ (T_C - T_{\text{air}}) \tag{4.74}$$

During the first laboratory tests and test flights of PCFH, the maximum temperature differences reached by the PE were well below those advertised in the datasheet, likely due to an extra load on the cold side. From the model optimization and validation shown in Chapter 6, we found it to be proportional to the temperature difference between the cold and hot side. To account for this extra load, we added an extra multiblock heat contribution ($\dot{Q}_{mb}$) to the cold side. For future PCFH designs, we hope to reduce this contribution to zero.

$$\dot{Q}_{mb} = \frac{A_{mb}\ k_{mb}}{l_{mb}}\ (T_H - T_C) \tag{4.75}$$

$\dot{Q}_L$: ice sublimation and condensation heat due to change in the mass of the ice layer. L_V is the ice latent heat in J kg^{-1}.

$$\dot{Q}_L = \dot{m_{\text{ice}}}\ L_V \tag{4.76}$$

For implementation in the PCFH model Equation 4.69 needs to be simplified. Table 4.3 summarizes the expected range of each of the heat transfer contributions.

Table 4.3: Mirror heat transfer contributions

$\dot{Q}_{Pc}$ (W)	$\dot{Q}_{PE-air}$ (W)*	$\dot{Q}_{mb}$ (W)**	$\dot{Q}_L$(W)
0.65 - 2	0 - 0.005	0 - 0.4	10^{-4}-10^{-3}

* [10-1000] hPa, see Section 4.3.
** ad hoc estimate

Accounting only for the dominant heat transfer ranges, we simplify Equation 4.69 to Equation 4.77.

$$m_C\ c_{p_C}\ \frac{dT_C}{dt} = +\dot{Q}_{Pc} + \dot{Q}_{PE-air} + \dot{Q}_{mb} \tag{4.77}$$

where m_C is the mirror's mass and c_{p_C} is the specific heat of the mirror which is made of aluminium.

4.4.2.1 Hot side temperature

The hot side temperature (T_H) is a 'transition state' temperature to the heat sink temperature (T_{HS}). It can be computed from the heat transferred from the PE hot side to the heat sink according to Equation 4.78. It is included in the PCFH dynamic system description, because the PE hot side temperature influences the PE operation.

$$\dot{Q}_{Ph-HS} = -\alpha_P\,(T_C, T_H)\ T_H\ I_P + \dot{Q}_{R_P} - \dot{Q}_{K_P} = \left(\frac{k_{Cu} \cdot A_{PE}}{l_{Cu}} + \frac{k_{gl}\ A_{PE}}{l_{gl}}\right)\ (T_H - T_{HS}) \tag{4.78}$$

$\dot{Q}_{Ph-HS}$ is the PE hot side heat in Equation 4.78 with $\dot{Q}_{R_P}$ and $\dot{Q}_{K_P}$ as in Equations 4.72 and 4.73 respectively. Note the different sign of $\dot{Q}_{K_P}$. The Seebeck effect heat is now calculated with the

PE hot side temperature (T_H) instead of the PE cold side temperature (T_C) as in Equation 4.71. For more information on the thermodynamic and electrical description of PE refer to Appendix C.1. The heat transferred from the Peltier hot side to the heat sink is conducted through the copper finger. We use the copper thermal conductivity (k_{Cu}), the Peltier surface (A_{PE}), and the length of the multiblock from the PE hot side to the heat sink (l_{mb}) for a first estimate of the total heat transfer proportionality to the temperature difference between hot side and heat sink. During the optimization of the model in Chapter 6, this proportionality was left as a 'free' parameter because it is also important to consider the thermal glue conductivity (k_{gl}) and thickness (l_g) for this balance.

4.4.3 Multiblock and heat sink balance

The multiblock and heat sink (MB and HS) is the next relevant reservoir, because the temperature experienced by the hot side of the Peltier element is influenced by the temperature of the heat sink.

This reservoir is composed of three elements: the multiblock, made of 3D printed aluminium with a heat capacity $c_{P_{3D;Al}} = 890 \pm 50$ J kg^{-1} K^{-1}; the copper finger with $c_{P_{Cu}} = 390$ J kg^{-1} K^{-1}; and the heat sink made of regular aluminium with $c_{P_{Al}} = 910$ J kg^{-1} K^{-1} (see Table 3.7). We assume uniformity of the multiblock's temperature (T_{HS}) for equation 4.79. T_{sink} is measured at the interface of the multiblock to the heat sink. Furthermore, the nature of heat transfer from the multiblock and heat sink faces is very different. Heat is inserted by the PE at a small contact surface (high heat density) and removed at the heat-sink air interface, which is comparatively large. The contact PE between hot-side and multiblock is established by thermally conductive glue, while the contact between the multiblock and reference surface board and heat sink uses thermal paste. There are also small contributions of cooling and heating from inside the intake tube and inside the housing of the PCFH. With altitude, the cooling capability of ambient air decreases due to a decrease of air density (see Section 4.3).

Equation 4.79 is built from the heat transfer contributions to the MB and HS. On the left-hand side, there is the derivation of Equation 4.28 for the MB and HS mass at T_{HS}. On the right hand side, there are the heat flow contributions.

$$(m_{mb}\, c_{P_{mb}} + m_{Cu}\, c_{P_{Cu}} + m_{HS}\, c_{P_{HS}})\ \frac{dT_{HS}}{dt} = \\ = \dot{Q}_{Ph-HS} + \dot{Q}_{RS-HS} + \dot{Q}_{HS} + \dot{Q}_{R_{HS}} + \dot{Q}_{mb-air} + \dot{Q}_{inst} \quad (4.79)$$

$\dot{Q}_{Ph-HS}$ is as defined in Equation 4.78.

$\dot{Q}_{RS-HS}$: heat transferred by conduction from the reference surface to MB and HS, where A_{RS} and l_{RS} are the area and thickness of the reference surface PCB, and k_{Al} is the thermal conductivity of aluminium, since the PCB is made of aluminium.

$$\dot{Q}_{RS-HS} = \frac{A_{RS}\, k_{\mathrm{Al}}}{l_{RS}}\ (T_{RS} - T_{HS}) \quad (4.80)$$

$\dot{Q}_{HS}$ is the heat transferred by forced convection from an n-fin heat sink (HS) to ambient air when the HS base is at T_{HS}. A_c is the fin cross sectional area in m^2. k_{Al} is the thermal conductivity of the fin's material, in this case aluminium in W m^{-1} K^{-1}. h_{HS} is the convective heat coefficient of air

in W m^{-1} K^{-2}. Convective heat transfer coefficients are cumbersome to estimate. They depend on the fluid properties which are temperature and geometry dependent. We examine in more detail the estimation of each of the convective heat transfer coefficient in Section 4.3. p is the fin perimeter in m. L is the fin's length in m. t is the fin's thickness in m ($t = 2 \times A_c/p$).

$$\dot{Q}_{HS} = n \times \sqrt{k_{\text{Al}}\, A_c\, h_{HS}\, p}\ (T_{\text{air}} - T_{HS})\ \tanh(a\, L_c) \tag{4.81a}$$

$$a = \frac{h_{HS}\, p}{k_{\text{Al}}\, A_c} \tag{4.81b}$$

$$L_c = L + t/2 \tag{4.81c}$$

$\dot{Q}_{R_{HS}}$: radiative heat transfer from the environment. T_{rad} is the temperature of the HS surroundings and A_{HS} the surface of the HS exposed to radiation. T_{rad} will be different for day and night flights.

$$\dot{Q}_{R_{HS}} = \epsilon\, \sigma\, A_{HS} \left(T_{\text{rad}}^4 - T_{HS}^4\right) \tag{4.82}$$

$\dot{Q}_{mb-air}$: heat transferred by forced convection from the MB to the air inside the intake tube. Where h_{IT} is the same as in Equation 4.74 and A_{mb} is the surface of the MB inside the intake tube.

$$\dot{Q}_{mb-air} = h_{IT}\, A_{mb}\ (T_{\text{air}} - T_{HS}) \tag{4.83}$$

$\dot{Q}_{inst}$: heat transferred by natural convection from inside the instrument's housing to the MB. T_{ref} is the temperature inside the housing and A_{inst} is the natural convection contact surface area of the multiblock.

$$\dot{Q}_{inst} = h_{inst}\, A_{inst}\ (T_{\text{ref}} - T_{HS}) \tag{4.84}$$

Table 4.4: Multiblock + heat sink heat transfer contributions

$\dot{Q}_{Ph-HS}$ (W)	$\dot{Q}_{RS-HS}$(W)	$\dot{Q}_{HS}$ (W)	$\dot{Q}_{R_{HS}}$ (W)	$\dot{Q}_{mb-air}$ (W)	$\dot{Q}_{inst}$ (W)
0.65 - 2	0 - 8	0 - 20	1 -6	0 - 0.4	-0.5 - 0.2

The range of heat flows in the MB and HS complex do not allow for further simplification of Equation 4.79.

4.4.4 Reference surface

$$m_{RS}\, c_{P_{RS}}\, \frac{dT_{RS}}{dt} = \dot{Q}_{RS-air} + \dot{Q}_{J_{RS}} - \dot{Q}_{RS-HS} \tag{4.85}$$

Equation 4.85 considers the temperature of the reference surface (T_{RS}). This part of the system can be controlled independently. The main heat transfer contributions are joule heating and cooling from the intake tube flow. The control goal ($r_2(t)$) is

$$T_{RS} > T_{air} + 3°C \tag{4.86}$$

The connection to the other thermal reservoirs is done through $\dot{Q}_{RS-HS}$, which is the heat trans-

ferred by conduction from the reference surface to the heat sink as in Equation 4.80, but with opposing sign.

$\dot{Q}_{J_{RS}}$: heat added by joule heating on the reference surface board. R_{RS} is the resistance of the reference surface in Ω and I_H the heater current in A.

$$\dot{Q}_{J_{RS}} = R_{RS}\, I_H^2 \tag{4.87}$$

$\dot{Q}_{RS-air}$: heat transferred by forced convection from reference surface to the air in the intake tube. h_{IT} is the same convective heat transfer coefficient as in Equations 4.74 and 4.83.

$$\dot{Q}_{RS-air} = h_{IT}\, A_{RS}\, (T_{RS} - T_{\text{air}}) \tag{4.88}$$

Table 4.5: Reference surface heat transfer contributions

$\dot{Q}_{J_{RS}}$ (W)*	$\dot{Q}_{RS-HS}$ (W)	$\dot{Q}_{RS-air}$ (W)
0 - 8	0 - 8	0 - 0.2

* Only less than 10% of the reference mirror surface joule heating range will be used

4.4.5 Reflectance

So far, the description of the thermodynamic system of the PCFH fits into a 'white-box' model type. All the parameters can be estimated theoretically. However, experiments will be used to confirm certain parameters. On the other hand, reflectance – ice-layer interaction is treated as a 'grey-box' model. A change in reflectance is related to a change of the ice layer: when the ice layer grows, the reflectance decreases and when the ice layer shrinks the reflectance increases. Hence, the signal change is inversely proportional to the ice layer thickness change. The proportion of how this happens is unknown. In laboratory environments, we will find the ice coverage set-point where the ice mass change yields a maximum reflectance change, and define this as control $r_1(t)$.

Furthermore, the ice layer mass change is related to the ice layer temperature difference (T_C) to the actual frost point temperature (T_{frost}). When the ice layer temperature is colder than the frost point temperature, the ice layer will grow. When the ice layer temperature is warmer, the ice layer will shrink. We assume the 'gain' to be correlated to the water vapour diffusivity, which is a function of the frost point temperature. Other factors that might play a role are the uniformity of the ice layer, the speed of the flow in the intake tube, the height of the boundary layer inside the intake tube, and other unknowns. This is summarized as factors A and B of Equation 4.89.

$$\frac{dR}{dt} = -A\, \dot{m} = -B\,(T_{\text{frost}}) \cdot (\, T_{\text{frost}} - T_C) \tag{4.89}$$

4.4.6 Control function

FPH controls the reflectance of the ice layer to 79.1% of the light that would reflect off a clean mirror. This value comes from previous implementations of the FPH as NOAA/CMDL and it has not been changed since 1980. Laboratory testing has shown that increasing the set-point value by >7% does not affect the frost point temperature measured by the instrument. Hall et al. (2016) concludes that maintaining a constant condensate layer is much more important than the actual set-point value used. The CFH uses 88% as set-point [Holger Vömel, personal communication, 2019].

An ideal control definition for PCFH is given in Equation 4.90. However, this might be unrealistic. A control scheme needs feedback to cope with disturbances and feedback acts on deviations from the set point ($dR/dt \neq 0$). Without further constrains, a feedback loop will just maximize or minimize the reflectance. A more realistic conditions is to keep the reflectance equal to a set-point, which we imagine to be in the range shown in Equation 4.91. Hopefully, we will be able to implement a combination of the two controls functions.

$$\frac{dR}{dt} = 0 \tag{4.90}$$

$$70\% < R < 90\% \tag{4.91}$$

Chapter 5

Field and laboratory tests

It is very demanding to simulate UTLS conditions on the ground, mainly because of the low pressures, cold temperatures, and low water vapour content. For tests of the PCFH, we decided on an in-flight test strategy instead of procuring a climate chamber. Nevertheless, we ran several proof-of-concept tests at surface conditions in the laboratory.

In this chapter, we present the results of the laboratory and field tests with the first versions of the PCFH. We describe the set-up and the instrument communication interface for the laboratory. We also introduce the partnership with DWD (Deutsch Wetter Dienst - German meteorological service) whose ballooning knowledge allowed for smooth in-flight testing of the PCFH. We also introduce pre-flight calibration and system activation procedures for the PCFH.

For these initial tests, the PCFH was not operating as a frost point hygrometer. The system was run without feedback control, except for two in-flight tests where a feedback loop with ground optimized PID parameters was implemented. The main goal of the open loop tests was to measure the system dynamics ($G(s)$) or transfer function.

The transfer function can be inferred from a Bode amplitude and phase plot. It just requires a function generator and oscilloscope, which can measure the amplitude and phase between signals. The input can be a sine wave. One then records the dynamic response of the system output ($y(t)$) in relation to different frequencies of the input ($u(t)$) (Bechhoefer, 2005).

However, it is not recommend to measure a slow transfer function in the frequency domain. To measure the transfer function in the time domain, the system is excited with a known input ($u(t)$) and the response ($y(t)$) is measured. One then computes the correlation function $R_{uy}(\tau)$ between the input and output $R_{uy}(\tau) = \langle u(t)y(t+\tau)\rangle$ and also $R_{uu}(\tau) = \langle u(t)u(t+\tau)\rangle$, the autocorrelation function of the input. The transfer function $G(s)$ is calculated by taking the Fourier transforms of R_{uy} and R_{uu} and computing $G = R_{yu}/R_{uu}$ (Bechhoefer, 2005).

Recommended inputs for this type of measurement are: impulse functions, which implies that $R_{uy}(\tau)$ is an impulse response function; input step functions, which have a power spectrum $1/\omega^2$ and inject enough energy at lower frequencies; a pseudo random binary sequence (PRBS), a randomly switching square wave that alternates stochastically between two values; and a linearity check, where the input amplitude is varied and the output amplitude measured (Bechhoefer, 2005).

Due to time constraints, we were not able to compute the correlation functions for the PCFH, but we performed two $\times$ five flights with different instruments of non-identical assemblies with a mixture

of the recommended input functions for the measurement of the transfer function. Each instrument has two independent sub-units, which doubles the number of tests per flight. In this chapter, we present the results from these five flights, compare them to laboratory tests, and point out which design modifications were motivated by the observations. In Chapter 6, we compare the results to the model presented in Chapter 4.

5.1 Input for transfer function measurement

Although the inputs to the system are currents: the Peltier current (I_P) and the reference surface heater current (I_H), we are only able to set the voltage supplied to the Peltier element (PE) and the reference surface (RS) heating scheme through a PWM (Pulse Width Modulator). As the transfer function input we set a PWM sequence of 20 second steps, first with increasing amplitude followed by a reset and impulse function of 20 seconds and repeat. Table 5.1 provides the PWM sequences, as duty cycle percentages, implemented as input for transfer function measurement for the PCFH in the different tests.

Table 5.1: PWM input for Peltier current driver for different lab and in-flight tests (duty cycle percentage %). Negative numbers imply cooling.

Lab tests	0	-0.05	-0.08	-0.10	-0.15	-0.20	-0.25	-0.30	0	0	-0.30	0	0
Flights 01 & 02	0	-0.05	-0.10	-0.15	-0.20	-0.30	-0.40	-0.50	0	0.05	0	-0.20	0
Flights 04 & 05	0	-0.08	-0.15	-0.20	-0.30	-0.40	-0.50	-0.60	0	0.08	0	-0.40	0
Flight 06	0	-0.08	-0.12	-0.20	-0.27	-0.35	-0.40	-0.45	0	0.08	-0.40	-0.40	

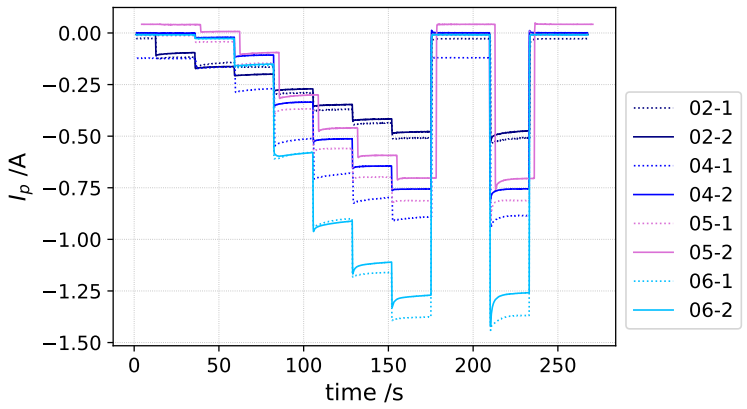

Figure 5.1: Laboratory tests input for transfer function measurement

In Figure 5.1, we show how the lab PWM sequence presented in Table 5.1 translates to different Peltier currents for different PCFH instruments. The Peltier current (I_P) is measured internally in the PCFH, in a resistor placed in series with the PE. After the first PCFH flights (01 & 02), we added an extra battery pack to flights 04 & 05 and for flight 06 the PCFH used the new electronics, where the PE driver and RS heater power supply were separated from the thermocouple module power supply. We can see how the different power supplies influence the correspondence between PWM and I_P for the different PCFH's. The PCFH with more power availability, e.g. PCFH06, shows a larger

I_P, in absolute value, for the same PWM command. This is also why different PWM sequences were implemented in the different flights, see Table 5.1, so the same I_P range would be covered independent of power supply.

Although the PWM stays constant during any step, the I_P shows a transient behaviour, in which its amplitude decreases. This behaviour is caused by the Seebeck effect changing the Peltier voltage as described in Equation C.4 of Appendix C.1. The increasing ΔT across the PE decreases the PE voltage and hence the measured current.

5.2 Laboratory tests

For each assembled instrument we ran laboratory tests to ensure all systems were operational and that all components have been assembled properly. We also ran tests to characterize the instrument.

5.2.1 Flow set-up

It is very important to test the Peltier element with air flow, because air flow strongly influences the PE performance as Sugidachi and Fujiwara (2018) observed in their studies of PE's for frost point hygrometry. With the laboratory set up presented in Figure 5.2b, we are able to generate flow conditions equivalent to those observed in flight. We use a 412 J/2HH Fan (ebmpapst, 2019) with 40 mm diameter matching the PCFH intake tube and capable of providing 24.0 m^3 h^{-1} when operated at nominal conditions (12 V), which is equivalent to 5 m s^{-1} flow through the intake tube. The fan is shown in Figure 5.2a and identified in Panel (b). Two other fans are used to recreate flow for heat sink cooling although this is not very informative at ground conditions. The instrument may be rotated, so each sub-unit can be tested.

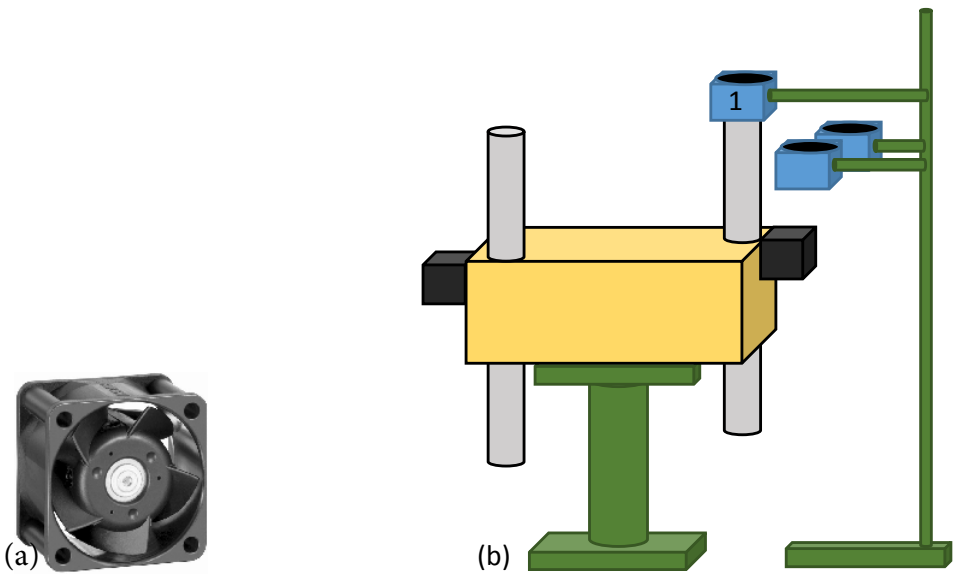

Figure 5.2: (a) 412 J/2HH Fan (ebmpapst, 2019). (b) Laboratory tests set-up with one fan identified as (1) to create intake tube flow and two fans to recreate flow through the heat sink.

5.2.2 Serial communication

Although during flight the PCFH communicates via the radiosonde, in the lab we use serial communication. The serial communication is set at 9600 baud rate, 8 bit data, parity, and 1 stop bit. Every line, received and transmitted ends with a CR+LF (carriage return and line feed). The most important commands for the laboratory tests are setting of the PWM duty cycle for the reference surface (RS) heaters and Peltier element (PE) drivers and the diagnostic function output activation. The commands are summarized in Table 5.2. Table 5.3 presents the data output when the diagnostic function output is active.

Table 5.2: Serial communication: RS heater and PE driver PWM and diagnostics output

	command		example
Set PWM for RS heaters	th<n>,<v>	n: number sub-unit (1 or 2) v: pwm value (float) (0 ... 1)	A00th1,0.5xxx M11:OK,xxx
Set PWM for PE drivers	tp<n>,<v>	n: number sub-unit (1 or 2) v: pwm value (float) (-1 ... 1)	A00tp1,-0.5xxx M11:OK,xxx
Activate diagnostics	td<n>,<m>	n: number of the diagnostic (11 or 12) m: 0 to access all parameters	SU1: A00td11,0xxx SU2: A00td12,0xxx

Table 5.3: PCFH diagnostics output

Data		Time stamp	PWM_P	PWM_{RS}	I_P	U_{bat45}
Message	M01:SEN_ 1:	····· 32537 ,	· 0.000 ,	·0.000 ,	·0.001 ,	3.966 ,
Start position		10	22	29	42	42
Length of value	9	11	6	5	5	5

R_{mirror}	$R_{\text{ref surf}}$	T_{mirror}	T_{air}	T_{hot}
··6262 ,	··7070 ,	· 25.81 ,	·25.65 ,	· 25.86 ,
48	55	62	69	76
6	6	6	6	6

$T_{\text{ref surf}}$	T_{sink}	Check sum
·25.86 ,	·25.92 ,	698
83	90	97
6	6	3

5.2.3 Labview

The data acquisition is done with a LabView program developed specifically for this application (Jorge and Cesbron, 2018b).

5.3 DWD collaboration

The Richard Assmann observatory of DWD is the host institution of the GRUAN Lead Center (GRUAN LC) (Immler et al., 2010) in Lindenberg, Germany. Its staff has extensive experience in ballooning and high quality water vapour measurements with the CFH (Vömel et al., 2016; Dirksen et al., 2014; Brunamonti et al., 2018). Part of their mission is to foster development of instruments for high quality measurements of relevant atmospheric constituents and climate drivers. In addition, they have developed a very successful recovery program for payloads and permits to launch payloads up to 4 kg per balloon, which is particularly helpful for instrument still in development phase. The two PCFH test campaigns were generously hosted by the DWD team at Lindenberg in July and December 2018.

5.4 Pre-flight procedures

5.4.1 Current and reflectance calibration

As mentioned above, although the system input is a current, we are only able to set PWM values, which translate to voltages applied to the PE. Internally, the PCFH measures the current applied to the PE by measuring the voltage across a sensing resistor in series with the PE. A span parameter corrects for hardware tolerances, while an offset is needed for bipolar measurements with a single (asymmetric) power supply. Through a calibration procedure we can translate this voltage into current. The Peltier current (I_P) is output through serial communication and through telemetry. The calibration procedure consists of connecting a multimeter in series between the PE and the PE driver in ammeter mode. At PWM 0, we can measure the offset of the current which according to the measurement principle is just half of the 3.3 V regulated supply. A sequence of PWM values and the corresponding currents and voltages at the PCFH, provides enough to determine the current span. Table 5.4 shows the calibration values used for PCFH04-1. Table 5.5 shows the commands to save these values in the instrument. The current calibration only needs to be done once for each sub-unit, as it is component dependent.

Table 5.4: PE current calibration: PCFH04 Sub-unit 1

PWM	0	-0.05	-0.1	-0.15	-0.2	-0.25	-0.3	-0.35	-0.4
V_P (V)*	1.631	1.632	1.727	1.915	2.099	2.231	2.358	2.430	2.543
I_P (A)	0	0	-0.09	-0.26	-0.43	-0.56	-0.68	-0.75	-0.82

span	offset
-0.980	1.602

* Standard deviation (STD) ranges from 0.1% to 0.8% for V_P

Table 5.5: PE current calibration commands. Example for PCFH02 sub-unit 1 and 2 on 2018-07-19.

A00PW30:1.677xxx	Sub-unit 1 I_P offset
A00PW31:1.060xxx	Sub-unit 1 I_P span
A00PW32:1.695xxx	Sub-unit 2 I_P offset
A00PW33:0.934xxx	Sub-unit 2 I_P span
A00DWxxx	Write device configuration to EEPROM (Save command)

I_P is transmitted as a percentage of a full scale (FS), which is set in the PCFH firmware; it is not programmed by serial communication. For flights 01 and 02, I_P FS was 1.2 A. For flight 04, 05, and 06, I_P FS was 2.0 A

The mirror and reference surface reflectance values (R_{mirror} and $R_{\text{ref surf}}$) are transmitted as a percentage (%) of full scale (FS), which is 'calibrated' before flight. Although the LED's used are from the same production lot and there are no differences between the electronics of each sub-unit, the LED brightness strongly varies between LED's and depends on the optical and mechanical set-up as well. For calibrating the full scale, we acquire the clean mirror and reference surface reflectance values with fresh batteries for 20 s. Ideally the values should be averaged, although the measurement is quite stable. LED brightness varies with temperature and decreasing temperature leads to brightness increase. However, the expected change is in the range of ±5%. Therefore, we take the measured reflectance for the mirror and reference of each unit and multiply it by 1.1, increasing the full scale by 10%.[1] These values are stored in the device as shown in Table 5.6.

Table 5.6: Reflectance calibration commands. Example for PCFH02 sub-unit 1 and 2 on 2018-07-19.

A00PW40:5400.0xxx	FS R_{mirror1}
A00PW41:6700.0xxx	FS $R_{\text{ref surf1}}$
A00PW42:5050.0xxx	FS R_{mirror2}
A00PW43:6200.0xxx	FS $R_{\text{ref surf2}}$
A00DWxxx	Write device configuration to EEPROM (Save command)

5.4.2 Telemetry

The PCFH has different telemetry options, which can be controlled via a parameter mask sent to the PCFH shown in Table 5.7.

Table 5.7: Telemetry activation mask

bit 0	Individual instrument identification (II) message
bit 1	Regular one second data sub-unit 1 message
bit 2	Regular one second data sub-unit 2 message
bit 3	Regular five second data message
bit 4	First experimental data message
bit 5	Second experimental data message
bit 6	Third experimental data message
bit 7	Fourth experimental data message
bit 16	Simulated data instead of measured data

For example, if we want to activate the individual instrument identification message, the regular one second data for sub-unit 1 and 2, and the five second data message, the number to provide to PCFH would be:

[1] During several of the PCFH flights, we lost reflectance data due to an overflow of the full scale. The measured reflectance during flight was higher than the full scale measured at the ground. The telemetry is programmed to send a value between 0 and 100%. If the reflectce ratio to the full scale is bigger than 100%, the sent value is truncated to 100%. The full scale is now set to 10'000 counts on all sub-units. (2019-11-19)

$2^0 + 2^1 + 2^2 + 2^3 = 1 + 2 + 4 + 8 = 15 \Rightarrow$ A00IW6:15xxx

On the other hand, if we would like to receive simulated data instead of the actual instrument out-put we can provide the following message:

$2^0 + 2^1 + 2^2 + 2^3 + 2^{16} = 1 + 2 + 4 + 8 + 65536 = 65551 \Rightarrow$ A00IW6:65551xxx

5.4.3 Controller activation

In the lab, the PE drivers and RS heaters can be controlled with serial commands as shown in Table 5.2. For the flights, the action of each of these needs to be defined before power on. Programmed in the PCFH firmware, there are several options, which are listed in the Appendix D.2, and which can be set with the commands in Table 5.8. We set the parameters for each option with the commands in Table 5.9.

Table 5.8: Controller activation and telemetry commands

A00IW6:_xxx	telemetry mask
A00IW7:_xxx	Sub-unit 1 PE mode
A00IW8:_xxx	Sub-unit 2 PE mode
A00IW9:_xxx	Sub-unit 1 RS heater mode
A00IW10:_xxx	Sub-unit 2 RS heater mode
A00DWxxx	Write device configuration to EEPROM (Save command)

Table 5.9: Controller parameters

sub-unit 1	sub-unit 2		
A00PW60:_xxx	A00PW80:_xxx	K_p PE	PID parameters
A00PW61:_xxx	A00PW81:_xxx	$1/K_i$ PE	
A00PW62:_xxx	A00PW82:_xxx	K_{ds} PE	
A00PW63:_xxx	A00PW83:_xxx	K_p RS	
A00PW64:_xxx	A00PW85:_xxx	$1/K_i$ RS	
A00PW65:_xxx	A00PW85:_xxx	K_{ds} RS	
A00PW66:_xxx	A00PW86:_xxx	% of reflectance from clean mirror	
A00PW69:_xxx	A00PW89:_xxx	$T_{\text{ref surf}} - T_{\text{air}}$	
A00PW71:_xxx	A00PW91:_xxx	Time t_1	
A00PW72:_xxx	A00PW92:_xxx	Time t_2	
A00PW73:_xxx	A00PW93:_xxx	Value X_1	
A00PW74:_xxx	A00PW94:_xxx	Value X_2	
A00DWxxx	Write device configuration to EEPROM (Save command)		

For flights 01 and 02 sub-unit 1, and flights 04, 05, and 06 both sub-units, the 'step mode' controller (1, explanation of the types of controller in Appendix D.2) for the PE was activated with the sequences shown in Table 5.1 each step with the duration of 20 s. For flights 01 and 02 sub-unit 2, the 'alternating set-point PID controller' (5) for the mirror and reference surface reflectance was activated. This controller is a PID with parameters optimized for ground conditions, where the set-point alternates between two values. The set-point is 70% of the clean mirror reflectance for 20 s and 80% of the clean mirror reflectance for 30 s.

The reference surface temperature ($T_{\text{ref surf}}$) for the flights was controlled with a PID controller (10) with set-point $T_{\text{air}}^{\text{PCFH}} + 3$ °C, where $T_{\text{air}}^{\text{PCFH}}$ is the air temperature measured by the PCFH air thermocouple. Each PCFH measures $T_{\text{air}}^{\text{PCFH}}$ twice, once for each sub-unit. In this chapter we make a distinction between $T_{\text{air}}^{\text{PCFH}}$ and T_{air}, the air temperature measured by the RS41.

The telemetry mask loaded into the PCFH's 01, 02, 04 and 05 activates the individual instrument identification message, the regular one second data for sub-unit 1 and 2, and the five second data message. In the first flights, we noticed some data gaps. We suspected and verified that the data rate of the radiosonde RS41 was exceeded when the individual instrument identification message was being sent at the same time as the other three messages. The telemetry scheduling has been altered and the individual instrument identification message is only sent when the five second regular data message is not sent. To implement optimal control in the PCFH or to implement a controller different than a PID, the PCFH firmware needs to be changed.

Field Campaigns July and December 2018

5.5 Objectives

Although the PCFH was not yet a functioning frost point hygrometer, because it was still not capable of measuring the frost point temperature, there were many things we could learn from deploying the instrument. The objectives for the first PCFH campaigns were:

- **Peltier element**: Which temperature can the cold side of the Peltier element reach in each layer of the atmosphere? How does this compare to the frost point temperature provided by the CFH? Does the Peltier current change with operating temperature of the Peltier? Is it more dependent on the power supply?
- **Thermal management**: Is the thermal insulation from the exterior sufficient to maintain a reasonable operating temperature inside the housing? How effective is the heat sink? What is the thermal response of the PCFH at critical thermal locations: T_{hot}, $T_{\text{ref surf}}$, T_{sink}, and T_{mirror}?
- **Model Validation**: By providing the adequate input for measuring the transfer function, we will be able to validate and optimize the PCFH model using the observations. The goal is to learn which are the dominant heat contributions for the PCFH thermal balance, so the instrument design can be optimized accordingly.
- **Water vapour diffusivity**: Can we estimate a water vapour diffusivity from observing the change in reflectance together with the temperature difference from PE mirror to frost point temperature provided by the CFH?
- **Power supply**: Can the batteries last for an entire flight period – ascent and descent?
- **Internal systems of the PCFH**: Can the PCFH operate during the entire flight?
- **Telemetry**: Will data transmission work? Will it work during the entire flight time? Will it work well with other instruments in the daisy chain?
- **Robustness**: Will the mechanical construction and the thermocouples survive the flight through the stratosphere and the landing? How much refurbishment should we expect after recovery?

- **Recovery**: Observe and learn from the DWD team how to perform a successful payload recovery so we can implement it in Zürich - addressed in Appendix D.1.

5.6 Payloads

All of the PCFH flights so far have been hosted by the radiosonde RS41-SGP (Vaisala, 2017), here refereed to as RS41. Each of these flights had different add-on instruments in different configurations. In Table 5.10 we present the payload constituents in daisy chain order for the five PCFH flights. In Appendix D.3 we present a schematic of each payload configuration and a picture of the payload.

Table 5.10: Payload constituents in daisy chain order for the five PCFH flights

PCFH	radiosonde	0	1	2	3	4	Launch date and time
01	RS41	OIF411	PCFH				2018-07-25, 02UT, 04LT
02	RS41	OIF411	COBALD	PCFH	CFH		2018-07-25, 20UT, 22LT
04	RS41	OIF411	ECC O_3	PCFH	CFH		2018-12-12, 16UT, 18LT
05	RS41	OIF411	COBALD	PCFH			2018-12-12, 16UT, 18LT
06	RS41	OIF411	ECC O_3	COBALD	PCFH	CFH	2018-12-13, 22UT, 24LT

Table 5.11: Sub-units (SU) construction differences

	PCFH	SU	PE	mb+HS	$T_{\text{air}}^{\text{PCFH}}$	controller	electronics	batteries	other
summer	01	1	ds	v1 + 7 fins	IT	1-steps	version 1		
		2	ds	v1 + 7 fins	IT	5-PID			
	02	1	ds	v1 + 7 fins	IT	1-steps	version 1		
		2	ds	v1 + 5 fins	IT	5-PID			
winter	04	1	ss	v2 + 8 fins	OH	1-steps	version 1	1 extra pck	*
		2	ss	v2 + 8 fins	OH	1-steps			
	05	1	ss	v2 + 8 fins	OH	1-steps	version 1	1 extra pck	
		2	ds	v2 + 8 fins	OH	1-steps			
	06	1	ss	v2 + 8 fins	OH	1-steps	version 2		
		2	ds	v2 + 8 fins	OH	1-steps			

PE: Peltier element, ds: double stage, ss: single stage, see Section 3.1.1.
mb: multiblock, v1: version 1, v2: version 2, see Figure B.13.
HS: heat sink, 7/8 fins, see Figure B.14,
5 fins: the 7 fins HS was cut in half in the flow direction and 2 fins were cut away.
$T_{\text{air}}^{\text{PCFH}}$: measurement location of $T_{\text{air}}^{\text{PCFH}}$: inside the intake tube (IT) or outside the housing (OH).
controller: see Table D.2
electronics: version 1, see Figures B.15a and B.15b, and version 2, see Figures 3.13a and 3.13b.
*: T_{sink} and T_{air} in PCFH04-2 were accidentally switched.

PCFH01 was launched on the same balloon as the scientific GRUAN payload (LI236) comprising a RS41, OIF411 + ECC O_3 (Komhyr et al., 1995), COBALD, and CFH. The first launch of PCFH

was with just one radiosonde. Since the first flight was successful in terms of communication with the radiosonde and telemetry, the following flights had other add-on instruments. The frost point temperature from the CFH flown in flight LI236 is used as frost point temperature reference for the PCFH data from flight PCFH01. There was no PCFH03, and PCFH04 and PCFH05 were launched simultaneously on two independent balloons. The frost point temperature measurement from the CFH flown with PCFH04 is used as a reference for PCFH05. A second payload with RS41 and FLASH B (Vömel et al., 2007c) was launched simultaneously with PCFH06 on two independent balloons. Unfortunately FLASH B stop working shortly after launch.

In some of the payloads, we use the OIF411 interface without ECC O_3. The OIF411 interface allows for the connection of the add-on instruments in the daisy chain to the RS41. It can operate without being connected to the ECC O_3, because it is powered by the radiosonde. Another option for the connection of the add-on instruments to the RS41 is to refurbish the usual 4-pin telemetry cable to include a special plug, necessary for the connection to RS41, in one of the ends.

Although the different PCFHs had important construction differences and were flown in different atmospheric conditions (summer and winter mid-latitudes), we will analyse the flight data of the two sub-units of each flight simultaneous in the next sections. In Table 5.11, we highlight some of the most relevant differences between the instruments and sub-units.

5.7 House keeping

In the next sections, we present the atmospheric data in 1 s intervals, as it is received from the radiosonde. We present balloon ascent and descent, depending of the comparison goal. Each will be identified in the corresponding section. In this study, pressure from the RS41 radiosonde is the main vertical coordinate for all instruments. We do not remove CFH clearing and freezing cycles (Vömel et al., 2016), which occur twice per flight at -15 °C and -53 °C frost point temperature approximately.

5.7.1 Reference temperature and power supply

First, we investigate the reference temperature (T_{ref}) in the thermocouple module board, which we take as proxy for the temperature inside the PCFH housing. T_{ref} for the five PCFHs flights is shown in Figure 5.3a. We can identify two clusters corresponding to the PCFHs flown in warm summer conditions: 01 and 02 and the PCFHs flown in colder conditions: 04, 05 and 06. T_{ref} for PCFHs 04 and 05 shows isolated patches deviating from the main line. These flight's were performed with electronic version's 1 and power supply but with the much more demanding controller step cycle, which involved higher I_P being drained from the power supply. When the step with higher I_P was run the thermocouple module was no longer supplied with a voltage of 3.3 V leading to a failure of the temperature measurements. This effect can be seen since launch in flights 04 and 05, and in flights 01 and 02 only towards the end of the descent. We flag the temperature measurements made in this 'failure' condition by comparing the temperature measurement by the PCFH to the RS41 temperature measurement (see Section 5.7.2). All the other simultaneous temperature measurements: T_{mirror}, T_{hot}, $T_{\mathrm{ref\ surf}}$, and T_{sink}, which were transmitted to the ground in the same second, are also considered bad. For flight 06 the temperature measurement failure does not occur any more due to the improvement in the power supply of the electronics version 2.

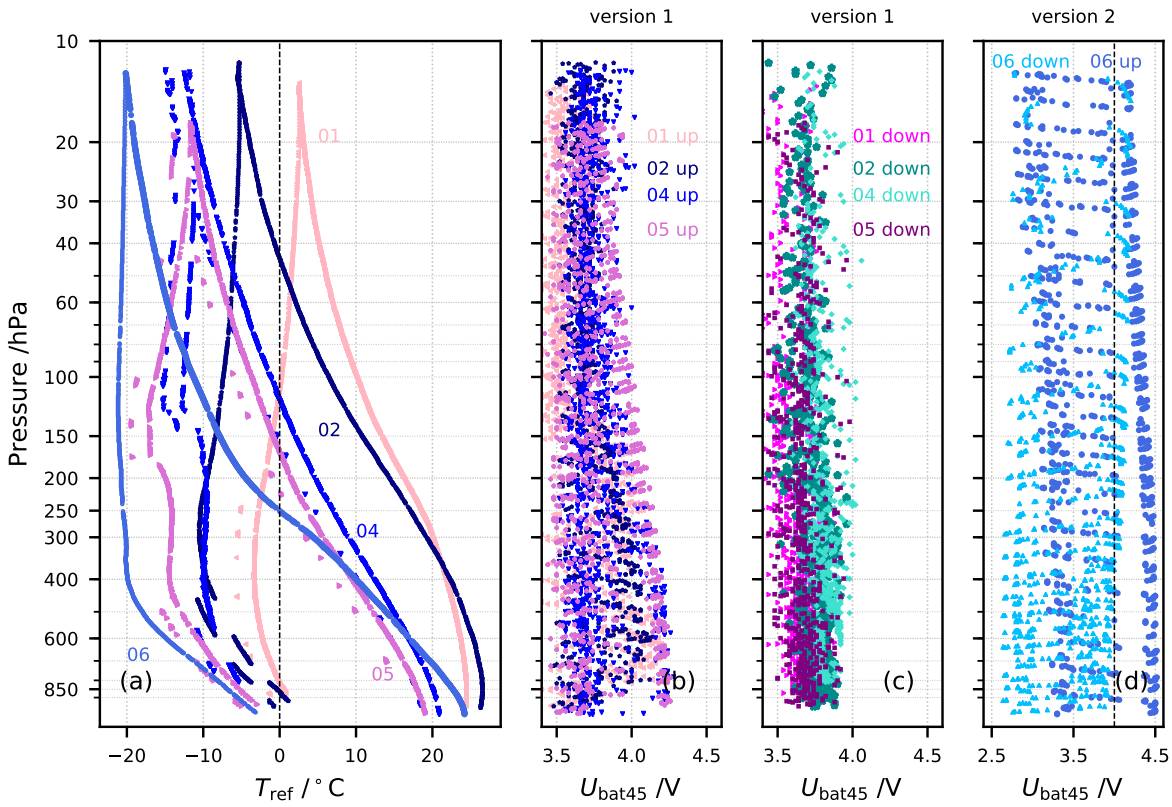

Figure 5.3: Reference temperature and 4.5 V power supply for the 5 PCFH flights ascent and descent. (a) Reference temperature in the thermocouple module board ascent and descent, light pink: PCFH01, navy: PCFH02, blue: PCFH04, pink: PCFH05, royal blue: PCFH06; (b) 4.5 V power supply voltage for the PCFH's first generation ascent, light pink: PCFH01, navy: PCFH02, blue: PCFH04, pink: PCFH05; (c) same for descent, fuchsia: PCFH01, darkcyan: PCFH02, turquoise: PCFH04, purple: PCFH05; (d) 4.5 V power supply voltage for the PCFH with electronics version 2: PCFH06, royal blue: ascent, deep sky blue: descent.

T_{ref} for flight PCFH06 shows the coldest temperatures and the fastest cooling during ascent, although flights 04 and 05 also took place in winter and in very similar tropospheric air temperatures (see Figure 5.4 panels (c) and (d)). In the version 1 electronics, the thermocouple module is below the controller and reflex board (Figure B.15b), while in the electronics version 2 the thermocouple module is above the main board (Figure 3.13a). The different behaviour of the T_{ref} for the three flights 04, 05 and 06 can be related to this change of placement of the thermocouple module board. Other possibilities, is that the housing of PCFH's 04 and 05 was better insulated than that of PCFH 06, or had more water packs inside which help maintain the temperature inside the housing.

Another observation relating to the T_{ref} is that the version 1 of the thermocouple module board had a reference thermometer calibrated only until -5 °C. Future versions of the PCFH will have thermocouple module boards with reference thermometers calibrated down to -20 °C. A correct reference temperature is essential for a correct temperature measurement with thermocouples (see Section 3.2). The descents of flights 02, 04, 05 and 06 had all reference temperatures below -5 °C, so all temperature measurements for these periods are affected. Despite the increase of the reference thermometer

calibration range, we should strive to keep the temperature inside the PCFH housing warmer, possibly by better thermal insulation or active heating of the electronic boards.

With the telemetry, information on the 4.5 V power supply ($U_{\mathrm{bat4.5}}$) is also sent to the ground. We can see this information in panels (b), (c), and (d) of Figure 5.3. Panel (b) and (c) shows ascent and descent data respectively for flight 01, 02, 04 and 05 all based of the electronics and power supply version 1. In this version, PE drivers and RS heaters are supplied out by the same power supply as the thermocouple module. The voltage does not drop below 3.4 V, but we see a clear decrease of the maximum voltage to below 4 V in the stratosphere and descent. In Figure 5.3d we see $U_{\mathrm{bat4.5}}$ for PCFH 06 whose electronics and power supply are different. The PE drivers and RS heater are supplied with a different power supply than that for the thermocouple module, which allows the PE supply voltage to drop below 3.4 V. Either way, we also see a decrease of the power supply nominal voltage when no current is being drained from 4.5 V before launch to 4 V at landing. The new power supply seems to be sufficient for the PCFH power requirements from launch to landing during one balloon flight.

5.7.2 Air temperature

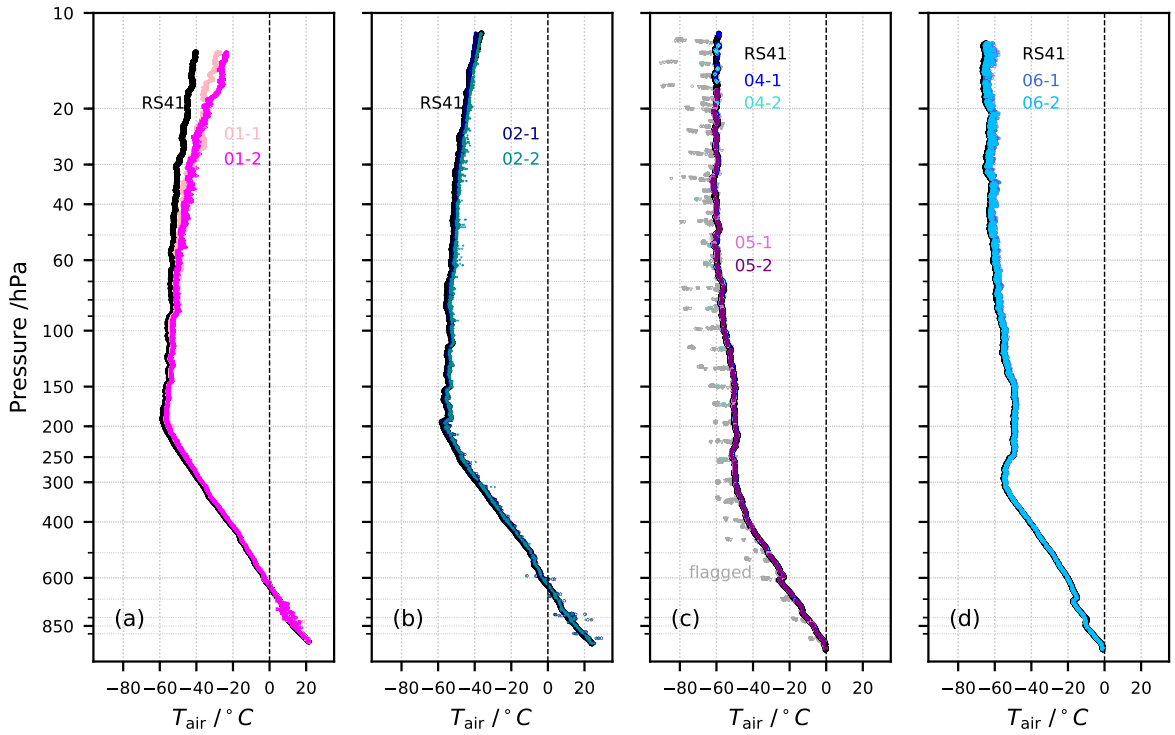

Figure 5.4: PCFH vs RS41 air temperature ascent. (a) PCFH01 2018-07-25 02UT, black: RS41, light pink: sub-unit (SU) 1, fuchsia: SU 2; (b) PCFH02 2018-07-25 20UT, black: RS41, navy: SU 1, darkcyan: SU 2; (c) PCFH04 and PCFH05 2018-12-12 16UT, black: RS41, blue: PCFH04-1, turquoise: PCFH04-2, pink: PCFH05-1, purple: PCFH05-2, grey: flagged; (d) PCFH06 2018-12-13 22UT, black: RS41, royal blue: SU 1, deep sky blue: SU 2.

Figure 5.4 shows air temperature (T_{air}) profiles for the 5 PCFH's flights grouped by day of flight. PCFH has one $T_{\mathrm{air}}^{\mathrm{PCFH}}$ measurement per sub-unit. PCFH04 and PCFH05 were simultaneous flights.

Due to the intermittent failure of the thermocouple board, some of the temperature measurements are considered bad. They are shown for flight PCFH04 and 05 as flagged measurements (grey). They have been identified by $|\Delta T_{\mathrm{air}}| > 1$ °C, an ad hoc value which excludes noise.

$$\Delta T_{\mathrm{air}} = T_{\mathrm{air}}^{\mathrm{PCFH}} - T_{\mathrm{air}} \tag{5.1}$$

Figure 5.5 shows the differences between air temperature measured by the RS41 and each of the PCFH's sub-units (ΔT_{air}). The air temperature by the PCFH appears to have a warm bias in relation to RS41, in particular PCFH01 and 02. In these two cases, we attribute the warm bias to the placement of the $T_{\mathrm{air}}^{\mathrm{PCFH}}$ thermocouple 1 to 2 cm inside of the intake tube. It passed between the bottom of the PCB board and the top of the bottom plastic 3D printed part from the inside of the housing to the inside of the intake tube. These air temperature measurements were highly influenced by the multiblock and heat sink temperature.

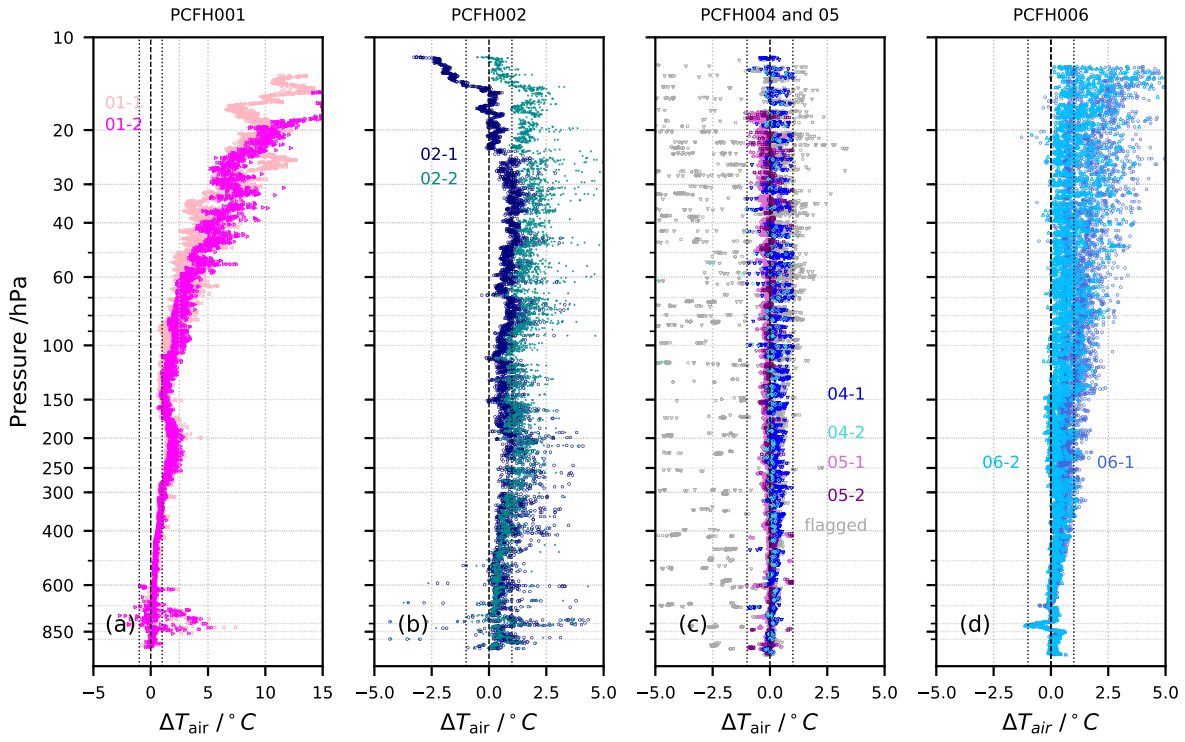

Figure 5.5: PCFH and RS41 air temperature difference (ΔT_{air}) ascent. (a) PCFH01 2018-07-25 02UT, Light pink: SU 1, fuchsia: SU 2; (b) PCFH02 2018-07-25 20UT, navy: SU 1, darkcyan: SU 2; (c) PCFH04 and PCFH05 2018-12-12 16UT, blue: PCFH04-1, turquoise: PCFH04-2, pink: PCFH05-1, purple: PCFH05-2, grey: flagged; (d) PCFH06 2018-12-13 22UT, royal blue: SU 1, deep sky blue: SU 2.

For PCFH 04, 05 and 06 flight, the location of the $T_{\mathrm{air}}^{\mathrm{PCFH}}$ thermocouple was changed, so that it has no contact with the multiblock or the heat sink; it leaves the PCFH housing through a rubber tube. In panels (c) and (d) of Figure 5.5, we can see a decreased warm bias. Despite the flagged measurements, $T_{\mathrm{air}}^{\mathrm{PCFH}}$ in PCFH04 and PCFH05 seems to agree better with the RS41 T_{air} measurement and is less noisy. However, PCFH06 $T_{\mathrm{air}}^{\mathrm{PCFH}}$ is again very noisy and has an increasing warm bias with decreasing

pressure. Temperature measurements with thermocouples are known to be more sensitive than PTR (Platinum type resistor) measurements; however, other implementations of thermocouples for T_{air} measurements have been shown to be less noisy (Kräuchi et al., 2016). The design of $T_{\mathrm{air}}^{\mathrm{PCFH}}$ needs to be altered.

5.7.3 Heat sink temperature

Figure 5.6 panels (a), (b), (c) and (d) shows the heat sink temperatures (T_{sink}) for the PCFHs flights during ascent. The air temperature of the respective RS41 is also included. Due to the intermittent failure of the thermocouple board of PCFH 04 and 05, some of the temperature measurements are considered bad. They are still shown but flagged in grey. They are the simulatenous T_{sink} measurements of the identified bad T_{air} measurements in Section 5.7.2 plus other T_{sink} when $\Delta T_{\mathrm{sink}} <$ -5 °C as in

$$\Delta T_{\mathrm{sink}} = T_{\mathrm{sink}} - T_{\mathrm{air}} \tag{5.2}$$

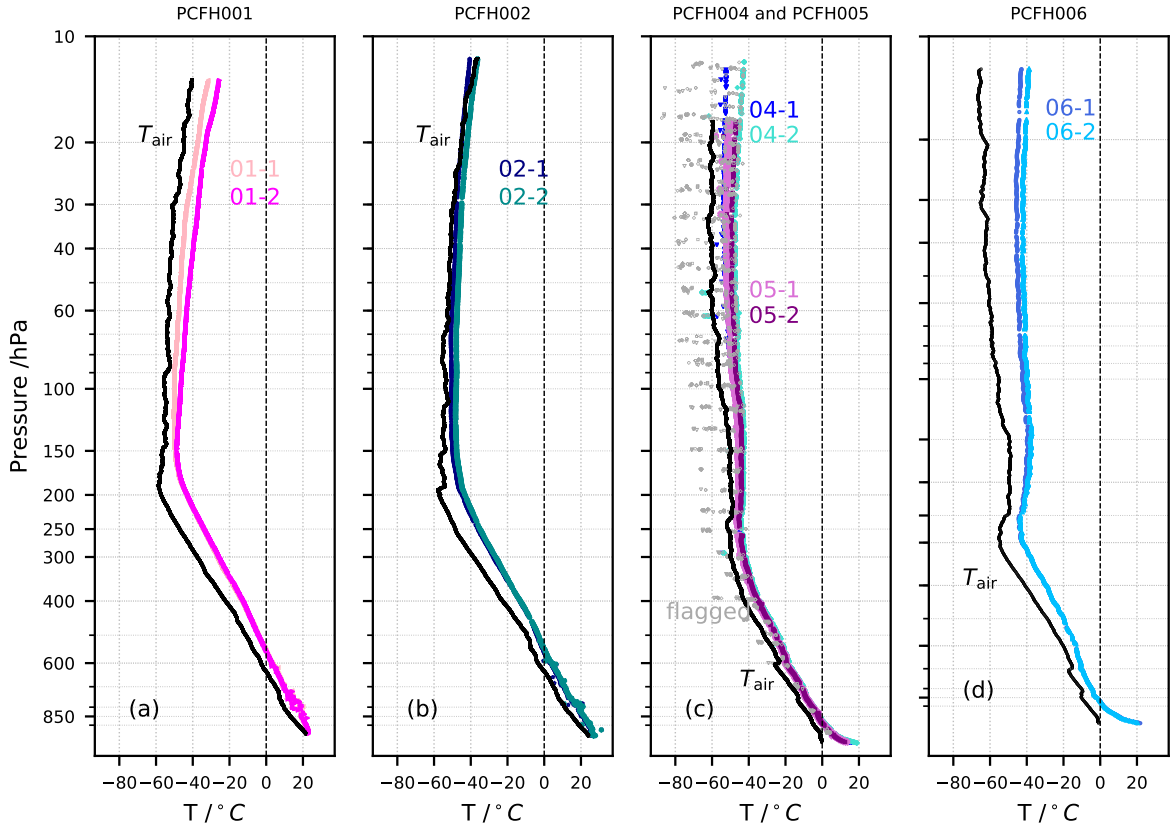

Figure 5.6: Heat sink temperature (T_{sink}) ascent. (a) PCFH01 2018-07-25 02UT, black: T_{air}, light pink: SU 1, fuchsia: SU 2; (b)PCFH02 2018-07-25 20UT, black: T_{air}, navy: SU 1, darkcyan: SU 2; (c) PCFH04 and PCFH05 2018-12-12 16UT, black: T_{air}, blue: PCFH04-1, turquoise: PCFH04-2, pink: PCFH05-1, purple: PCFH05-2, grey: flagged; (d) PCFH06 2018-12-13 22UT, black: T_{air}, royal blue: SU 1, deep sky blue: SU 2. (e) ΔT_{sink}, light pink: PCFH01-1, fuchsia: PCFH01-2, navy: PCFH02-1, darkcyan: PCFH02-2, blue: PCFH04-1, turquoise: PCFH04-2, pink: PCFH05-1, purple: PCFH05-2, royal blue: PCFH06-1, deep sky blue: PCFH06-2, grey: flagged.

The limit of $\Delta T_{\text{sink}} <$ -5 °C is estimated from the observations. It is used to remove some outliers which were not synchronous with the bad T_{air} measurements. In Panels (c) and (e), we can still observe some outliers for PCFH04-2, which have not been flagged by these methods.

Figure 5.6e shows the temperature difference (ΔT_{sink}) between each heat sink of each sub-unit of each PCFH in relation to the respective air temperature measured by the RS41 according to Equation 5.2. Figure 5.7 shows the same variables but for the descent.

For the analysis of the heat sink temperatures (T_{sink}) it is important to look at ascent and descent for each of the flights simultaneously and to differentiate between the flight with the heat sink (HS) version 1 and the HS version 2. The relevant difference is not the length or number of fins, but the mass of the HS. The HS version 1 mass is about 150 g while the HS version 2 mass is half of that, about 70 g.

First we focus on the two flights during the summer, in which each PCFH sub-unit had a version 1 HS, except PCFH02 sub-unit 2. The HS of PCFH02 sub-unit 2 was an altered version 1 HS. We had cut the length of the fins in half in flow direction and removed two fins. In addition flight PCFH01 was done at sunrise, so in the stratosphere, although there was a radiation protection for the HSs, they were exposed to solar radiation. Lastly, each sub-unit in the two PCFHs had a different control scheme implemented, which translates in different heat loading. The step controller creates a high heat load when high I_Ps are explored, but this happens for less than 20% of the stepping cycle. The PID, especially for PCFH01 sub-unit 2 in the stratosphere tapped into very high I_Ps to cool the mirror, which led to high heat loading of the HS.

During the winter, all flights were performed at night and had the same configuration of multiblock plus HS. The only differences worth mentioning is that some sub-units 04-1, 04-2, 05-1 and 06-1 had single stage (ss) PEs and the others, 05-2 and 06-2, had double stage (ds) PEs. However, this should not influence the heat loading of the HS, since the programmed step cycle into the PCFH did not distinguish between single stage or double stage PEs. The actual difference of flight PCFH 06 is the use of the electronics version 2. To probe the same range of I_Ps with the version 2 electronics, the PWM step cycle for this PCFH was adjusted, because the available power is at least 2× more than for PCFHs 04 and 05, which leads to higher I_P for the same PWM command.

Regarding the anomalous behaviour of PCFH04-2, it must be noted that here the thermocouples for the HS and for air were accidentally switched. This caused a positive feedback of the reference surface temperature since $T_{\text{ref surf}}$ is controlled to 3 °C warmer than $T_{\text{air}}^{\text{PCFH}}$. If T_{sink} is taken as $T_{\text{air}}^{\text{PCFH}}$ due to the thermocouple switch, the RS heater will always be actively warming the RS and consequently increasing T_{sink}, because the heat deposited in the RS warms the HS, creating a positive feedback.

Before launch in the summer (flights 01 and 02), the heat sinks are in equilibrium with ambient temperature. After launch, a temperature difference builds up between HS and ambient (ΔT_{sink}) of around 5 °C. During the winter (flights 04, 05 and 06), the payloads were kept inside, in warm conditions, until launch. After release, we can see a fast cooling of the HSs to about 5 °C warmer than ambient air. This ΔT_{sink} remains approximately constant for all flights up to 500 hPa.

Ignoring for now flight PCFH 06, which is not yet fully understood, we focus on the comparison of HS version 1 and summer flights: 01 and 02 vs HS version 2 and winter flights: 04 and 05. ΔT_{sink} builds up in the summer flights up to 15 °C above ambient air at the tropopause, at about 200 hPa, while ΔT_{sink} remains approximately constant at 5 °C for the winter flights.

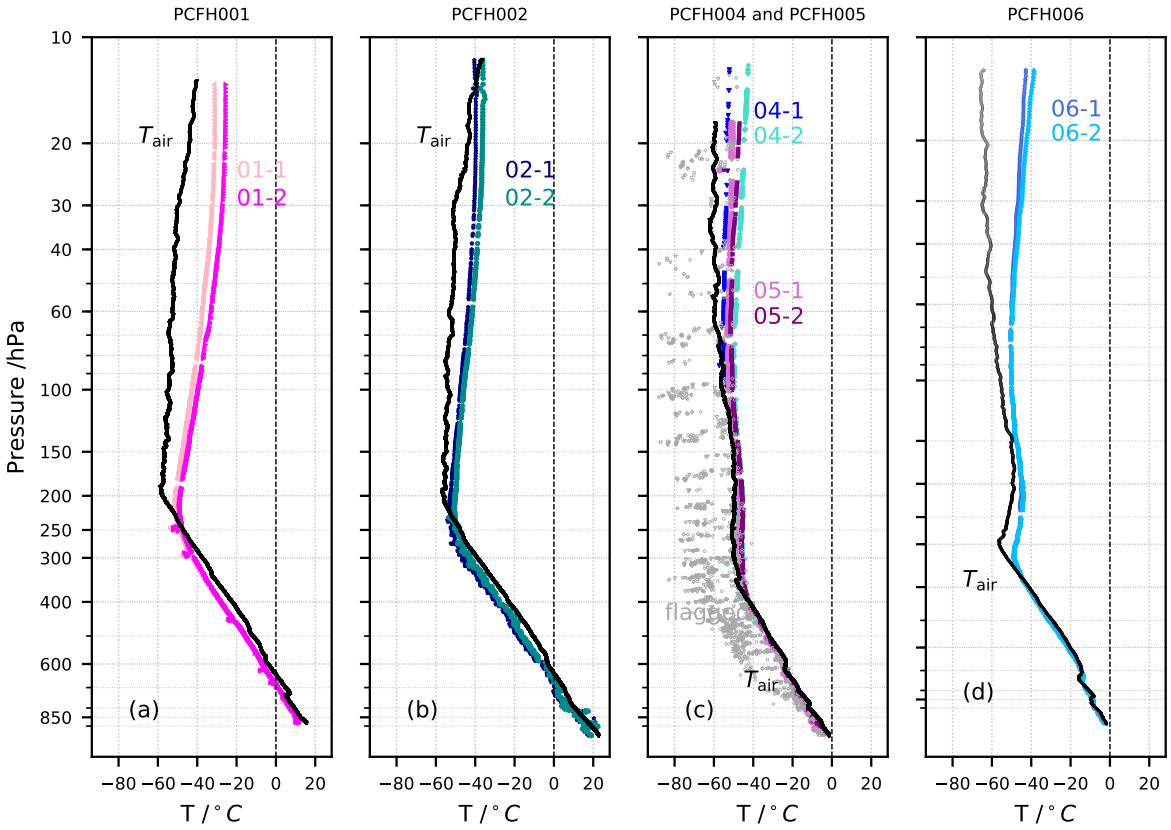

Figure 5.7: Heat sink temperature (T_{sink}) descent. (a) PCFH01 2018-07-25 02UT, black: T_{air}, light pink: SU 1, fuchsia: SU 2; (b)PCFH02 2018-07-25 20UT, black: T_{air}, navy: SU 1, darkcyan: SU 2; (c) PCFH04 and PCFH05 2018-12-12 16UT, black: T_{air}, blue: PCFH04-1, turquoise: PCFH04-2, pink: PCFH05-1, purple: PCFH05-2, grey: flagged; (d) PCFH06 2018-12-13 22UT, black: T_{air}, royal blue: SU 1, deep sky blue: SU 2. (e) ΔT_{sink}, light pink: PCFH01-1, fuchsia: PCFH01-2, navy: PCFH02-1, darkcyan: PCFH02-2, blue: PCFH04-1, turquoise: PCFH04-2, pink: PCFH05-1, purple: PCFH05-2, royal blue: PCFH06-1, deep sky blue: PCFH06-2, grey: flagged.

When the payloads reach the stratosphere, the behaviour of the payloads becomes less consistent. First, the instruments whose HS showed ΔT_{sink} of the order of 15 °C (flights 01 and 02) go back to having a smaller ΔT_{sink}, again in the range of 5 °C. This change is likely due to the T_{air} increase in the stratosphere. At about 150 hPa, PCFH 01 and 02 show very different behaviours. ΔT_{sink} for PCFH 01-1 increases up to 10 °C and ΔT_{sink} for PCFH 01-2 increases up to 15 °C for pressure below 20 hPa; while ΔT_{sink} for PCFH 02 decreases until the point when $\Delta T_{\text{sink}} < 0$, the HSs are colder than ambient air.

The ΔT_{sink} increase in the stratosphere is the expected behaviour, especially with the decrease convective cooling and the radiation exposure during the day-time flight (PCFH01). We attribute the 5 °C difference between the two sub-units to the different controller schemes. The cooling of the HS down to $\Delta T_{\text{sink}}<0$ observed in PCFH02 is harder to explain, but the observation of the descent can help clarify this behaviour. The difference between the two sub-units of PCFH02 in the ascent in the stratosphere can be explained by the smaller heat sink for sub-unit 2, since the controlling of 02-2 was

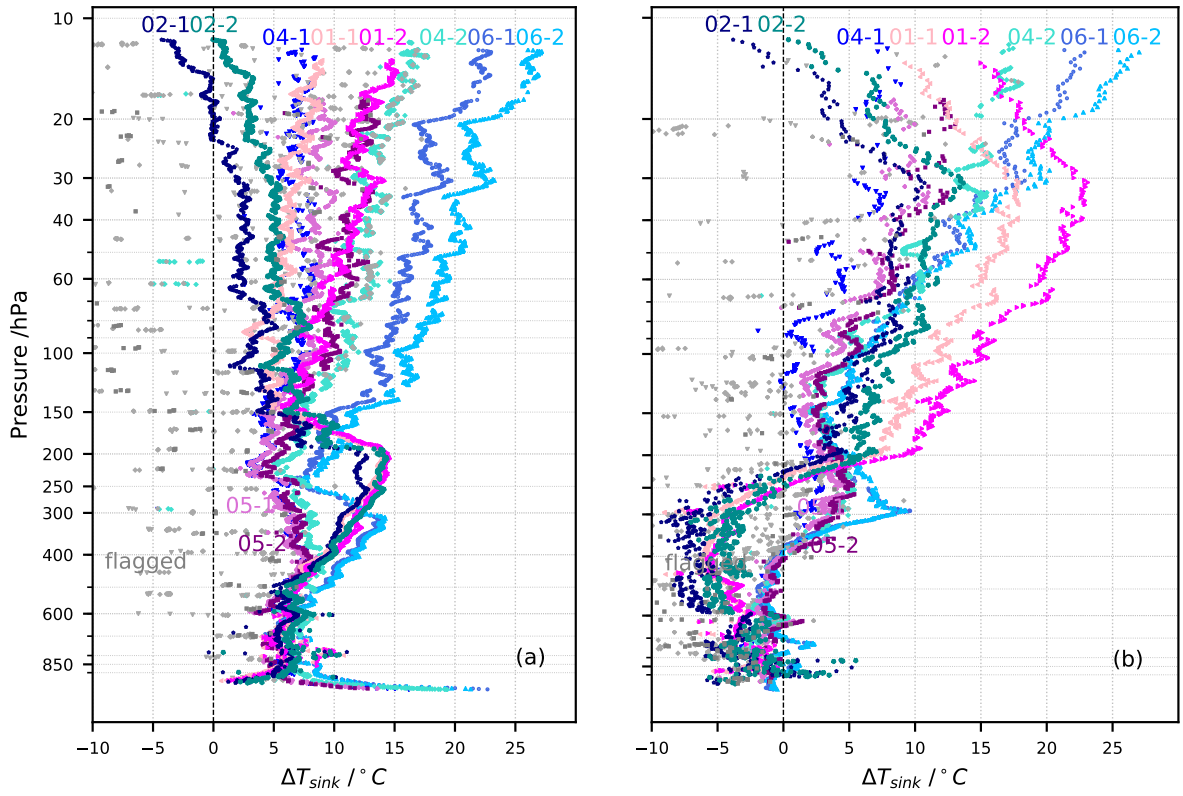

Figure 5.8: Heat sink temperature (T_{sink}) descent. (a) PCFH01 2018-07-25 02UT, black: T_{air}, light pink: SU 1, fuchsia: SU 2; (b)PCFH02 2018-07-25 20UT, black: T_{air}, navy: SU 1, darkcyan: SU 2; (c) PCFH04 and PCFH05 2018-12-12 16UT, black: T_{air}, blue: PCFH04-1, turquoise: PCFH04-2, pink: PCFH05-1, purple: PCFH05-2, grey: flagged; (d) PCFH06 2018-12-13 22UT, black: T_{air}, royal blue: SU 1, deep sky blue: SU 2. (e) ΔT_{sink}, light pink: PCFH01-1, fuchsia: PCFH01-2, navy: PCFH02-1, darkcyan: PCFH02-2, blue: PCFH04-1, turquoise: PCFH04-2, pink: PCFH05-1, purple: PCFH05-2, royal blue: PCFH06-1, deep sky blue: PCFH06-2, grey: flagged.

not working as planned.

On descent, ΔT_{sink} increases after burst for all HSs of flight 01 and 02. As the tropopause is crossed on descent, all HSs are suddenly colder than T_{air}, which means they are no longer being cooled by the air, but warmed. This is due to the thermal capacitance C_{HS} (Equation 5.3), which is related to the specific heat capacity and the mass of all the heat sink components: the actual heat sink, the multiblock, and the copper finger as described in Sections 3.6 and 4.4.3.

$$C_{HS} = (m_{mb} \cdot c_{p_{mb}} + m_{Cu} \cdot c_{p_{Cu}} + m_{HS} \cdot c_{p_{HS}}) \tag{5.3}$$

C_{HS} is the time constant of the HS thermal balance equation (Eq. 4.79). When C_{HS} is large and the payload moves from colder to warmer air (during ascent in the stratosphere and descent in the troposphere), the HS requires time to adjust to the warmer temperature. This effect is more pronounced on descent in the troposphere than on ascent in the stratosphere because the tropospheric temperature gradient is larger than the stratospheric. This hypothesis was proven in the next flights (04 and 05) using lighter HS. The thermal delay on ascent in the stratosphere and on descent in the

troposphere was not as pronounced as for the flights with the heavier HS (01 and 02).

Although PCFH 06 has the light HS as PCFH 04 and 05, ΔT_{sink} for PCFH 06 resembles more PCFH 01 and 02 on ascent in the troposphere than 04 or 05. This could also be due to the sharper tropopsause temperature change in flight 06 than in flights 04 and 05, which resembles more the summer air temperature profile. ΔT_{sink} in the stratosphere is increasing significantly more for PCFH06 than for PCFH 04 and 05. ΔT_{sink} for PCFH 04 and 05 is not decreasing in the stratosphere; however, T_{air} is decreasing in winter in the stratosphere, and decreasing more significantly in flight 06 than in flights 04 and 05 which could be enough to justify different ΔT_{sink} behaviour. Another argument to support the different behaviour of PCFH06 is that the electronics version 1 have higher power availability due to the re-design of the power supply. Higher I_Ps were reached during operation, which deposited more heat in the HS of PCFH 06, making it substantially warmer than the ones of flight 04 and 05.

The descent in flight 06 is compatible with the above hypothesis. ΔT_{sink} on descent in the troposphere is less than 0, but not as low as what was registered for 01 and 02, which supports a faster equilibration time due to lighter HS's.

5.7.4 Reference surface temperature

For the analysis of the reference surface temperature ($T_{\text{ref surf}}$) we decided not to show $T_{\text{ref surf}}$ profiles vs P_{air} but to show the difference to other relevant variables such as air temperature ($T_{\text{air}}^{\text{PCFH}}$), which is part of $T_{\text{ref surf}}$ controller function (Eq. 4.86), and heat sink temperature (T_{sink}), to which the reference surface (RS) is thermally coupled.

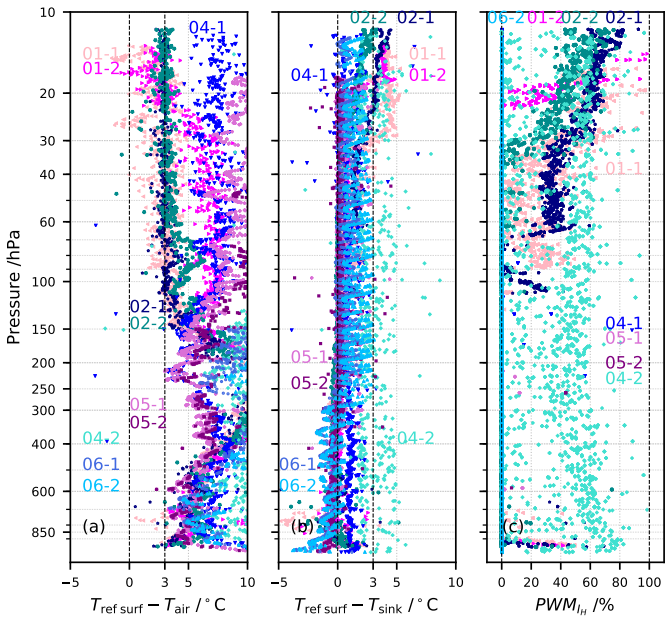

Figure 5.9: Reference surface temperature ($T_{\text{ref surf}}$) analysis ascent. PCFH01 2018-07-25 02UT, PCFH02 2018-07-25 20UT, PCFH04 and PCFH05 2018-12-12 16UT, PCFH06 2018-12-13 22UT. All panels, light pink: PCFH01-1, fuchsia: PCFH01-2, navy: PCFH02-1, darkcyan: PCFH02-2, blue: PCFH04-1, turquoise: PCFH04-2, pink: PCFH05-1, purple: PCFH05-2, royal blue: PCFH06-1, deep sky blue: PCFH06-2.

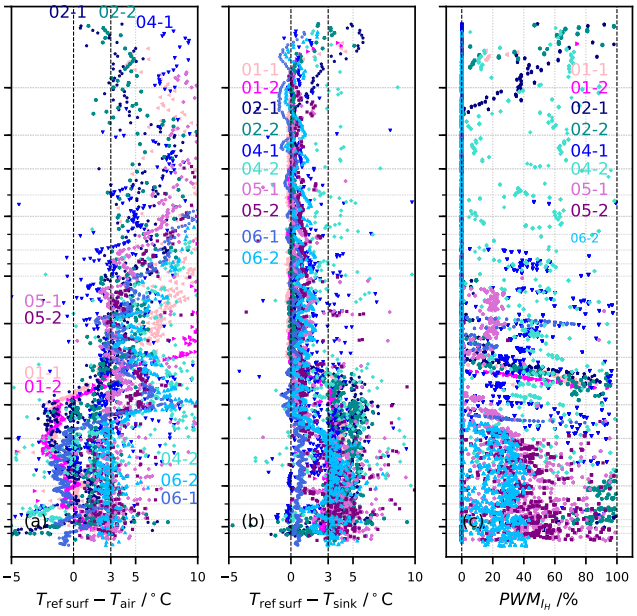

Figure 5.10: Reference surface temperature ($T_{\mathrm{ref\,surf}}$) analysis descent. PCFH01 2018-07-25 02UT, PCFH02 2018-07-25 20UT, PCFH04 and PCFH05 2018-12-12 16UT, PCFH06 2018-12-13 22UT. All panels, light pink: PCFH01-1, fuchsia: PCFH01-2, navy: PCFH02-1, darkcyan: PCFH02-2, blue: PCFH04-1, turquoise: PCFH04-2, pink: PCFH05-1, purple: PCFH05-2, royal blue: PCFH06-1, deep sky blue: PCFH06-2.

Figure 5.9a and Figure 5.10a shows the temperature difference between the RS and the air temperature measured by the respective sub-unit thermocouples ($\Delta T = T_{\mathrm{ref\,surf}} - T_{\mathrm{air}}^{\mathrm{PCFH}}$) for ascent and descent, respectively. In Figures 5.9b and 5.10b, we can see the temperature difference between the RS and the respective heat sink ($\Delta T = T_{\mathrm{ref\,surf}} - T_{\mathrm{sink}}$) for ascent and descent. In Figure 5.9c and 5.10c, we show the PWM duty cycle fraction for the RS heaters of each PCFH sub-unit for ascent and descent. Panels (a) and (b) of both figures are limited to 10 °C because we are just interested in the range around 3 °C although the differences are sometimes bigger.

The RS heaters are only active towards the end of the ascent and mainly on the PCFHs flown in summer. Due to the good thermal coupling of the RS and the heat sink (HS), the RS is kept above air temperature at almost all times. Although for PCFH01 (Figure 5.6e) the HS and hence the RS are well above air temperature in the stratosphere, the RS heaters are still activated because $T_{\mathrm{air}}^{\mathrm{PCFH}}$ is warm biased by the HS (Figure 5.5a). For the RSs of PCFH02, the problem is the contrary, since the HS cold biasses $T_{\mathrm{air}}^{\mathrm{PCFH}}$, the RS is not 3 °C warmer than ambient air. In the stratosphere (Figure **??**a) the PID controller is able to maintain the RS at 3 °C warmer than $T_{\mathrm{air}}^{\mathrm{PCFH}}$.

As mentioned in Section 5.7.3, $T_{\mathrm{air}}^{\mathrm{PCFH}}$ for PCFH04-2 was misplaced in the T_{sink} location, hence we see the reference heater active through the entire ascent trying to keep $T_{\mathrm{ref\,surf}}$ warmer by 3 °C in relation to T_{sink}. Another potential issue is the oscillation of the temperature difference seen for both sub-units of PCFH06 (Figure 5.9b), which resembles the transfer function identification steps applied to the PE. These are not applied by the RS heater, since the PWM duty cycle is zero. A possible explanation might be thermal coupling between the PE, either hot or cold side, and the reference

surface.

Figure 5.10 shows the descent data. As in Section 5.7.3, on descent in the troposphere, the HSs and RSs are colder than air, and due to good thermal coupling so is the RS. Unfortunately, we can not see in Figure 5.10c that the RS heaters of almost all PCFHs are active and at maximum PWM, due to a telemetry fault, which overflows for 100% PWM .

In PCFHs with version 1 electronics,on descent, maximum RS heaters PWM was not enough to maintain the RS at 3 °C warmer than $T_{\text{air}}^{\text{PCFH}}$, but it could keep the RS at 3 °C warmer than T_{sink}. For PCFH06-2 using the electronics version 2, the RS is regulated at 3 °C above $T_{\text{air}}^{\text{PCFH}}$ and T_{sink} during the descent in the troposphere due to more effective RS heaters. The RS heaters of PCFH06-01 were not operational, hence its absence from Panel (c).

5.8 Frost point temperature

Figures 5.11 shows the frost point temperature measured by the CFH and the air temperature measured by the RS41 together with the mirror temperature and hot side temperature for the sub-units of PCFH 01 and 02 flown in July 2018. Sub-unit 1 of PCFH 01 and 02 was running the transfer function identification steps introduced in Table 5.1 and sub-unit 2 of PCFH 01 and 02 was running the alternating set-point PID controller introduced in Section 5.4.3.

PCFH 01 sub-unit 1 could have reached the frost point temperature in this flight up to 170 hPa which is just above the tropopause. The PID controller of sub-unit 2 tracks the frost point temperature observed by the CFH up to 200 hPa. However, there is some under-estimation of T_{frost} in the first kilometres of the atmosphere, until 700 hPa, in which the condensate in the PCFH mirror is a mixture of liquid and ice [Personal communication Holger Vömel, 2019], and then again from 500 hPa until 250 hPa. Above 150 hPa, the PE is operated at $I_{P_{\max}}$, but the cooling is not sufficient to follow the frost point temperature.

Sub-unit 1 of PCFH 02 would have been able to follow the frost point temperature in this flight up to 150 hPa. This is 30 hPa above sub-unit 1 of PCFH 01 and 50 hPa above the cold point tropopause.

The step sequence implemented in sub-unit 1 of PCFH 02 looks slightly different than the one implemented in sub-unit 1 of PCFH 01. In this flight, the hot side of the PE does not reach the observed high temperatures seen in flight 01. It is as if the heat is being transferred easier in this PCFH from the hot side to the heat sink because of a smaller thermal resistance between the two, or as if T_{hot} thermocouple was displaced. In Section 5.9.2, we will look into this aspect of this flight in more detail.

Sub-unit 2 of PCFH 02 was only able to follow the frost point from 700 hPa to 550 hPa during the ascent. In this case, the PID values implemented in the controllers were the same; however, they were obtained and 'optimized' for PCFH 01 and implemented in PCFH 02. The malfunction of PCFH02-2 looks strange; the PE is not cooling to form an ice layer but rather heating as if the reflectance was too small and ice needed to be evaporated. Possibly, the optical path of the PE mirror or RS was disturbed. On ascent, in the entire stratosphere, the cold side is warmer than the hot side.

Sub-units 2 of PCFH 01 and 02, which were running the alternating set-point PID recover on descent and track the frost point acceptably from 400 hPa to 600 hPa.

Figures 5.12 and 5.13 show the frost point temperature measured by the CFH and the air tem-

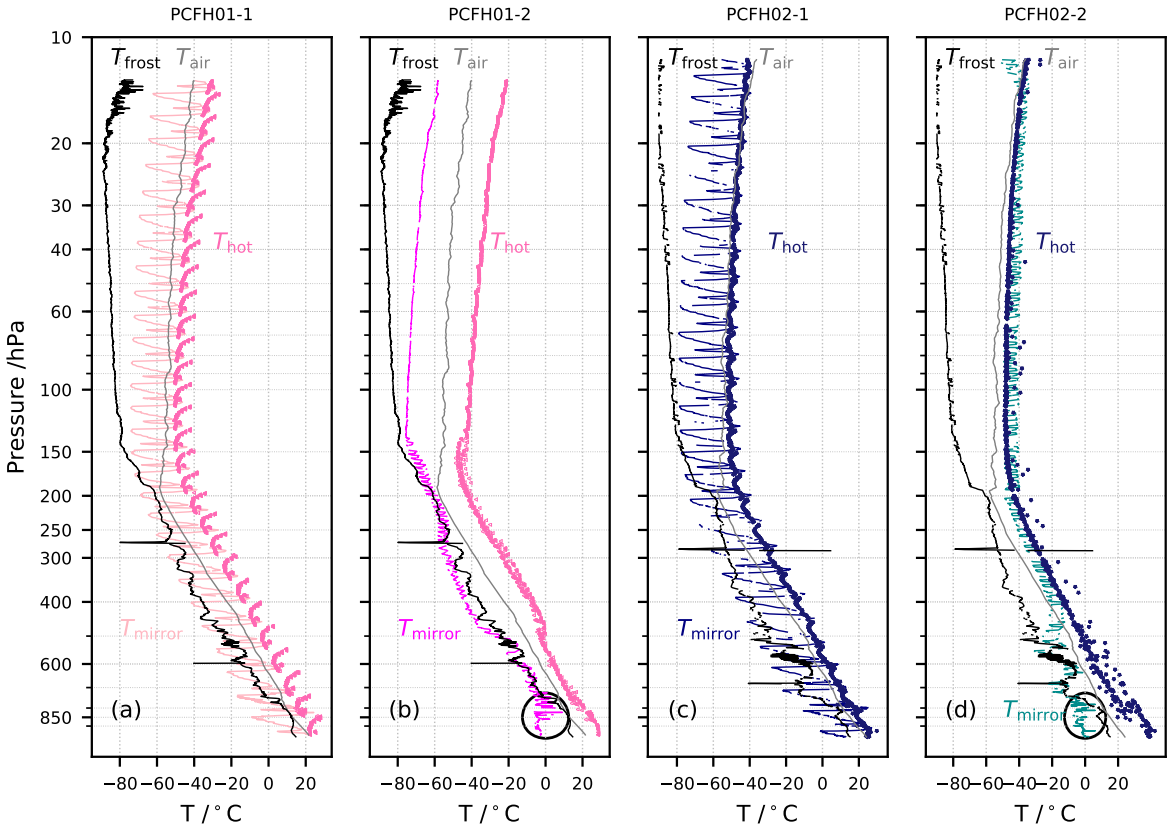

Figure 5.11: PCFH 01 (2018-07-25 02UT) and 02 (2018-07-25 20UT) T_{mirror}, T_{frost}, T_{air} and T_{hot} ascent. (a) Black: CFH T_{frost}, grey: RS41 T_{air}, light pink: PCFH01-1 T_{mirror} and hot pink: PCFH01-1 T_{hot}; (b) black: CFH T_{frost}, grey: RS41 T_{air}, fuchsia: PCFH01-2 T_{mirror} and hot pink: PCFH01-2 T_{hot}; (c) black: CFH T_{frost}, grey: RS41 T_{air}, navy: PCFH02-1 T_{mirror} and midnight blue: PCFH02-1 T_{hot}; (d) black: CFH T_{frost}, grey: RS41 T_{air}, dark cyan: PCFH02-2 T_{mirror} and midnight blue: PCFH02-2 T_{hot}. Ellipses in (b) and (d) identify when the condensate in the PCFH mirror is a mixture of liquid and ice [Personal communication Holger Vömel, 2019]

perature measured by the RS41 together with the mirror temperature and hot side temperature for the sub-units of PCFH 04, 05 and 06 flown during the PCFH second campaign in December 2018. As for T_{air} (Fig. 5.4 and 5.5) and T_{sink} (Fig. 5.6 and 5.7), we show flagged values of T_{mirror} and T_{hot} for PCFH 04 and 05 as grey dots in Figures 5.12. All sub-units in this group were running the transfer function identification steps introduced in Table 5.1.

During the first PCFH campaign in July 2018, we observed that the ΔT range of chosen double stage PE (2MDX04-022-0510) was smaller than expected. We attributed this reduction to an underestimation of the cold side heat load. For the second campaign, we re-evaluated the design of the PE assembly and the multiblock. We opened the space around the PE (see Figure B.12 and B.13) to reduce the thermal coupling of the mirror and PE cold side to the multiblock and RS. We increased the cross section of the copper finger in the multiblock, in PCFH 01 and 02 it was Ø 5 mm, and in PCFH 04, 05 and 06 it was Ø 7 mm to reduce the thermal resistance between PE hot side and heat sink. We assembled the PCFHs sub-units with single and double stage PEs to investigate if a stiffer

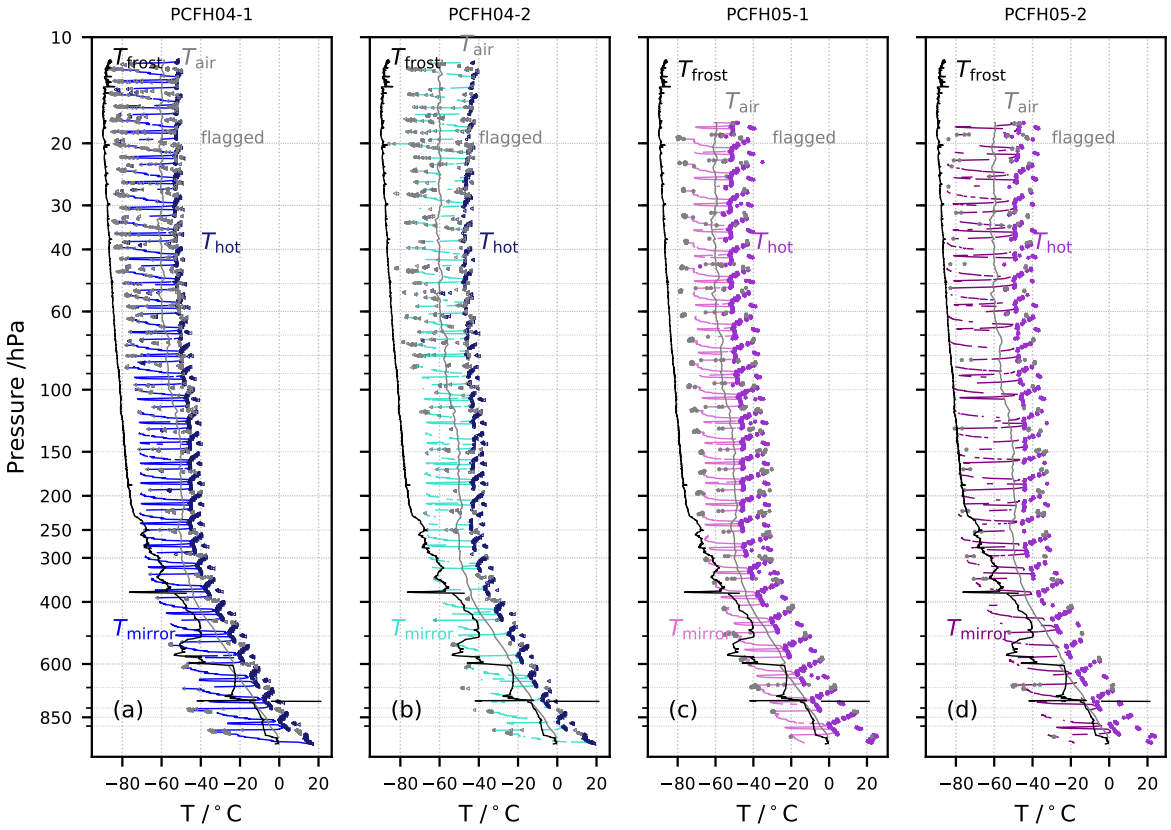

Figure 5.12: PCFH 04 and 05 (2018-12-12 16UT) T_{mirror}, T_{frost}, T_{air} and T_{hot} ascent. (a) Black: CFH T_{frost}, grey: RS41 T_{air}, blue: PCFH04-1 T_{mirror} and midnight blue: PCFH04-1 T_{hot}; (b) black: CFH T_{frost}, grey: RS41 T_{air}, turquoise: PCFH04-2 T_{mirror} and hot midnight blue: PCFH04-2 T_{hot}; (c) black: CFH T_{frost}, grey: RS41 T_{air}, pink: PCFH05-1 T_{mirror} and purple: PCFH05-1 T_{hot}; (d) black: CFH T_{frost}, grey: RS41 T_{air}, violet: PCFH05-2 T_{mirror} and purple: PCFH05-2 T_{hot}.

PE would provide a larger ΔT.

5.8.1 First successful flight

One of the new assemblies, PCFH 05 sub-unit 2, in which a double stage was implemented, was able to reach mirror temperatures in the stratosphere comparable to the frost point temperatures measured by the CFH, regardless of the flagged measurements. At air temperatures of -45 °C to -50 °C, the double stage PE assembled in sub-unit 2 of PCFH 05 reached temperatures of -80 °C to -85 °C, up to a pressure altitude of 40 hPa.

However, the other new assemblies were not as successful as expected. Some of them provided extremely high T_{hot} with a maximum of almost 20 °C warmer than the HS, as was the case for both sub-units of PCFH 05. Others had a high T_{sink} compared to T_{air} and an undesirable thermal coupling with RS, as was the case for PCFH 06. In others, independent of stiffness, the single stage PE provided a too small ΔT, although T_{hot} and T_{sink} were not unreasonably high, as was the case of PCFH 04.

On descent, PCFH 04 and PCFH 05 mirror temperatures could reach stratospheric frost point temperature ranges. However, most of these measurements have been flagged for thermocouple module

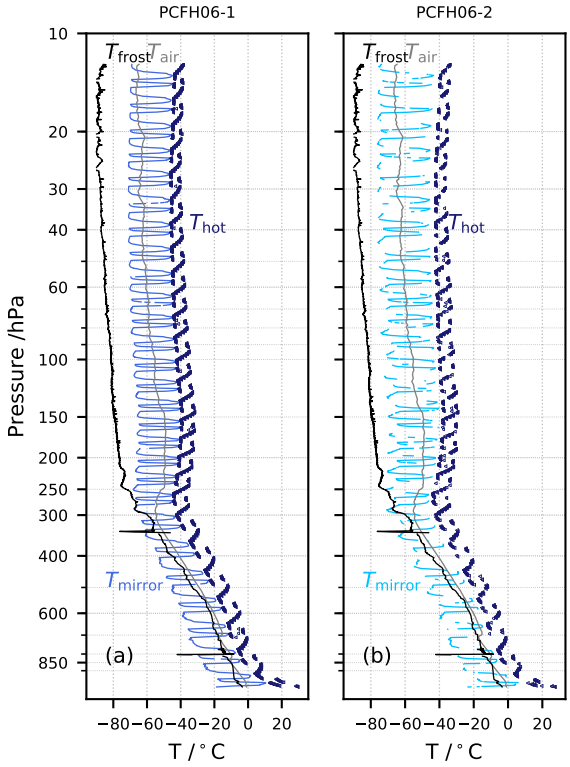

Figure 5.13: PCFH 06 (2018-12-13 22UT) T_{mirror}, T_{frost}, T_{air} and T_{hot} ascent. (a) Black: CFH T_{frost}, grey: RS41 T_{air}, royal blue: PCFH06-1 T_{mirror} and midnight blue: PCFH06-1 T_{hot}; (b) black: CFH T_{frost}, grey: RS41 T_{air}, deep sky blue: PCFH06-2 T_{mirror} and midnight blue: PCFH06-2 T_{hot}.

failure, which makes the temperature measurements questionable.

5.9 Laboratory vs field testing

For PCFHs 02, 04, 05 and 06 we ran laboratory tests with the PWM duty cycle sequence identified in Table 5.1, with and without flow. The conditions of the laboratory tests were 22 °C $< T_{\mathrm{air}} <$ 26 °C and flow was 5 m s^{-1} at about 1000 hPa, i.e. ground conditions. In this section we compare the results from these tests with the results from the in-flight tests.

5.9.1 Peltier element characterization

First, we compare the Peltier element characteristics. In Figure 3.4c, we show the characteristic curve (ΔT vs I_P) at ambient temperature of 300 K (27 °C) of the double stage PE 2MDX04-022-0510 and single stage PE 1MC04-017-05. These are the PEs used in the different PCFH sub-units, see Table 5.11. ΔT for the PE characterization is calculated according to

$$\Delta T = T_{\mathrm{hot}} - T_{\mathrm{mirror}} \tag{5.4}$$

In Figures 5.14 and 5.15 we show PE characteristics curves (ΔT vs I_P) for PCFH01, 02, 04, 05 and

06 both sub-units on ascent. In these figures we show the respective datasheet curve, the laboratory test curves, with and without flow and the in-flight curve. The data are color coded with air pressure (p_{air}) with a logarithmic color scale. Figure 5.14 shows the Peltier element characteristics for both sub-units of PCFH01 and 02, all equipped with double stage Peltier element. Figure 5.15 displays the Peltier element characteristics for both sub-unit of PCFH04 and 05 (electronics version 1) and PCFH06 (version 2). All sub-units are equipped with single stage Peltier elements, but sub-units 2 of PCFH05 and 06, which are equipped with double stage Peltier elements.

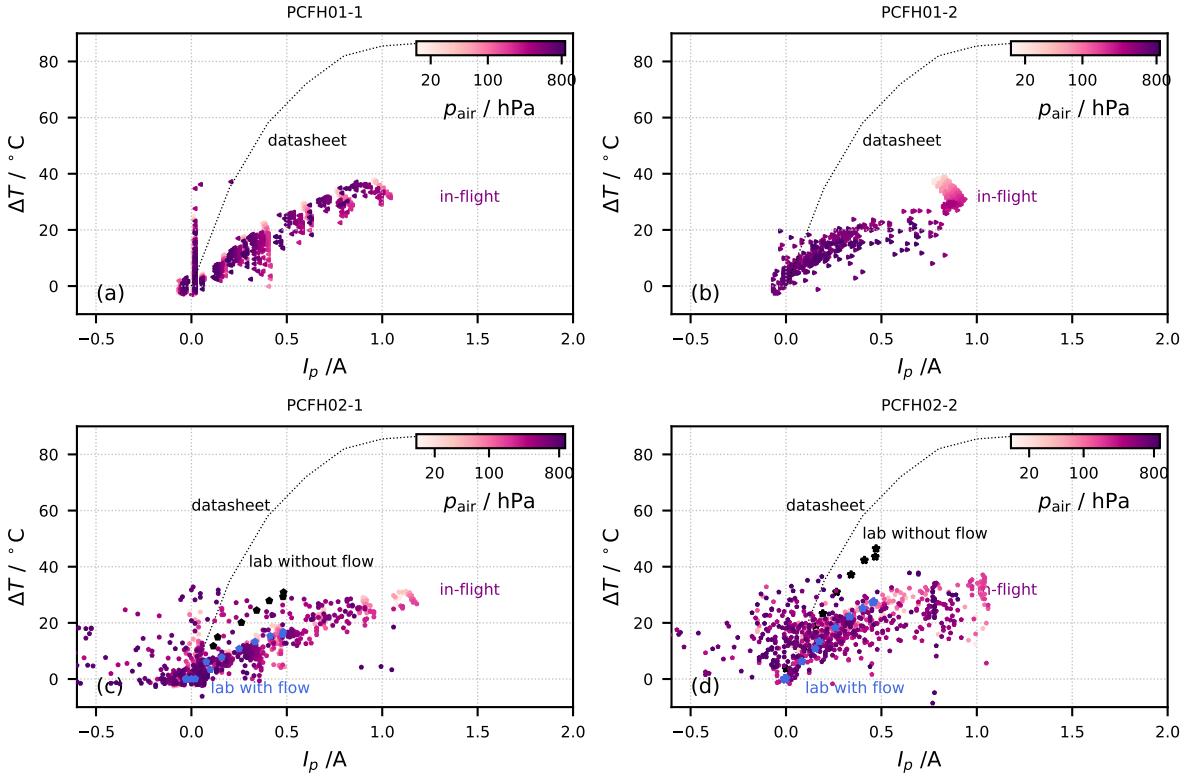

Figure 5.14: PCFH01 and PCFH02, SU 1 and 2, PE characteristics (ΔT vs I_P). (a) PCFH01-1, black dashed: ΔT vs I_P according to the datasheet, colourful dots: ΔT vs I_P in flight color coded with air pressure (p_{air}); (b) same as (a) for PCFH01-2 (c) PCFH02-1, black dashed: ΔT vs I_P according to the datasheet, black dots: ΔT vs I_P from lab tests without flow, blue dots: ΔT vs I_P from lab tests with ~ 5 m s^{-1} air flow, colourful dots: ΔT vs I_P in flight color coded with air pressure (p_{air}); (d) same as (c) for PCFH02-2.

From Figure 5.14, we can observe how the same PEs can have very different characteristic curves. As we saw in Figure 3.4 the PE characteristics (ΔT vs I_P) is influenced by the transferred heat from the cold side of the PE ($\dot{Q}_c$ - Figure 3.2 and 3.4) and the internal temperature of the PE. An increasing $\dot{Q}_c$ will decrease ΔT for the same I_P. A decreasing T_P will also decrease ΔT for the same I_P.

By comparing the datasheet with the laboratory test without flow, we can identify the influence the PE assembly into the PCFH has on the PE characteristic curve. The ambient conditions of these two curves are approximately the same, ground conditions at 25 °C and 1000 hPa. Therefore, the shift of the ΔT vs I_P curve must be due to the heat load $\dot{Q}_c$. In the cold side heat balance equation (Eq.

4.77), we account for this heat as $\dot{Q}_{mb}$ which is driven by $\Delta T = T_{\text{hot}} - T_{\text{mirror}}$ as in Eq. 4.75.

Looking at Panels (c) and (d) of Figure 5.14, we can see how different this influence can be for two PEs, both double stage, supposedly assembled in the same way. $\dot{Q}_{mb}$ seems to be much smaller for PCFH02-2 than for PCFH02-1. In Figure 5.15a, we see the $\dot{Q}_{mb}$ effect in the single stage PE; the loss of ΔT from the datasheet curve to the lab without flow is much smaller than for the double stage PE. Unfortunately ΔT was already smaller for single stage PE. In Figure 5.15d, we see again the $\dot{Q}_{mb}$ effect in the double stage PE. For PCFH05-2 and PCFH06-2 we had the 'open' multiblock design which we expected to cause smaller $\dot{Q}_{mb}$. This was the case for PCFH05-2, not so much for PCFH06-2.

Looking at the laboratory curves with and without flow, we can see the influence of air flow of about 5 m s^{-1} on the PCFH system, which is more or less what happens when the instrument is rising on a balloon. The heat load on the cold side increases and the ΔT vs I_P curve is again shifted towards smaller ΔT's. In the cold side heat balance equation (Eq. 4.77), we account for this heat as $\dot{Q}_{air}$ which is driven by $\Delta T = T_{\text{mirror}} - T_{\text{air}}$ (Eq. 4.74). As the temperature difference between the mirror and ambient air increases so will $\dot{Q}_{air}$, which adds to the heat load on the mirror, decreasing ΔT between mirror and hot side (Eq. 5.4).

In Figures 5.14 and 5.15, we can see the effect of the flow decreasing ΔT in all PE PCFH implementations. However, the magnitude of the effect varies. As expected, the difference caused by the flow is less significant for the single stage PE due to their stiffness in comparison with the double stage PE. However, it also appears that implementations less affected by $\dot{Q}_{mb}$ are also less affected by $\dot{Q}_{air}$.

The analysis of the PE characteristic curves becomes less straightforward for in-flight measurements, as concurring effects start occurring. $\dot{Q}_{mb}$ stays constant through the entire flight, since it is a characteristic of the assembly. However, $\dot{Q}_{air}$ is based of convective heat transfer from the mirror into the surrounding air. The convective heat transfer coefficient of the air inside the intake tube changes from about 20 W K^{-1} m^{-2} at the ground to less than 5 W K^{-1} m^{-2} in the stratosphere (Section 4.3.3). In the troposphere, the ascent speed also influences the convective heat transfer coefficient. A change in the ascent speed from 6 m s^{-1} to 3 m s^{-1}, can cause a decrease of the convective heat transfer coefficient by a factor of 2. Theoretically, for a $\Delta T = T_{\text{mirror}} - T_{\text{air}}$ of 40 °C on the ground, we can expect $\dot{Q}_{\text{air}_{\text{max}}} = 0.01$ W and in the stratosphere $\dot{Q}_{\text{air}_{\text{max}}} = 25$ mW.

A decrease of $\dot{Q}_{air}$ with height would mean an increase of ΔT for the PE with height. However, as the balloon rises in the troposphere, the air temperature decreases, as does the Peltier internal temperature (T_P), which lowers ΔT of the PE. In the mid latitude lower stratosphere cases seen here, the temperature increase is not very large. The Peltier element flight characteristics indicate that the two concurring effects of $\dot{Q}_{air}$ and T_P cancel each other, and the characteristic curve is unchanged during the entire flight.

A third factor is the PE power supply. To analyse this effect we can look at Figure **??** and compare the implementations of a single and double stage PE with the electronics version 1 for PCFH05 in Panels (c) and (d) and the implementation of a single and double stage PE with electronic version 2 for PCFH06 in Panels (e) and (f). The power supplies of the two electronic versions were different. On version 1 the power supply is shared with the thermocouple board and limited to 3.3 V (Figure 5.3).

The ΔT of the characteristic curve for PCFH02-1 decreases with decreasing T_P and decreasing p_{air} (Figure 5.14c). I_P is not constant throughout the flight, although the PWM commands are. I_P seems to increase with decreasing T_P up to the 50 hPa-level. At pressures lower than 50 hPa, it decreases

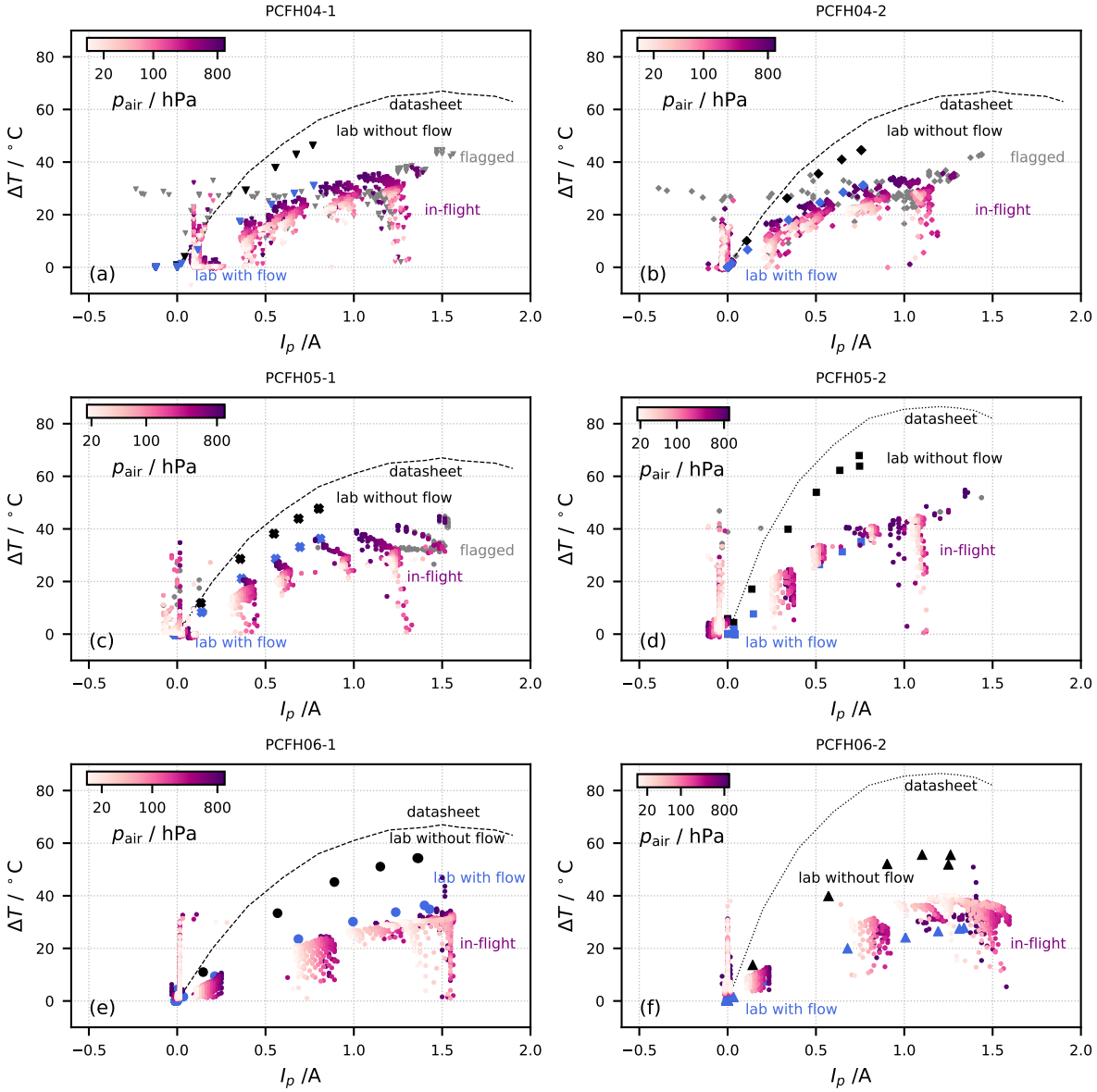

Figure 5.15: PCFH04, PCFH05 and PCFH06, SU 1 and 2, PE characteristics (ΔT vs I_P). (a) PCFH04-1, black dashed: ΔT vs I_P according to the datasheet, black dots: ΔT vs I_P from lab tests without flow, blue dots: ΔT vs I_P from lab tests with ~ 5 m s^{-1} air flow, colourful dots: ΔT vs I_P in flight color coded with air pressure (p_{air}); (b) same for PCFH04-2; (c) same for PCFH05-1; (d) same for PCFH05-2; (e) same for PCFH06-1; and (f) same for PCFH06-2.

with decreasing p_{air} and increasing T_P. The main driver of I_P is possibly the supply voltage, but since this value is only transmitted every 5 s and changes with PWM step, the data is difficult to interpret.

PCFH02-2 (Figure 5.14d) had a promising characteristic curve with low ΔT loss after assembly and a ΔT at high p_{air} of about 40 °C. Unfortunately, something happened in the optical path. Since the PID controller was active, only low I_P and low ΔT was recorded at low p_{air} and cold T_P. Only a small range I_Ps was explored, so the PE was not well characterized.

The characteristic curve of PCFH05-1 (Figure 5.15c) is the clearest example of changing PE characteristic with T_P or p_{air}. I_P clearly increases for each PWM step with decreasing T_P and decreasing p_{air}. However, ΔT decreases with decreasing T_P in spite of the I_P increase. The PE of PCFH05-1 is a single stage which is less influenced by $\dot{Q}_c$, so maybe T_P has a stronger effect in single stage PE's. An increasing I_P should be related to an increasing power of the power supply, which was not observed in any of the flights. The laboratory observations with flow agree with the in-flight observations at ground pressure-level. The characteristic of PCFH05-1 is similar to the characteristic curves of PCFH04-1 and 04-2, also fitted with single stage PEs.

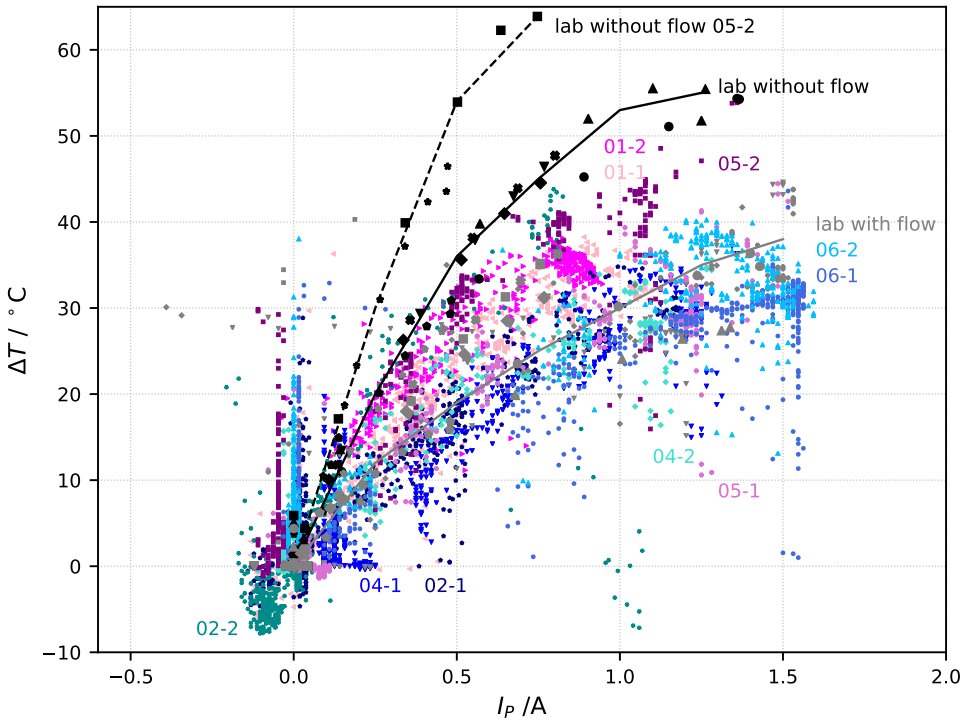

Figure 5.16: PE characteristics (ΔT vs I_P) all lab tests and flights ascent; dashed black: in the lab without flow for PCFH05-2, black: 'average' for all instruments, except PCFH02-2 and PCFH05-2, in the lab without flow, grey: 'average' in the lab with $\sim$ 5 m s^{-1} air flow, all the other colors: in-flight data, light pink: PCFH01-1, fuchsia: PCFH01-2, navy: PCFH02-1, darkcyan: PCFH02-2, blue: PCFH04-1, turquoise: PCFH04-2, pink: PCFH05-1, purple: PCFH05-2, royal blue: PCFH06-1, deep sky blue: PCFH06-2.

On the other hand, the characteristic of PCFH06-1, also with a single stage PE (Figure 5.15e), looks very different. In this implementation of the PCFH there seems to be no effect of T_P nor p_{air} on the PE characteristic curve, only of the I_P. This time a more understandable effect, a decrease of I_P

as the flight progresses although the PCFH06 implementation is with electronics version 2. However, for each PWM step or I_P, there seems to be a bigger variety of ΔT's for the same T_P and same p_{air}. This could be an indication of a slower equilibration time of the mirror temperature.

PCFH05-2 (Figure 5.15d) shows the best characteristic of all the PCFH implementations. PCFH05-2 reached the highest ΔT observed in flight for all the PCFHs, independent of flagged measurements, more than 50 °C at surface conditions and 40 °C at stratospheric conditions. This is also the sub-unit that reached temperatures in the range of the frost point temperature up to the 40 hPa-level.

For PCFH06-2 (Figure 5.15f) I_Ps beyond $I_{P_{\max}}$ show decreasing ΔT's with increasing I_P. As for PCFH06-1, I_P for the same PWM step also decreases with decreasing T_P, p_{air} or flight duration. The slower equilibration times observed for 06-1 can also be seen here. Although 06-2 is also a double stage PE as is 05-2, in a new version multiblock, its performance is not as good.

Figure 5.16 summarizes all characteristic curves for all flown PCFHs plus laboratory tests with and without flow. In this figure, PCFH05-2 (the 'successful' PCFH flight) stands out not just in flight, but also in the lab test without flow. This is a very promising result, because we will be able to evaluate a good PCFH assembly in the lab.

5.9.2 Hot side temperature

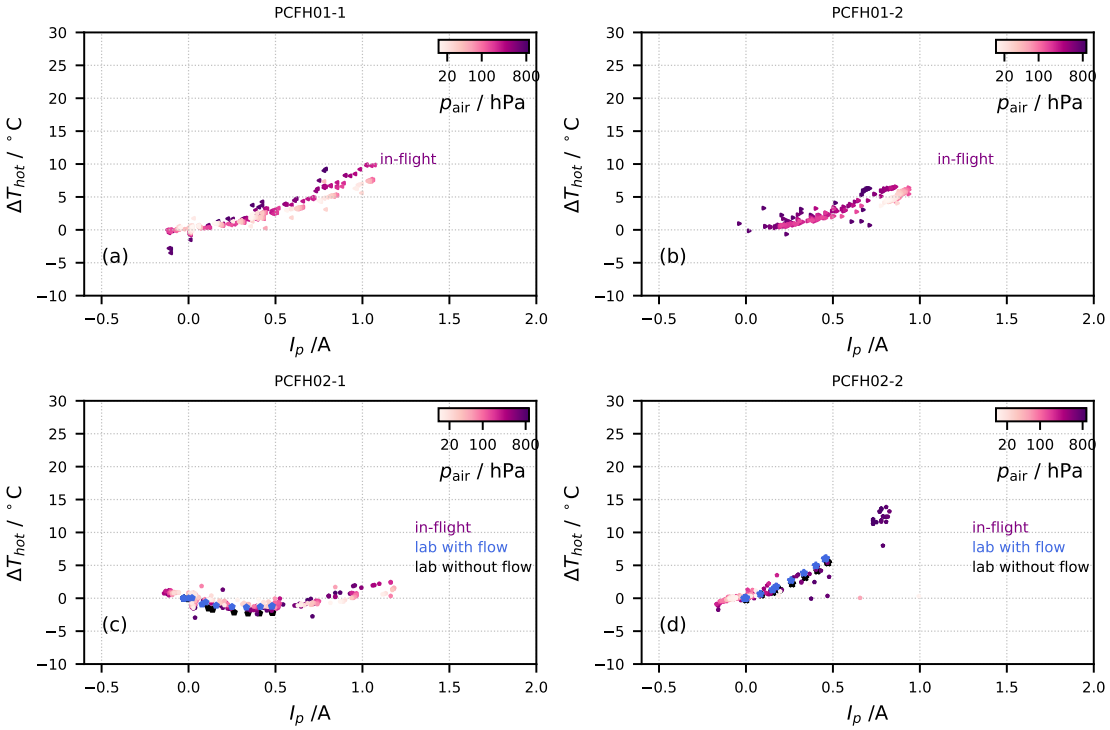

Figure 5.17: PCFH01 and 02, SU 1 and 2, hot side characteristics. (a) PCFH01-1, colourful dots: ΔT_{hot} vs I_P in flight color coded with air pressure (p_{air}); (b) same for PCFH01-2; (c) PCFH02-1, black dots: temperature difference between Peltier hot side and heat sink vs Peltier element current (ΔT_{hot} vs I_P) from lab tests without flow, blue dots: ΔT_{hot} vs I_P from lab tests with ~ 5 m s^{-1} air flow, colourful dots: ΔT_{hot} vs I_P in flight color coded with air pressure (p_{air}); (d) same for PCFH02-2.

In Figures 5.17 and 5.18, we show the temperature difference between hot side and heat sink, defined as ΔT_{hot} according to

$$\Delta T_{\text{hot}} = T_{\text{hot}} - T_{\text{sink}} \tag{5.5}$$

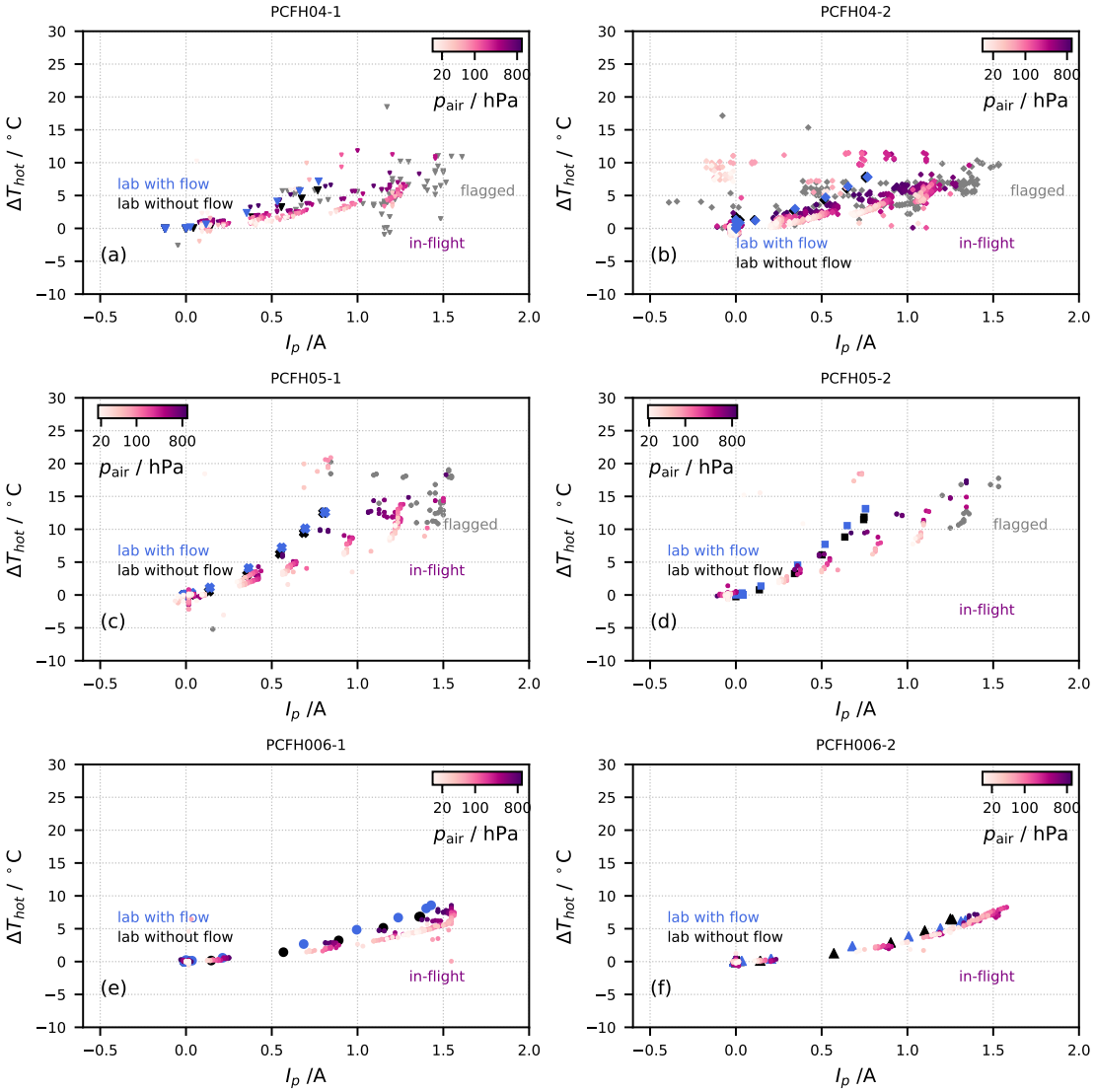

Figure 5.18: PCFH04, 05 and 06, SU 1 and 2, hot side characteristics. (a) PCFH04-1, black dots: temperature difference between Peltier hot side and heat sink vs Peltier element current (ΔT_{hot} vs I_P) from lab tests without flow, blue dots: ΔT_{hot} vs I_P from lab tests with ~ 5 m s^{-1} air flow, colourful dots: ΔT_{hot} vs I_P in flight color coded with air pressure (p_{air}); (b) same for PCFH04-2; (c) same for PCFH05-1, small grey dots: flagged data; (d) same for PCFH05-2 also with flagged data; (e) same for PCFH06-1; (f) same for PCFH06-2.

as function of I_P. We chose a color code with p_{air} for the in-flight observations because it allows a clearer interpretation. Figures 5.17 shows ΔT_{hot} vs I_P characteristics of PCFH01 and PCFH02, SU 1 and 2. Figures 5.18 shows ΔT_{hot} vs I_P characteristics of PCFH04, 05 and 06, SU 1 and 2.

Except for PCFH04 and 05, the other PCFH's shown in Figures 5.17 and 5.18 seem to have a

pretty unchanged ΔT_{hot} vs I_P characteristic in the lab with or without flow and in-flight with duration of flight, T_P, or p_{air}. For PCFH05-1 and 05-2, ΔT_{hot} appears to decrease with flight duration, T_P, or p_{air} decrease. In the lab with or without flow and at $p_{\text{air}} \sim 800$ hPa, ΔT_{hot} as high as 20 °C is reached for high I_P. This means 20 °C of cooling are lost on top of the already 5 °C warmer heat sink and the 40 to 50 °C ΔT the PE is able to provide. Nevertheless, PCFH05-2 reached the coldest mirror temperatures in the stratosphere, possibly because the ΔT_{sink} of the heat sink was smaller than 15 °C, and for the PCFH06 it was larger. The reduction of ΔT_{hot} is a crucial step towards the improvement of the PCFH cooling range as well as efficient cooling of the heat sink.

PCFH02-2, 06-1, and 06-2 do not reach as high ΔT_{hot} during flight as PCFH 05-1 and 05-2, but their ΔT_{hot} for high I_P's are still in the range of 10 °C to 15 °C, which is still undesirable for an instrument as the PCFH relying only on air cooling.

PCFH02-1 (Figure 5.17c) shows $\Delta T_{\text{hot}} < 0$ °C for some currents. We believe this T_{hot} measurement in PCFH02-1 to be incorrect. For PCFH02-1 ΔT_{max} is < 35 °C, which is the smallest for any of the double stage PE implementations. We believe this to be due to T_{hot} not measuring the real T_{hot}, but a lower temperature, hence $\Delta T_{\text{hot}} < 0$ for some I_P's. Though unrealistic, $\Delta T_{\text{hot}} = 0$ °C would be the ideal behaviour. $\Delta T_{\text{hot}} < 3$ °C for $I_{P_{\text{max}}}$ would be a realistic design target.

For the improvement of ΔT_{hot}, we have increased the diameter of the copper finger on both ends. The largest improvement might come from a reduction of the glue thickness to the minimum necessary which implies the repositioning of the T_{hot} thermocouple, which might change the accuracy of the measurement and reduce our knowledge of T_P. However, if the thermal resistance of this connection is well characterized we might not need any information about T_{hot}, as we can model it from T_{sink}.

5.10 Reflectance

Figure 5.19 shows the mirror and reference surface reflectance (R_{mirror} and R_{refsurf}) for the ascent of PCFH02-2 in Panel (a) and the descent in Panel (b). The reflectance is shown as a percentage of the Full Scale (FS) value measured before flight Panel (c) and (d) of Figure 5.19 shows the ratio of the mirror and reference surface reflectance ($R_{\text{mirror}}/R_{\text{refsurf}}$) for ascent and descent respectively. This sub-unit was running the alternating set-point PID.

Figure 5.11d shows T_{mirror}, T_{frost}, T_{air}, and T_{hot} for the ascent of PCFH02-2. From 400 hPa upwards the alternating set-point PID controller lost track of the ice layer and instead of cooling was warming the PE: $T_{\text{mirror}} > T_{\text{air}}$. We hypothesized that something happened with the optical path. Figure 5.19a shows how R_{mirror} and $R_{\text{ref surf}}$ changed, causing the ratio of the two to fluctuate and be smaller than the defined controller set-point. The controller reacted by warming the PE to sublimate a 'non-existing' ice layer to re-establish the controller set-point. Fortunately, the optics recovered on descent as can be seen in Panel (b) and (d) of Figure 5.19, and from 200 hPa downwards, T_{mirror} is kept near T_{frost}.

In this section we will only work with data from PCFH02-2. It was the most relevant flight for the analysis of the reflectance, because it was controlled using the alternating set-point PID controller, which was able to keep the mirror temperature (T_{mirror}) for some parts of the ascent and descent in the troposphere within a few degrees of the frost point temperature (T_{frost}) measured by the CFH. The proximity and oscillation of T_{mirror} around T_{frost} allows us to analyses the change in reflectance of the frost/dew layer as it grows and/or sublimates/evaporates. Furthermore, the CFH and PCFH were on

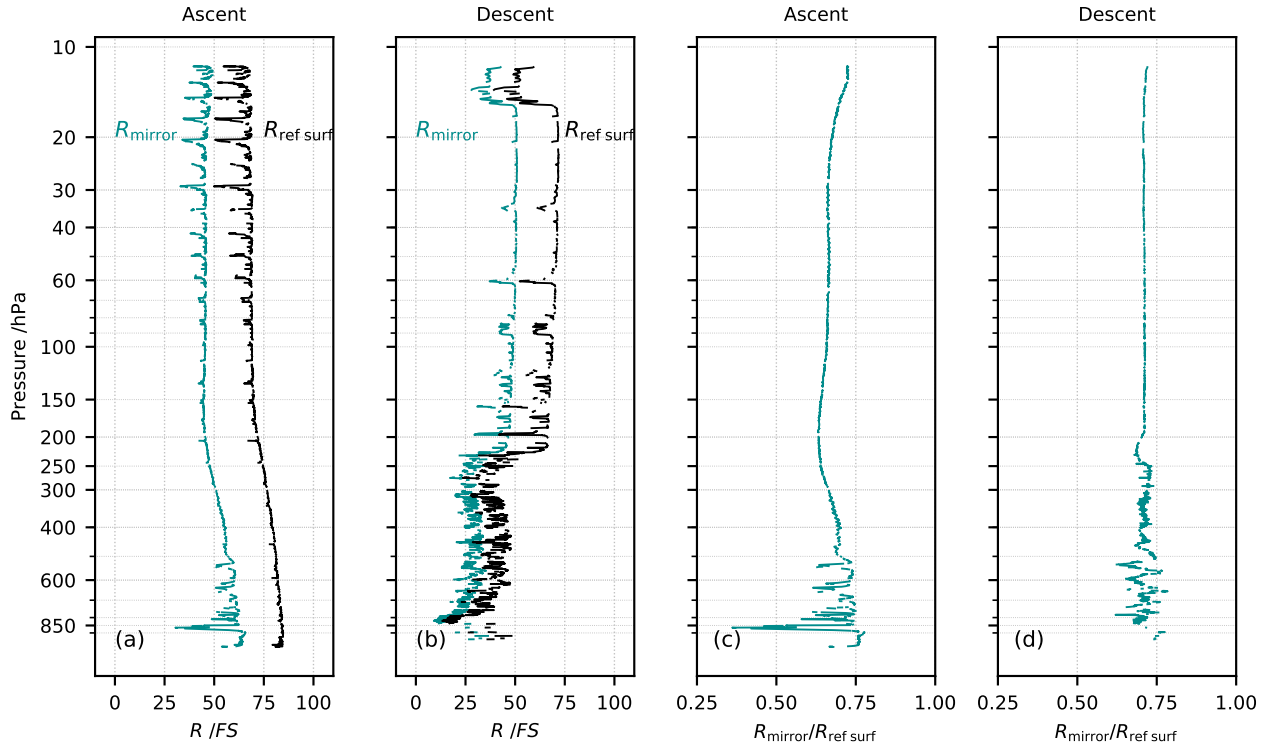

Figure 5.19: PCFH02-2 reflectance. (a) dark cyan: mirror reflectance (R_{mirror}), black: reference surface reflectance ($R_{\text{ref surf}}$), both for ascent; (b) same as (a) for descent; (c) darkcyan: ratio of mirror and reference surface reflectance ($R_{\text{mirror}}/R_{\text{ref surf}}$) for ascent, (d) same as (c) for descent.

the same payload and transmitted their telemetry through the same radiosonde. Therefore, we can do a time analysis and time derivatives of the reflectance ($d(R_{\text{mirror}}/R_{\text{ref surf}})/dt$) and direct comparisons with $T_{\text{frost}} - T_{\text{mirror}}$.

In Figures 5.20 and 5.21, we show the process towards the description of the ice layer reflectance in the PCFH Model (Eq. 4.89). Figure 5.20 shows the ascent from 700 hPa to 525 hPa and Figure 5.21 the descent from 400 hPa to 600 hPa. Both figures are set-up in a similar way. In Panels (a) we show the T_{air} from the RS41, T_{frost} and T_{mirror} for the selected stretch of the flight. In Panels (b) we show the time series of $R_{\text{mirror}}/R_{\text{ref surf}}$ and $T_{\text{mirror}} - T_{\text{frost}}$ in the selected intervals. The curves have been smoothed with a running average of ± 3 kernel. When $R_{\text{mirror}}/R_{\text{ref surf}}$ decreases, less light is being reflected from the mirror and condensate layer – dew or frost – is building up. When $R_{\text{mirror}}/R_{\text{ref surf}}$ increases, the reflected light increases, deposit is evaporating/sublimating from the mirror. $T_{\text{mirror}} - T_{\text{frost}} = 0$ is marked with a solid horizontal black line. Above this line the mirror temperature is higher than the frost point temperature, the deposit evaporates/sublimates from the mirror or the mirror is clean. Below the $T_{\text{mirror}} - T_{\text{frost}} = 0$ line, the mirror is colder than the frost point temperature, the deposited layer – dew or ice – grows. Panels (c) share the y axis $R_{\text{mirror}}/R_{\text{ref surf}}$ with Panel (b) but we replace the time coordinate by $T_{\text{mirror}} - T_{\text{frost}}$. The dashed horizontal line marks the $(R_{\text{mirror}}/R_{\text{ref surf}})_{\text{max}}$ for this interval. The black vertical dashed line marks $T_{\text{mirror}} - T_{\text{frost}} = 0$. In Panels (d) and (e) we replace the reflectance ratio ($R_{\text{mirror}}/R_{\text{ref surf}}$) by the change of reflectance ratio with time ($d(R_{\text{mir}}/R_{\text{ref}})/dt$)

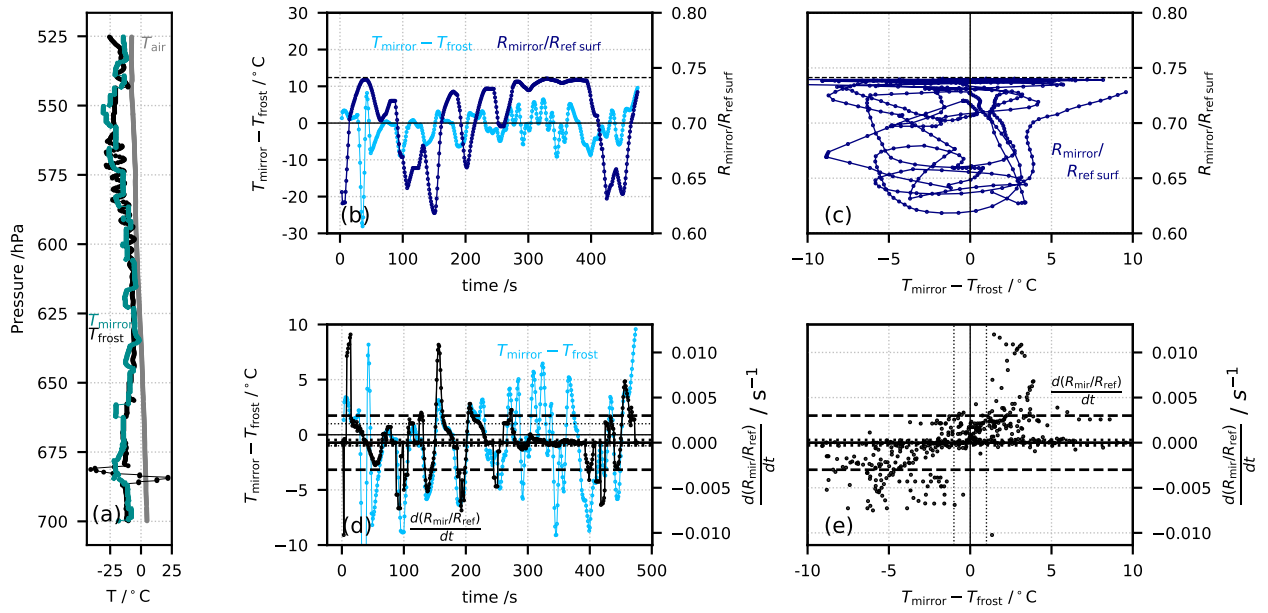

Figure 5.20: Reflectance grey model analysis ascent. (a) Grey: RS41 air temperature (T_{air}), black: CFH frost point temperature (T_{frost}), darkcyan: PCFH02-2 mirror temperature (T_{mirror}); (b) deep sky blue: temperature difference between mirror temperature and frost point temperature ($T_{\text{mirror}} - T_{\text{frost}}$), navy: ratio of the mirror and reference surface reflectance ($R_{\text{mirror}}/R_{\text{ref surf}}$); (c) navy: $R_{\text{mirror}}/R_{\text{ref surf}}$ vs $T_{\text{mirror}} - T_{\text{frost}}$; (d) deep sky blue: $T_{\text{mirror}} - T_{\text{frost}}$, black: time derivative of the ratio of the mirror and reference surface reflectance ($d(R_{\text{mir}}/R_{\text{ref}})/dt$); (e) black: $d(R_{\text{mir}}/R_{\text{ref}})/dt$ vs $T_{\text{mirror}} - T_{\text{frost}}$.

calculated as

$$\left.\frac{dR_{\text{mir}}/R_{\text{ref}}}{dt}\right|_i = \frac{(R_{\text{mir}}/R_{\text{ref}})_{i+1} - (R_{\text{mir}}/R_{\text{ref}})_i}{\Delta t},\ \Delta t = 1s \tag{5.6}$$

$d(R_{\text{mir}}/R_{\text{ref}})/dt$ is calculated from the smoothed curve of $R_{\text{mirror}}/R_{\text{ref surf}}$. In Panel (d), we see $d(R_{\text{mir}}/R_{\text{ref}})/dt$ as a time series together with $T_{\text{mirror}} - T_{\text{frost}}$. The agreement between the peaks of $T_{\text{mirror}} - T_{\text{frost}}$ and $d(R_{\text{mir}}/R_{\text{ref}})/dt$ in Figures 5.20d and 5.21d is remarkable. The only exception is the stretch in the ascent between 600 hPa and 580 hPa, which in the time series translates to the interval between 250 s and 400 s. In this interval, we see oscillations in $T_{\text{mirror}} - T_{\text{frost}}$ but neither in $R_{\text{mirror}}/R_{\text{ref surf}}$ nor in $d(R_{\text{mir}}/R_{\text{ref}})/dt$. We believe in this interval we see CFH controller oscillations, not a real frost point oscillation. The relative humidity measurement of RS41 confirms this assumption. The remarkable agreement of the peaks of $d(R_{\text{mir}}/R_{\text{ref}})/dt$ and $T_{\text{mirror}} - T_{\text{frost}}$ in Figures 5.20d and 5.21d, translates to an almost linear relation in Panels (e) of the respective figures where we see $d(R_{\text{mir}}/R_{\text{ref}})/dt$ vs $T_{\text{mirror}} - T_{\text{frost}}$.

Using the reflectance equation of PCFH Model (Eq. 4.89), we can estimate parameter B for the two stretches in Figures 5.20 and 5.21, the results are in Table 5.12. The results differ by a factor of 2, but we can estimate an order of magnitude for the relation.

$$\frac{dR}{dt} = -A\,\dot{m} = -B\,(T_{\text{frost}})\ (\ T_{\text{frost}} - T_C)\,,\ T_C = T_{\text{mirror}}$$

This is a preliminary results based on very few data. We expect the water vapour diffusivity the

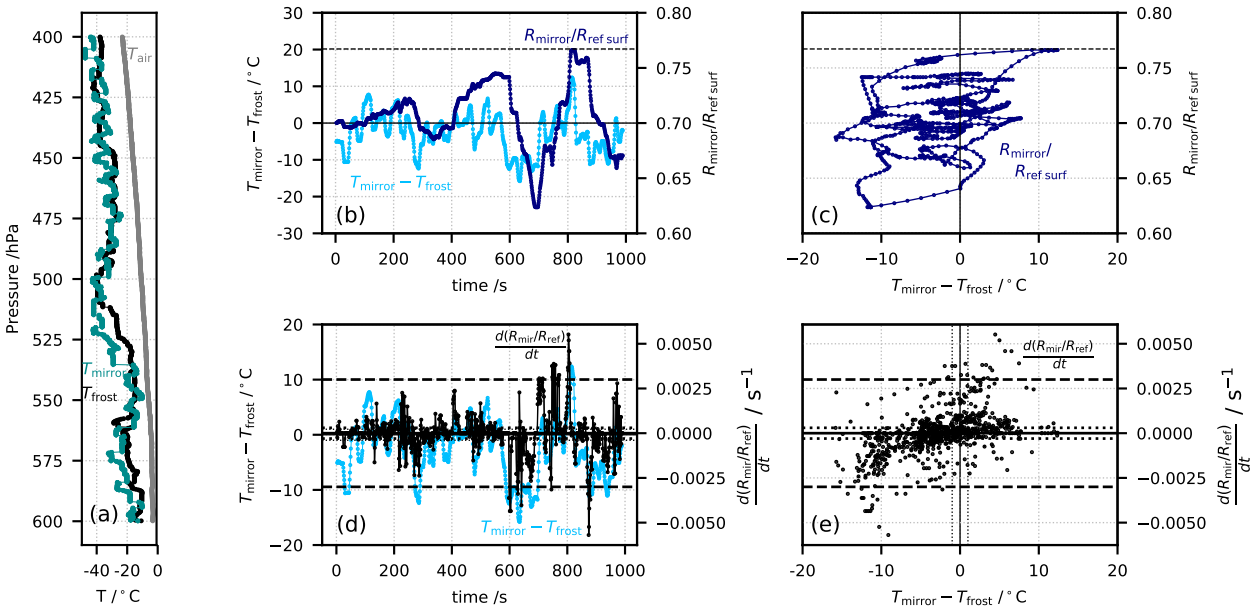

Figure 5.21: Reflectance grey model analysis descent. (a) Grey: RS41 air temperature (T_{air}), black: CFH frost point temperature (T_{frost}), darkcyan: PCFH02-2 mirror temperature (T_{mirror}); (b) deep sky blue: temperature difference between mirror temperature and frost point temperature ($T_{\mathrm{mirror}} - T_{\mathrm{frost}}$), navy: ratio of the mirror and reference surface reflectance ($R_{\mathrm{mirror}}/R_{\mathrm{ref\ surf}}$); (c) navy: $R_{\mathrm{mirror}}/R_{\mathrm{ref\ surf}}$ vs $T_{\mathrm{mirror}} - T_{\mathrm{frost}}$; (d) deep sky blue: $T_{\mathrm{mirror}} - T_{\mathrm{frost}}$, black: time derivative of the ratio of the mirror and reference surface reflectance ($d(R_{\mathrm{mir}}/R_{\mathrm{ref}})/dt$); (e) black: $d(R_{\mathrm{mir}}/R_{\mathrm{ref}})/dt$ vs $T_{\mathrm{mirror}} - T_{\mathrm{frost}}$.

parameter B represents to be dependent on the frost point temperature. For a more comprehensive understanding of relation 4.89 we need more data in different tropospheric and stratospheric conditions, different water vapour abundances, different set points and more. From a similar analysis of other flight stretches without ice deposit change, we were able to estimate the reflectance variability to be about 0.3 % of the FS reflectance.

Table 5.12: Parameter B from reflectance equation of PCFH Model estimated from selected flight stretches

	Fig.5.20	Fig. 5.21
B	6.0×10^{-4} K^{-1}	2.5×10^{-4} K^{-1}

5.11 Conclusion

The PCFH was not yet flown as frost point hygrometer and it is not yet capable of measuring the frost point temperature. However, there were many things we learnt from flying these instruments. The main take home message after the first PCFH campaigns are:

- **Peltier element**: We obtained ΔT for the double stage PE of 40 °C in the stratosphere, which is higher than for any PE frost point hygrometer implementation so far. However, high ΔT

losses betwen the hot side, heat sink, and ambient air limit reaching stratospheric T_{frost}, except in the case of PCFH02-2. We have decided to continue the PCFH design with a double stage PE. We have a good understanding of the ΔT losses due to assembly ($\dot{Q}_{mb}$), which can be reduced. ΔT losses due to flow ($\dot{Q}_{air}$) are unavoidable but decrease at higher altitudes in the atmosphere. However, the improved performance due to smaller air flow heat load at greater heights is compensated by the colder operating temperature of the Peltier element (T_P). These compensating effects of $\dot{Q}_{air}$ and T_P could be beneficial for the modelling goals of this project, but further investigation is necessary.

- **Thermal management**: The housing needs better thermal insulation. The thermal resistance between the hot side of the PE and the HS needs to be reduced, so smaller ΔT_{hot}'s are attainable. There are still questions regarding the most desirable thermal behaviour for the HS and hence T_{sink}: What is more relevant for the PCFH operation and thermal balance, using a light HS that equilibrates faster with ambient air and makes the instrument lighter or a heavier HS, which provides colder temperatures than air on ascent in the stratosphere and on descent in the troposphere? The PID controller of $T_{\text{ref surf}}$ works, but $T_{\text{air}}^{\text{PCFH}}$ needs to be more accurate and less noisy. Improving the $T_{\text{air}}^{\text{PCFH}}$ construction and placement outside of the housing might address these issues.
- **Model Validation**: We will address the PCFH model optimization and validation in Chapter 6.
- **Water vapour diffusivity**: We have a method to determine the relation between $T_{\text{mirror}} - T_{\text{frost}}$ and $d(R_{\text{mir}}/R_{\text{ref}})/dt$, now more experiments and data are needed. This parameter is part of the mirror reflectivity grey model. It closes the model and will allow us to use optimal control.
- **Power supply**: There were clear improvements in the implementation of the electronics version 2 with the separated power supplies. There was no more interruption of operation of the thermocouple module board during flight. However, we need a proper characterization of I_P vs PWM including the power supply drainage during flight.
- **PCFH internal systems**: The calibration range for the reference thermometer of the thermocouple module board as been extended down to -20 °C. Yet, the PCFH needs better thermal insulation or a dedicated internal heating. So far, the PCFH has flown in moderate conditions; in the tropics or in winter polar regions ambient temperatures may be much colder.
- **Telemetry**: The PCFH can successfully fly as an RS41 add-on instrument. We identified a telemetry package conflict, which was overloading the RS41 when the instrument identification package was sent simultaneously with the other three regular telemetry packages. The telemetry scheduling has been altered, so the instrument identification package is only sent when the regular 5 s package is not sent.
- **Recovery**: The five deployed instruments were successfully recovered by the DWD team. We did not launch any PCFH from Zürich, so we had no chance to test the recovery on our own.
- **Robustness**: All PCFH systems were functional after recovery, besides some rough landings in tree tops and lakes. The design of the air thermocouple needs improvement with respect to warm bias during ascent and noise.

Chapter 6

Model optimization and validation

Considering the complexity of the PCFH model, its behaviour, especially of the Peltier element (PE) and the goal of implementing optimal control in the PCFH, we implemented the PCFH model in Simulink (Simulink, 2019). When Simulink and MATLAB are used together they combine textual and graphical programming. Small MATLAB functions can be used to program Simulink blocks, and Simulink models can be called in MATLAB and combined with MATLAB tool boxes such as the Optimization and Control toolbox (OptimizationToolbox, 2019; ControlToolbox, 2019). The graphical interface allows a better understanding of the model and saves the need for expensive C, C++, or HDL code writing.

We can import real world data into the Simulink program, such as air pressure, air temperature, and frost point temperature in flight, and then evaluate the system response. We can then apply different control functions and schemes to the system and run thousands of simulations without ever launching a balloon. When the systems new dynamics are satisfactory, we can automatically generate C or HDL code, which behaves as the model in Simulink and embed it directly into the FPGA or/and micro controller of the PCFH. Since Simulink is widely used for system modelling and for optimization and controller design, it is easier to get on-line support for the PCFH application.

6.1 Simulink implementation

The PCFH-Model Simulink implementation can be found on-line (Jorge and Cesbron, 2018a). To run the model, we need three files: the Simulink model file (with .slx ending), a MATLAB file to initiate some of the Simulink variables, and a data file from which to import the flight data (an excel file is provided as example). From the data file, we import air pressure (p_{air}), air temperature (T_{air}), thermocouple module reference temperature (T_{ref} - proxy for the instrument temperature), and frost point temperature (T_{frost}); as well as the PCFH's inputs Peltier current (I_P) and RS heater current (I_H). As output of the model, we get the state space variables cold side temperature (T_C), heat sink temperature (T_{HS}), reference surface temperature (T_{RS}), and reflectance (R), and the 'transition state' variable hot side temperature (T_H). The state space variables can be compared to the corresponding measured parameters:T_{mirror}), T_{sink}, $T_{\text{ref surf}}$, $R_{\text{mirror}}/R_{\text{ref surf}}$, and T_{hot}.

The model is implemented in the time domain. The time interval between each of the entries of the imported arrays is 1 s, the data rate of the telemetry. Data gaps have been filled by linear interpolation.

The model runs once for each of the entries and provides outputs every second. The simulation time is faster than the simulated time, a 2-hour flight can be simulated in less than 20 seconds. In the PCFH Model Simulink implementation, we can identify each of the state space derivative equations (Eq.'s: 4.77, 4.79, 4.85 and 4.89) by the integrator block that integrates them into the state space variable. Each of this integrators needs an initial value. which is imported from the flight data.

6.2 Model optimization

Model optimization is a more wholesome concept than fitting a function to data, and was used to adjust proportionality parameters so the model can better describe the observations. The optimization of the PCFH Model was inspired by a MATLAB example to estimate model parameters of an aircraft model (MathWorksDoc, 2019b). For the PCFH example, we divided the initial Simulink model into smaller models and focused on optimizing each of the state space equations separately. The model was divided into reference surface loop, Peltier element loop, heat sink loop and reflectance loop. They were optimized in the referred order because of increasing level of complexity and thermal connections between them.

For each of the loops, we introduced optimization parameters, usually one for each of the relevant heat contributions. To account for system uncertainties, for each parameter we specified a range between 0.1 and 10, which means the heat contributions can be re-scaled up to 10× smaller or 10× bigger than the theoretical prediction. The optimization parameters are introduced for each of the loops below. Once a parameter was optimized, it was used as such in any other occurrence in other loops. The different loops are connected through heat transfer contributions. For continuity purposes they should have one unique value across loops.

Then, we identified the optimization goal: to estimate the state variable of each loop, using the simulink model, as close as possible to what was measured in the flight. All other values were taken from the flight data: uncontrollable inputs such as T_{air}, controllable inputs such as I_H, and even other state variables, which were not the focus of the optimization, for example T_{sink} for the reference surface case.

For the optimization, we took data from the first two PCFH flights: 01 and 02 analysed in Chapter 5. We consider data from the two sub-units of each. We did not do the optimization for the three flights in the winter campaign, because of time constrains. From the flights, we chose periods considered more relevant for the optimization process, usually the tropopause region because the air temperature regime changes from the troposphere to the stratosphere. For the reference surface, a period when the RS heaters are active is a good example of a relevant region.

The algorithm used for the optimization is the nonlinear least-squares solver from MATLAB ('lsqnonlin' (MathWorksDoc, 2019a)). I did not complete the optimization process for the reflectance loop, because there was not enough data (see Section 5.10) .

6.3 Reference surface loop

The files used for the optimization of the reference surface (RS) loop are available on-line (Jorge, 2018c). Equation 6.1, is the state space equation for the reference surface temperature (T_{RS}) (Eq. 4.85) including three optimization parameters G_a, G_b, and G_c.

$$m_{RS}\, c_{p_{RS}}\, \frac{dT_{RS}}{dt} = G_a\, \dot{Q}_{RS-air} + G_b\, \dot{Q}_{J_{RS}} + G_c\, \dot{Q}_{RS-HS} \tag{6.1}$$

$$\begin{aligned} \dot{Q}_{RS-air} &= h_{IT}\, A_{RS}\, (T_{RS} - T_{\text{air}}) \\ \dot{Q}_{J_{RS}} &= R_{RS}\, I_H^2 \\ \dot{Q}_{RS-HS} &= \frac{A_{RS}\, k_{\text{Al 3D}}}{l_{RS}}\, (T_{\text{sink}} - T_{RS}) \end{aligned}$$

$\dot{Q}_{RS-air}$ (Eq. 4.88) represents the heat transferred between the RS and the air flow inside the intake tube. $\dot{Q}_{J_{RS}}$ (Eq. 4.87) is the joule heating generated by the RS heaters. $\dot{Q}_{RS-HS}$ (Eq. 4.80) is the heat transferred between the RS and the heat sink complex (multiblock included). Table 6.1 provides the value of the model constants. The material properties are referenced in Table 3.7.

Table 6.1: Model optimization: reference surface loop constants

m_{RS} (g)	$c_{p_{RS}}$=$c_{p_{\text{Al}}}$ (J g^{-1} K^{-1})	A_{RS} (mm^2)	$k_{\text{Al 3D}}$ (W m^{-1} K^{-1})	l_{RS} (mm)	R_{RS} Ω
1.3	0.91	33.6	180	10	2.5

T_{sink}, T_{air}, and p_{air} are imported from the flight data. h_{IT} is calculated in the model from T_{air} and p_{air} (see Section 4.3.3).

Results

Using data between 150 and 10 hPa of PCFH02-1 on ascent for the optimization, we derived the optimized parameters provided in Table 6.2.

Table 6.2: Model optimization: reference surface loop optimized parameters

G_a	G_b	G_c
0.7	1	0.2611

A value for G_c of less than 1 is an indication of a poor thermal connection between the reference surface and the heat sink. This is less than theoretically expected, but acceptable considering that the theoretical l_{RS} is an under-estimation of the distance between the RS and HS. The connection between the two, using thermal paste, is not ideal and contributes to the thermal resistance.

Using the optimized reference surface loop to the calculate simulated reference surface temperature (T_{RS}), we can compare it to the in-flight measured reference surface temperature ($T_{\text{ref surf}}$) for the ascent of flight PCFH02-1 and the ascent of the other flights of the first campaign PCFH01-1, 01-2 and 02-2.

The results are presented in Figure 6.1. Figure 6.1a shows the measured ($T_{\text{ref surf}}$) and simulated (T_{RS}) reference surface temperature for PCFH01 both sub-units ascent and the air temperature measured by the RS41 (T_{air}). Figure 6.1b shows the same variables but for PCFH02 both sub-units ascent. Figure 6.1c shows the difference between the measured and simulated reference surface temperatures (ΔT_{RS})

$$\Delta T_{RS} = T_{\text{ref surf}} - T_{RS} \tag{6.3}$$

Figure 6.2a and 6.2b shows ΔT_{RS} as histogram format for the stratosphere ($p_{air} < 200$ hPa) and the troposphere ($p_{air} > 200$ hPa). The agreement is very good for more that 90% of the cases: $|\Delta T_{RS}| < 1$ °C. The model over-estimates $T_{\text{ref surf}}$ in the troposphere ($\langle \Delta T_{RS} \rangle < 0$) and under-estimates $T_{\text{ref surf}}$ in the stratosphere ($\langle \Delta T_{RS} \rangle > 0$).

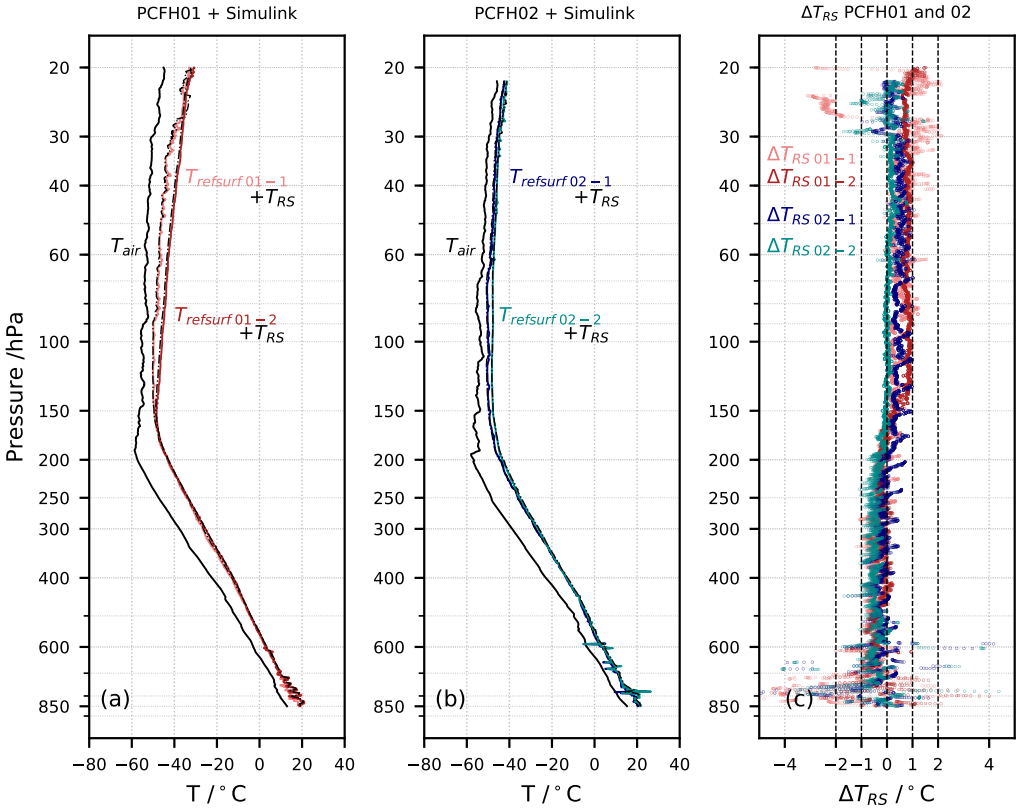

Figure 6.1: Model optimization: reference surface (ascent only). (a) Black: RS41 air temperature (T_{air}), light coral and dashed black: PCFH01-1 measured reference surface temperature ($T_{\text{ref surf}}$) and simulated reference surface temperature (T_{RS}), red and dashed black: PCFH01-2 $T_{\text{ref surf}}$ and T_{RS}; (b) black: RS41 T_{air}, navy + dashed black: PCFH02-1 $T_{\text{ref surf}}$ and T_{RS}, dark cyan + dashed black: PCFH02-2 $T_{\text{ref surf}}$ and T_{RS}; (c) light coral: difference between measured reference surface temperature and simulated reference surface temperature (ΔT_{RS}) for PCFH01-1, red: ΔT_{RS} for PCFH01-2, navy: ΔT_{RS} for PCFH02-1, darkcyan: ΔT_{RS} for PCFH02-2.

The under-estimation of $T_{\text{ref surf}}$ in the stratosphere and over-estimation in the troposphere is most likely related to G_a and $\dot{Q}_{RS-air}$. $\dot{Q}_{RS-air}$ is changing with p_{air} and T_{air} on ascent and we over simplified the optimization process by considering one G_a for the entire profile. The agreement of

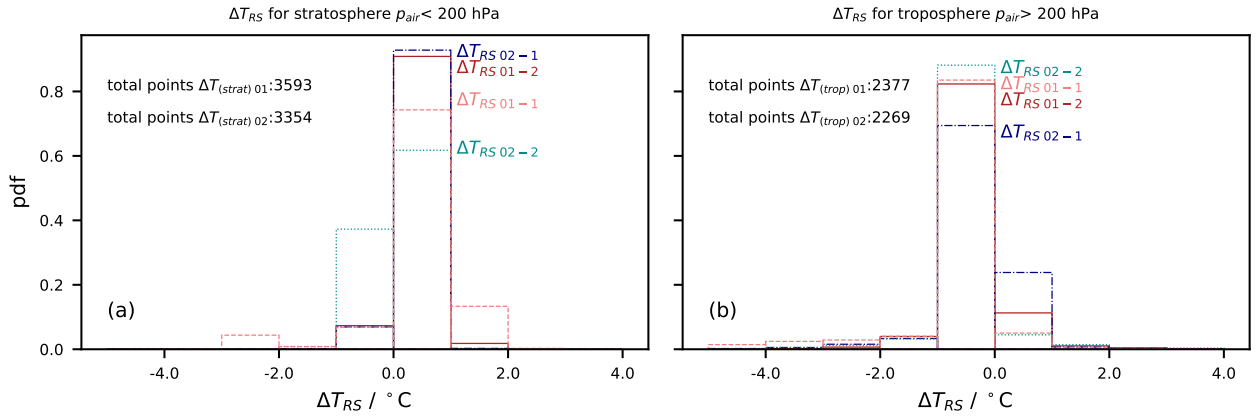

Figure 6.2: Model optimization: reference surface (ascent only) - histogram. (a) Light coral: distribution of PCFH01-1 ΔT_{RS} for the stratosphere ($p_{\text{air}} < 200$ hPa), red: same for PCFH01-2, navy: same for PCFH02-1, darkcyan: same for PCFH02-2; (b) light coral: distribution of PCFH01-1 ΔT_{RS} for the troposphere ($p_{\text{air}} > 200$ hPa, red: same for PCFH01-2, navy: same for PCFH02-1, darkcyan: same for PCFH02-2.

the optimization can possibly be improved by optimizing G_a for the troposphere and stratosphere separately.

6.4 Peltier element loop

Next comes the optimization of the Peltier element loop. The files used for this optimization are available on-line (Jorge, 2018b). Equation 6.4 uses the state space equation for the cold side temperature (Eq. 4.77), including optimization parameter G_a, G_d, G_e, and G_f.

$$m_C \, c_{p_C} \, \frac{dT_C}{dt} = +G_a \, \dot{Q}_{PE-air} + G_d \, \dot{Q}_{\alpha_P} + G_e \, \dot{Q}_{R_P} + G_f \, \dot{Q}_{K_P} \tag{6.4}$$

The Peltier heat contributions ($\dot{Q}_{P_C}$) is explicit. The heat contribution from the PE assembly $\dot{Q}_{mb}$ is included in $\dot{Q}_{K_P}$. $\dot{Q}_{mb}$ and $\dot{Q}_{K_P}$ are driven by the temperature difference between PE cold and hot side. The optimization accounts for both. G_a is the same as for the reference loop optimization, with the value shown in Table 6.2. The new optimization parameters G_d, G_e, and G_f are associated with the PE coefficients α_P, R_P, and K_P respectively. These coefficient are dependent on PE internal temperature (Appendix C.1) as are the optimization parameters (Eq. 6.5).

$$G_d = G_{d\,a} \, T_P + G_{d\,b} \tag{6.5a}$$

$$G_e = G_{e\,a} \, T_P + G_{e\,b} \tag{6.5b}$$

$$G_f = G_{f\,a} \, T_P + G_{f\,b} \tag{6.5c}$$

$\dot{Q}_{PE-air}$ (Eq. 4.74) represents the heat transferred between the mirror and the flow inside the intake tube. $\dot{Q}_{\alpha_P}$ (Eq. 4.71) is the heat removed by the Peltier effect. $\dot{Q}_{R_P}$ (Eq. 4.72) is the joule heating generated by the Peltier current (I_P) in the PE. $\dot{Q}_{K_P}$ (Eq. 4.73) is the hot to cold side heat

transfer through the PE due to the temperature difference of the cold and hot side.

$$\dot{Q}_{PE-air} = A_m \, h_{IT} \; (T_C - T_{\text{air}}) \tag{6.6a}$$

$$\dot{Q}_{\alpha_P} = \alpha_P \, (T_C, T_H) \; T_C \; I_P \tag{6.6b}$$

$$\dot{Q}_{R_P} = \frac{1}{2} \, R_P \, (T_C, T_H) \; I_P^2 \tag{6.6c}$$

$$\dot{Q}_{K_P} = K_P \, (T_C, T_H) \; (T_H - T_C) \tag{6.6d}$$

Since the hot side temperature is strongly dependent on the heat generated by the Peltier element we include the hot side temperature in the Peltier element optimization loop. Equation 6.7 is based on the transition state equation for the PE hot side temperature (Eq. 4.78). The same optimization parameters are used for the different components of the Peltier heat (G_d, G_e and G_f) since they are associated with the PE coefficients. A fourth optimization parameter (G_g) is added the thermal resistance between the PE hot side and the heat sink. We do not explicitly include the thermal resistance of the glue. This can be accounted for by the optimization of G_g.

$$\dot{Q}_{Ph-HS} = -G_d \, \alpha_P \, (T_C, T_H) \; T_H \; I_P + G_e \, \dot{Q}_{R_P} - G_f \, \dot{Q}_{K_P} = \\ = G_g \left(\frac{k_{\text{Cu}} \, A_{PE}}{l_{\text{Cu}}} \right) \; (T_H - T_{\text{sink}}) \tag{6.7}$$

The implementation of Equation 6.7 in the Peltier element loop causes an algebraic loop. Equation 6.7 represents a heat flow, it does not describe a state variable. So, it is not associated with an integrator and it does not have an initial value. To prevent the algebraic loop, we implemented a delay element. The delay element allows T_H to be initialized. After the first iteration of the model, T_H can be calculated on-line in the model. In Table 6.3 I provide the value of the Peltier element loop constants. The material properties are referenced in Table 3.7.

Table 6.3: Model optimization: Peltier element loop constants

m_C (g)	c_{p_C}=$c_{p_{\text{Al}}}$ (J g^{-1} K^{-1})	A_m =A_{PE} (mm^2)	k_{Cu} (W m^{-1} K^{-1})	l_{Cu} (mm)
0.054	0.91	16	380	20

T_{sink}, T_{air}, and p_{air} are imported from the flight data. h_{IT} is calculated in the model from T_{air} and p_{air} (Section 4.3.3). For simplicity, we assume an accent velocity of 5 m s^{-1} instead of taking the measured values in flight. α_P, R_P, and K_P are calculated in the model from T_H and T_C (Appendix C.1).

Results

The Peltier element loop was optimized separately, using the entire ascent of flight PCFH01 sub-unit 1 (PCFH01-1) and using the ascent of flight PCFH02 sub-unit 1 (PCFH02-1). The resulting optimized parameters are provided in Table 6.4.

Most of the optimized parameters shown in Table 6.4 show similar values between the two optimizations as is the case of G_d. The optimized values G_d are in the range 0.1 to 0.5, depending on T_P.

Table 6.4: Model optimization: Peltier element optimized parameters

	G_d	G_e	G_f	G_g
PCFH01-1	$(-2.8 \times 10^{-3}\, T_P + 0.97)$	$(-5.0 \times 10^{-4}\, T_P + 0.55)$	$(2.2 \times 10^{-3}\, T_P + 1.00)$	4.89
PCFH02-1	$(-2.9 \times 10^{-3}\, T_P + 0.97)$	$(-15 \times 10^{-4}\, T_P + 0.72)$	$(1.9 \times 10^{-3}\, T_P + 1.14)$	0.22

This means that the Peltier effect is smaller than expected from the datasheet. Although G_e looks different for the two optimizations, it ranges between 0.35 to 0.45 with T_P for both. This optimization result means the Joule heating is over-estimated in the PE datasheet. G_f boosts the effect of the hot side temperature on the PE thermal balance as we expected from the flight analysis in Chapter 5.

The significantly different optimization parameter is G_g, which motivated the second optimization. As we saw in Section 5.9.2, T_{hot} had a very different behaviour for PCFH02-1 than for the other PCFH fligths, as if the thermal resistance between PE hot side and heat sink was much smaller for this instrument. As a result from the optimization G_g is 20× smaller for PCFH02-1 than for PCFH01-1. We preferred the ascent of flight PCFH01-1 for the optimization, because this sub-unit was running the system identification function, which probed a large range of I_Ps and ΔTs, while the other sub-unit had a PID controller.

We then use the PCFH01-1 optimization of the Peltier element loop to calculate simulated cold side and hot side temperature (T_C and T_H) and compare them to the in-flight measured mirror and hot side temperature (T_{mirror} and T_{hot}) for the ascent of flights PCFH01-1, PCFH01-2 and PCFH02-2. We use PCFH02-1 optimization for the simulated vs in-flight comparison of flight PCFH02-1 separately. The results are presented in Figures 6.3 and 6.5 for PCFH01 and PCFH02, respectively.

Figure 6.3a shows the measured mirror (T_{mirror}) and hot side temperature (T_{hot}), and the simulated cold side (T_C) and hot side (T_H) temperature for PCFH01-1, as well as the air temperature (T_{air}) measured by the RS41 and the frost point temperature (T_{frost}) measured by the CFH. Figure 6.3b shows the same variables for PCFH01-2 ascent. Figure 6.3c shows the difference between the measured and simulated cold and hot side temperatures, ΔT_C and ΔT_H, defined as

$$\Delta T_C = T_{\text{mirror}} - T_C \tag{6.8a}$$

$$\Delta T_H = T_{\text{hot}} - T_H \tag{6.8b}$$

Figure 6.4 shows histograms for ΔT_C and ΔT_H for the stratosphere ($p_{\text{air}} < 200$ hPa) and the troposphere ($p_{\text{air}} > 200$ hPa). We can see a slight over-estimation of T_{mirror} in the troposphere ($\langle \Delta T_C \rangle < 0$) for PCFH01-1, to which the parameters were optimized and a slight under-estimation for PCFH01-2 ($\langle \Delta T_C \rangle > 0$). T_{hot} is slightly under-estimated for the two sub-units ($\langle \Delta T_H \rangle > 0$). In the stratosphere, the distribution of $\Delta T_{C\,01-1}$ is well centred around zero. The other variables are slightly under-estimated ($\langle \Delta T \rangle > 0$). The width of the histogram is wider for the troposphere (Fig. 6.4b) than for the stratosphere (Fig. 6.4a) and more or less equivalent for the 4 variables ($\Delta T_{C\,01-1}$, $\Delta T_{C\,01-2}$, $\Delta T_{H\,01-1}$ and $\Delta T_{H\,01-2}$) in each region (stratosphere and troposphere). The width of the histograms for the Peltier loop optimization is also bigger than for the reference loop optimization seen in Figure 6.2. Nevertheless, the agreement for both sub-units is within $|\Delta T_C| < 5$ °C and $|\Delta T_H| < 5$ °C in the

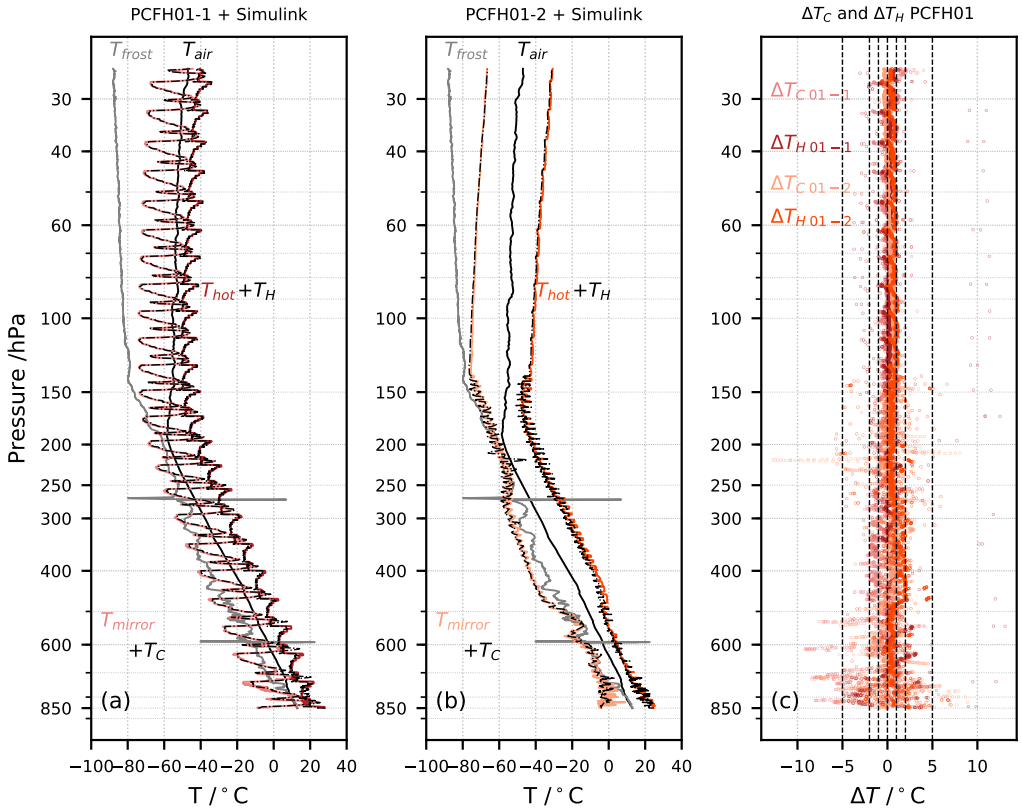

Figure 6.3: Model optimization: mirror and hot side temperature PCFH01 (ascent only). (a) Grey: CFH frost point temperature (T_{frost}), black: RS41 air temperature (T_{air}), light coral and dashed black: PCFH01-1 measured mirror temperature (T_{mirror}) and simulated cold side temperature (T_C), red and dashed black: PCFH01-1 measured hot side temperature (T_{hot}) and simulated hot side temperature (T_H); (b) grey: CFH T_{frost}, black: RS41 T_{air}, light salmon and dashed black: PCFH01-2 T_{mirror} and T_C, orange and dashed black: PCFH01-2 T_{hot} and T_H; (c) light coral: difference between measured mirror temperature and simulated cold side temperature (ΔT_C) for PCFH01-1, red: difference between measured hot side temperature and simulated hot side temperature (ΔT_H) for PCFH01-1, light salmon: ΔT_C for PCFH01-2, orange: ΔT_H for PCFH01-2.

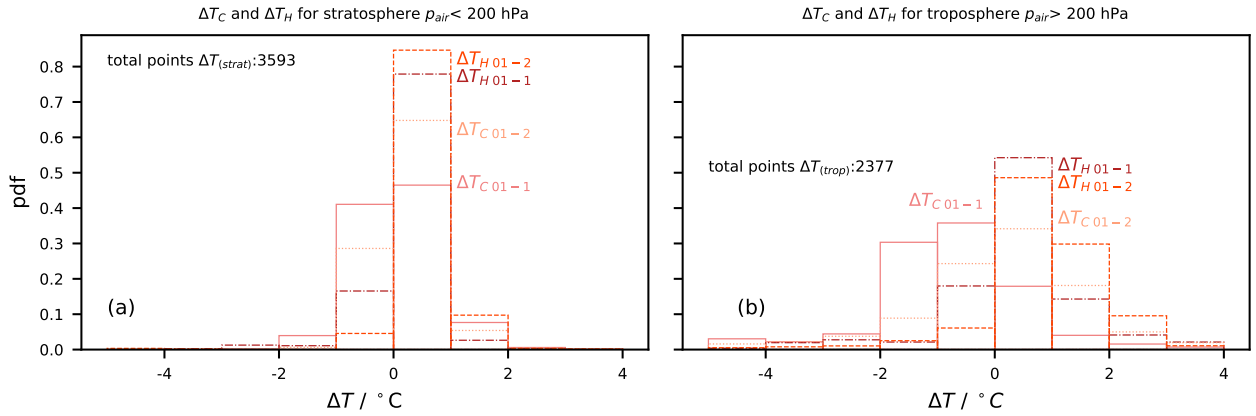

Figure 6.4: Model optimization: mirror and hot side temperature PCFH01 (ascent only) histogram. (a) Light coral: distribution of PCFH01-1 ΔT_C for the stratosphere ($p_{\text{air}} < 200$ hPa), light salmon: same for PCFH01-2, red: distribution of PCFH01-1 ΔT_H for the stratosphere ($p_{\text{air}} < 200$ hPa), orange: same for PCFH01-2; (b) light coral: distribution of PCFH01-1 ΔT_C for the troposphere ($p_{\text{air}} < 200$ hPa), light salmon: same for PCFH01-2, red: distribution of PCFH01-1 ΔT_H for the troposphere ($p_{\text{air}} < 200$ hPa), orange: same for PCFH01-2.

troposphere and $|\Delta T_C| < 2$ °C and $|\Delta T_H| < 2$ °C in the stratosphere, except for a few outliers.

Figure 6.5 and 6.6 show the same variables per panel as Figure 6.3 and 6.4 but for PCFH02. Looking at Figure 6.5c and Figure 6.6, we can say the agreement between simulations and measurements is worse for PCFH02 than for PCFH01. The distribution averages and widths are significantly less homogeneous for PCFH02 than for PCFH01. As we saw in Chapter 5, the operation of the two sub-units was notstandard considering the T_{hot} thermocouple of PCFH02-1 might have been displaced and PCFH02-2 operated mainly in the positive range of I_P, using the PE as a warming device instead of a cooling device.

In the troposphere there is an over-estimation of T_{mirror} ($\langle \Delta T_C \rangle < 0$) for the two sub-units of PCFH02. $|\Delta T_{C\,02-1}|$ can still be constraint within the 5 °C barrier, but $|\Delta T_{C\,02-2}|$ exceeds 10 °C in some cases. $T_{\text{hot}\,02-1}$ is on average over-estimated by 2 °C, which is understandable since we saw $\Delta T_{hot}<0$ (Eq. 5.5) for PCFH02-1 in Section 5.9.2. Our physical model can not replicate this behaviour. $T_{\text{hot}\,02-2}$ is slightly under-estimated ($\langle \Delta T_H \rangle > 0$) and shows the smallest width of the 4 variables observed in Figure 6.6b. The trends of $\Delta T_{C\,02-1}$, $\Delta T_{C\,02-2}$, $\Delta T_{H\,02-1}$, and $\Delta T_{H\,02-2}$ in the stratosphere are similar to those observed in the troposphere; however, their distributions are narrower, but still wider than the equivalent distributions for PCFH01.

The Peltier element state variables (T_C and T_H) behaviour is more challenging to model than the other state variables. The differences may be too big for one standard system description, even considering the usage of a very robust control law. It may be necessary to measure the transfer function for each assembly, for which a lab to flight transition procedure would be needed. More work is necessary to standardize the production of PCFHs, so reproducibility of sub-units is possible, and to develop a lab test that can predict the performance of the sub-units in flight.

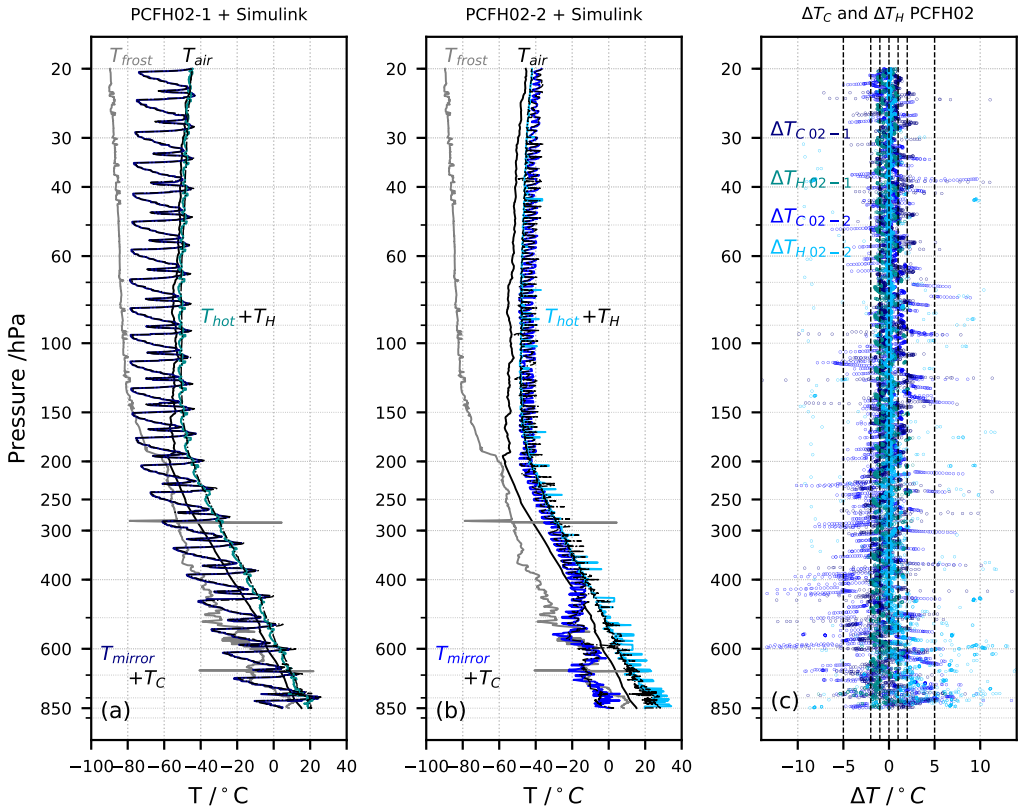

Figure 6.5: Model optimization: mirror and hot side temperature PCFH02. (a) Grey: CFH frost point temperature (T_{frost}), black: RS41 air temperature (T_{air}), navy and dashed black: PCFH02-1 measured mirror temperature (T_{mirror}) and simulated cold side temperature (T_C), darkcyan and dashed black: PCFH02-1 measured hot side temperature (T_{hot}) and simulated hot side temperature (T_H); (b) grey: CFH T_{frost}, black: RS41 T_{air}, blue and dashed black: PCFH02-2 T_{mirror} and T_C, deep sky blue and dashed black: PCFH02-2 T_{hot} and T_H; (c) navy: difference between measured mirror temperature and simulated cold side temperature (ΔT_C) for PCFH02-1, darkcyan: difference between measured hot side temperature and simulated hot side temperature (ΔT_H) for PCFH02-1, blue: ΔT_C for PCFH02-2, deep sky blue: ΔT_H for PCFH02-2.

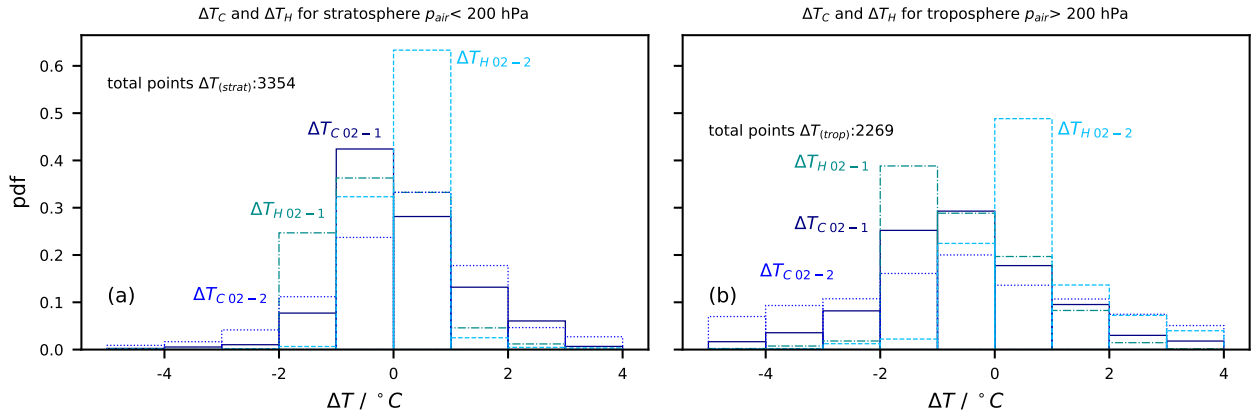

Figure 6.6: Model optimization: mirror and hot side temperature PCFH02 histogram. (a) Navy: distribution of PCFH02-1 ΔT_C for the stratosphere ($p_{\text{air}} < 200$ hPa), blue: same for PCFH02-2, darkcyan: distribution of PCFH02-1 ΔT_H for the stratosphere ($p_{\text{air}} < 200$ hPa), deep sky blue: same for PCFH02-2; (b) navy: distribution of PCFH02-1 ΔT_C for the troposphere ($p_{\text{air}} < 200$ hPa), blue: same for PCFH02-2, darkcyan: distribution of PCFH02-1 ΔT_H for the troposphere ($p_{\text{air}} < 200$ hPa), deep sky blue: same for PCFH02-2.

6.5 Heat sink loop

The files used for the optimization of the heat sink (HS) loop are available on-line (Jorge, 2018a). For the heat sink loop optimization, we followed a different strategy than for the optimization of the other loops. Instead of optimizing the heat contributions to the heat balance, we decided to focus on optimizing the system's time constant. As we saw from the analysis of the heat sink temperatures during flight in Section 5.7.3, the heat sink shows a thermal delay in relation to the air temperature due to its thermal mass. In Equation 5.3, we can see how the combination of the heat capacitances of the three components of heat sink complex: the actual heat sink ($m_{HS}\ c_{p_{HS}}$), the multiblock ($m_{mb}\ c_{p_{mb}}$) and the copper finger ($m_{Cu}\ c_{p_{Cu}}$) can cause some uncertainty, especially if we consider their temperature to be homogeneous. With this in mind, we optimized the heat sink complex heat capacitance (C_{HS}), which is shown in Equation 6.9 based on the state space equation for the heat sink temperature (T_{HS}) (Eq. 4.79).

$$C_{HS}\ \frac{dT_{HS}}{dt} = G_a\ \dot{Q}_{air-mb} + G_c\ \dot{Q}_{RS-HS} + G_g\ \dot{Q}_{Ph-HS} + G_h\ \dot{Q}_{HS} + G_i\ \dot{Q}_{inst} + G_r\ \dot{Q}_{R_{HS}} \tag{6.9}$$

Equation 6.9 includes the optimization parameters, which have been optimized in the other two loops: G_a, G_c and G_g for the respective heat contributions. G_a is connected to the convective heat transfer of the flow inside the intake tube ($\dot{Q}_{mb-air}$, Eq. 4.83). G_c is connected to the heat transfer from the reference surface to the heat sink ($\dot{Q}_{RS-HS}$, Eq. 4.80). We kept it as optimized in the RS loop (Table 6.2). G_g is connected to the thermal resistance between the heat sink and the PE hot side ($\dot{Q}_{Ph-HS}$, Eq. 4.78).

In the HS loop optimization when using G_g from the optimized PE loop (Table 6.4, T_{HS} started oscillating. We did not see this behaviour during flight for T_{sink}. For the G_g=0.22, the HS heat load was severely under-estimated. We decided to keep G_g equal to unity in this loop's optimization.

We added three new optimization parameters: G_h, G_i and G_r. G_h is associated with the forced convective cooling of the heat sink by the passing air flow on ascent ($\dot{Q}_{HS}$, Eq. 4.81). G_i is associated with the natural convective heat transfer into the multiblock inside the PCFH housing ($\dot{Q}_{inst}$, Eq. 4.84). Finally, G_r is associated with the radiative heat transfer ($\dot{Q}_{R_{HS}}$, Eq. 4.82). For the optimization, we set G_h and G_r to one and G_i to zero. For the effect of radiative heat, we optimized T_{rad}. Below, we summarize the calculation of each of the heat components presented in Equation 6.9.

$$C_{HS} = (m_{mb}\, c_{p_{mb}} + m_{Cu}\, c_{p_{Cu}} + m_{HS}\, c_{p_{HS}}) \tag{6.10a}$$

$$\dot{Q}_{Ph-HS} = \frac{k_{\text{Cu}}\, A_{PE}}{l_{\text{Cu}}}\ (T_{\text{hot}} - T_{HS}) \tag{6.10b}$$

$$\dot{Q}_{RS-HS} = \frac{A_{RS}\, k_{\text{Al 3D}}}{l_{RS}}\ (T_{\text{ref surf}} - T_{HS}) \tag{6.10c}$$

$$\dot{Q}_{HS} = n \times \sqrt{k_{\text{Al}}\, A_c\, h_{HS}\, p}\ (T_{\text{air}} - T_{HS})\ \tanh(a\, L_c) \tag{6.10d}$$

$$a = \frac{h_{HS}\, p}{k_{\text{Al}}\, A_c};\ L_c = L + t/2 \tag{6.10e}$$

$$\dot{Q}_{R_{HS}} = \epsilon\, \sigma\, A_{HS} \left(T_{\text{rad}}^4 - T_{HS}^4\right) \tag{6.10f}$$

$$\dot{Q}_{mb-air} = h_{IT}\, A_{mb}\ (T_{\text{air}} - T_{HS}) \tag{6.10g}$$

$$\dot{Q}_{inst} = h_{inst} \cdot A_{inst} \cdot (T_{\text{ref}} - T_{HS}) \tag{6.10h}$$

Table 6.5 provides the values of the heat sink loop constants, which are not included in Tables 6.1 and 6.3. The material properties are referenced in Table 3.7 ($c_{p_{mb}} = c_{p_{\text{Al 3D}}}$, $c_{p_{HS}} = c_{p_{\text{Al}}}$).

Table 6.5: Model optimization: Heat sink loop constants

m_{mb} (g)	m_{Cu} (g)	m_{HS} (g)	A_c (cm^2)	p (cm)	L (cm)	t (mm)	A_{HS} (cm^2)	A_{mb} (cm^2)	A_{inst} (cm^2)
60.8	unknown	150	2.5	11	3	5	125.8	31.4	11

T_{hot}, $T_{\text{ref surf}}$, T_{air}, and p_{air} are imported from the flight data. h_{IT}, h_{HS}, and h_{inst} are calculated in the model for T_{air} and p_{air} with the methods presented in Sections 4.3.3 and 4.3.4.

Results

For the optimization, we set the values of G_a, G_e, G_g, G_h, and G_i to the values shown in Table 6.6, and optimized parameters C_{HS} and T_{rad}. C_{HS}=279 J K^{-1} shown in Table 6.6 was optimized for flight PCFH02-2 where the smaller 5-fin heat sink version was used.

Table 6.6: Model optimization: heat sink loop optimized parameters

$C_{P_{HS}}$ (J K^{-1})	G_a	G_c	G_g	G_h	G_i	T_{rad} (K)
294 279	0.7	0.261	1	1	0	258 see Table 6.7

We then used the optimized heat sink loop to calculate the simulated heat sink temperature (T_{HS}) and to compare them to the in-flight measured heat sink temperature (T_{sink}) for the ascent of flights

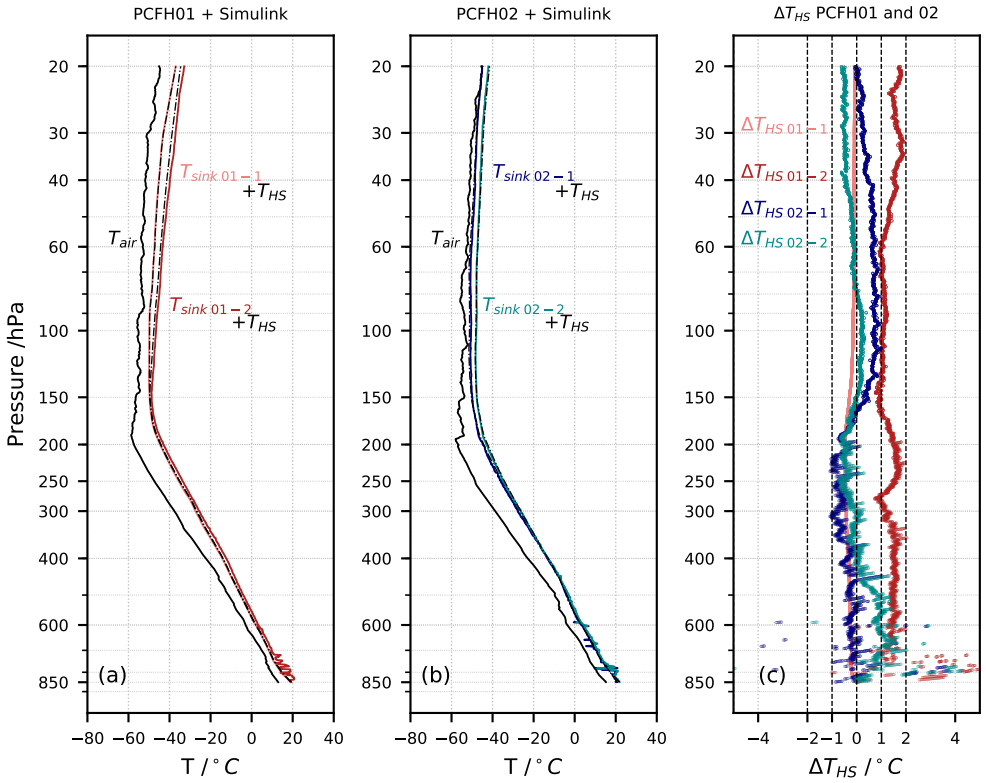

Figure 6.7: Model optimization: heat sink temperature (T_{rad} = 258 K). (a) Black: RS41 air temperature (T_{air}), light coral and dashed black: PCFH01-1 measured heat sink temperature (T_{sink}) and simulated heat sink temperature (T_{HS}), red and dashed black: PCFH01-2 T_{sink} and T_{HS}; (b) black: RS41 T_{air}, navy + dashed black: PCFH02-1 T_{sink} and T_{HS}, dark cyan + dashed black: PCFH02-2 T_{sink} and T_{HS}; (c) light coral: difference between measured heat sink temperature and simulated heat sink temperature (ΔT_{HS}) for PCFH01-1, red: ΔT_{HS} for PCFH01-2, navy: ΔT_{HS} for PCFH02-1, darkcyan: ΔT_{HS} for PCFH02-2.

PCFH01 and 02. The results using T_{rad}= 258 K are shown in Figure 6.7. The agreement between T_{HS} and T_{sink} within 2 °C was acceptable for all PCFH sub-units considered.

However, using a schedule for T_{rad} with pressure for each of the PCFH sub-units improves the model (Table 6.7). The scheduling is based of the increasing effect of radiative heating in the stratosphere, when compared to the decreasing effect of convective cooling (Section 4.3). The scheduling applies to $p_{\mathrm{air}} < 280$ hPa; below this level the radiation heating is not active, G_r=0. Radiative heating depends on the surrounding temperature of the exposed object. In the stratosphere, for the considered flights in the summer season, the air temperature is increasing with the decreasing air pressure. The scheduling mimics this. For future implementations of the model, we will consider T_{rad} as a linear function of T_{air}, considering its rate of change in the stratosphere, and that in this optimization there is a temperature difference between T_{rad} and T_{air} of about 40 to 50 °C during the day and 20 to 30 °C at night.

The comparison of T_{HS} and T_{sink} from the improved optimization is shown in Figure 6.8. Panel (a) shows the measured and simulated heat sink temperature (T_{sink} and T_{HS}) for PCFH01 ascent and the air temperature measured by the RS41 (T_{air}). Panel (b) shows the same variables for PCFH02

Table 6.7: Model optimization: T_{rad} scheduling for heat sink.

	p_{air} interval (hPa)	T_{rad} (K)	T_{rad} (°C)	
PCFH01-1	[280 - 160]	263	-10	
	[160-20]	273	0	
PCFH01-2	[280 - 160]	253	-20	day
	[160-30]	263	-10	
	[30-20]	283	10	
PCFH02-1	[280 - 60]	238	-35	
	[60-20]	248	-25	night
PCFH02-2	[280 - 20]	263	-10	

ascent. Panel (c) shows the difference between the measured and simulated heat sink temperature ΔT_{HS}, defined as

$$\Delta T_{HS} = T_{\text{sink}} - T_{HS} \tag{6.11}$$

The same panel description applies to Figure 6.7.

Figures 6.9 and 6.10 show a histogram forΔT_{HS} for the stratosphere ($p_{\text{air}} < 200$ hPa) and for the troposphere ($p_{\text{air}} > 200$ hPa) for the two optimizations: with the constant $T_{\text{rad}} = 258$ K and T_{rad} scheduling according to Table 6.7. Comparing the two figures we can appreciate the improvement due to T_{rad} scheduling. $|\Delta T_{HS}|$ in the stratosphere and troposphere (Figure 6.8) is now smaller than 1 °C, excluding some outliers in the troposphere.

The thermal mass of the different heat sinks was optimized to two different values as seen in Table 6.6. The theoretically estimated thermal mass for each heat sink, based on their mass and materials heat capacity, excluding the copper, was 197 J K^{-1} and 104 J K^{-1} for the heavier 7-fin heat sink and the lighter 5-fin heat sink, respectively. The optimized thermal masses were about 50% and 150% higher than expected. The under-estimation of the thermal capacity of the heavier 7-fin heat sink can be attributed to the copper insert. The heat capacity of copper is less than half of the heat capacity of aluminium (Table 3.7), but the density of copper ($\rho_{\text{Cu}} = 8.96$ g cm^{-3}) is three times higher than the density of aluminium ($\rho_{\text{Al}} = 2.70$ g cm^{-3}).

However, by flying a lighter heat sink, we expected a significant reduction of the overall thermal capacitance and time constant of the multiblock plus heat sink complex. Possibly, the heat sink itself does not play as significant role as we expected, and the major contributors for the thermal capacitance and time constant of this system are the multiblock and copper insert.

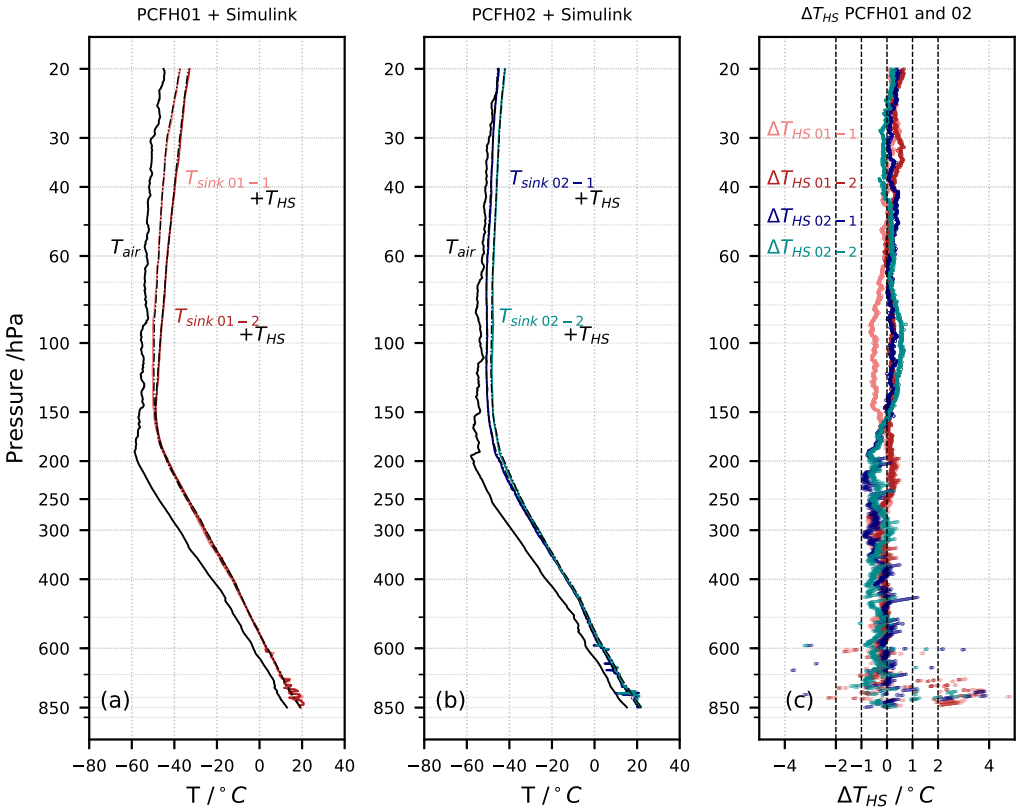

Figure 6.8: Model optimization: heat sink temperature with T_{rad} scheduling]. (a) Black: RS41 air temperature (T_{air}), light coral and dashed black: PCFH01-1 measured heat sink temperature (T_{sink}) and simulated heat sink temperature (T_{HS}), red and dashed black: PCFH01-2 T_{sink} and T_{HS}; (b) black: RS41 T_{air}, navy + dashed black: PCFH02-1 T_{sink} and T_{HS}, dark cyan + dashed black: PCFH02-2 T_{sink} and T_{HS}; (c) light coral: difference between measured heat sink temperature and simulated heat sink temperature (ΔT_{HS}) for PCFH01-1, red: ΔT_{HS} for PCFH01-2, navy: ΔT_{HS} for PCFH02-1, darkcyan: ΔT_{HS} for PCFH02-2.

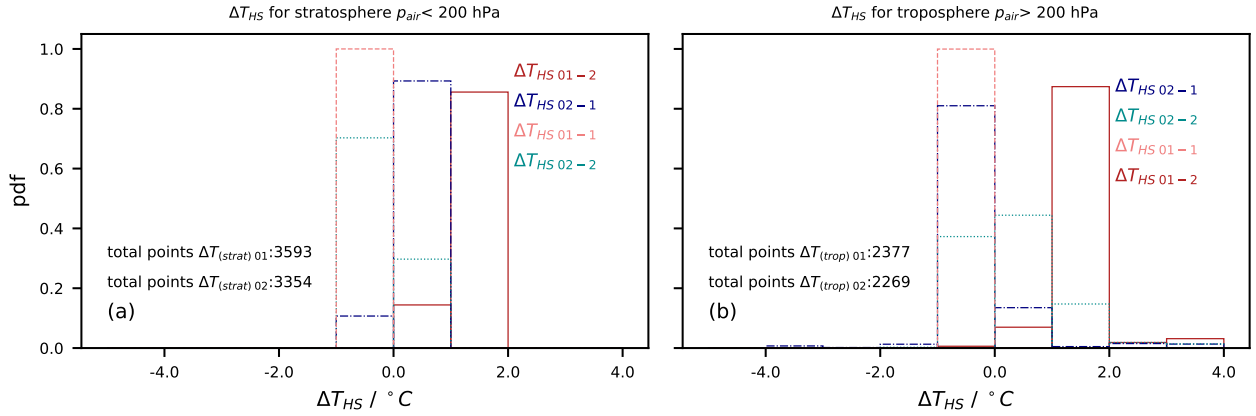

Figure 6.9: Model optimization: heat sink temperature ($T_{\mathrm{rad}} = 258$ K) - histogram. (a) Light coral: distribution of PCFH01-1 ΔT_{HS} for the stratosphere ($p_{\mathrm{air}} < 200$ hPa), red: same for PCFH01-2, navy: same for PCFH02-1, darkcyan: same for PCFH02-2; (b) light coral: distribution of PCFH01-1 ΔT_{HS} for the troposphere ($p_{\mathrm{air}} > 200$ hPa, red: same for PCFH01-2, navy: same for PCFH02-1, darkcyan: same for PCFH02-2.

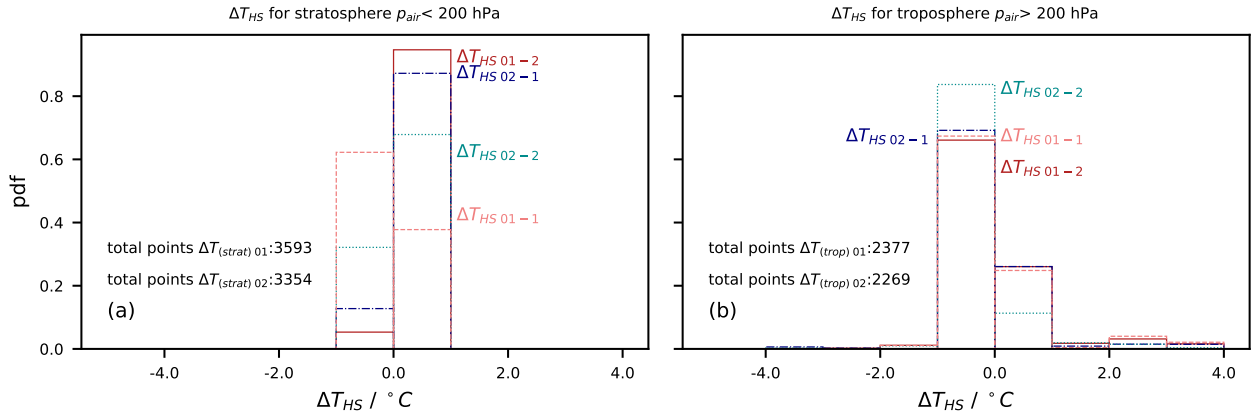

Figure 6.10: Model optimization: heat sink temperature with T_{rad} scheduling - histogram. (a) Light coral: distribution of PCFH01-1 ΔT_{HS} for the stratosphere ($p_{\mathrm{air}} < 200$ hPa), red: same for PCFH01-2, navy: same for PCFH02-1, darkcyan: same for PCFH02-2; (b) light coral: distribution of PCFH01-1 ΔT_{HS} for the troposphere ($p_{\mathrm{air}} > 200$ hPa, red: same for PCFH01-2, navy: same for PCFH02-1, darkcyan: same for PCFH02-2.

6.6 Conclusion

In this study, weoptimized the PCFH model for selected intervals of test flights 01 and 02, and validated the optimized model with flight data from different iterations of the same instrument design. The model describes satisfactorily the thermal balances within the instrument, especially for the slow changing temperature reservoirs such as the heat sink and the reference surface. This confirms the theoretical considerations for heat transfer and empirical relations for convective heat transfer coefficient estimation.

The Peltier element is well represented by the model. There is a significant improvement after optimization compared to simulations with the datasheet specifications. However, each Peltier element assembly into the PCFH is different and the optimized model has trouble simulating the behaviour of the PE in different assemblies up to an error of ±10 °C in one case. I also attribute some of the model optimization difficulties to the different control schemes used during the flights. Optimization was done for the instruments running the transfer function identification steps, and validated with an instrument running the alternating set-point PID controller. In the instrument running the transfer function identification steps, equal weight was given to the full range of the I_P current used, while for the alternating set-point PID controller, specific ranges of I_P were used in different regions of the troposphere and stratosphere. The model optimization can be more tailored to the desired operation to improve the agreement between model and observations.

The model describes the present design of the PCFH. If the design is altered this model may no longer be applicable. The design and assembly methods of the PCFH need to be fixed, so the PCFH model can be completed. Next steps on the PCFH model are optimizing the reflectance loop, for which more data is needed, computing the correlation function $R_{uy}(\tau)$ between the input and output of $R_{uy}(\tau) = \langle u(t)y(t+\tau)\rangle$ and of $R_{uu}(\tau) = \langle u(t)u(t+\tau)\rangle$, the autocorrelation function of the input, and finding the transfer function $G(s)$ by taking the Fourier transforms of R_{uy} and R_{uu} and computing $G = R_{yu}/R_{uu}$.

Further steps will be to experiment with different controller schemes such as PIDs, linear quadratic regulators (LQR) (Wikipedia, 2019a), and others within the MatLab development environment. One important decision regarding the direction of the modelling is the accuracy expected from the PCFH model. The accuracy of the optimization in this chapter is fairly good, i.e. the state space variables can be predicted to within ± 1 °C for slow varying variables and to within ± 5 °C for the mirror temperature within the tropospheric and stratospheric range of a balloon flight. T_{mirror} prediction is not yet within an acceptable range, considering we hope to measure T_{frost} with a ± 0.25 K uncertainty. These modelled to measured differences are calculated in separate loops for each state variable, once the different loops are integrated into one model these differences will accumulate. Some control techniques, such as robust control, may be able to cope with such uncertainty but a lot of work is still necessary to improve the model and instrument stability.

Summary

Contamination modelling

In Chapter 2 we investigated contaminated water vapour measurements by means of cryogenic frost point hygrometers during the 2016-2017 StratoClim balloon campaigns on the southern slopes of the Himalayas. We analysed extensively three distinct cases where these contaminated values were observed. In these cases, we encountered clouds in the troposphere, and using of observations and modelling, we proved liquid water could be present in all of them. By novel interpretation of the GPS data and using computational fluid dynamic (CFD) simulations, we quantified the balloon pendulum movement and estimated the impact of the pendulum motion on the collision efficiency of supercooled liquid droplets on the inner wall of the intake tube. We found that the inlet flow angles in the intake tube are larger than the pendulum oscillation angles due to horizontal velocity of the payload induced by the pendulum and rotating movements. We also compared the impact of different size droplets. Big droplets have higher collision efficiency rates than smaller droplets. For example, less than 50% of liquid droplets with $r \sim 10$ μm freeze in the intake tube at inlet angles on the order of 50°, while 100% of droplets with $r > 70$ μm will freeze already at angles $> 5°$.

We matched the contaminated water vapour measurements in the stratosphere to simulation results for a 5 cm deep icy wall coverage at the top of the intake tube for most of the simulations. We showed the recovery of contaminated water vapour measurements can be explained in terms of smaller surface ice coverages eventually leading to uncontaminated water vapour observation in the stratosphere after all ice in the intake tube has sublimated. We provided a clear picture on the evolution of the ice layer inside of the intake tube during the sublimation process. Ice layers closer to the top of the intake tube will sublimate more efficiently than layers closer to the center. However, because collisions are less efficient closer to the center of the tube, they generate a thinner ice layer and sublimate first. The last layers to sublimate will be those around 4 to 5 cm from the top of the intake tube. By comparison with the Vaisala RS41, we found that water vapour measurements in the upper troposphere could also be contaminated, especially at S_{ice} lower than 0.7, after passing through the mixed-phase cloud, if a flight presents contaminated water vapour values in the stratosphere.

Characteristics common to flights NT011 and NT029 are the presence of cold mixed-phase clouds, at air temperature lower than -20 °C, a fast ascent balloon velocity between 6 and 7.5 m s^{-1}, and the total sublimation of any ice coverage on the intake tube before balloon burst. In flight NT007 a warm mixed-phase cloud was present at air temperatures between 0 and -5 °C, the balloon rose slower through the entire flight at between 3 and 4 m s^{-1}, and the water vapour contamination persisted in the stratosphere until burst. It was known that liquid clouds and mixed-phase clouds could irreversibly

contaminate water vapour observations by cryogenic frost point hygrometers [Holger Vömel, personal communication, 2016]. Our results show that even cold mixed-phase clouds with very low LWC, can affect the operation of the CFH.

We also show that neither the balloon envelope nor the instrument package are a likely cause for the water vapour values observed in these cases. However, the balloon could be responsible for the enhanced and contaminated water vapour values observed above the 20-hPa level (Brunamonti et al., 2018). The intake tube successfully shields sampled air from package contamination.

Design and operation recommendations

To reduce the pendulum oscillation of the payload, we recommend investigating using a two balloon tandem separated by a rigid triangle as described by Kräuchi et al. (2016). However, it would need further investigation to confirm that by reducing the oscillation, we would be reducing the contamination. The payload would fly more often in the wake of the balloons and hence be subject to contamination by the balloon. Furthermore, the oscillatory movement would not be completely avoided, but smaller oscillations might result in faster sublimation, shorter contamination in the stratosphere and faster recovery of the instrument.

We recommend widening of the intake tubes to increase inlet flow (Mastenbrook, 1965, 1968) and the placement of the measurement head as far from any of the intake tubes walls as possible. As seen in Figure 2.9, ambient air can enter the tube and remain unperturbed in terms of water vapour for a few centimetres. The wider the tubes the longer the air can remain unperturbed and the closer the measurement is to the inlet the better. However, the tubes are effective at protecting the measurement from contamination from the instrument package, so we do not recommend shortening or removing them. The two sub-units of PCFH will provide an opportunity to evaluate these proposals.

Heating of the intake tubes has been suggested; however, this would perturb the measurement of water vapour (Kämpfer, 2013). Heated tubes will evaporate liquid or ice water present in the air and contaminate the measurement of water vapour turning it into a near total water measurement, making it more difficult to assess supersaturation in cloud. We suggest performing one heating cycle of the inlet tubes after the region of mixed-phase cloud, at air temperatures colder than -38 °C, similar to what is done in the mirror clearing and freezing cycle (Vömel et al., 2007b), but for the inlet tube. The measurement would be perturbed for a few seconds or minutes in the upper troposphere, but a clean stratospheric water vapour profile might be the reward.

Many assumptions had to be made throughout this study due to the lack of information about the observed clouds, because the backscatter from COBALD does not suffice to derive cloud drop sizes and physical states. One instrument that could provide useful additional information is a hot-wire probe to measure liquid water content (LWC) and total water content (TWC) in mixed-phase clouds. This type of instrument instrument is mainly used on aircraft and we are not aware of its use for balloon soundings. The principle is simple and detection limits are on the order of 0.003 to 0.005 $\mathrm{g\,m^{-3}}$ (Korolev et al., 2003a). However, a limitation for implementation in balloon sounding could be the available power.

PCFH

Five prototypes of PCFH have been assembled and tested in the lab. Air flow is a critical aspect for the Peltier element, because of the thermal load, which the flow represents. The prototypes flew in mid-latitudes in summer and winter; however, so far only for the purpose of instrument characterization and not yet aiming at obtaining reliable water vapour measurements. Since each prototype is composed of two sub-units, testing opportunities per prototype were doubled and allowed us to test the performance of different components such as single and double stage Peltier elements and heavier and lighter heat sinks with different number of cooling fins. The goal of the initial flights was a proof of concept and to validate the systems model, essential for the implementation of optimal control. For this purpose, a sequence of steps with different Pulse Width Modulator (PWM) duty cycles, which the instrument perceives as Peltier current, was given as input to the system to evaluate the systems transfer function. This characterization is essential for the modelling of thermal reservoirs of the PCFH in flight and to evaluate the cooling range of the Peltier element once assembled into the PCFH.

The five deployed instruments were successfully recovered by the DWD team. We did not launch any PCFH from Zürich and had no chance to test the recovery on our own. There were clear improvements from the implementation of the electronics version 2 with separated power supplies. There was no more interruptions of operation of the thermocouple module board during flight. However, we need a proper characterization of Peltier element current vs PWM duty cycle including the power supply drainage during flight. Although, the calibrated range of the reference thermometer of the thermocouple module board has been extended to -20 °C, the PCFH needs housing with better thermal insulation or a dedicated internal heater. So far, PCFH has flown in moderate conditions, while in the tropics or the winter polar regions ambient temperatures are much colder. The PCFH can successfully fly as a RS41 add-on instrument. We identified a telemetry package conflict, which was overloading the RS41 when the instrument identification package was sent simultaneously with the other three regular telemetry packages. The telemetry scheduling has been altered, so the instrument identification package is only sent when the regular 5 s package is not sent. All PCFH systems were functional after recovery, despite some rough landings in tree tops and lakes. The PID controller of $T_{\mathrm{ref\ surf}}$ works, but the design of the air thermocouple ($T_{\mathrm{air}}^{\mathrm{PCFH}}$) needs improvement with respect to warm bias on ascent and noise.

After comparing the performance of double and single stage Peltier elements in the PCFH, we decided to use double stage Peltier elements for future prototypes. Nevertheless, the cooling range of the instrument design remains critical. We demonstrated the accessibility to stratospheric frost point temperatures reaching T_{frost} = -85 °C at p_{air} = 40 hPa and T_{air} = -60 °C, but only for one instrument out of the five. While this is an important step in the proof-of-concept, there is no proof yet of the reproducibility, and optimal control has not yet been implemented. The assembled double Peltier element has reached a maximum temperature depression between the hot and cold side of $\Delta T_{\mathrm{max}} = 40$ K at T_{air} = -60 °C and reached $\Delta T_{\mathrm{max}} = 65$ K during lab tests without air flow while the Peltier element datasheet advertises $\Delta T_{\mathrm{max}} = 86$ K at ground conditions ($T_{\mathrm{air}} = 27$ °C, $p_{\mathrm{air}} \sim 1000$ hPa). We attribute the loss of ΔT from the datasheet specifications to the lab tests without air flow to the assembly of the Peltier element into the PCFH. A reduction by 20 K is the best assembly so far. With air flow of ~ 5 m s^{-1}, as is the case for an instrument under field conditions, the ΔT reduction becomes even more significant. The flow effect decreases as the air becomes less dense, which partially compensates

the ΔT reduction of the Peltier element at colder operation temperatures, as is in the stratosphere. Furthermore, $\Delta T_{\max}$ = 40 K at T_{air} = -60 °C corresponds to about 20 K between cold side and ambient temperature due to losses between the Peltier hot side, heat sink, and ambient air.

The reflectance of the ice/dew layer on the mirror responds to the temperature difference between the mirror temperature and the actual frost point temperature, which we tested by equipping two out of the ten flown sub-units with an alternating set-point proportional-integral-derivative (PID) controller. From one of these flights, we designed a method to determine the relation between $T_{\text{mirror}} - T_{\text{frost}}$ and $d(R_{\text{mir}}/R_{\text{ref}})/dt$, i.e. the water vapour diffusivity. More experiments in the lab and in-flight will be required.

Model optimization and validation

In Chapter 6, the mathematical model of the instrument was optimized for the first prototype version and validated with in-flight data. By model optimization we mean a broader concept than fitting a function, which was used to adjust the proportionality parameters so that the model can better describe the observations. After optimization, the model describes satisfactorily the thermal balances in the instrument, especially the slow changing thermal reservoirs such as the heat sink and the reference surface. This confirms the validity of the theoretical considerations for heat transfer and empirical relations for the convective heat transfer coefficient estimation.

The Peltier element is well represented by the model. There is significant improvement after optimization compared to simulations with the datasheet specifications. However, each Peltier element assembly is different and the optimized model has trouble simulating the behaviour of the PE in different assemblies up to an error of ±10 °C in one case. Some model difficulties may stem from the different controlling schemes used during the flights. Optimization was done for the instruments running the transfer function identification steps and validated with an instrument running the alternating set-point PID controller. In the instrument running the transfer function identification steps, equal weight was given to the full range of the Peltier element current (I_P) used during the entire flight, while for the alternating set-point PID controller, specific ranges of I_P were used in different regions of the troposphere and stratosphere. The model optimization can be more tailored to the desired operation to improve the agreement between model and observations.

Outlook

Development, Validation and Implementation of a GRUAN-Worthy Plug-and-Play Balloon-Borne Hygrometer

In 2017, we submitted a proposal to the GAW-CH (MeteoSwiss, 2018) call for the *Development, Validation, and Implementation of a GRUAN-Worthy Plug-and-Play Balloon-Borne Hygrometer*. The proposal was funded for the full period, until the end of 2021. This will support the development, validation, and further implementation of the PCFH into an atmospheric monitoring network at least until the end of 2021.

Figure 6.11 shows the time-plan from the submitted proposal with nine work packages. Some of the work packages (WP) of the project have been accomplished during this PhD work, in particular WP1 to WP4, and some tasks from other work packages, e.g. the instrument mathematical model in WP5 and the temperature reference comparison in WP7. Progress within the project has not been linear and some of the tasks needed and still need to be repeated, as is the case of the proof of concept of WP4. Every time the instrument is re-designed, as was the case of the electronics version 2, the single stage Peltier element or the lighter heat sink, a new proof-of-concept is required. We hope the reduction of the thermal resistance between the PE hot side and heat sink is last major alteration to the PCFH design.

During the development of the PCFH, we realized the strong connection between the instrument mathematical model and the instrument proof of concept. As was seen in Chapter 6, the adaptation of the mathematical model to the observations is fundamental as is the measurement of the instrument transfer function in-flight. The evaluation of the ice growth and evaporation will allow closing the PCFH model description by defining the water vapour diffusivity (B) in Equation 4.89. As seen in Section 5.10, the use of an alternating set-point PID controller in-flight with an additional CFH supported by the same radiosonde is a viable method to evaluate the ice/dew layer response, through its reflectance, to the temperature difference between the mirror temperature and the actual frost point temperature. We have decided to do also tests in a cold chamber at ETH without controlled pressure but with temperature possibilities down to -20 °C.

On the PCFH team, Uwe Weers had to leave for health reasons, and was eventually replaced by Nico Germann, an electronics technician, since August 2019. In the next months, ten more PCFHs will be build with the most recent design and electronics. These will be used for testing of the ice lawyer growth and sublimation in the ETH cold chamber, and tested in flight in two field campaigns in November and December 2019 at Lindenberg together with DWD and the GRUAN Lead Center. The goals of the campaign in November are to measure the transfer function of the new PCFH prototypes,

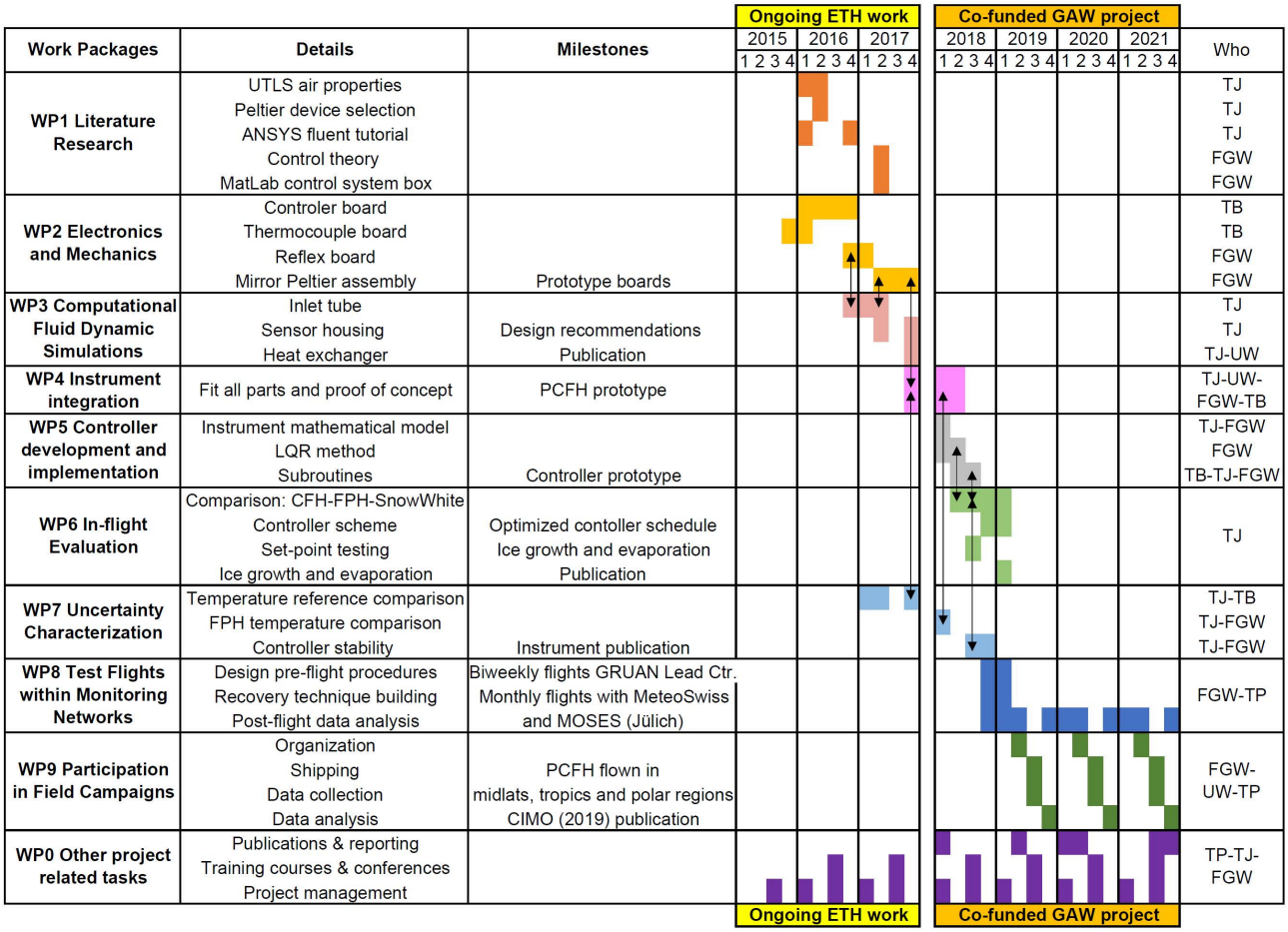

Figure 6.11: Time table showing 9 work packages (WPs 1-9) and the project management WP 0 including milestones and WP interactions (marked by black arrows in particularly important cases). Responsible personnel (last column) is: TJ = Teresa Jorge; FWG = Frank Wienhold; TB = Thomas Brossi (Mylab); UW = Uwe Weers; TP = Thomas Peter. Adapted from 'Development, Validation and Implementation of a GRUAN-Worthy Plug-and-Play Balloon-Borne Hygrometer' proposal to GAW + CH.

re-evaluate and optimize the PCFH model to the new prototypes and explore controller solutions with the validated model in Simulink and MatLab. In the campaign in December, we want to test the implementation of controller solutions found from the analysis of the November campaign flights.

Polar Access Fund: PCFH testing in polar regions, Ny Ålesund field trip

Following the goals of the *Development, Validation, and Implementation of a GRUAN-Worthy Plug-and-Play Balloon-Borne Hygrometer* project of testing the PCFH in polar regions, I submitted a proposal to the Swiss Polar Institute (SPI, 2019) Polar Access Fund Grant together with Dr. Marion Maturilli from AWIPEV (https://www.awipev.eu/). The proposal was accepted and the field trip is to take place in February 2020. The goals of the field trip are to assess differences between the PCFH operation in mid-latitudes and polar regions, since its operation is strongly dependent on its

environment.

Further development

The PCFH has been designed with two additional PWM drivers, besides the Peltier element drivers and reference surface heaters. After the PCFH is established as a balloon-borne frost point hygrometer, these additional drivers can be used to investigate the implementation of a intake tube clearing cycle after the mixed-phase region to prevent contaminated observations in the stratosphere or to implement a hot wire probe for Liquid Water Content (LWC) and Total Water Content (TWC) measurements in mixed-phase clouds as suggested in Chapter 2.

There has been an increasing number of UTLS projects supporting long duration balloon flights, for which PCFH might prove to be suitable. Its operation does not depend on consumables, such as a cryogenic liquid, which limits the cryogenic frost point hygrometer operation to a maximum of 4 hours. With some consideration to the power supply and flow intake, the PCFH could be adapted for operation on long duration balloons. In the next years, we look forward to participate in intercomparison campaigns such as the MOHAVE (Leblanc et al., 2011), whose second edition is planned for May 2020 and the CIMO-17 upper-air instrument intercomparison to take place in 2021 (Dirksen et al., 2019).

The development of PCFH is now in its fourth year. It proves to be a formidable task. Several aspects were not easily accomplished. However, the perspectives for this instrument are fully intact and the hope remains that one day it will be able to compete with CFH and FPH.

Appendices

Appendix A

Contaminated water vapour measurements

A.1 Flight NT029

Figure A.1 shows the full profile of flight NT029 on the 30 August 2016. As for the flight NT011, there are contaminated water vapour mixing ratios in the stratosphere, and recovery of operation by the CFH still during ascent before balloon burst. From COBALD we can identify the presence of three clouds: one very thin cloud in the liquid phase regime, at air temperatures higher than 0 °C; a second one, in the mixed-phase regime with very interesting features in the backscatter ratio (BSR) and color index (CI); and a third cloud at air temperature colder than -38 °C, which is in the cirrus or ice cloud regime. We do not consider the liquid cloud to be the source of the contamination, because the cloud finishes at $T = 0$ °C and between the end of the liquid cloud and the start of the mixed-phase cloud the payload flies through a sub-saturated region. Liquid water on the intake tube wall would evaporate in the sub-saturated region.

Figure A.2 shows a detail of the mixed-phase cloud of flight NT029. We consider the mixed phase cloud to exist between the temperatures of -15 °C and -21 °C, when S_{ice} by the CFH is between 1.1 and 1.05, S_{liq} by the RS41 is between 0.95 and 0.85, and the COBALD CI is above 20. This confines the mixed-phase cloud to the interval between 8.1 and 9.1 km height.

Figure A.3 shows the evaporation simulation results for the mixed-phase cloud of flight NT029. From the integration of water vapour in the upper troposphere and stratosphere of flight NT029 we have determined the upper and lower limit of liquid water content (LWC) in the mixed-phase cloud of NT029 to be 0.160 g m^{-3} and 0.032 g m^{-3} respectively (see Table 2.3). For the simulation, we have defined the initial distribution with the same ice crystal and liquid droplets sizes as for the NT011 simulation: $r_{\text{ice}} = 10$ μm, $r_{\text{liq,1}} = 10$ μm, $r_{\text{liq,2}} = 100$ μm, and $r_{\text{liq,3}} = 200$ μm. The bigger droplets extend the glaciation time and prolong the duration of the cloud liquid phase. The initial ice crystal concentration is the same as the expected for ice nucleation particles (INP) at these temperatures: $n_{\text{ice}} = 0.02$ cm^{-3} (DeMott et al., 2010). The upper limit of LWC starts with $n_{\text{liq,1}} = 70$ cm^{-3} and $n_{\text{liq,2}} = 0.030$ cm^{-3} and the lower limit of LWC starts with $n_{\text{liq,1}} = 30$ cm^{-3} and $n_{\text{liq,2}} = 0.002$ cm^{-3}, both simulations had $n_{\text{liq,3}} = 0.001$ cm^{-3}. Both upper and lower limit clouds exist for about $\Delta t \sim 40$ minutes at the S_{liq} and S_{ice} conditions observed in the NT029 mixed-phase cloud. The average velocity

of the payload in this part of the flight is 6 m s^{-1}, which means the payload was in the 1000-m-long cloud for about 3 minutes.

Figure A.4 shows the pendulum analysis for the mixed-phase cloud of flight NT029. We observe payload oscillations with up to 40 m amplitude. Figure A.5 summarizes the observed horizontal velocities (v_h), ascent velocities (w_n) and inlet angles (β) experienced during the mixed-phase cloud of flight NT029.

Figure A.6 shows the FLUENT simulations results for the collision/ freezing efficiency of hydrometeors inside the intake tube for flight NT029. We only show results for 100 μm radius droplets. The results for 200 μm droplets are very similar to the ones seen in Figure A.14. As for flight NT011, we confirm that all big droplets freeze on the intake tube wall. Again, with higher inlet angles, the freezing efficiency is higher at the top of the intake tube. The ice layer thickness for the first 5 cm of the intake tube are shown in Figure A.6k for the two scenarios of LWC in the mixed-phase cloud.

Figure A.7 shows the stratosphere of flight NT029, and the FLUENT simulation input values and results. The ascent velocity for NT029 is less variable, about ± 1 m s^{-1}, than for flight NT011. As for flight NT011, we were able to match the contaminated water vapour mixing ratio values observed in the stratosphere to simulation results for a 5 cm ice wall coverage at the top of the intake tube. The contamination lasts longer for flight NT029 than for flight NT011, but the burst is also at higher altitude. The measurement starts recovering at 26 km height. We can match the observation at 27 km height with the $\langle \chi_{\mathrm{H_2O}} \rangle_{\mathrm{Vol}}$ for the 1 cm ice wall coverage at the top of the intake tube simulation and at higher altitude levels, for smaller surfaces such as thinner layers of 0.15 cm length, and radially asymmetric patches as shown in Figure 2.9g or smaller, with only 0.45 cm height instead of the shown 1 cm.

For the upper tropospheric sublimation study, we consider two regions where sublimation of an icy intake tube wall could happen: from 11 km height to the start of the cirrus cloud, where $S_{\mathrm{ice}} < 1$, and from above the cirrus cloud at 15.5 km height to the CPT. We exclude the region directly above the mixed-phase cloud, from 9 to 11 km. The backscatter ratio, as can be seen from COBALD in Figure A.1 and A.2, is very perturbed and $S_{\mathrm{ice}} > 1$, so, we can not exclude that the payload was in cloud. We also do not consider the cirrus cloud region, because at $S_{\mathrm{ice}} = 1$ there is no sublimation of the ice coverage at the top of the intake tube. Although, the four locations chosen for the upper tropospheric sublimation simulations were not all with $S_{\mathrm{ice}} < 0.7$, there is good agreement between the $\chi_{\mathrm{H_2O}}$ for the RS41, $\langle \chi_{\mathrm{H_2O}} \rangle_{\mathrm{Vol}}$, and $\chi_{\mathrm{H_2O}}$ by CFH: the fluent simulations with $\chi_{\mathrm{H_2O}}$ RS41 as background and additional water vapour from sublimation from 1 cm, 5 cm, and 15 cm walls do not over estimated $\chi_{\mathrm{H_2O}}$ from CFH.

The excess integrated water vapour in the stratosphere of NT029 is 15.7 mg. The excess integrated water vapour in the upper troposphere of NT029 is 3.5 mg for the first sub-saturated region between the mixed-phase cloud and the cirrus cloud, and 60.5 mg between the cirrus cloud and the tropopause, for a total excess integrated water vapour of 79.7 mg in flight NT029. All these values are in Table 2.3.

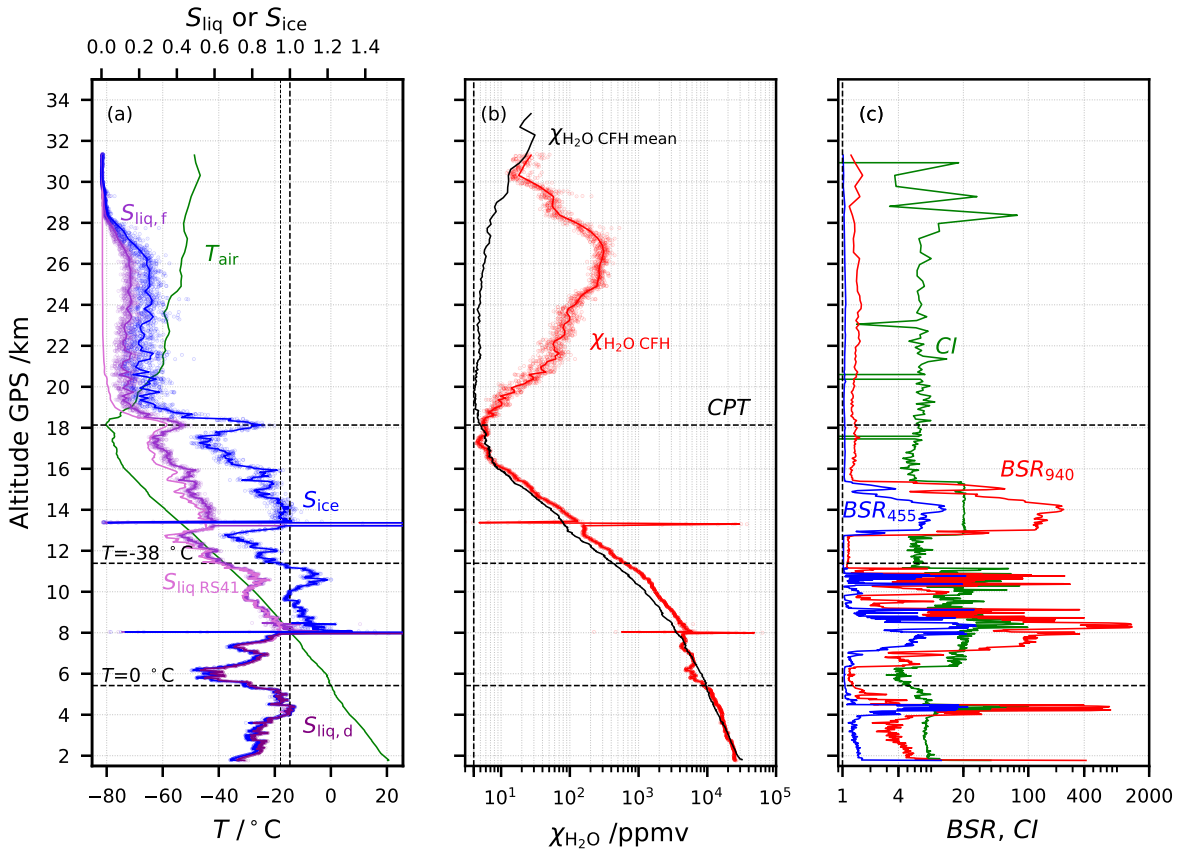

Figure A.1: Flight NT029 in Nainital, India, on 30 August 2016. Lines: 1 hPa interval averaged values. Dots: 1 s data. (a) Green: air temperature measurement from Vaisala RS41; pink: relative humidity ($S_{\mathrm{liq\ RS41}}$) by RS41; blue: ice saturation (S_{ice}) from CFH; purple: saturation over water ($S_{\mathrm{liq,d}}$) from CFH considering the deposit on the mirror to be dew; violet: saturation over water ($S_{\mathrm{liq,f}}$) from CFH considering the deposit on the mirror to be frost. (b) Red: H_2O mixing ratio from CFH in ppmv; black: average H_2O mixing ratio from uncontaminated CFH for the Nainital 2016 summer campaign (Brunamonti et al., 2018); 'CPT' marks the cold point tropopause. (c) Red: 940-nm backscatter ratio from COBALD; blue: same for 455 nm; green: color index (CI) from COBALD.

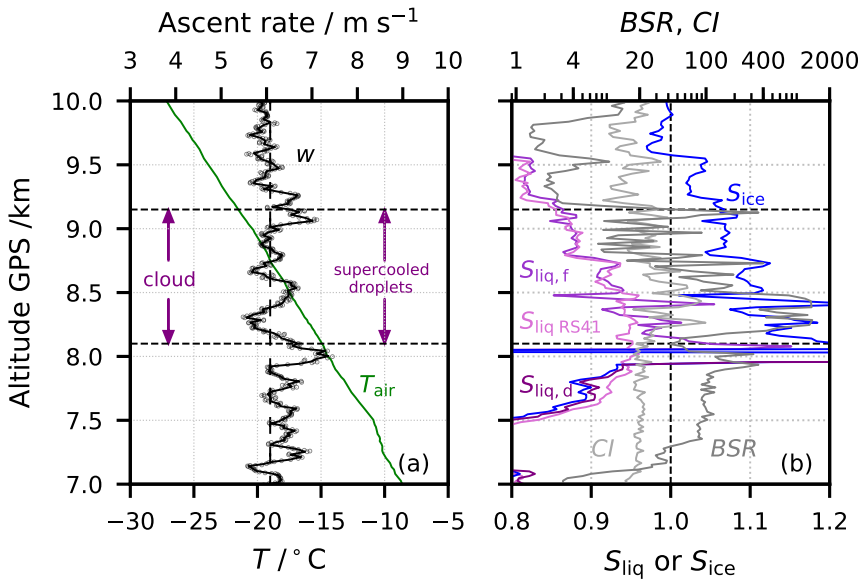

Figure A.2: Mixed-phase cloud detail of flight NT029. Lines: 1 hPa interval averaged values. (a) Green: air temperature; black: ascent velocity measured by RS41 in m s^{-1}. (b) Pink: saturation over water ($S_{\mathrm{liq\ RS41}}$) measured by RS41; purple: saturation over water ($S_{\mathrm{liq,d}}$) from CFH considering the deposit on the mirror to be dew; violet: saturation over water ($S_{\mathrm{liq,f}}$) from CFH considering the deposit on the mirror to be frost; blue: ice saturation (S_{ice}) from CFH; dark grey: 940-nm backscatter ratio from COBALD; light grey: color index (CI) from COBALD. Horizontal dashed lines mark supercooled droplet region.

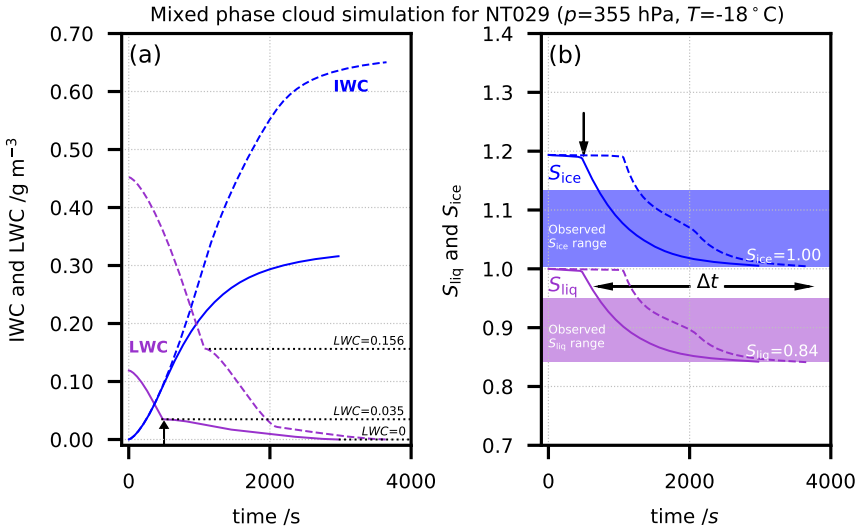

Figure A.3: Mixed-phase cloud modelling of the Wegener- Bergeron-Findeisen process demonstrating that flight NT029 likely flew through supercooled liquid droplets. Solid lines: lower limit of liquid water content (LWC). Dashed lines: upper limit (see text). Initial size distributions for lower limit simulation: $n_{\mathrm{ice}} = 0.02$ cm^{-3}, $r_{\mathrm{ice}} = 10$ μm; $n_{\mathrm{liq},1} = 20$ cm^{-3}, $r_{\mathrm{liq},1} = 10$ μm; $n_{\mathrm{liq},2} = 0.002$ cm^{-3}, $r_{\mathrm{liq},2} = 100$ μm; $n_{\mathrm{liq},3} = 0.001$ cm^{-3}, $r_{\mathrm{liq},3} = 200$ μm. Initial size distributions for upper limit simulation are identical but with 3.5× larger $n_{\mathrm{liq},1}$ and 15× larger $n_{\mathrm{liq},2}$. (a) Blue: ice water content (IWC); purple: liquid water content (LWC); vertical arrows: time when smaller liquid droplets fully evaporated. (b) Blue: ice saturation ratio (S_{ice}); purple: liquid water saturation ratio (S_{liq}) for lower and upper limits. Glaciation times of small droplets $\tau_{g,1}$ $\sim$ 8 - 18 minutes, of big droplets $\tau_{g,2-3}$ $\sim$ 45 - 50 minutes. Shaded saturation ratios: observed ranges from Figure A.2. The computed time interval with S_{ice} and S_{liq} matching flight observations is Δt $\sim$ 30 - 40 minutes.

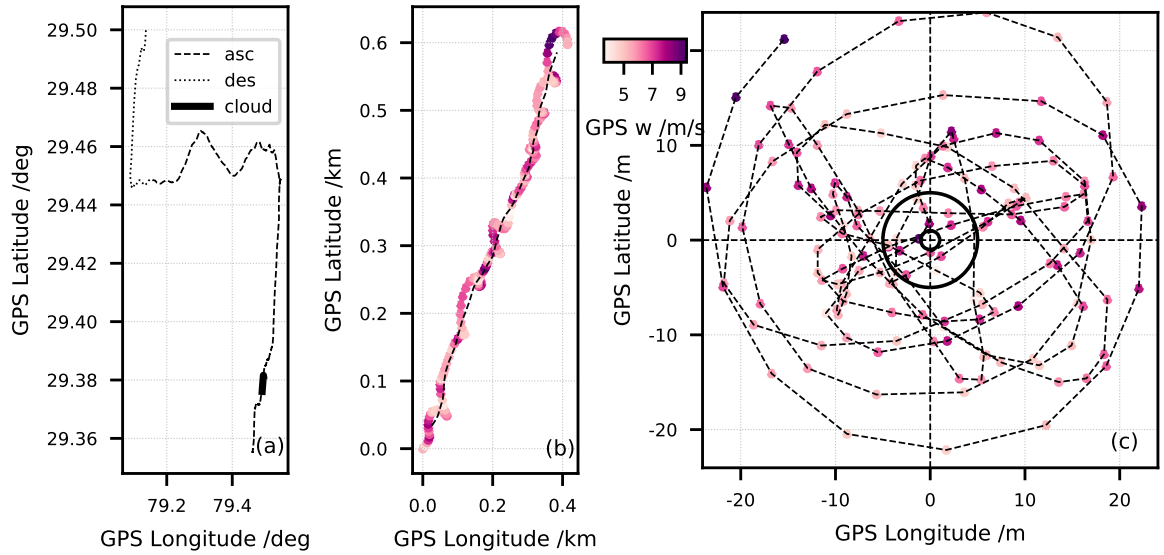

Figure A.4: Pendulum analysis for mixed-phase cloud of flight NT029. (a) Payload trajectory: ascent (dashed), descent (dotted) and mixed-phase cloud between 8.1 and 9.15 km height (thick black). (b) Zoom in on the mixed-phase cloud with 1-second GPS data of payload trajectory (symbols) and balloon trajectory (dashed). (c) Detrended payload oscillations; approximate balloon sizes on the ground ($r = 1$ m) and at burst ($r = 5$ m) are shown by two circles. Colour code in (b) and (c): balloon ascent velocity.

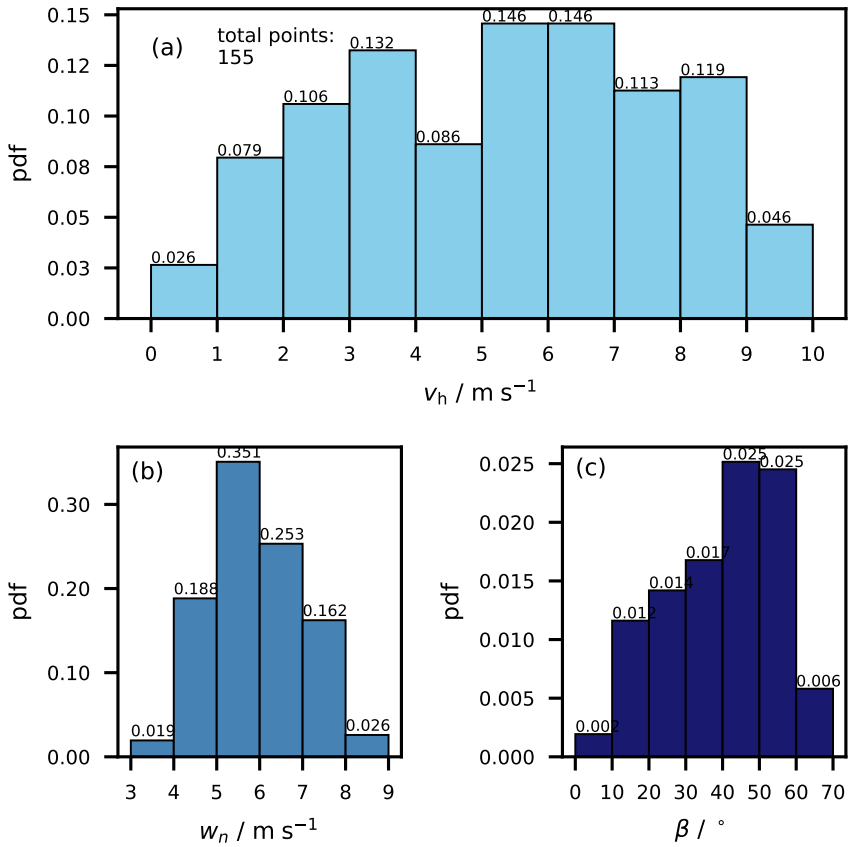

Figure A.5: Probability density functions (pdf) of impingement parameters at the inlet plane of the CFH intake tube during the passage through the mixed-phase cloud of flight NT029. (a) Horizontal velocity (v_h); (b) normal velocity (w_n); (c) inlet angle (β).

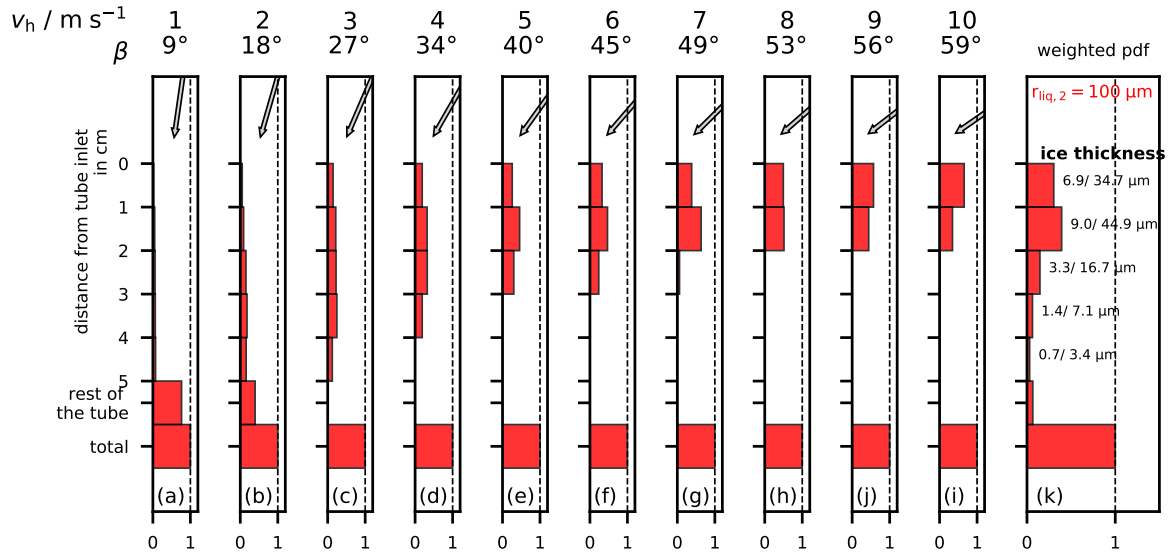

Figure A.6: Collision/freezing efficiency of hydrometeors in the intake tube for the flight NT029 mixed-phase cloud with vertical inlet velocity $\langle w_n \rangle = 6.0$ m s^{-1}. $r_{\mathrm{liq},2} = 100$ μm (red). (a-i) Freezing efficiency for various horizontal inlet velocities: (a) 1 m s^{-1}, 9°; (b) 2 m s^{-1}, 18°; (c) 3 m s^{-1}, 27°; (d) 4 m s^{-1}, 34°; (e) 5 m s^{-1}, 40°; (f) 6 m s^{-1}, 45°; (g) 7 m s^{-1}, 49°; (h) 8 m s^{-1}, 53°; (i) 9 m s^{-1}, 56°; (i) 10 m s^{-1}, 59°. The 'rest of the tube' takes account of all collisions occurring deeper than 5 cm inside the tube, including the mirror holder. (k) Weighted sum of the efficiencies in panels (a-i) by the horizontal velocity pdf of Figure A.5a, in front of each bar we write the thickness of the subsequent ice layer considering radially homogeneous cover of the intake tube and the lower (left) and upper (right) LWC limit for the cloud.

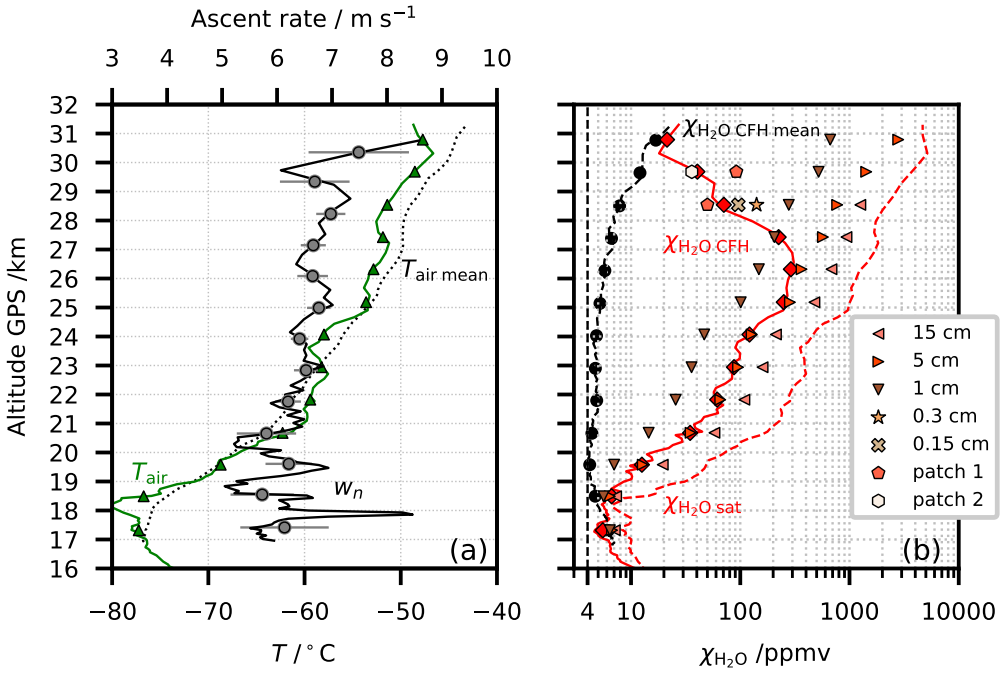

Figure A.7: Stratospheric part of flight NT029 and FLUENT simulation results for the stratospheric sublimation. (a) Green: air temperature; green triangles: 1 km interval averaged air temperature; dotted black: average air temperature for the 2016 Nainital summer campaign; black: ascent velocity; grey circles: 1 km interval averaged ascent velocity; horizontal grey lines: 1 km interval averaged ascent velocity standard deviation. (b) Red: H_2O mixing ratio from the CFH; red diamonds: 1 km interval averaged H_2O mixing ratio from the CFH; dashed black: average H_2O mixing ratio for the uncontaminated soundings during the 2016 Nainital summer campaign; black dots: 1 km interval averaged χ_{H_2O} 2016 Nainital summer campaign; dashed red; saturation H_2O mixing ratio for the air temperature; other markers: FLUENT simulation results for the tube average mixing ratios $\langle \chi_{H_2O} \rangle_{Vol}$ in tubes with different ice coating depths d (full circumference): ◀ d = 15 cm, ▶ d = 5 cm, ▼ d = 1 cm, ★ d = 0.3 cm, cross d = 0.15 cm; (1/8 intake tube circumference): pentagon d =1 cm, hexagon d = 0.45 cm.

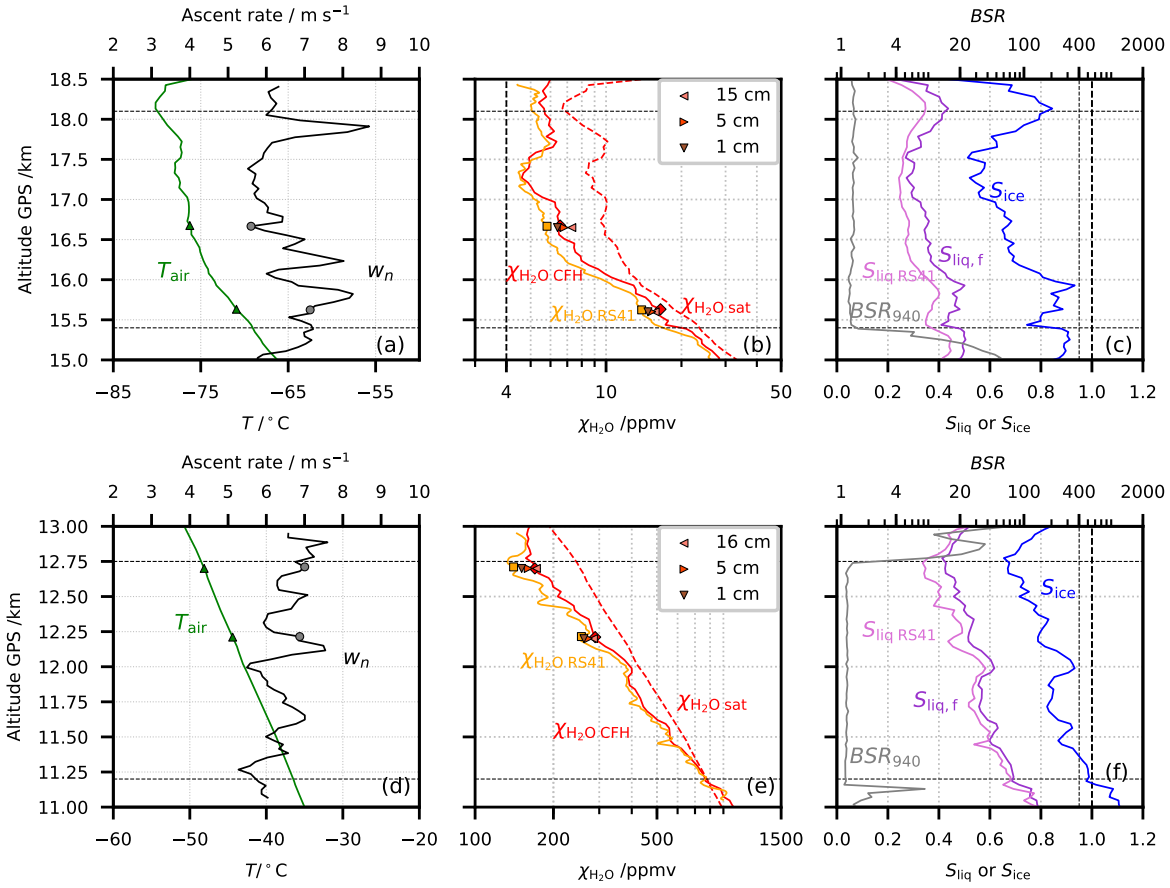

Figure A.8: Upper tropospheric part of flight NT029 and FLUENT simulation results for the upper tropospheric sublimation: (a-c) between cirrus cloud and CPT; (d-f) between mixed-phase cloud and cirrus cloud. (a and d) Green: air temperature; green triangles: air temperature simulation input; black: ascent velocity; grey circles : ascent velocity simulation input. (b and e) Red and red diamonds: H_2O mixing ratio by the CFH; orange: H_2O mixing ratio RS41; orange squares: H_2O mixing ratio RS41 simulation input; dashed red: saturation H_2O mixing ratio for the air temperature; other markers: FLUENT simulation results for the tube average mixing ratios $\langle \chi_{H_2O} \rangle_{Vol}$ in tubes with different ice coating depths d (full circumference): ◀ d = 15 cm, ▶ d = 5 cm, ▼ d = 1 cm. (c and f) Pink: saturation over water ($S_{liq\,RS41}$) by RS41; violet: saturation over water ($S_{liq\,f}$) from CFH considering the deposit on the mirror to be frost; blue: ice saturation (S_{ice}) from CFH; grey: 940-nm backscatter ratio from COBALD. Horizontal dashed lines limit the integration interval used for estimating the sublimated water in the upper troposphere.

Table A.1: FLUENT stratospheric and upper tropospheric simulations input data and results for flight NT029.

Measurements						Simulations		
						1 cm	5 cm	10 cm
h	p	T	w_n	χ_{H_2O}	$\chi_{H_2O\ mean}$	$\langle\chi_{H_2O}\rangle_{Vol}$	$\langle\chi_{H_2O}\rangle_{Vol}$	$\langle\chi_{H_2O}\rangle_{Vol}$
(km)	(hPa)	(°C)	(m s^{-1})	(ppmv)	(ppmv)	(ppmv)	(ppmv)	(ppmv)
30.8	11	-47.7	8.1	21	17	666	2792	NC[1]
29.7	13	-48.5	6.6	40	12	521	1422	NC[1]
28.5	15	-51.4	7.2	71	8	278	771	1256
27.4	18	-51.9	6.8	224	7	205	571	938
26.3	21	-52.8	6.6	291	6	148	364	684
25.2	25	-53.6	6.9	250	5	101	285	477
24.1	30	-58.0	6.5	121	5	47	127	212
22.9	36	-58.2	6.6	88	5	36	95	160
21.8	43	-59.4	6.2	61	5	26	66	109
20.7	52	-62.3	5.9	35	4	15	35	58
19.6	62	-68.7	6.2	13	4	7	13	20
18.5	75	-76.7	6.1	7	5	6	6	7
17.3	92	-77.2	6.0	6	6	7	7	7
16.7	103	-76.2	5.7	6	6 [2]	6	7	7
15.6	123	-70.7	7.0	16	14[2]	15	15	16
12.7	196	-48.1	6.9	170	142[2]	151	160	172
12.2	211	-44.3	7.3	289	249[2]	262	272	285

[1] NC: no convergence

[2] $\chi_{H_2O\ RS41}$

A.2 Flight NT007

Figure A.9 shows the full profile of flight NT007 on the 11 August 2016. As was observed in flights NT011 and NT029, there are contaminated water vapour mixing ratios values in the stratosphere, and contrary to the other flights, there is no recovery of the operation of the CFH before balloon burst. From COBALD, we can identify the presence of two clouds: one extending from T_{air} = 0 °C to T_{air} = -38 °C, the entire mixed-phase cloud regime; and a second one in the cirrus or ice cloud regime, extending all the way to the tropopause.

We believe the lengthy mixed-phase cloud to be the cause of the contamination in the stratosphere, specifically two regions of the cloud, which we expect to be able to support liquid droplets at air temperatures below 0 °C. Details of these two clouds are shown in Figure A.10. Panels (a) and (b) refer to a warmer cloud in air temperatures between -4 and -7 °C, and between 6.25 and 7 km height. Actually, the cloud starts earlier, but we can not be sure if the cloud is liquid, mixed-phase or fully glaciated in this region, because although the S_{ice} and S_{liq} measurements are very close to 1, S_{liq} from RS41 is not precisely 1, which is the expected performance of RS41 in a liquid cloud. Fully glaciated clouds are uncommon at these temperatures (Korolev et al., 2003a). Furthermore, CFH was not operating properly in this region. The deposit on the CFH mirror might be liquid or a mixture of liquid water and ice, rendering the S_{ice} measurement by the CFH senseless. The $S_{\mathrm{liq,d}}$ CFH measurement agrees with S_{liq} by the RS41 to some degree. To continue this analysis we have calculated S_{ice} from RS41 (black) in Figure A.10b. At 6.25 km, there is supersaturation over ice and sub-saturation over water, these conditions allow big supercooled liquid droplets to exist and impact the top of the intake tube. Above 7 km height, the cloud is also sub-saturated in relation to ice, which is consistent with a sublimating glaciated cloud. In this part of the cloud, CFH loses control of the deposit and we see controller oscillations (Vömel et al., 2016). The instrument recovers after the freezing cycle. The presence of a cloud is supported by the COBALD backscatter (BS) measurements. At no other point within the cloud is S_{liq} equal to 1. However, between 9.2 and 9.85 km height, Figure A.10c and A.10d, there is a similar scenario to the one explored for the mixed-phase clouds of flights NT011 and NT029, with S_{ice} = 1.2 and S_{liq} = 0.95.

We modelled the two clouds and results are presented in Figure A.11. Again the lower and upper limit of LWC are defined by the water vapour sublimated in the stratosphere and upper tropopshere. However, for flight NT007, both the upper and lower limit of LWC are lower limits, because the water vapour measurement in the stratosphere by the CFH did not recover. Again, we have considered similar droplets and ice crystal sizes for the distributions of both NT007 clouds. With the exception, that we considered the bigger size droplets of $r_{liq,3}$ = 200 μm to be present in cloud 1, between 6.25 and 7 km height, and not in cloud 2, between 9.2 and 9.85 km height. With the prescribed initial liquid droplet and ice crystal distributions, cloud 1 existed at the observed S_{ice} and S_{liq} for about 1 hour, and cloud 2 for about 12 minutes. In both cases, reasonable time for the payload to travel through them at about 3 to 5 m s^{-1} ascent velocity.

Figure A.12 shows the pendulum analysis for the two mixed-phase cloud regions of NT007. The amplitude of the oscillation in these two cloud regions is smaller than the ones observed for the clouds of flights NT011 and NT029. The maximum amplitude of oscillation for the two clouds is about 25 to 30 m, while for the other clouds was 40 m. The smaller amplitudes are related to the slower ascent

velocities of this balloon. The ascent velocities (w_n) are smaller, but so are the horizontal velocities (v_h) experienced at the intake tube inlet, which still causes big impingement angles (β), as can be seen in Figure A.13: Panels (a), (b) and (c) refer to the warmer cloud region (cloud 1), and Panels (d), (e) and (f) refer to the colder cloud region (cloud 2).

Figure A.14 shows the FLUENT simulation results for the collision/ freezing efficiency of hydrometeors in the intake tube for the mixed-phase cloud 1 of flight NT007. For this simulation we consider the presence of small droplets ($r_{\mathrm{liq},1} = 10$ μm) also inside the mixed-phase cloud because the balloon comes from a region where S_liq might have been 1 (see Figure A.9). As mentioned in Section 2.4.2.2, the small droplets are more connected with the flow and their collision/ freezing efficiency is much smaller than for bigger droplets. At small angles, e.g. 13° shown in Figure A.14a, most of the droplets, which freeze in the intake tube, freeze in the 'rest of the tube' category, below the mirror extrusion in this case. For bigger angles, the contribution from the 'rest of the tube' category decreases. At angles of 50° the small liquid droplets are colliding at the top of the intake tube, but less than 50%, unlike the bigger droplets (e.g. $r_{\mathrm{liq},2} = 100$ μm droplets), which freeze at 100% rate. The freezing efficiency of the bigger droplets, $r_{\mathrm{liq},3} = 200$ μm, does not differ significantly from the freezing efficiency for $r_{\mathrm{liq},2}$-droplets, so, when calculating the ice layer thickness and overall efficiency, we do not differentiate between droplet size if they are bigger than or equal to $r_{\mathrm{liq},2} = 50$ μm. Figure A.15 shows the FLUENT simulation results for collision/ freezing efficiency of hydrometeors in the intake tube for the cold cloud region (cloud 2) of flight NT007. If we consider the thickest ice layer inside the intake tube after both clouds: the layer between 1 - 2 cm, and the upper limit of LWC, the ice layer is only 25 μm thick, which represents a 0.4 % decrease of air flow in the intake tube.

Figure A.16 shows the stratosphere, and FLUENT simulation input, and results for flight NT007. We can see again how slow flight NT007 was in comparison to the other two flights and how the temperature in the stratosphere shows a wave-like behaviour around the average temperature profile of the season. For flight NT007, we did less FLUENT simulations than for the other two flights. We took 1 km interval averaged values as input, but only used these values once every two kilometres: only the values shown in Table A.2 were used for the simulations. Some of the simulations with lower pressures (11 hPa), higher temperatures and longer intake tube ice coverage (15 cm) did not converge. After 24 km height, we do not have any more converged 15 cm intake tube ice covered wall simulations. After this height, also the $\langle\chi_{\mathrm{H_2O}}\rangle_{\mathrm{Vol}}$ of the 5 cm intake tube ice covered wall simulation starts overestimating the water vapour mixing ratio ($\chi_{\mathrm{H_2O}}$) observed by CFH which is consistent with the intake tube ice covered surface decreasing. To sustain the contamination up to these heights and for the duration of this flight, there should have been a very thick ice layer in the intake tube, maybe the 25 μm mentioned before is thick enough, either way the contamination should have been about to recover. The integrated excess water vapour in the stratosphere for flight NT007 is 65.5 mg.

To evaluate the upper tropospheric sublimation of the ice covered intake tube during flight NT007, we chose the two location shown in Figure A.17. Both locations show $S_\mathrm{ice} < 0.7$ and the simulation results are consistent with the other two flights. It is worth mentioning that RS41 is measuring lower water vapour mixing ratio than the CFH in the upper tropopshere as expected, but, once S_ice approaches 1 at 13.8 km height, CFH under-estimates the water vapour measurement in relation to the RS41. We suppose that the icy intake tube top is having the opposite effect now in contaminating the CFH measurement. It is depleting the gas phase water vapour, and growing the ice coverage, reducing

the supersaturation which in a clean intake tube case would have been observed. COBALD sees no cloud in this region. The observed part of the upper troposphere includes the CFH clearing cycle. We remove the clearing cycle part for the excess water vapour integration in this region. The integrated water vapour for the upper troposphere of flight NT007 is 4.4 mg below the clearing cycle and 43.5 mg above the clearing cycle. In total, we observe 113 mg more of water in flight NT007 than what was expected without contamination. Results are presented in Table 2.3.

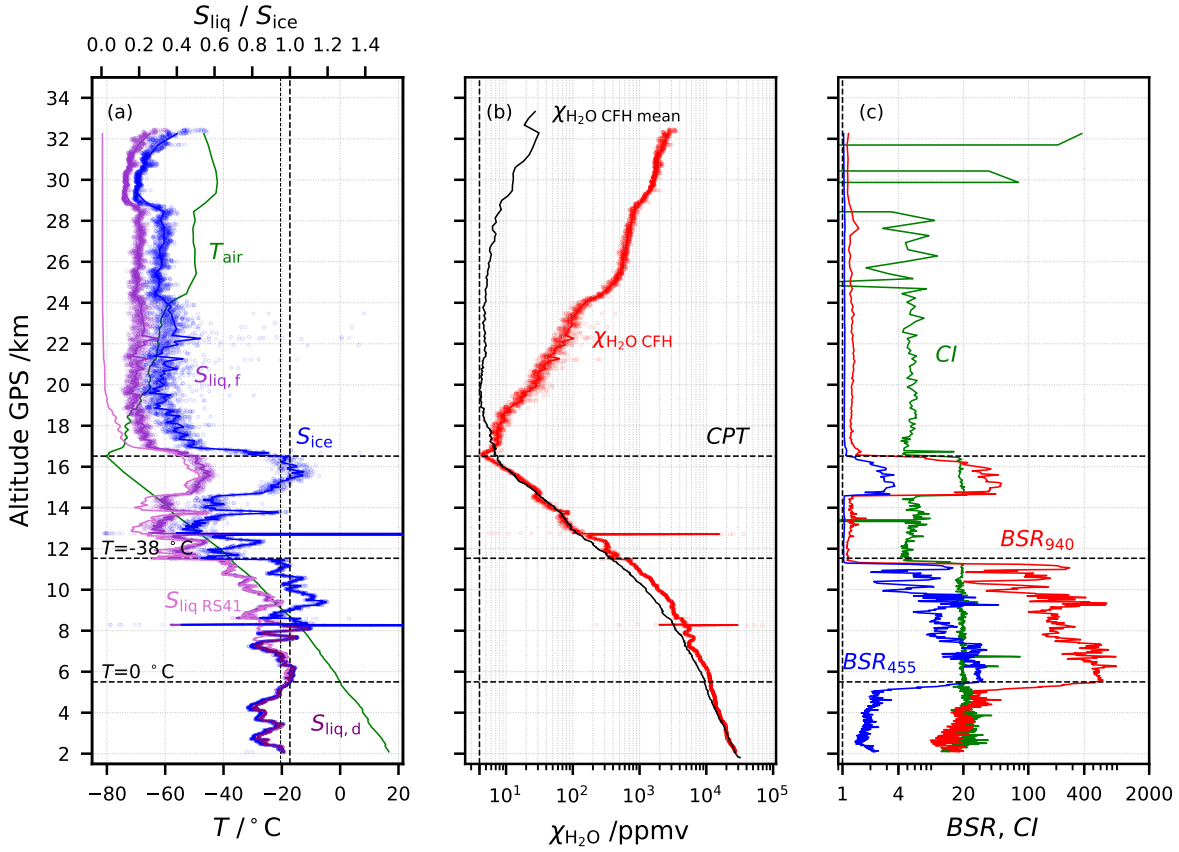

Figure A.9: Flight NT007 in Nainital, India, on 11 August 2016. Lines: 1 hPa interval averaged values. Dots: 1 s data. (a) Green: air temperature measurement from Vaisala RS41; pink: saturation over water ($S_{\mathrm{liq\ RS41}}$) measured by RS41; blue: ice saturation (S_{ice}) from CFH; purple: saturation over water ($S_{\mathrm{liq,d}}$) from CFH considering the deposit on the mirror to be dew; violet: saturation over water ($S_{\mathrm{liq,f}}$) from CFH considering the deposit on the mirror to be frost. (b) Red: H_2O mixing ratio from CFH in ppmv; black: average H_2O mixing ratio from uncontaminated CFH for the Nainital 2016 summer campaign (Brunamonti et al., 2018); 'CPT' marks the cold point tropopause. (c) Red: 940-nm backscatter ratio from COBALD; blue: same for 455 nm; green: color index (CI) from COBALD.

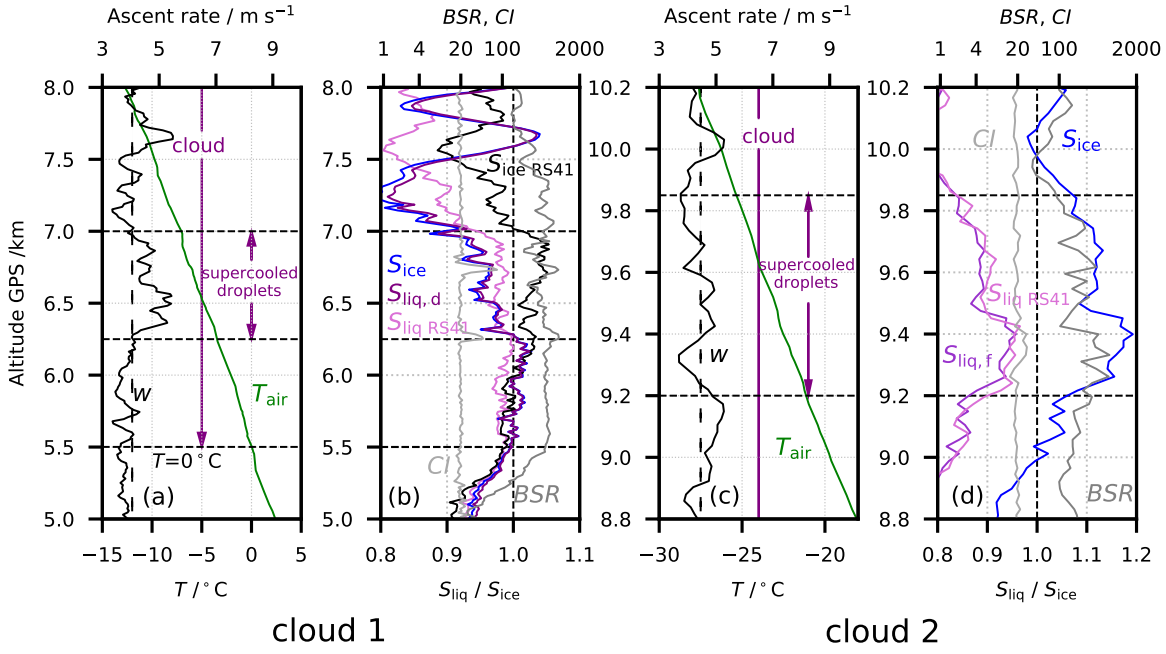

Figure A.10: Mixed-phase cloud details of flight NT007. Lines: 1 hPa interval averaged values. (a-b) Cloud 1; (c-d) cloud 2. (a and c) Green: air temperature; black: ascent velocity by RS41 in m s^{-1}. (b and d) Pink: saturation over water ($S_{\mathrm{liq\,RS41}}$) by RS41; purple: saturation over water ($S_{\mathrm{liq,d}}$) from CFH considering the deposit on the mirror to be dew; violet: saturation over water ($S_{\mathrm{liq,f}}$) from CFH considering the deposit on the mirror to be frost; blue: ice saturation (S_{ice}) from CFH; black: ice saturation ($S_{\mathrm{ice\,RS41}}$) from RS41; dark grey: 940-nm backscatter ratio from COBALD; light grey: color index (CI) from COBALD. Horizontal dashed lines mark supercooled droplet region and T_{air}= 0 °C.

Table A.2: FLUENT stratospheric and upper tropospheric simulations input data and results for flight NT007.

Measurements						Simulations		
						1 cm	5 cm	10 cm
h	p	T	w_n	χ_{H_2O}	$\chi_{H_2O\ \mathrm{mean}}$	$\langle\chi_{H_2O}\rangle_{\mathrm{Vol}}$	$\langle\chi_{H_2O}\rangle_{\mathrm{Vol}}$	$\langle\chi_{H_2O}\rangle_{\mathrm{Vol}}$
(km)	(hPa)	(°C)	(m s^{-1})	(ppmv)	(ppmv)	(ppmv)	(ppmv)	(ppmv)
30.7	11	-43.4	3.3	1831	16	NC[1]	NC[1]	NC[1]
28.6	15	-48.3	4.0	897	8	551	1477	NC[1]
26.3	22	-49.9	3.9	590	6	319	849	NC[1]
24.1	30	-56.8	3.5	190	5	72	193	314
21.8	43	-62.6	3.7	66	5	22	53	86
19.6	63	-67.0	3.4	21	4	9	19	29
17.4	92	-74.0	3.8	7	6	7	8	9
14.1	158	-59.6	3.1	44	31	32	38	38
13.0	188	-50.4	4.5	93	56	64	79	97

[1] NC: no convergence

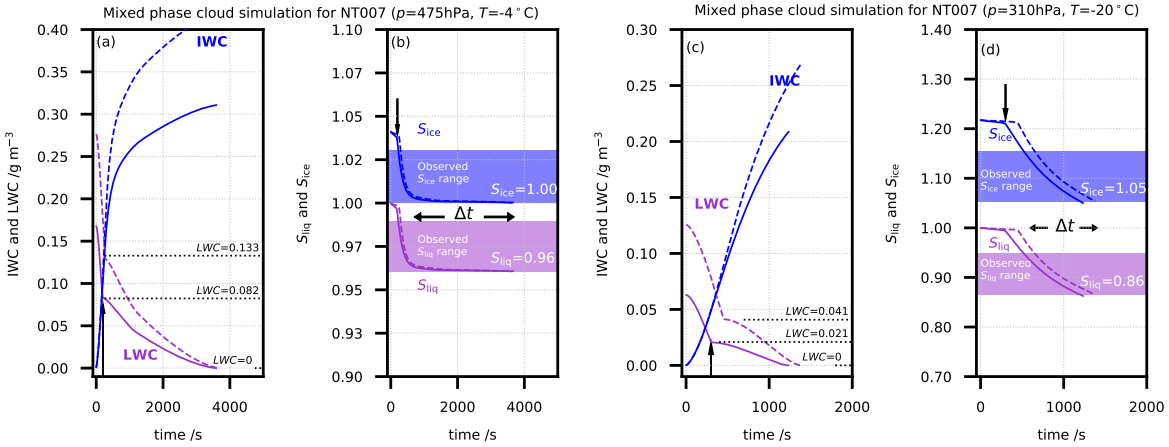

Figure A.11: Mixed-phase cloud modelling of the Wegener- Bergeron-Findeisen process demonstrating that flight NT007 likely flew through supercooled liquid droplets in two occasions: (a-b) refer to cloud 1 between 6.25 and 7 km height and (c-d) refer to cloud 2 between 9.2 and 9.85 km height. Solid lines: lower limit of liquid water content (LWC). Dashed lines: upper limit (see text). **(a-b)** Initial size distributions for lower limit simulation: $n_{\mathrm{ice}} = 0.02$ cm^{-3}, $r_{\mathrm{ice}} = 10$ μm; $n_{\mathrm{liq},1} = 20$ cm^{-3}, $r_{\mathrm{liq},1} = 10$ μm; $n_{\mathrm{liq},2} = 0.004$ cm^{-3}, $r_{\mathrm{liq},2} = 100$ μm; $n_{\mathrm{liq},3} = 0.002$ cm^{-3}, $r_{\mathrm{liq},3} = 200$ μm. Initial size distributions for upper limit simulation are identical but with 75% larger $n_{\mathrm{liq},1}$ and $n_{\mathrm{liq},2-3}$. (a) Blue: ice water content (IWC); purple: liquid water content (LWC); vertical arrows: time when smaller liquid droplets fully evaporated. (b) Blue: ice saturation ratio (S_{ice}); purple: liquid water saturation ratio (S_{liq}) for lower and upper limits. Glaciation times of small droplets $\tau_{g,1} \sim 4$ minutes, of big droplets $\tau_{g,2-3} \sim 60$ minutes. Shaded saturation ratios: observed ranges from Figure A.10b. The computed time interval with S_{ice} and S_{liq} matching flight observations is $\Delta t \sim 60$ minutes. **(c-d)** Initial size distributions for lower limit simulation: $n_{\mathrm{ice}} = 0.02$ cm^{-3}, $r_{\mathrm{ice}} = 10$ μm; $n_{\mathrm{liq},1} = 10$ cm^{-3}, $r_{\mathrm{liq},1} = 10$ μm; $n_{\mathrm{liq},2} = 0.005$ cm^{-3}, $r_{\mathrm{liq},2} = 100$ μm. Initial size distributions for upper limit simulation are identical but with 2× larger $n_{\mathrm{liq},2}$. (c) Blue: ice water content (IWC); purple: liquid water content (LWC); vertical arrows: time when smaller liquid droplets fully evaporated. (d) Blue: ice saturation ratio (S_{ice}); purple: liquid water saturation ratio (S_{liq}) for lower and upper limits. Glaciation times of small droplets $\tau_{g,1} \sim 8$ minutes, of big droplets $\tau_{g,2} \sim 18$ minutes. Shaded saturation ratios: observed ranges from Figure A.10d. The computed time interval with S_{ice} and S_{liq} matching flight observations is $\Delta t \sim 12$ minutes.

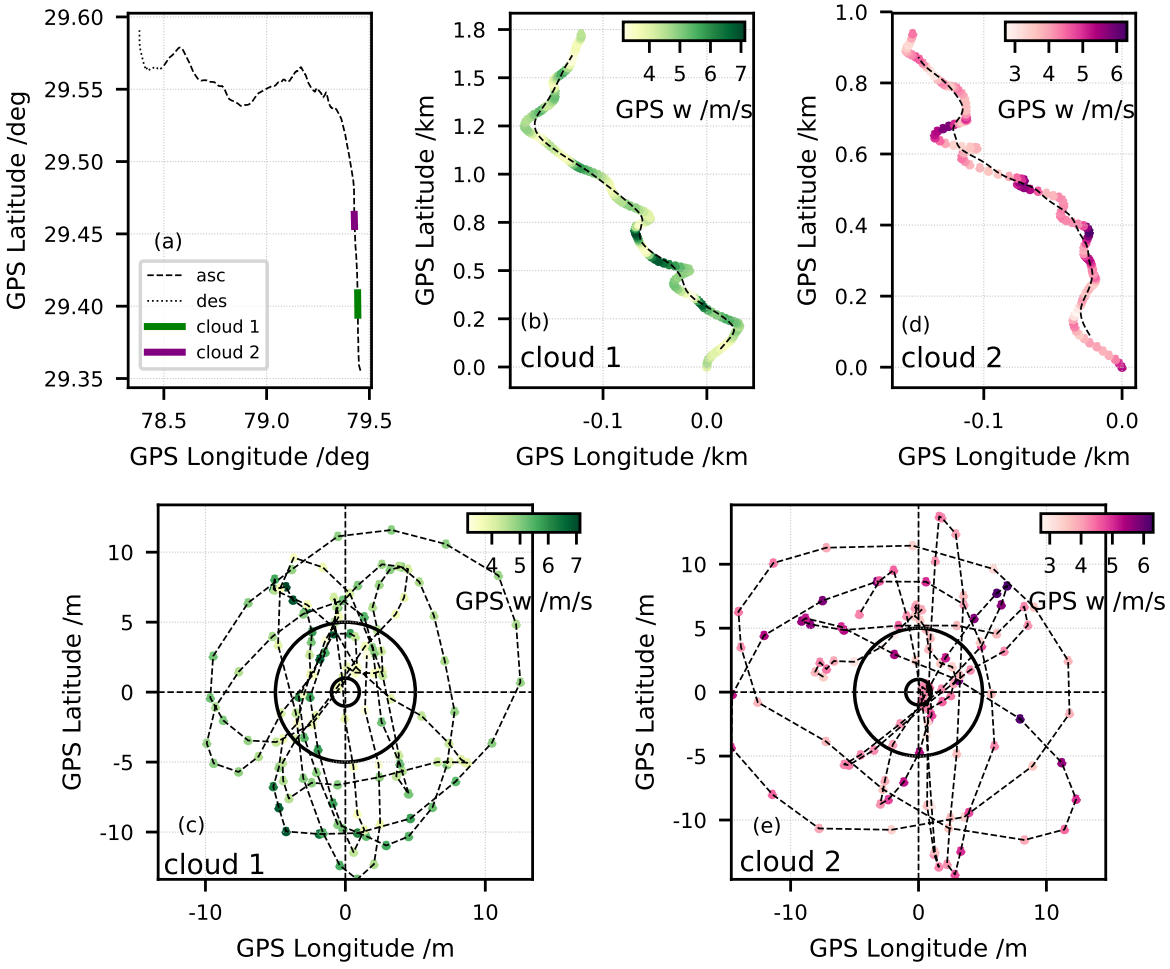

Figure A.12: Pendulum analysis for mixed-phase clouds of flight NT007. (a) Payload trajectory: ascent (dashed), descent (dotted), mixed-phase cloud 1 between 6.25 and 7 km height (thick green) and mixed-phase cloud 2 between 9.2 and 9.85 km height (thick purple). (b) Zoom in on the mixed-phase cloud 1 with 1-second GPS data of payload trajectory (symbols) and balloon trajectory (dashed). (c) Detrended payload oscillations for cloud 1 ; approximate balloon sizes on the ground (r = 1 m) and at burst (r = 5 m) are shown by two circles. (d) Same as in (b) but for cloud 2. (e) Same as in (c) but for cloud 2. Colour code in (b-e): balloon ascent velocity.

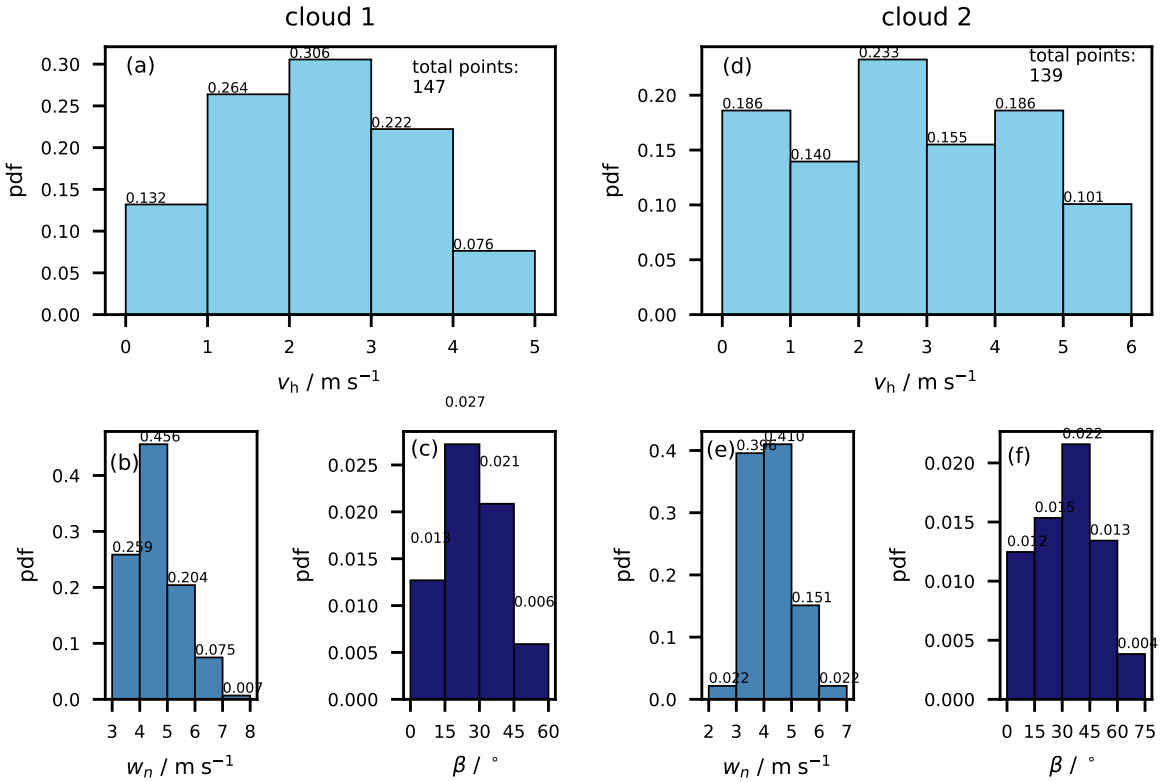

Figure A.13: Probability density functions (pdf) of impingement parameters at the inlet plane of the CFH intake tube during the passage through the mixed-phase cloud of flight NT007. (a-c) cloud 1 between 6.25 and 7 km height; (d-f) refer to cloud 2 between 9.2 and 9.85 km height. (a and d) Horizontal velocity (v_h); (b and e) normal velocity (w_n); (c and f) inlet angle (β).

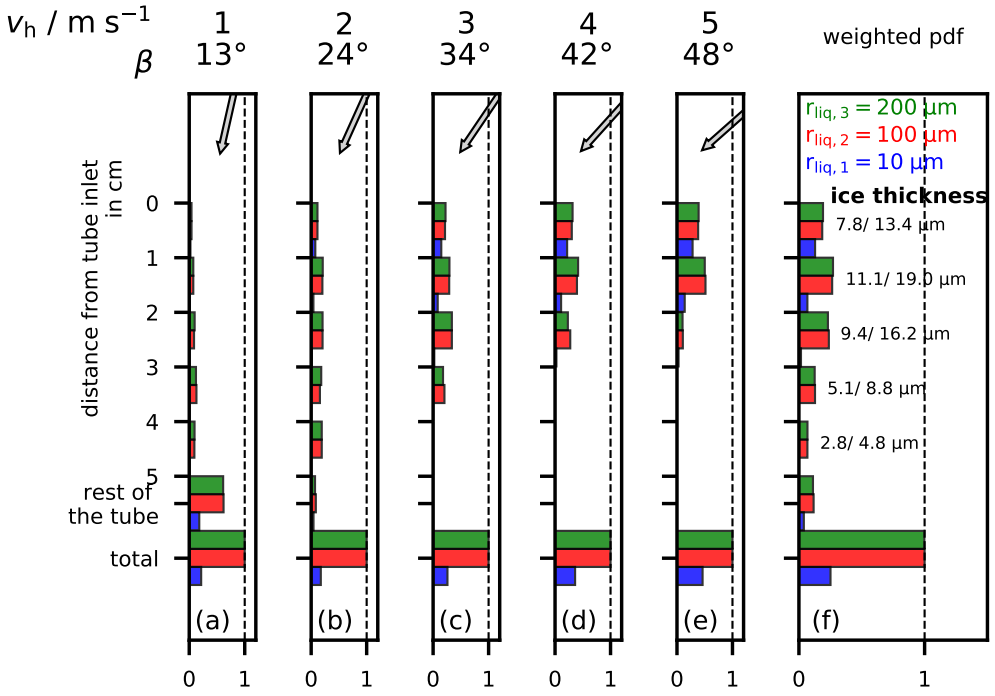

Figure A.14: Collision/freezing efficiency of hydrometeors in the intake tube for mixed-phase cloud 1 of flight NT007 with vertical inlet velocity $\langle w_n \rangle = 4.5$ m s^{-1}. $r_{liq,3} = 200$ μm (green), $r_{liq,2} = 100$ μm (red), $r_{liq,1} = 10$ μm (blue). (a-e) Freezing efficiency for various horizontal inlet velocities: (a) 1 m s^{-1}, 13°; (b) 2 m s^{-1}, 24°; (c) 3 m s^{-1}, 34°; (d) 4 m s^{-1}, 42°; (e) 5 m s^{-1}, 48°. The 'rest of the tube' takes account of all collisions occurring deeper than 5 cm inside the tube, including the mirror holder. (f) Weighted sum of the efficiencies in panels (a-e) by the horizontal velocity pdf of Figure A.13a, in front of each bar we write the thickness of the subsequent ice layer considering radial homogeneous cover of the intake tube and the lower (left) and upper (right) LWC limit for the cloud.

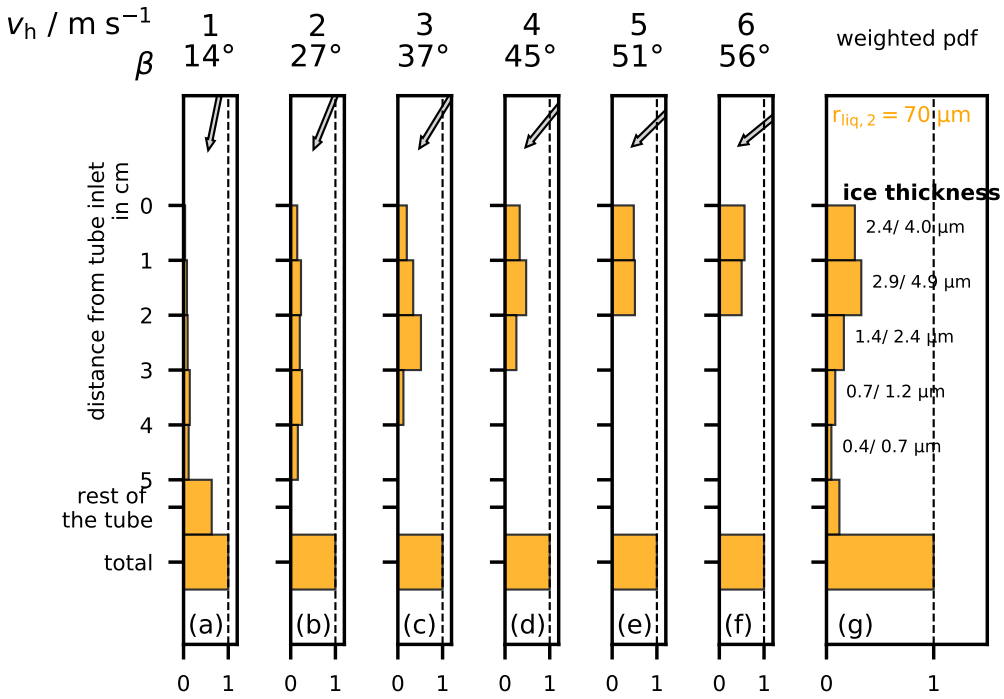

Figure A.15: Collision/freezing efficiency of hydrometeors in the intake tube for mixed-phase cloud 2 of flight NT007 with vertical inlet velocity $\langle w_n \rangle = 4.0$ m s^{-1}. $r_{\mathrm{liq},2} = 70$ μm (yellow). (a-f) Freezing efficiency for various horizontal inlet velocities: (a) 1 m s^{-1}, 14°; (b) 2 m s^{-1}, 27°; (c) 3 m s^{-1}, 37°; (d) 4 m s^{-1}, 45°; (e) 5 m s^{-1}, 51°; (e) 6 m s^{-1}, 56°. The 'rest of the tube' takes account of all collisions occurring deeper than 5 cm inside the tube, including the mirror holder. (g) Weighted sum of the efficiencies in panels (a-f) by the horizontal velocity pdf of Figure A.13d, in front of each bar we write the thickness of the subsequent ice layer considering radial homogeneous cover of the intake tube and the lower (left) and upper (right) LWC limit for the cloud.

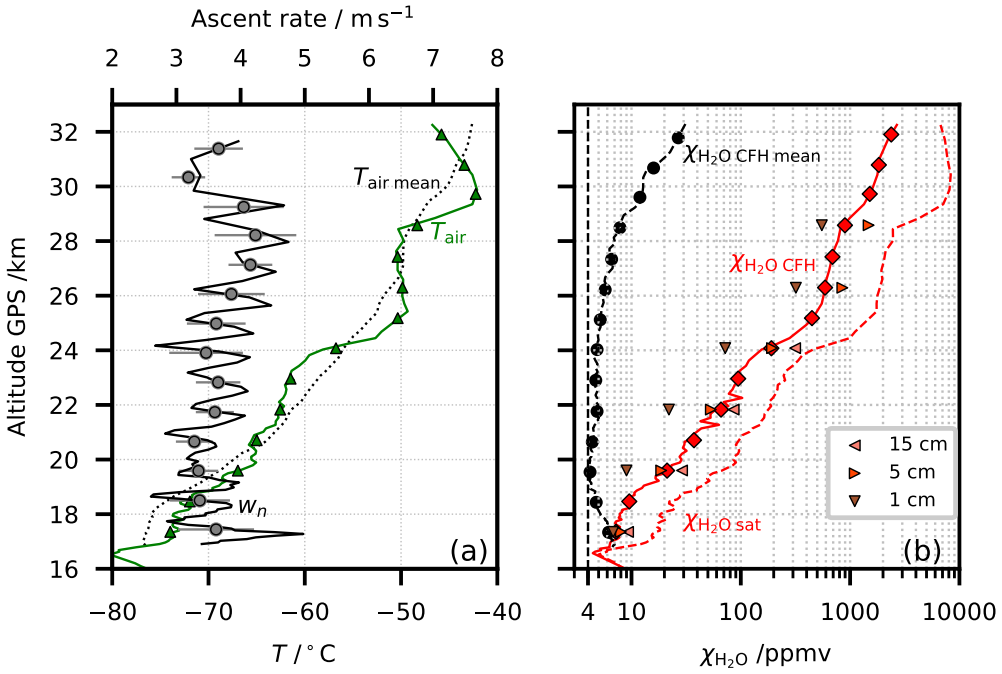

Figure A.16: Stratospheric part of flight NT007 and FLUENT simulation results for the stratospheric sublimation. (a) Green: air temperature; green triangles: 1 km interval averaged air temperature; dotted black: average air temperature for the 2016 Nainital summer campaign; black: ascent velocity; grey circles: 1 km interval averaged ascent velocity; horizontal grey lines: 1 km interval averaged ascent velocity standard deviation. (b) Red: H_2O mixing ratio from the CFH; red diamonds: 1 km interval averaged H_2O mixing ratio from the CFH; dashed black: average H_2O mixing ratio for the uncontaminated soundings during the 2016 Nainital summer campaign; black dots: 1 km interval averaged χ_{H_2O} 2016 Nainital summer campaign; dashed red; saturation H_2O mixing ratio for the air temperature; other markers: FLUENT simulation results for the tube average mixing ratios $\langle\chi_{H_2O}\rangle_{Vol}$ in tubes with different ice coating depths d (full circumference): ◀ $d = 15$ cm, ▶ $d = 5$ cm, ▼ $d = 1$ cm.

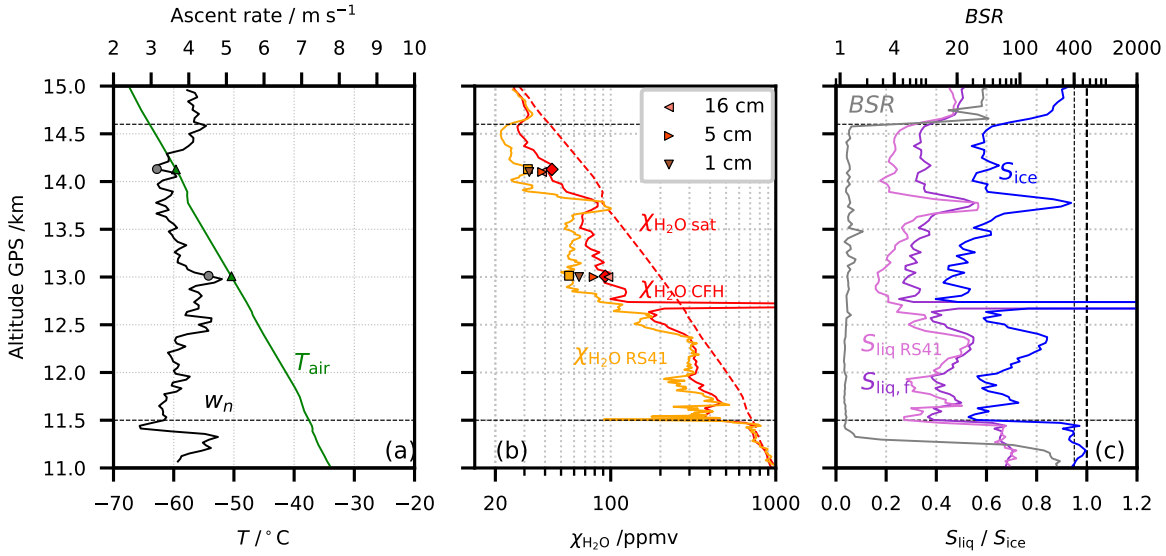

Figure A.17: Upper tropospheric part of flight NT007 and FLUENT simulation results for the upper tropospheric sublimation. (a) Green: air temperature; green triangles: air temperature simulation input; black: ascent velocity; grey circles : ascent velocity simulation input. (b) Red and red diamonds: H_2O mixing ratio by the CFH; orange: H_2O mixing ratio RS41; orange squares: H_2O mixing ratio RS41 simulation input; dashed red: saturation H_2O mixing ratio for the air temperature; other markers: FLUENT simulation results for the tube average mixing ratios $\langle\chi_{H_2O}\rangle_{Vol}$ in tubes with different ice coating depths d (full circumference): ◀ d = 15 cm, ▶ d = 5 cm, ▼ d = 1 cm. (c) Pink: saturation over water ($S_{liq\,RS41}$) by RS41; violet: saturation over water ($S_{liq\,f}$) from CFH considering the deposit on the mirror to be frost; blue: ice saturation (S_{ice}) from CFH; grey: 940-nm backscatter ratio from COBALD. Horizontal dashed lines limit the integration interval used for estimating the sublimated water in the upper troposphere.

A.3 FFT analysis

We performed a Fast Fourier Transform (FFT) analysis on the latitude and longitude time series of the payload's oscillatory motion. For this analysis we considered the detrended latitude and longitude GPS data for the mixed-phase cloud section of sounding NT011 using different length time kernels for the smoothing procedure: 7 s, 9 s, 11 s, 13 s and 20 s. The results from this analysis are shown in Figure A.18. We conclude that independently of the length of the applied kernel, the highest power frequency was $\nu \sim 0.06$ s^{-1},which corresponds to an oscillation period $\tau \sim 16.6$ s.

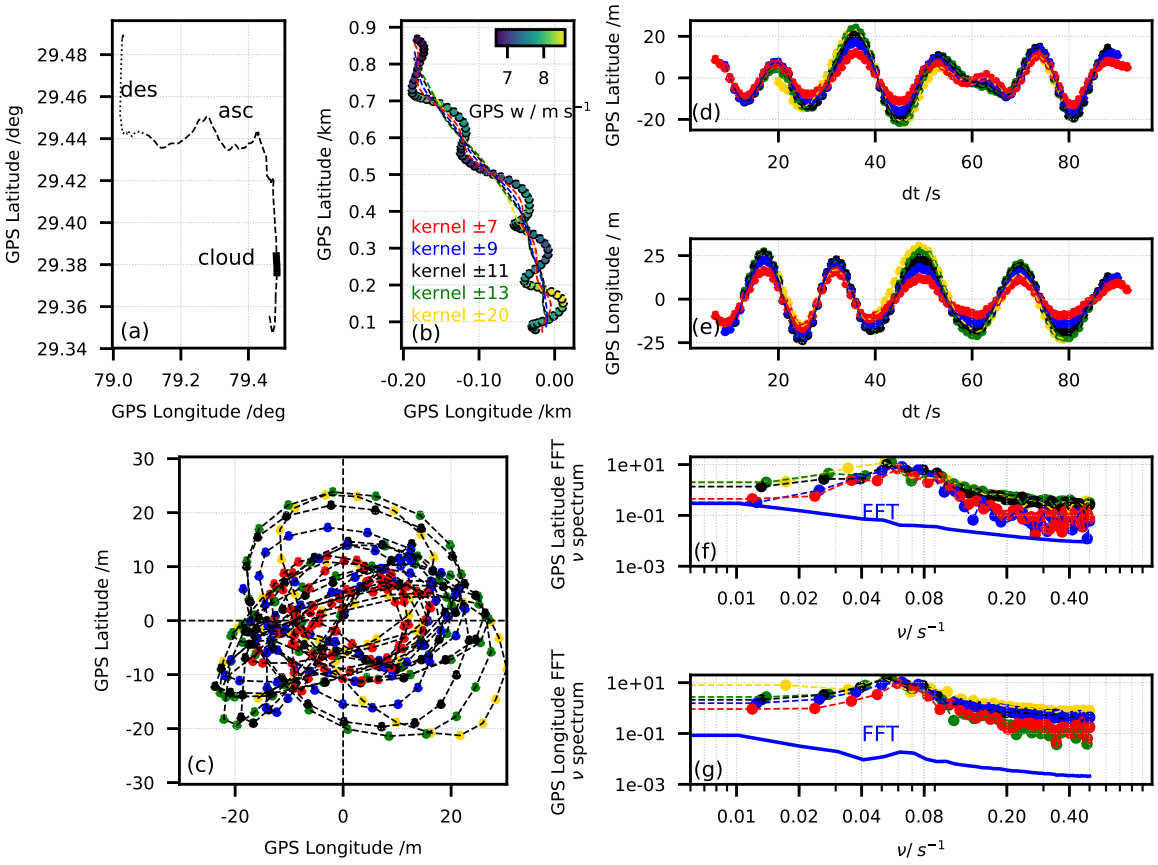

Figure A.18: Fast Fourier Transform (FFT) analysis for the determination of the pendulum oscillation period applied to mixed-phase cloud of flight NT011. (a) Payload trajectory: ascent (dashed), descent (dotted) and mixed-phase cloud between 9.25 and 10 km height (thick black). (b) Zoom-in of the mixed-phase cloud: payload trajectory (ascent velocity coloured dots) and balloon trajectories (dashed lines). The different lines have been smoothed from the payload trajectory with different kernels (moving average intervals); yellow: ±20 s; green: ±13 s; black: ±11 s; blue: ±9 s; red: ±7 s. The colour code applies to the subsequent panels. (c) De-trended payload oscillations; (d) time series of the latitude values used in panel (c); (e) time series of the longitude values used in panel (c); (f) power frequency spectrum of the latitude time series after FFT analysis; (g) power frequency spectrum of the longitude time series after FFT analysis.

A.4 Impingement angles

The balloon ascent velocity (w) can be decomposed in two components according to the payloads angle in relation to the balloon ascent direction: one perpendicular to the intake intake tube walls ($w_\perp$) and another parallel to the intake tube walls ($w_{||}$) respectively:

$$w_\perp = w\ \cos^{-1}(\alpha(t)) \tag{A.1a}$$

$$w_{||} = w\ \sin^{-1}(\alpha(t)) \tag{A.1b}$$

where α is the angle due to payload displacement.

$w_\perp$ is the $v_{\perp,\,\mathrm{tilt}}$ component of the inlet flow perpendicular component ($v_\perp$). The other component due to the payload rotational movement ($v_{\perp,\,\mathrm{rot}}$) can be calculated as

$$|v_{\perp,\,\mathrm{rot}}| = \frac{\sqrt{(R(t+1)_\mathrm{y} - R(t)_\mathrm{y})^2 + (R(t+1)_\mathrm{x} - R(t)_\mathrm{x})^2}}{\Delta t} \tag{A.2}$$

where $R(t)$ and $R(t+1)$ are consecutive de-trended trajectory points and $\Delta t = 1$ s.

The perpendicular component $w_\perp$ of the balloon ascent velocity, or $v_{\perp,\,\mathrm{tilt}}$ can be projected into the horizontal plane of the oscillation movement as $v_{\perp,\,\mathrm{tilt_x}}$ and $v_{\perp,\,\mathrm{tilt_y}}$. We believe $v_{\perp,\,\mathrm{tilt}}$ to be aligned towards the center of the oscillation (0,0) as shown in Figure 2.6b. We calculate this direction as $\theta(t)$:

$$\theta(t) = \tan^{-1}\left(\frac{R(t)_\mathrm{y}}{R(t)_\mathrm{x}}\right) \tag{A.3a}$$

$$v_{\perp,\,\mathrm{tilt_y}} = \mathrm{sign}\,(R(t)_\mathrm{y})\ v_{\perp,\,\mathrm{tilt}}\ \sin\theta(t) \tag{A.3b}$$

$$v_{\perp,\,\mathrm{tilt_x}} = \mathrm{sign}\,(R(t)_\mathrm{x})\ v_{\perp,\,\mathrm{tilt}}\ \cos\theta(t) \tag{A.3c}$$

We then calculate the total perpendicular component of inlet flow velocity $v_\perp$ as

$$v_\perp = \sqrt{(v_{\perp,\,\mathrm{rot_x}} + v_{\perp,\,\mathrm{tilt_x}})^2 + (v_{\perp,\,\mathrm{rot_y}} + v_{\perp,\,\mathrm{tilt_y}})^2} \tag{A.4}$$

The angle of $v_\perp$ on the horizontal plane is not relevant. We assume it is evenly distributed and hence the coating of the intake tube will be more or less radially homogeneous. The impingement angle can then be calculated as

$$\beta = \tan^{-1}\left(\frac{v_\perp}{w_{||}}\right) \tag{A.5}$$

from the parallel component of the ascent speed $w_{||}$ and perpendicular component $v_\perp$ of the inlet flow to the intake tube walls.

Appendix B

Instrument description

B.1 Thermoelectric effect: Peltier element and thermocouples operating principles

The Seebeck effect

In a thermoelectric material there are free electrons or holes which carry both charge and heat. To a first approximation, the electrons and holes in a thermoelectric semiconductor/metal behave like a gas of charged particles.

If a normal (uncharged) gas is placed in a box within a temperature gradient, where one side is cold and the other is hot, the gas molecules at the hot end will move faster than those at the cold end. The faster hot molecules will diffuse further than the cold molecules and so there will be a net build-up of molecules (higher density) at the cold end. The density gradient will drive the molecules to diffuse back to the hot end. In the steady state, the effect of the density gradient will exactly counteract the effect of the temperature gradient so there is no net flow of molecules. If the molecules are charged, the build-up of charge at the cold end will also produce a repulsive electrostatic force (and therefore electric potential) to push the charges back to the hot end.

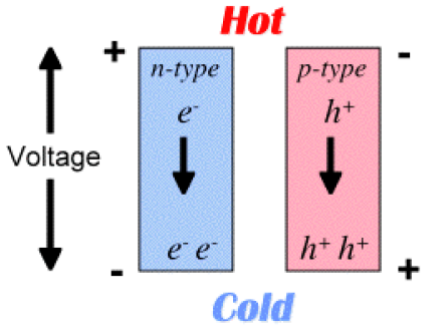

Figure B.1: Thermoelectric materials – Seebeck effect – electric potential produced by temperature difference

The electric potential (Voltage) produced by a temperature difference is known as the Seebeck

effect and the proportionality constant is called the Seebeck coefficient. If the free charges are positive (the material is p-type), positive charge will build up on the cold which will have a positive potential. Similarly, negative free charges (n-type material) will produce a negative potential at the cold end, see Figure B.1.

Thermal power peak and band gap

In a semiconductor at high enough temperature electrons will have high enough energy to excite across the band gap. When that happens there will be both n-type carriers in the conduction band and p-type carriers in the valence band such that the resultant thermal power (absolute value of Seebeck coefficient) will be compensated (reduced) because the two contributions subtract. In a heavily doped semiconductor, where the dopant produces many majority carriers (could be either n-type or p-type) the thermal power will be reduced at high temperature due to the excitation of minority carriers of opposite sign. Although there are fewer minority carriers than majority carriers, they have a larger thermal power. This leads to a peak in the thermal power as a function of temperature as seen in Figure B.2.

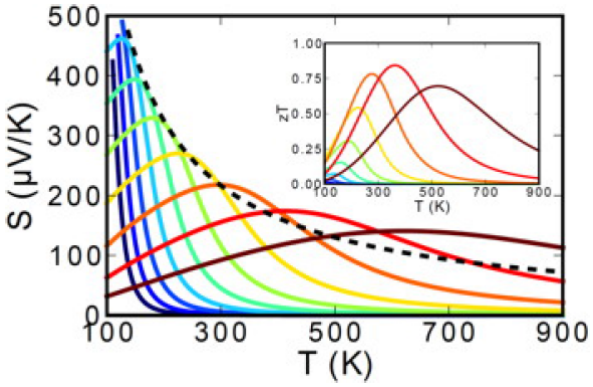

Figure B.2: Change of the Seebeck effect coefficient by changes in doping – lightly doped (blue) to heavily doped (red)

Thermo-electric power generation

If the hot ends of the n-type and p-type material are electrically connected, and a load connected across the cold ends, the voltage produced by the Seebeck effect will cause current to flow through the load, generating electrical power. The electrical power produced is the product of the voltage and electrical current across the load. The temperature difference provides the voltage but it is the heat flow which enables the current.

Electrical model

$$V = \alpha \cdot \Delta T - I \cdot R_{TE} \tag{B.1}$$

In equation B.1, V is the voltage across the thermo-element, I is the electrical current, R_{TE} is the resistance of the thermo-element, α is the Seebeck coefficient and ΔT the temperature difference

across the thermo-element.

The resistance of the thermoelectric elements depend on the electrical resistivity as well as the length and cross sectional area. Just as the power in a resistor is V^2/R the power produced in a thermoelectric generator depends on the square of the voltage (Seebeck coefficient and temperature difference) divided by the resistivity. Notice also that the power per area can be arbitrarily adjusted with the length of the elements.

$$R_i = \rho_i \cdot \frac{l}{A_i} \tag{B.2}$$

In equation B.2, R_i is the resistance of the thermoelectric element, ρ_i is the element's resistivity, l is the length of the element and A_i their cross-sectional area.

Thermal conductance is analogous to the electrical resistance, but with heat playing the role of current and temperature difference the role of voltage.

$$K_i = k_i \cdot \frac{A_i}{l} \tag{B.3}$$

In equation B.3, K_i is the thermal conductance of the thermoelectric element, k_i is the element's thermal conductivity, l and A_i are as in equation B.2.

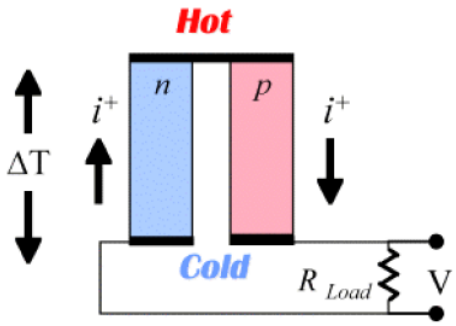

Figure B.3: Thermo-electric power generator

Thermoelectric Figure of Merit

The efficiency of a generator depends not just on the power produced but also how much heat is provided at the hot end. The heat input is needed for the thermoelectric process (Peltier effect) as well as the normal thermal conduction (Fourier's law) and is offset by the Joule heating in the device. The Fourier's law of thermal conduction of the thermoelectric materials adds a thermal path from hot to cold that consumes some heat and reduces the efficiency. It can be shown that the maximum efficiency of a thermoelectric material depends on two terms. The first is the efficiency (η), which for all heat engines cannot exceed Carnot efficiency (η_{max}, equation B.4). The second is a term that depends on the thermoelectric properties, Seebeck coefficient (α), electrical resistivity (ρ) and thermal conductivity (k). These material properties all appear together and thus form a new material property which we call zT - the Thermoelectric Figure of Merit. For small temperature difference this efficiency is given by equation B.5. Notice also that the extensive geometric parameters, length and area have

dropped out of this expression for maximum efficiency.

$$\eta_{max} = \frac{\Delta T}{T_h} \cdot \frac{\sqrt{1+zT}-1}{\sqrt{1+zT}+1} \tag{B.4}$$

$$zT = \frac{\alpha^2 \cdot T}{\rho \cdot k} \tag{B.5}$$

Peltier cooling

If instead of having the heat flow drive the charge flow, we use an external electric potential to drive the heat carrying charges, then we can force heat to flow from one end to the other as illustrated in Figure B.4. The coefficient of performance and the maximum temperature drop that can be achieved is related to the efficiency of the thermoelectric materials through the thermoelectric Figure of Merit zT.

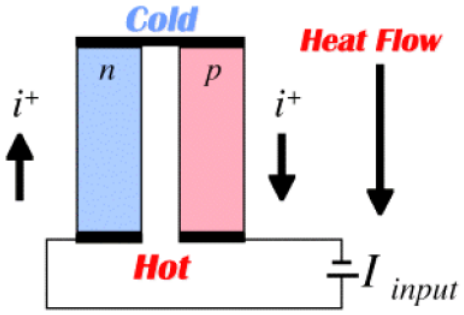

Figure B.4: Peltier cooling

Thermoelectric materials development

A material with a large thermoelectric power factor and therefore zT, needs to have a large Seebeck coefficient (found in low carrier concentration semiconductors or insulators) and a large electrical conductivity (found in high carrier concentration metals). The thermoelectric power factor maximizes somewhere between a metal and semiconductors, see Figure B.5. Good thermoelectric materials are typically heavily doped semiconductors with carrier concentration of 1020 carriers$\cdot cm^{-3}$. To ensure that the net Seebeck effect is large, there should only be a single type of carrier. Mixed n-type and p-type conduction will lead to opposing Seebeck effect and low thermal power (defined here as absolute value of Seebeck coefficient).

By having a band gap large enough, n-type and p-type carriers can be separated, and doping will produce only a single carrier type. Thus good thermoelectric materials have band gaps large enough to have only a single carrier type but small enough for sufficiently high doping and high mobility (which leads to high electrical conductivity). A good thermoelectric material also needs to have low thermal conductivity. Thermal conductivity in such materials comes from two sources of heat transport. Phonons travelling through the crystal lattice transport heat and lead to lattice thermal

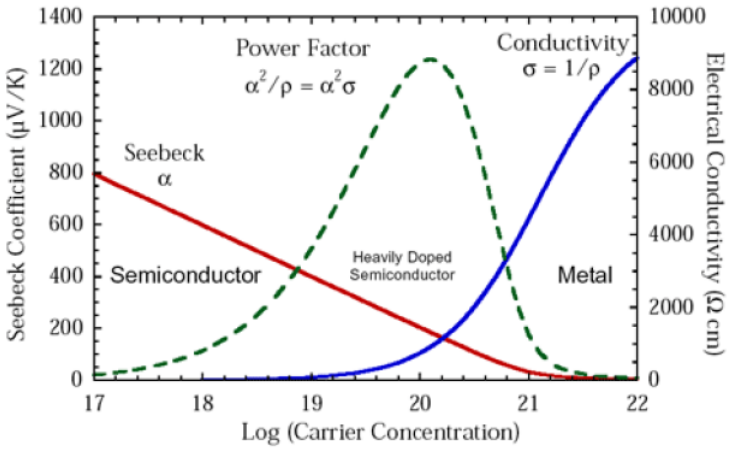

Figure B.5: Duality of thermal and electric effect

conductivity. The electrons (or holes) also transport heat and lead to electronic thermal conductivity. The greatest opportunity to enhance zT is to minimize the lattice thermal conductivity. This can be done by increasing the phonon scattering by introducing heavy atoms, disorder, large unit cells, clusters and rattling atoms. Figure B.6 shows an example of crystal structures with reduced phonon path and Figure B.7 shows the effect of introducing different phonon scattering mechanisms in $CoSb_3$.

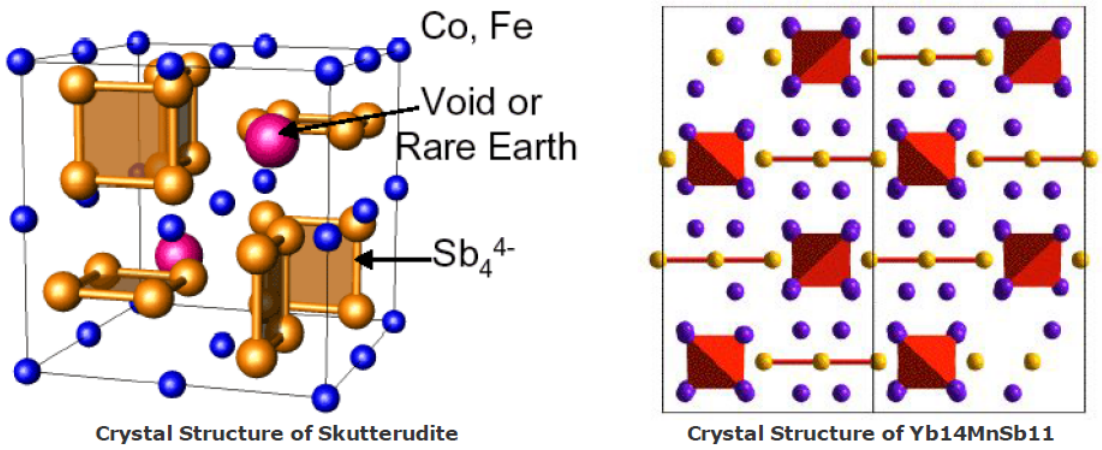

Figure B.6: Lattice of enhanced thermoelectric materials for lower thermal conductivity

The ideal thermoelectric material is then one which is an "Electron Crystal Phonon Glass" (Rowe, 1995) where high mobility electrons are free to transport charge and heat but the phonons are disrupted at the atomic scale from transporting heat. Using these principles, a variety of high zT materials have been developed. Many materials have an upper temperature limit of operation, above which the material is unstable. Thus no single material is best for all temperature ranges, so different materials should be selected for different applications based on the temperature of operation. This leads to the use of a segmented thermoelectric generator.

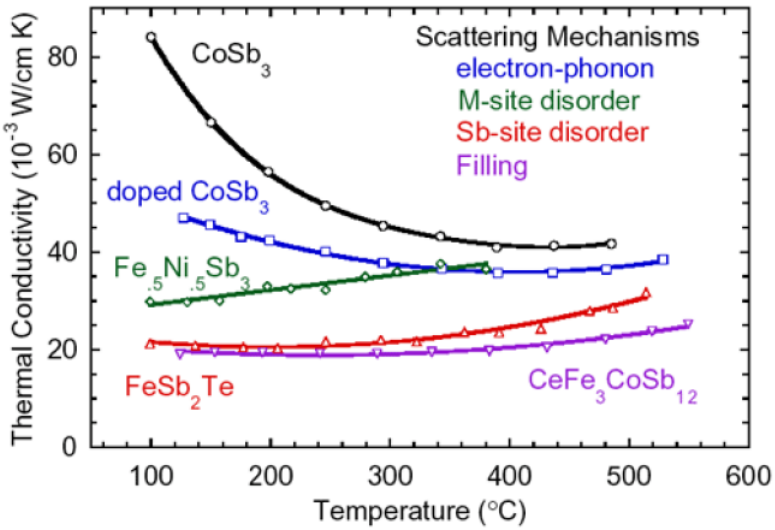

Figure B.7: Thermal conductivity decrease by introduction of various scattering mechanisms

Adapted from Thermoelectrics (2019)

Expert opinion Fraunhofer Institute IPM in Freiburg

Meeting with Dr. Jan König, group manager of the Thermoelectric group and Dr. Heinrich Höfler, head of department of Fraunhofer IPM – Institute for Physical Measurement Techniques with the goal of understanding which options would be available to improve the Peltier element for the PCFH implementation

Dr. König clarified that to build an application specific Peltier element would be extremely complicated. Of-the-shelf Peltier elements are optimized for laser applications. They use PbTe and their best thermoelectric properties (zT) are available at T = 400 K. To develop a solution for the temperature range of water vapour measurements in the atmosphere is interested in would mean a lot of investment – scientific and economical, which would probably have too little return. Thermoelectric material related development could not be offered by Fraunhofer IPM. The optimization IPM could provide is related to the design of the Peltier element itself. In the end of the meeting, we had the opportunity to visit the Laboratory facilities. There are facilities for "powder cooking" into wafers, wafer cutting and elements assembly. They could also provide different materials deposition in the ceramics surfaces – and make the connection to a heat exchanger in the hot side. The heat exchanger would be provided by a specialist and assembled by IPM. The initial costs to implement the assembly line would be €50.000. And each element would then, after implementation of assembly line be €700 approximately. Both estimations are rough numbers. Considering these costs, it has been decided to look for a solution from a distributor – of-the-shelf.

B.2 Thermocouples

Construction and assembly

Soldering

The thermocouples can be produced by two techniques: soldering or welding. Below the description of thermocouple production by soldering. Soldering requires the presence of a 3rd agent: solder which binds the metallic elements when it is liquid at a warmer temperature, in this case we used 330 °C, and solidifies when cooler.

- From the copper (Cu) and constantan (Ko) wire roll of the same diameter, roughly the same length of wire should be cut out – with a slightly shorter Ko wire. (See Figure B.8a)
- The copper wire is very fragile, hence the two wires should be twisted together to increase the thermocouple durability. The recommended method is to use 2 crocodiles at each end. Twist the wires together using a drill machine and a fixed location at the other end. Or in case they are short thermocouples, 15 to 30 cm, they can be hand twisted. Enough space should be left at the extremities. At one of the extremities the wires should have the same length.
- The insulation at the wires extremities should then be removed. A de-insulation ('sandpaper') machine is available for this purpose at ETH. In case this machine is not available, sand paper itself can be used or hot solder can burn the insulation away. (See Figure B.8b)
- The two wires at the same extremity of the thermocouple (Ko and Cu) should be soldered together. Little solder is necessary for this procedure. The left over wire, after the solder, can be cut out. See panel (c) of Figure B.8 for an example of a Ø 0.1 mm soldered thermocouple.
- The good contact of the thermocouple should be confirmed using a voltmeter.

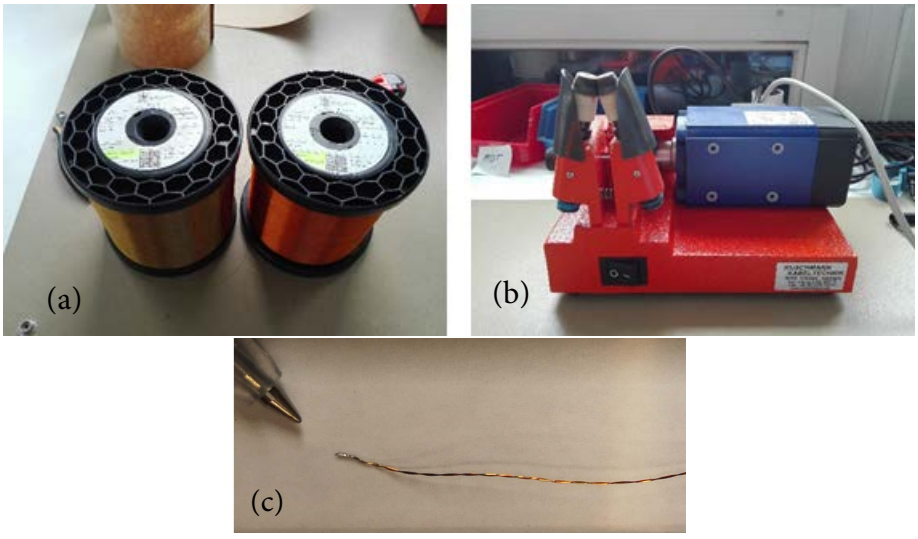

Figure B.8: (a) Cu and Ko wire roll; (b) de-insulation machine; (c) soldered Ø 0.1 mm thermocouple.

Welding

Welding binds the metal elements without the use of a 3rd agent. The technique used for the assembly of the thermocouples is point welding. The machine used can be seen in Figure B.9a. The machine produces a voltaic arch at tip 1 which fuses both metals together. The pulse is controlled with a pedal. The voltaic arch is isolated with argon gas – see Figure B.9b. The wires are short circuited at 2 (see Figure B.9 panels (c) and (d)). In Figure B.9, it is possible to observe the welding technique in panel (e) and the welded thermocouple in panel (f).

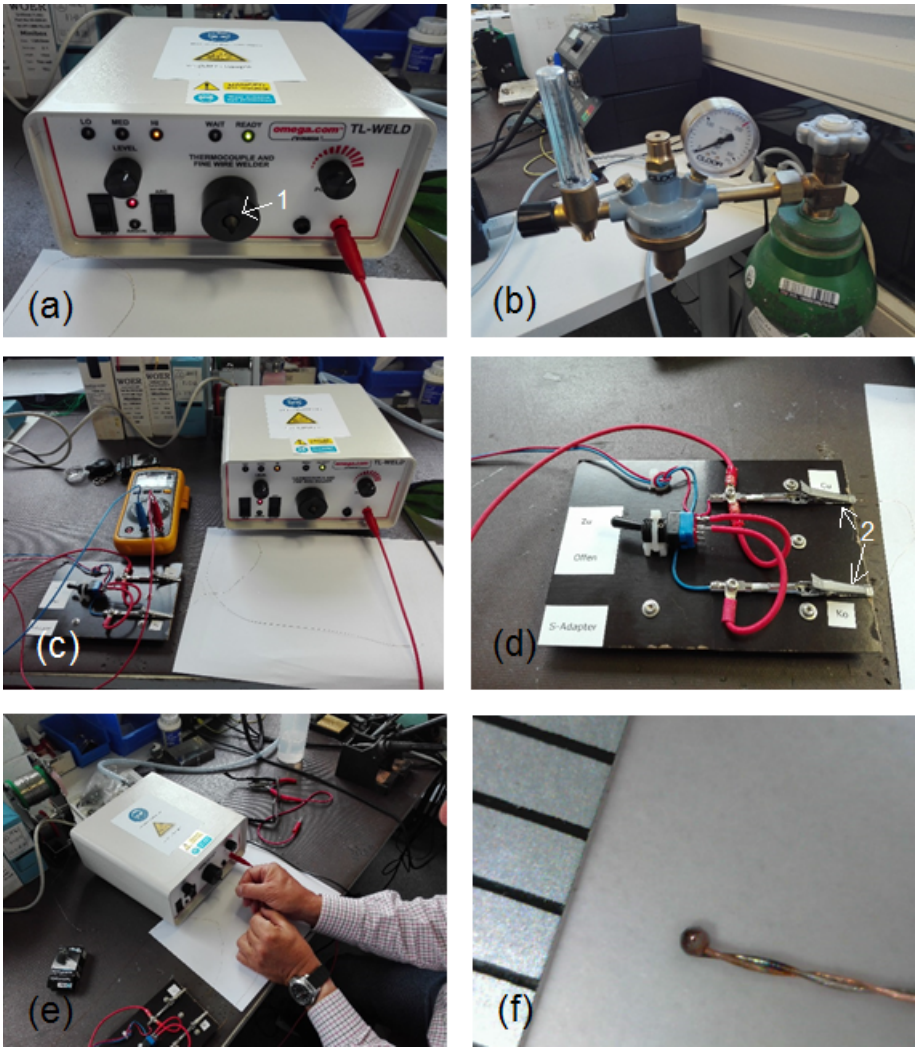

Figure B.9: (a) Point welding machine; (b) Argon gas bottle and dispenser; (c) point-welding set-up; (d) in-house (mylab) made short circuit for thermocouple welding; (e) thermocouple point welding technique; (f) welded Ø 0.1 mm thermocouple.

Soldering to the thermo-module board

The extremity of the thermocouple which has not been soldered or welded together, is soldered to the thermocouple module board.

- The Ko wire is soldered in tension in comparison to the Cu wire. Ko is stronger than Cu, being then more suited to support tension in case the thermocouple is strained. For this, the Ko extremity should be shorter than the Cu extremity.
- The Ko wire is inserted through the hole identified with a 1 in Figure B.10, passes under the PCB board and resurfaces in the hole identified as 2 in Figure B.10. This configuration was envisioned to equilibrate the Ko wire temperature to the PCB board before the electrical contact. The PCB conduction layer is made of Cu, a temperature gradient in the board can cause an error in the temperature reading with the thermocouples. Due to an extra thermocouple junction Ko-Cu at an unknown temperature.
- The Ko wire is soldered in 1 and 2 of Figure B.10. The soldering position of 1 is electrically insulated from the rest of the board. The wire insulation should be removed at the soldering position of 2, there happens the electrical contact with the board.
- The Cu wire is soldered in the corresponding hole identified as 3 in Figure B.10. The Cu wire is de-insulated at the soldering position of 3.
- Electrical contact is essential at positions 2 and 3.

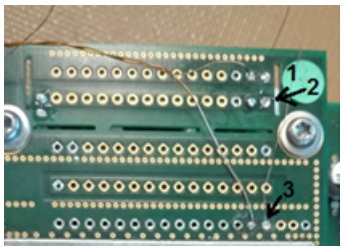

Figure B.10: PCFH thermocouple module board soldering pads: (1) thermal equilibration of Ko wire; (2) electrical connection of Ko wire; (3) electrical connection of Cu wire.

Thermocouple calibration: temperature to voltage

The temperature to voltage calibration is approximated as fourth order polynomial as shown Equation B.6. The calibration coefficients are given in Table B.1. In Figure B.11 we can see the difference from the measured voltage used for the calibration and the voltage calculated from the measured temperature using the calibration of Table B.1.

$$U = a_0 + T\ (a_1 + T\ (a_2 + T\ (a_3 + T\, a_4))) \tag{B.6}$$

Thermocouple wire resistance

Constantan is not an ideal conductor. With very long wires, 1.5 m, the resistance of the constantan is non-negligible. The resistance (R) of a wire is inversely proportional to its cross section (A), in our

Table B.1: Temperature to voltage calibration coefficients

mm	a_4	a_3	a_2	a_1	a_0
Ø 0.3	4.680279×10^{-8}	-4.081488×10^{-5}	4.463575×10^{-2}	3.870697×10^{1}	-2.217385×10^{-1}
Ø 0.1	2.369471×10^{-8}	-4.029055×10^{-5}	4.478910×10^{-2}	3.873721×10^{1}	-9.312526×10^{-1}
Ø 0.05	1.192644×10^{-8}	-3.942937×10^{-5}	4.521087×10^{-2}	3.875076×10^{1}	-7.298129×10^{-1}

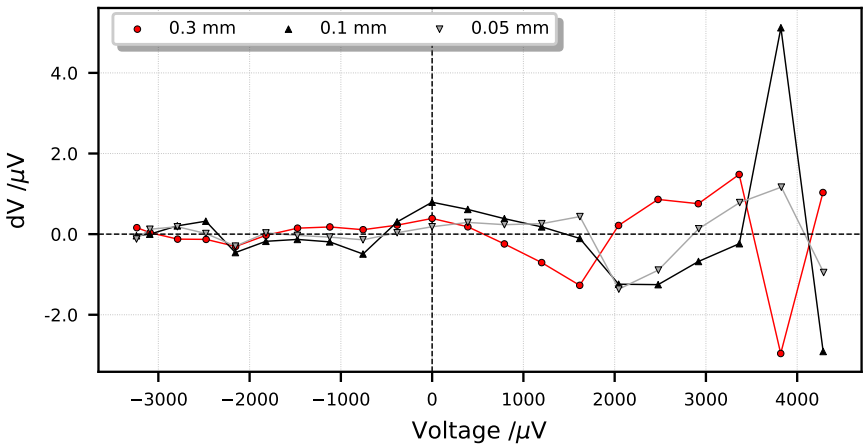

Figure B.11: Difference between measured and calculated values for temperature to voltage calibration of thermocouples. Circle: Ø 0.3 mm; up triangle: Ø 0.1 mm; down triangle: Ø 0.05 mm thermocouples.

case a circular cross section (πr^2) and proportional to its length (l): thinner wires, higher resistance and longer wires, higher resistance. The resistivity (ρ) of a material is an intrinsic property.

$$R = \rho \frac{l}{A} \tag{B.7}$$

For example, the resistance of a constantan wire of Ø 0.1 mm is 9× higher than that of a constantan wire of the same length of Ø 0.3 mm. With the decrease from Ø 0.1 mm to Ø 0.05 mm and the same length, the resistance will increase 4×. An increase of the wire length by 7% (0.1 m/1.5 m) leads to an increase of the wire resistance by 7%. The uncertainty of the wire resistance from length is linearly proportional to the uncertainty in the wire length. The resistance uncertainty is as

$$\sigma_R = \sqrt{\left(\frac{dR}{d\rho}\right)^2 s_\rho^2 + \left(\frac{dR}{dl}\right)^2 s_l^2 + \left(\frac{dR}{dA}\right)^2 s_A^2} = \sqrt{\left(\frac{l}{A}\right)^2 s_\rho^2 + \left(\frac{\rho}{A}\right)^2 s_l^2 + \left(-\frac{\rho l}{A^2}\right)^2 s_A^2} \tag{B.8}$$

An increase in temperature, results in an increase in resistance and a decrease in temperature, results in a decrease in resistance. All the way down to superconductors at near absolute zero temperatures. A linear approximation can be used to compute the influence of temperature in resistivity. This relation works with different temperature coefficients α measured at specific temperatures and

for small changes in temperature around it.

$$\Delta\rho = \alpha\,(T - T_0)\;\rho_0 \tag{B.9}$$

Table B.2: Thermocouple resistance

Material	temperature coefficient (K^{-1})	resistivity $\rho + \Delta\rho$ (Ω m)	Ø 0.3 mm	Ø 0.1 mm	Ø 0.05 mm
			wire resistance[3] R (Ω)		
Cu T = 0 °C	4.04×10^{-3} [1]	1.54×10^{-8}	0.327 ± 0.022	2.95 ± 0.20	11.79 ± 0.79
Cu T = -23 °C		1.39×10^{-8}	0.294 ± 0.020	2.65 ± 0.18	10.60 ± 0.71
Cu T = -73 °C		1.05×10^{-8}	0.222 ± 0.015	2.00 ± 0.13	7.99 ± 0.53
Ko T = 20 °C	8×10^{-6} [2]	4.90×10^{-7}	10.40 ± 0.69	93.58 ± 6.24	374 ± 25

[1] (Giancoli, 2009; Matula, 1979) at T_0 = 20 °C
[2] (O'Malley, 1992) at T_0 = 20 °C
[3] l = 1.5 ± 0.1 m

Copper resistivity is strongly influenced by the change in temperature of the copper: about 10% change from 0 °C to -20 °C and 32% from 0 °C to -80 °C. Constantan resistivity is barely influenced by temperature, hence its name and its usage in this application. However, constantan is not an ideal conductor, and it is the biggest contribution for the total resistance of the thermocouple wire. The temperature changes the resistance of the thermocouple by 0.3% from 0 °C to -20 °C and by 1% from 0 °C to -80 °C.

B.3 Previous designs

Reference surface

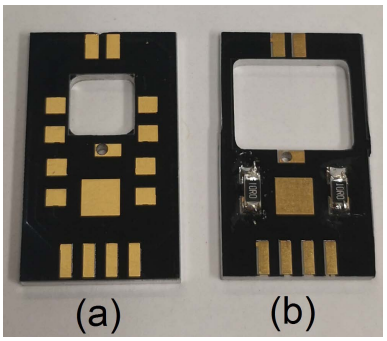

Figure B.12: Reference surface: (a) previous and (b) actual design

Multiblock

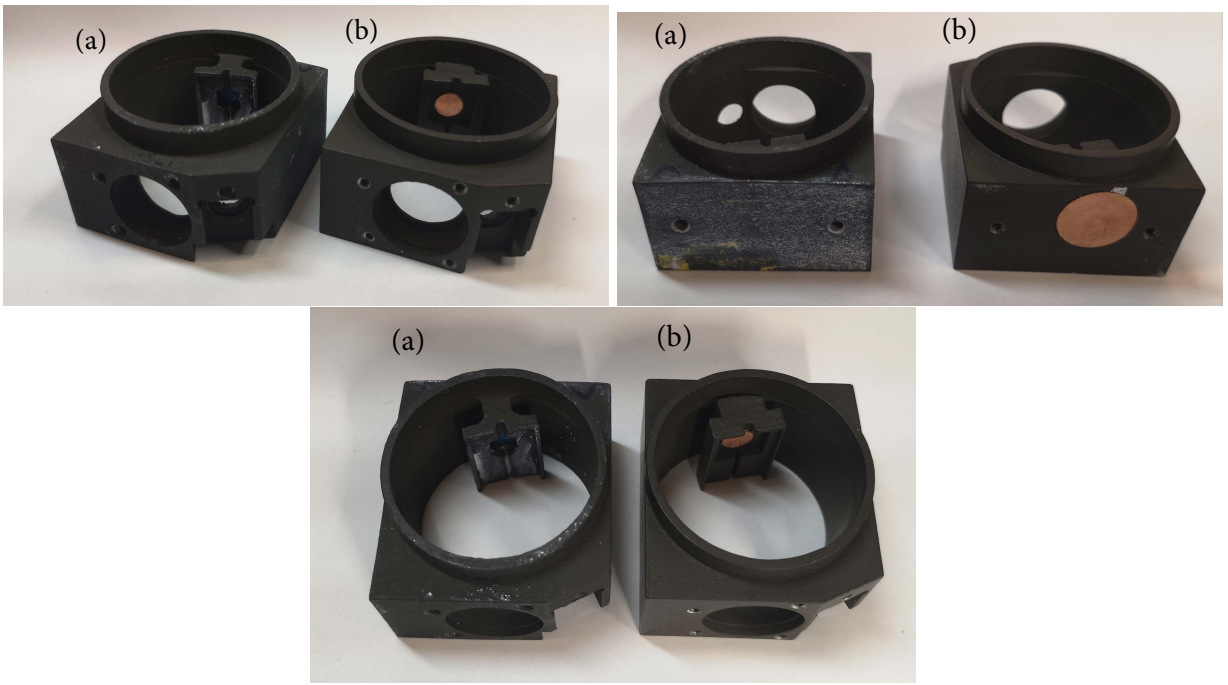

Figure B.13: Multiblock: (a) previous and (b) actual design

Heat sink

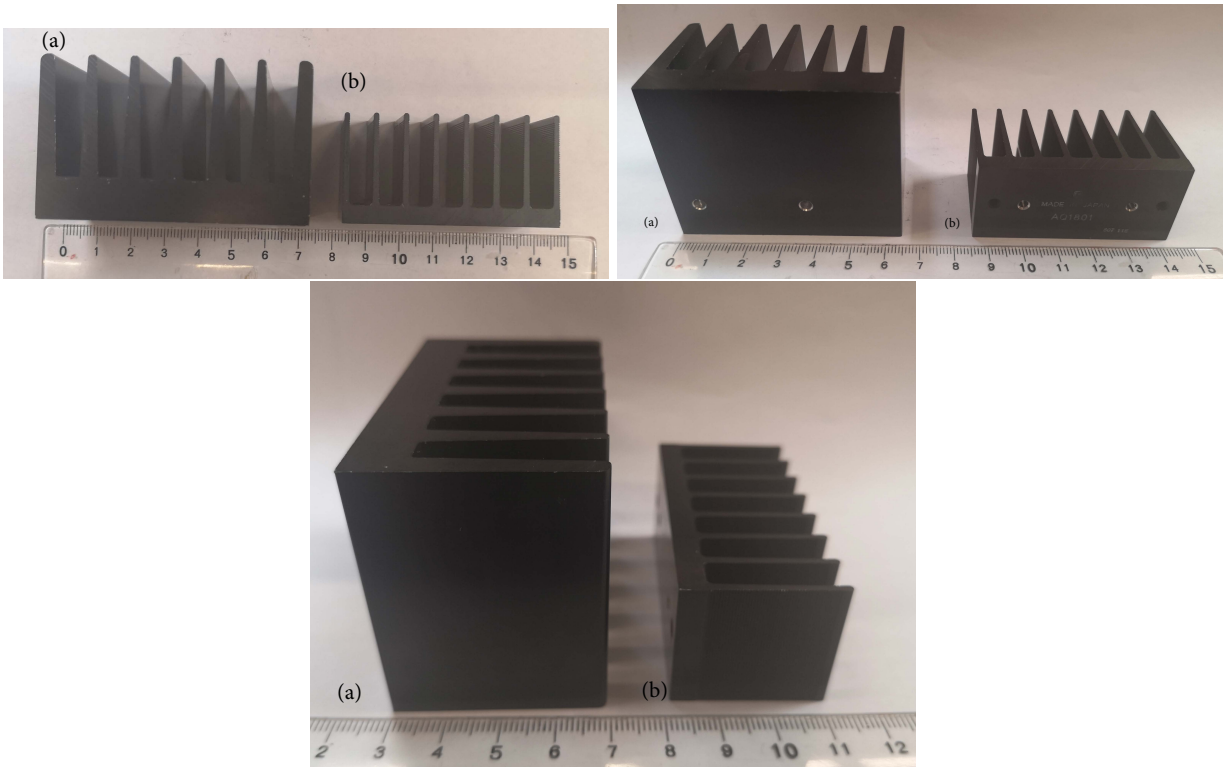

Figure B.14: Heat sink: (a) previous and (b) actual design

PCFH

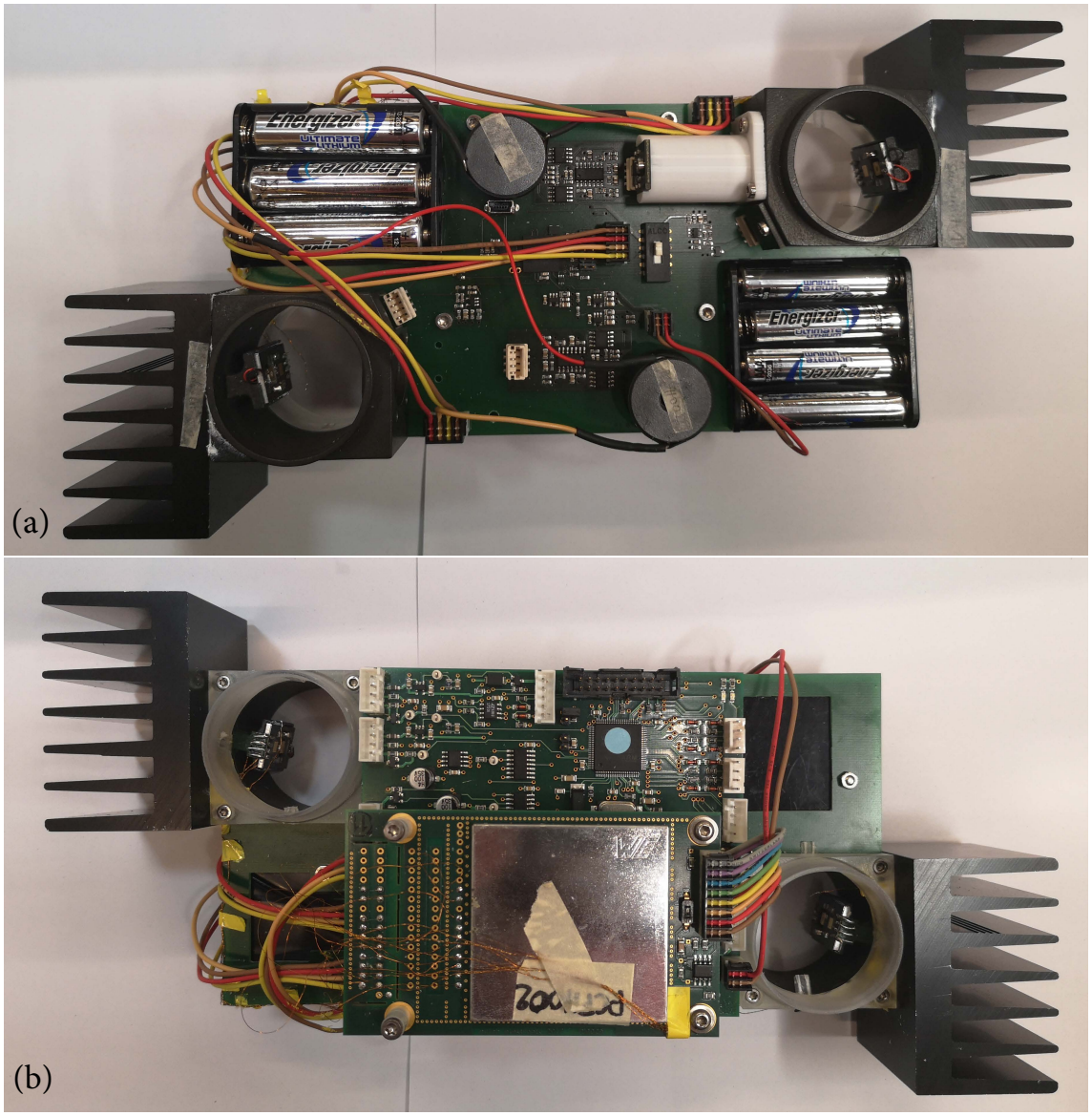

Figure B.15: PCFH: previous design (a) top view, note the missing optical tube, photo-detector and LED PCB's in sub-unit 2; (b) bottom view.

Appendix C

System modelling for control implementation

C.1 Peltier element

Peltier element heat balance equations

Heat on the hot side:

$$Q_H = \alpha_P \, T_H \, I_P + \frac{1}{2} \, R_P \, I_P^2 - K_P \, (T_H - T_C) \tag{C.1}$$

Heat on the cold side:

$$Q_C = \alpha_P \, T_C \, I_P - \frac{1}{2} \, R_P \, I_P^2 - K_P \, (T_H - T_C) \tag{C.2}$$

Heat balance with the dissipated electrical power:

$$\begin{aligned} &Q_H = P_E + Q_C \Rightarrow P_E = Q_H - Q_C \Rightarrow \\ &P_E = \alpha_P \, T_H \, I_P + \frac{1}{2} \, R_P \, I_P^2 - K_P \, (T_H - T_C) - \left(\alpha_P \, T_C \, I_P - \frac{1}{2} \, R_P \, I_P^2 - K_P \, (T_H - T_C) \right) \Rightarrow \\ &\Rightarrow P_E = \alpha_P \, (T_H - T_C) \, I_P + R_P \, I_P^2 \end{aligned} \tag{C.3}$$

PE electrical equation

$$V_P = \frac{P_E}{I_P} = \alpha_P \, (T_H - T_C) + R_P \, I_P \tag{C.4}$$

T_C: PE cold side temperature; T_H: PE hot side temperature; α_P: Seebeck coefficient, R_P: PE internal resistance; K_P: PE thermal conductivity, I_P: PE electrical current. V_P: PE voltage.

(Chen et al., 2012)

Datasheet values for 2MDX04-022-0510

Table C.1: Datasheet temperatures at different surfaces (see Figure 3.2) of the double stage PE 2MDX04-022-0510.

T_{amb} (K)	T_6@ Air (K)	T_5 (K)	T_4 (K)	T_3 (K)	T_2 (K)	T_1 (K)	T_0 @ Air (K)
300	300	300.7	303.8	260	260.9	217.4	217.5
290	290	290.7	293.6	252.1	253.0	212.0	212.1
280	280	280.7	283.4	244.6	245.1	206.7	206.8
270	270	270.6	273.2	236.6	237.4	201.6	201.7
260	260	260.6	263.0	229.2	229.9	196.6	196.7
250	250	250.6	252.8	221.8	222.5	191.7	191.7
240	240	240.5	242.6	214.4	215.4	186.8	186.8
230	230	230.5	232.4	207.0	207.6	181.9	181.9
220	220	220.4	222.2	199.6	200.2	176.9	177.0
210	210	210.4	212.0	192.2	192.7	171.9	172.0
200	200	200.3	201.7	184.6	185.1	166.9	166.9
190	190	190.3	191.5	177.0	177.4	161.6	161.7

Table C.2: Datasheet values for different operating temperatures of the PE 2MDX04-022-0510 @Air

T_{amb} (K)	ΔT_{max} (K)	I_{max} (A)	$\dot{Q}_{c_{max}}$ (W)	U_{max} (V)	R (Ω)	t_{const} (s)
300	86.04	1.19	0.72	2.00	1.39	4.98
290	81.46	1.20	0.69	1.90	1.32	4.91
280	76.70	1.20	0.65	1.80	1.25	4.83
270	71.80	1.20	0.62	1.69	1.18	4.74
260	66.80	1.20	0.58	1.59	1.12	6.64
250	61.73	1.20	0.54	1.49	1.05	4.53
240	56.61	1.19	0.50	1.39	1.00	4.41
230	51.49	1.17	0.45	1.29	0.94	4.29
220	46.41	1.15	0.41	1.19	0.89	4.17
210	41.40	1.13	0.37	1.09	0.85	4.04
200	36.50	1.09	0.32	0.99	0.80	3.92
190	31.76	1.06	0.28	0.90	0.76	3.79

PE 2MDX04-022-0510 coefficients

PE internal resistance:

$$R_P = \frac{U_{\max} - \alpha_P \, \Delta T_{\max}}{I_{P_{\max}}} \tag{C.5}$$

PE Seebeck coefficient:

$$\alpha_P = \frac{\frac{Q_{c\max}}{I_{P_{\max}}} + \frac{U_{\max}}{2}}{T_C + \frac{\Delta T_{\max}}{2}} \tag{C.6}$$

PE thermal conductance:

$$K_P = \frac{\alpha_P \, T_C \, I_{P_{\max}} - \frac{I_{P_{\max}}^2 \, R_P}{2}}{\Delta T_{\max}} \tag{C.7}$$

Table C.3: PE 2MDX04-022-0510 coefficients: internal resistance R_P, Seebeck coefficient α_P and thermal conductivity K_P calculated from the datasheet values for different operating temperatures @Air

T_6@ Air (K)	T_0@ Air (K)	T_P (K)	R_P (Ω)	α_P (W K^{-1} A^{-1})	K_P (W K^{-1})
300	217.5	258.8	1.15	7.38×10^{-03}	3.98×10^{-03}
290	212.1	251.1	1.10	7.19×10^{-03}	4.16×10^{-03}
280	206.8	243..4	1.05	6.97×10^{-03}	4.29×10^{-03}
270	201.7	235.9	1.00	6.75×10^{-03}	4.58×10^{-03}
260	196.7	228.4	0.96	6.50×10^{-03}	4.78×10^{-03}
250	191.7	220.9	0.92	6.23×10^{-03}	5.01×10^{-03}
240	186.8	213.4	0.88	5.97×10^{-03}	5.28×10^{-03}
230	181.9	206	0.85	5.66×10^{-03}	5.43×10^{-03}
220	177.0	198.5	0.82	5.38×10^{-03}	5.74×10^{-03}
210	172.0	191.0	0.78	5.07×10^{-03}	6.07×10^{-03}
200	166.9	183.5	0.75	4.72×10^{-03}	6.19×10^{-03}
190	161.7	175.9	0.72	4.42×10^{-03}	6.48×10^{-03}
180	156.2	168.1	0.69	4.11×10^{-03}	6.74×10^{-03}

$$T_P = \frac{T_6 + T_0}{2} = \frac{T_{\text{hot}} + T_{\text{mirror}}}{2} = \frac{T_H + T_C}{2} \tag{C.8}$$

$$\alpha_P = (0.0367 \cdot T_P - 1.97) \times 10^{-3}, \; 168.1 < T_P < 260, \; R^2 = 0.994 \tag{C.9}$$

$$R_P = 0.005 \cdot T_P - 0.1747, \; 168.1 < T_P < 260, \; R^2 = 0.994 \tag{C.10}$$

$$K_P = (-0.0031 \cdot T_P - 1.19) \times 10^{-2}, \; 168.1 < T_P < 260, \; R^2 = 0.996 \tag{C.11}$$

Appendix D

Field and laboratory testing

D.1 DWD collaboration: payload recovery program

For the recovery, DWD uses a multi-purpose nine seat van. The van has a portable Wi-Fi system from a mobile hot spot, which allows the team to follow the sounding through the GRUAN monitor (Oelsner, 2019). The GRUAN Monitor provides prediction of landing location, which works with on-line data from the radiosonde and previously up-loaded forecast data. The van is equipped with a radio receiving station with two flexible antennas (Antennas, 2019) with narrow band adjusted to the radiosonde frequency band. The antennas are connected to a small receiver (Figure D.1a and b), which is connected to a portable computer using Strato (Holger Vomel's decoding software for radio sounding). The system is powered by a battery system installed in the van (Figure D.1c). The payload includes an I-Met (US)(iMet 4, 2019) for recovery purposes. The I-Met transmits GPS location of the payload until landing.

Figure D.1: Recovery material. (a) Antenna connection inside the recovery van; (b) portable receiver; (c) batteries.

Once the payload is 120 km away from the main receiving station (launch location), and close to the ground, the radio signal does not reach the main receiving station and the last few meters of the descent are lost. Using a mobile receiving station, which moves close to the landing site allows the last few meters to be recorded as well as the exact GPS location of the landing, through the I-Met

radiosonde. DWD currently uses the I-Met system, but they plan to install a mobile MW41 system in the van.

In case the I-Met GPS location is not received, there is a portable GPS locator system, a twig locator (twig, 2015), inside of the payload. Using a regular cellphone, the operator sends a text message to the twig locator and gets a reply with the exact coordinates of the payload. This system only works if there is mobile phone connection.

The two recovery methods are complementary and very efficient. After receiving the exact coordinates, either from the I-Met radiosonde or from the twig locator, the operator inserts the coordinates in a hand-held GPS. The driver will bring the van as close to the landing location as possible, even if it means driving on forest roads or on agriculture fields.

The van is equipped with some tools to help with the recovery. There is an extendible arm to reach the tree tops. There is a hook attached to a rope which fits in the top of the extendible arm. There is a sling shot to pass the hook over the payload if the tree is taller than the reach of the arm. There are wet suits and rubber boots for recoveries in lakes and rivers. There is a ladder to climb on roofs. Due to wild fire risk in the summer 2018, we carried a fire extinguisher.

Figure D.2 shows the two recovery situations of the first PCFH campaign in July 2018.

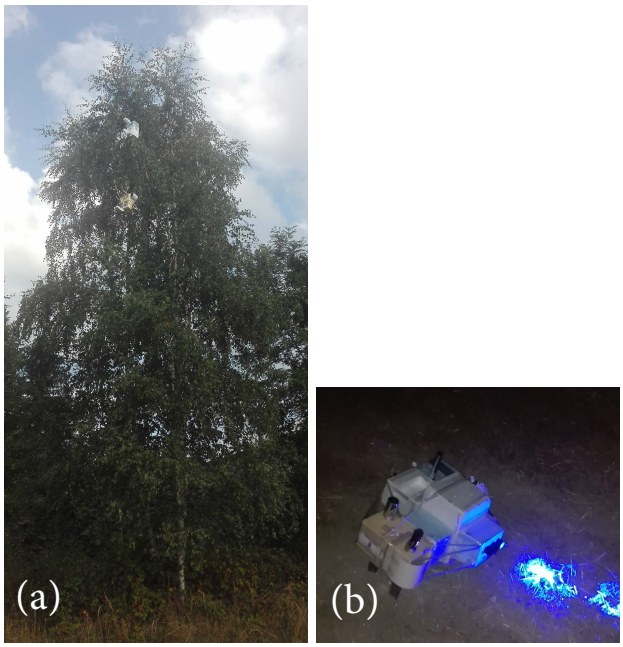

Figure D.2: Recovered payloads. (a) PCFH01 on the 25 July 2018. (b) PCFH02 on the 26 July 2018.

D.2 Controller flight mode options

Table D.1: Available flight modes for reference surface heater

	Description	Parameters to be set (example) sub-unit 1	sub-unit 2
0	Off mode: Control PWM by user commands	A00IW9:0xxx	A00IW10:0xxx
1	Alternating set-point PWM: Alternating set-point heating with PWM (t_1, t_2 =300 s; PWM X_1 = 0.4,X_1=0, fixed)	A00IW9:1xxx	A00IW10:1xxx
2	Alternating set-point H controller: Alternating set-point heating with H controller (t_1, t_2 = 300s ; PWM: X_1=3.0 °C, X_1=0.0 °C, fixed)	A00IW9:2xxx	A00IW10:2xxx
10	Normal mode H controller: Controller is permanent active	A00IW9:10xxx A00PW69:3xxx (°C)	A00IW10:10xxx A00PW89:5xxx (°C)

Table D.2: Available flight modes for Peltier element driver

	Description	Parameters to be set (example) sub-unit 1		sub-unit 2	
0	Off mode: Control PWM by user commands	A00IR7:0xxx		A00IR8:0xxx	
1	Step mode: Steps Peltier PWM in predefine values (in the firmware), possibility to change the duration of the steps with t_1	A00PW71:20xxx A00IW7:1xxx	(s)	A00PW91:20xxx A00IW8:1xxx	(s)
2	Alternating set-point PWM: Sets PWM to X_1 during time t_1, sets PWM to X_2 during time t_2	A00PW71:20xxx A00PW72:20xxx A00PW73:-0.5xxx A00PW74:-0.2xxx A00IW7:2xxx	(s) (s) [-0.5:0.1] [-0.5:0.1]	A00PW91:20xxx A00PW92:20xxx A00PW93:-0.4xxx A00PW94:-0.1xxx A00IW8:2xxx	(s) (s) [-0.5:0.1] [-0.5:0.1]
3	Alternating set-point mode current (uses PWM / Peltier current characteristic): Sets Peltier current to X_1 during time t_1, sets Peltier current to X_2 during time t_2	A00PW71:20xxx A00PW72:30xxx A00PW73:-0.5xxx A00PW74:-0.4xxx A00IW7:3xxx	(s) (s) (A) (A)	A00PW91:20xxx A00PW92:30xxx A00PW93:-0.2xxx A00PW94:-0.4xxx A00IW8:3xxx	(s) (s) (A) (A)
4	Alternating set-point mode T_{mirror} (PID controller): Sets T_{mirror} to X_1 during time t_1, sets T_{mirror} to X_2 during time t_2	A00PW71:20xxx A00PW72:30xxx A00PW73:25xxx A00PW74:-10xxx A00IW7:4xxx	(s) (s) °C °C	A00PW91:20xxx A00PW92:30xxx A00PW93:25xxx A00PW94:-9xxx A00IW8:4xxx	(s) (s) °C °C
5	Alternating set-point mirror/reference reflectance (PID controller): Sets mirror/reference reflectance to X_1 (percentage of clean measured ratio) during time t_1, sets mirror/reference reflectance to X_2 (percentage of clean measured ratio) during time t_2. Clean measured ratio measured at the beginning of the implementation of the mode.	A00PW71:20xxx A00PW72:30xxx A00PW73:0.8xxx A00PW74:0.85xxx A00IW7:5xxx	(s) (s) [0:1] [0:1]	A00PW91:20xxx A00PW92:30xxx A00PW93:0.8xxx A00PW94:0.9xxx A00IW8:5xxx	(s) (s) [0:1] [0:1]
10	PID Controller for reflectance with flight control	A00PW66:0.9xxx A00IW7:10xxx	[0:1]	A00PW86:0.9xxx A00IW8:10xxx	[0:1]

D.3 Payloads

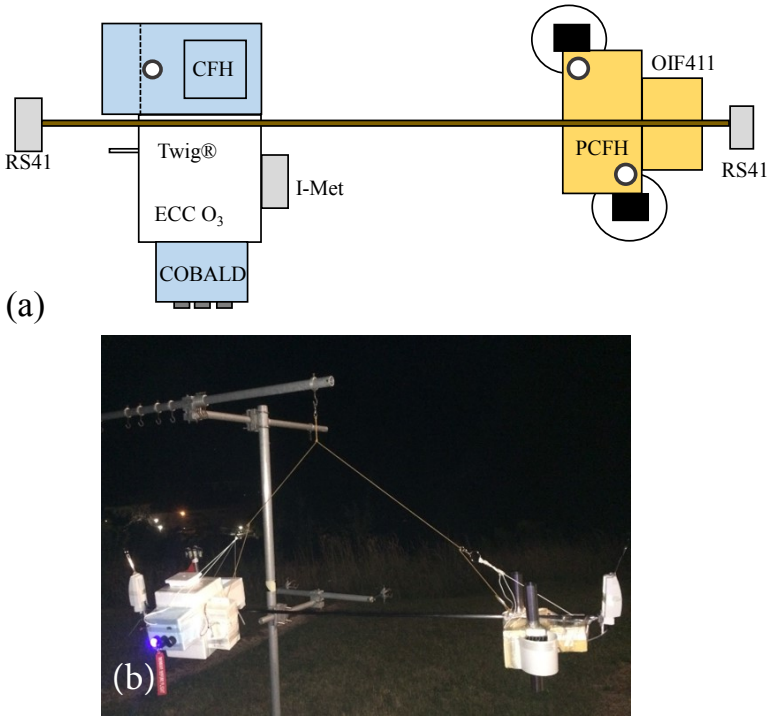

Figure D.3: Payload: PCFH01. (a) Schematics; (b) picture.

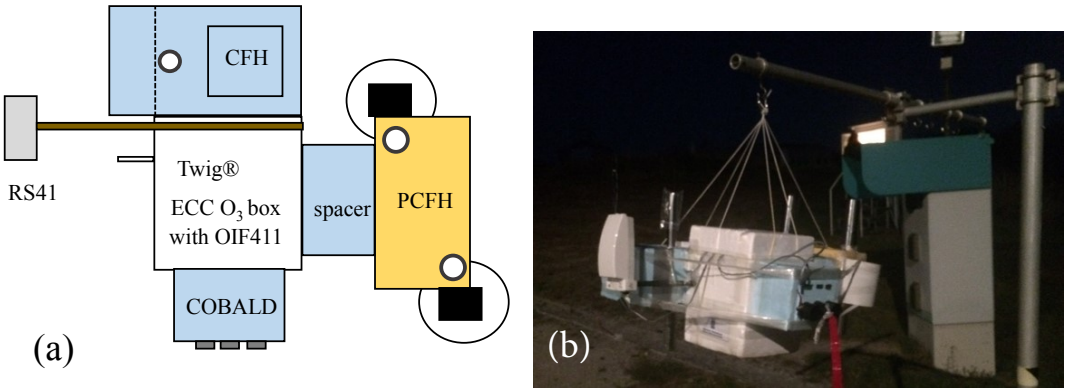

Figure D.4: Payload: PCFH02. (a) Schematics; (b) picture.

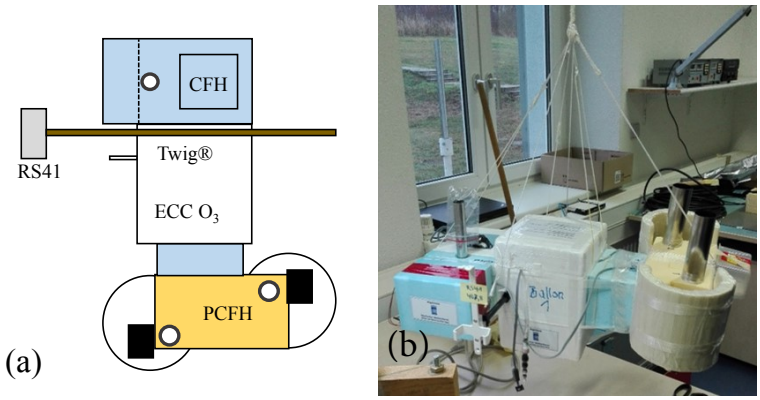

Figure D.5: Payload: PCFH04. (a) Schematics; (b) picture.

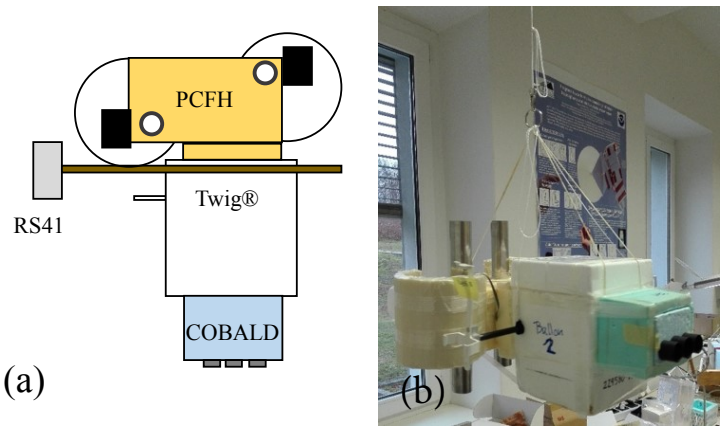

Figure D.6: Payload: PCFH05. (a) Schematics; (b) picture.

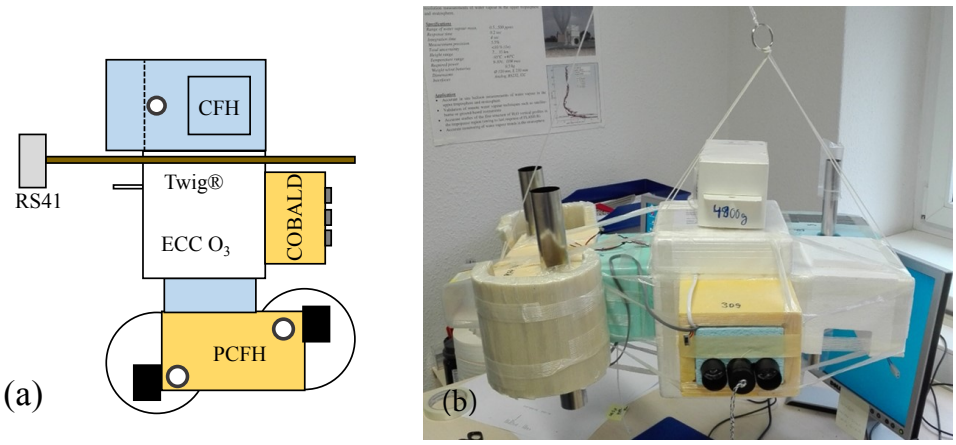

Figure D.7: Payload: PCFH05. (a) Schematics; (b) picture.

D.4 Housekeeping data

Air temperature descent

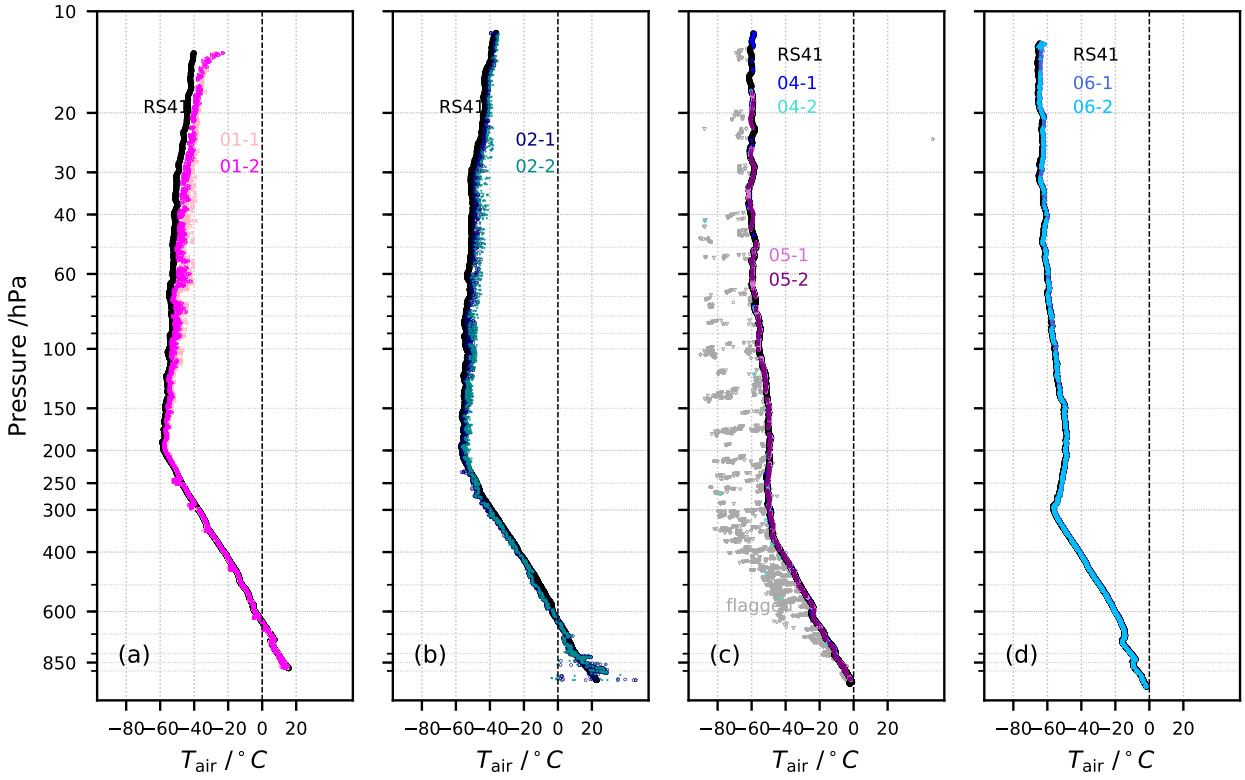

Figure D.8: Air temperature (T_{air}) PCFH vs RS41 descent. (a) Black: T_{air} RS41, light pink: T_{air} PCFH01-1, fuchsia: T_{air} PCFH01-2; (b) black: T_{air} RS41, navy: T_{air} PCFH02-1, darkcyan: T_{air} PCFH02-2; (c) black: T_{air} RS41, blue: T_{air} PCFH04-1, turquoise: T_{air} PCFH04-2, pink: T_{air} PCFH05-1, purple: T_{air} PCFH05-2, grey: flagged; (d) black: T_{air} RS41, royal blue: T_{air} PCFH06-1, deep sky blue: T_{air} PCFH06-2;

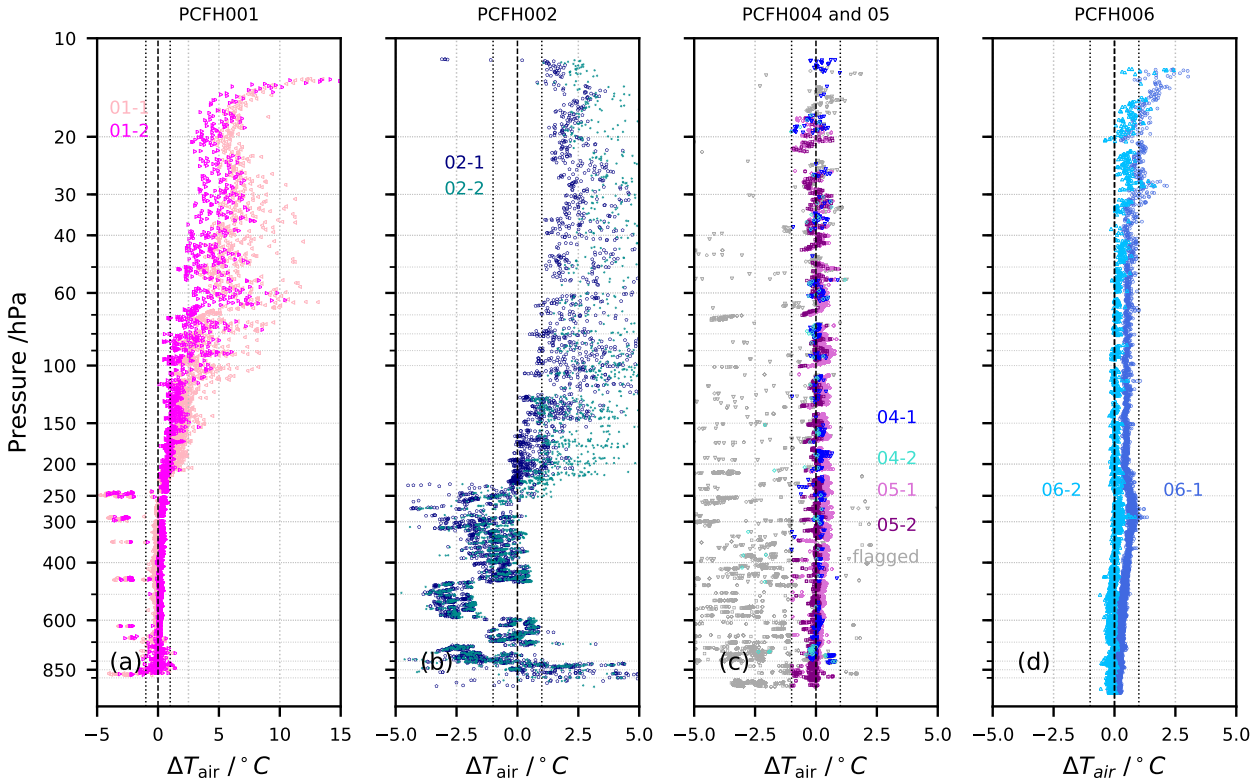

Figure D.9: Air temperature difference (ΔT_{air}) PCFH vs RS41 descent. (a) Light pink: ΔT_{air} PCFH01-1, fuchsia: ΔT_{air} PCFH01-2; (b) navy: ΔT_{air} PCFH02-1, darkcyan: ΔT_{air} PCFH02-2; (c) blue: ΔT_{air} PCFH04-1, turquoise: ΔT_{air} PCFH04-2, pink: ΔT_{air} PCFH05-1, purple: ΔT_{air} PCFH05-2, grey: flagged; (d) royal blue: ΔT_{air} PCFH06-1, deep sky blue: ΔT_{air} PCFH06-2

D.5 Frost point temperature

Frost point temperature descent

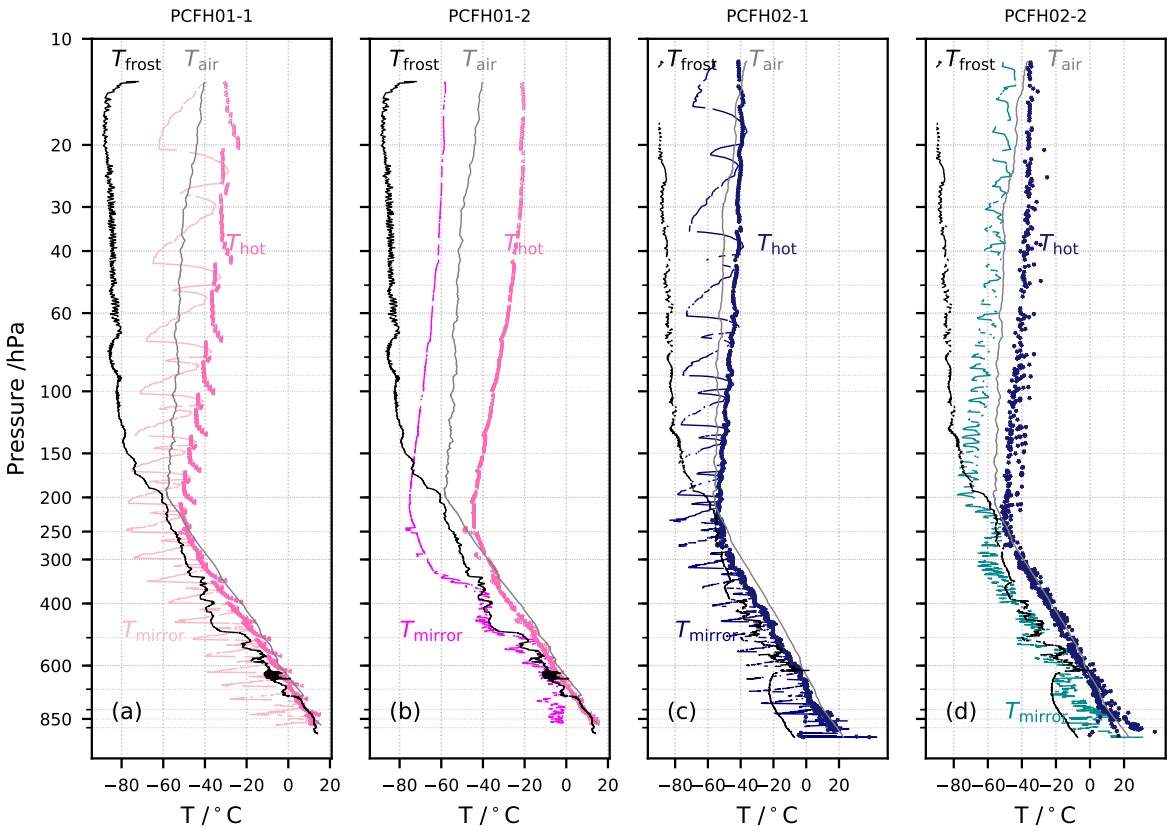

Figure D.10: T_{mirror}, T_{frost}, T_{air} and T_{hot} for PCFH 01 and 02 descent. (a) Black: CFH T_{frost}, grey: RS41 T_{air}, light pink: PCFH01-1 T_{mirror} and hot pink: PCFH01-1 T_{hot}; (b) Black: CFH T_{frost}, grey: RS41 T_{air}, fuchsia: PCFH01-2 T_{mirror} and hot pink: PCFH01-2 T_{hot}; (c) Black: CFH T_{frost}, grey: RS41 T_{air}, navy: PCFH02-1 T_{mirror} and midnight blue: PCFH02-1 T_{hot}; (d) Black: CFH T_{frost}, grey: RS41T_{air}, dark cyan: PCFH02-2 T_{mirror} and midnight blue: PCFH02-2 T_{hot}.

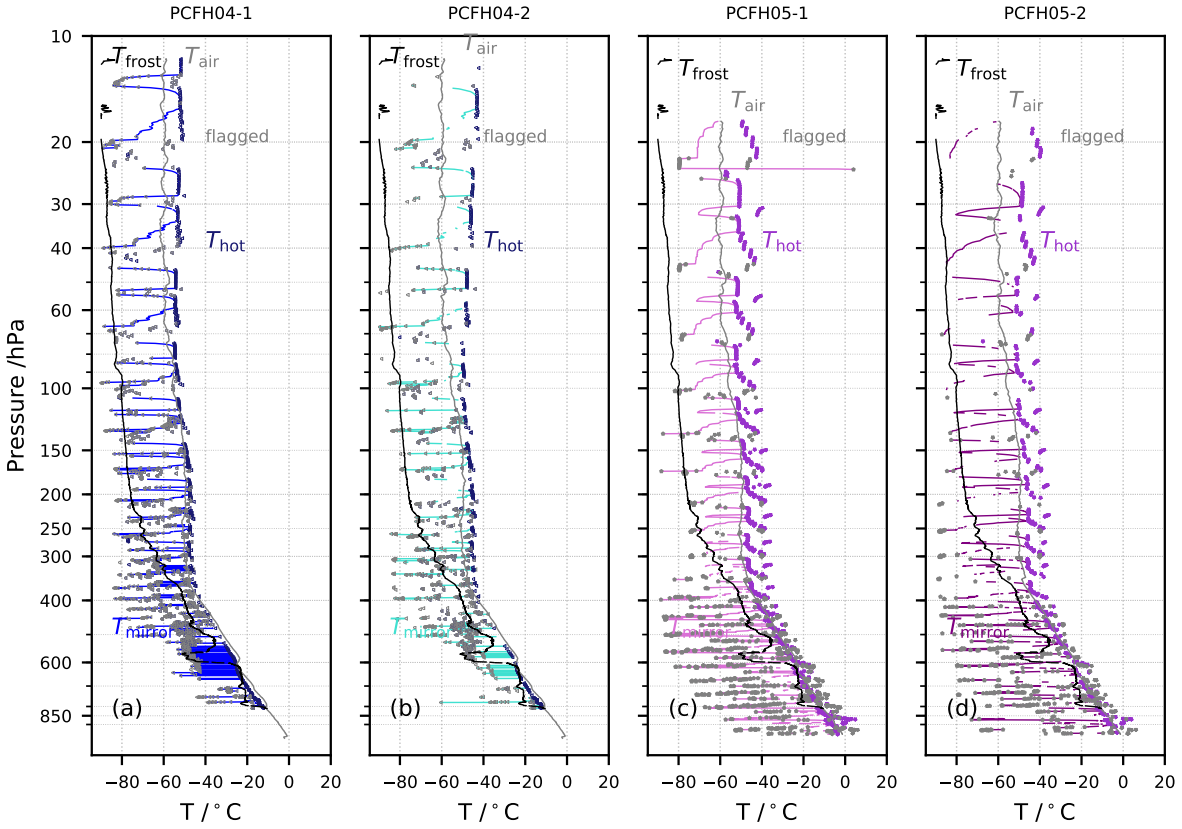

Figure D.11: T_{mirror}, T_{frost}, T_{air} and T_{hot} for PCFH 04 and 05 descent. (a) Black: CFH T_{frost}, grey: RS41 T_{air}, light pink: PCFH04-1 T_{mirror} and hot pink: PCFH04-1 T_{hot}; (b) Black: CFH T_{frost}, grey: RS41 T_{air}, fuchsia: PCFH04-2 T_{mirror} and hot pink: PCFH04-2 T_{hot}; (c) Black: CFH T_{frost}, grey: RS41 T_{air}, navy: PCFH05-1 T_{mirror} and midnight blue: PCFH05-1 T_{hot}; (d) Black: CFH T_{frost}, grey: RS41T_{air}, dark cyan: PCFH05-2 T_{mirror} and midnight blue: PCFH05-2 T_{hot}.

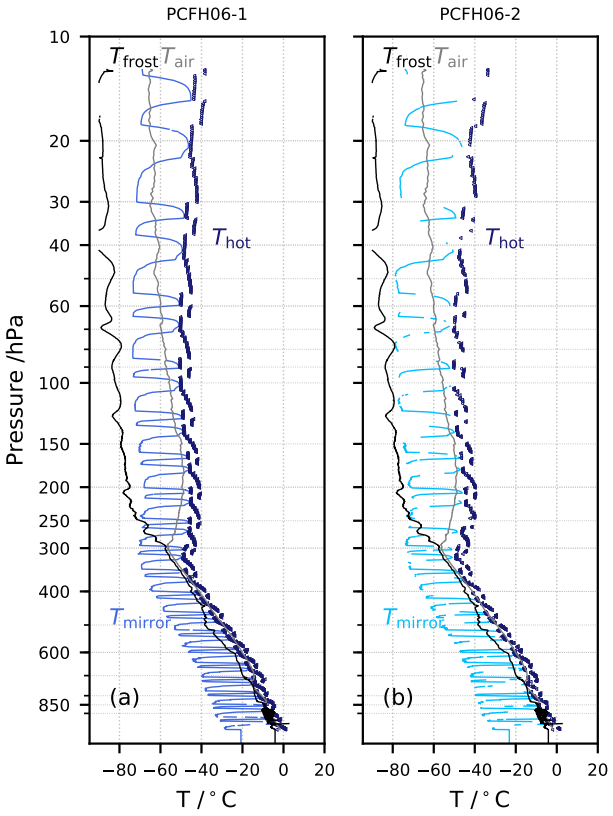

Figure D.12: T_{mirror}, T_{frost}, T_{air} and T_{hot} for PCFH 06 descent. (a) Black: CFH T_{frost}, grey: RS41 T_{air}, light pink: PCFH06-1 T_{mirror} and hot pink: PCFH06-1 T_{hot}; (b) Black: CFH T_{frost}, grey: RS41 T_{air}, fuchsia: PCFH06-2 T_{mirror} and hot pink: PCFH06-2 T_{hot}.

D.6 PE characteristics

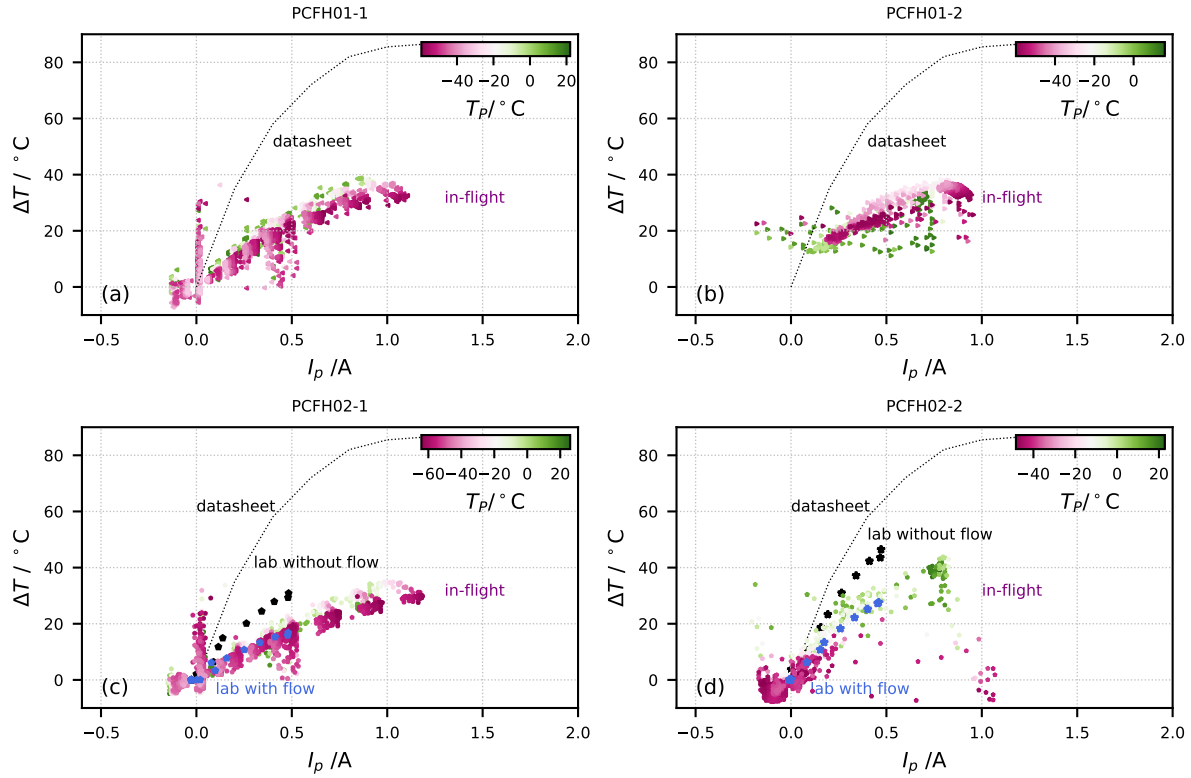

Figure D.13: PCFH01 and 02, SU 1 and 2, PE characteristics (ΔT vs I_P). (a) PCFH01-1, black dashed: ΔT vs I_P according to the datasheet, colourful dots: ΔT vs I_P in flight color coded with PE internal temperature (T_P); (b) same for PCFH01-2; (c) PCFH02-1, black dashed: ΔT vs I_P according to the datasheet, black dots: ΔT vs I_P from lab tests without flow, blue dots: ΔT vs I_P from lab tests with ~ 5 m s^{-1} air flow, colourful dots: ΔT vs I_P in flight color coded with PE internal temperature (T_P); (d) same for PCFH02-2.

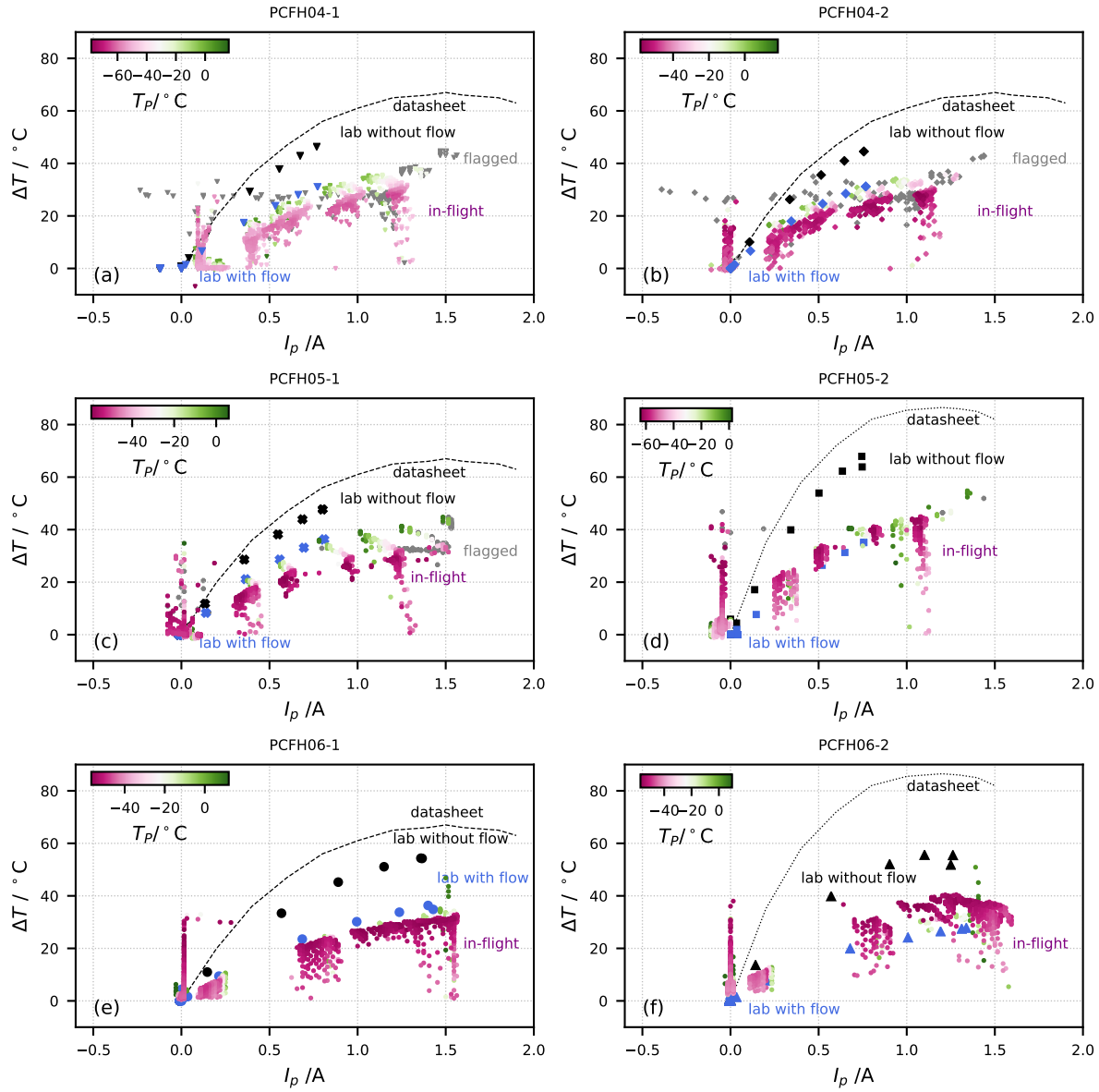

Figure D.14: PCFH04, 05 and 06, SU 1 and 2, PE characteristics (ΔT vs I_P). (a) PCFH04-1, black dashed: ΔT vs I_P according to the datasheet, black dots: ΔT vs I_P from lab tests without flow, blue dots: ΔT vs I_P from lab tests with ~ 5 m s^{-1} air flow, colourful dots: ΔT vs I_P in flight color coded with PE internal temperature (T_P); (b) same but in flight data color coded with air pressure (p_{air}); (c) same as (a) for PCFH01-2; (d) same as (b) for PCFH01-2; (e) same as (a) for PCFH04-1; (f) same as (b) for PCFH04-1; (g) same as (a) for PCFH04-2; (h) same as (b) for PCFH04-2; (d-h) small grey dots: flagged data.

List of Figures

List of Tables

Bibliography

Agilent: Agilent 34420A NanoVolt/Micro-Ohm Meter, https://datasheet.octopart.com/34420A-Agilent-datasheet-8542585.pdf, accessed:2019-07-21, 2019.

Aluminium, E.: EOS Aluminium $AlSi_{10}Mg$, https://gpiprototype.com/pdf/EOS_Aluminium_AlSi10Mg_en.pdf, accessed:2019-07-23, 2019.

ANSYS, F. .: User's Guide, ANSYS, Inc., Southpointe, 275 Technology Drive, Canonsburg, PA 15317, http://www.ansys.com, 2012.

Antennas, P.: AFM | Robust UHF 1/4 Wave Whip Antenna, http://www.panorama-antennas.com/site/index.php?route=product/product&product_id=211, accessed:2019-11-25, 2019.

Barret, E. W., Herndon, L. R., and Carter, H. J.: A preliminary note on the measurement of water vapor content in the middle stratosphere, The Journal of Meteorology publ.: American Meteorological Society, 6, 367–368, 1949.

Barret, E. W., Herdon, L. R., and Carter, H. J.: Some Measurements of the Distribution of Water Vapor in the Stratosphere1, Tellus, 2, 302–311, doi:10.1111/j.2153-3490.1950.tb00340.x, 1950.

Bechhoefer, J.: Feedback for physicists: A tutorial essay on control, Reviews of Modern Physics, 77, 783–836, doi:10.1103/RevModPhys.77.783, 2005.

Bian, J., Pan, L. L., Paulik, L., Vömel, H., Chen, H., and Lu, D.: In situ water vapor and ozone measurements in Lhasa and Kunming during the Asian summer monsoon, Geophysical Research Letters, 39, doi:10.1029/2012gl052996, 2012.

Brabec, M., Wienhold, F. G., Luo, B. P., Vömel, H., Immler, F., Steiner, P., Hausammann, E., Weers, U., and Peter, T.: Particle backscatter and relative humidity measured across cirrus clouds and comparison with microphysical cirrus modelling, Atmospheric Chemistry and Physics, 12, 9135–9148, doi:10.5194/acp-12-9135-2012, 2012.

Brewer, A. W.: Evidence for a world circulation provided by the measurements of helium and water vapour distribution in the stratosphere, Quarterly Journal of the Royal Meteorological Society, 75, 351–363, doi:doi:10.1002/qj.49707532603, 1949.

Brewer, A. W., Cwilong, B., and Dobson, G. M. B.: Measurement of Absolute Humidity in Extremely Dry Air, Proceedings of the Physical Society, 60, 52–70, doi:10.1088/0959-5309/60/1/307, 1948.

Brocard, E., Philipona, R., Haefele, A., Romanens, G., Mueller, A., Ruffieux, D., Simeonov, V., and Calpini, B.: Raman Lidar for Meteorological Observations, RALMO & Part 2: Validation of water vapor measurements, Atmospheric Measurement Techniques, 6, 1347–1358, doi:10.5194/amt-6-1347-2013, 2013.

Brunamonti, S., Jorge, T., Oelsner, P., Hanumanthu, S., Singh, B. B., Kumar, K. R., Sonbawne, S., Meier, S., Singh, D., Wienhold, F. G., Luo, B. P., Böttcher, M., Poltera, Y., Jauhiainen, H.,

Kayastha, R., Dirksen, R., Naja, M., Rex, M., Fadnavis, S., and Peter, T.: Balloon-borne measurements of temperature, water vapor, ozone and aerosol backscatter at the southern slopes of the Himalayas during StratoClim 2016-2017, Atmospheric Chemistry and Physics, 2018, 1–38, doi: 10.5194/acp-2018-222, 2018.

Brunamonti, S., Füzér, L., Jorge, T., Poltera, Y., Oelsner, P., Meier, S., Dirksen, R., Naja, M., Fadnavis, S., Karmacharya, J., Wienhold, F. G., Luo, B. P., Wernli, H., and Peter, T.: Water Vapor in the Asian Summer Monsoon Anticyclone: Comparison of Balloon-Borne Measurements and ECMWF Data, Journal of Geophysical Research: Atmospheres, doi:10.1029/2018jd030000, 2019.

Bucholtz, A.: Rayleigh-scattering calculations for the terrestrial atmosphere, Applied Optics, 34, 2765–2773, doi:10.1364/AO.34.002765, 1995.

Çengel, Y. A.: Heat transfer: A pratical approach, WBC McGraw-Hill, Boston, Massachusetts, 2nd edition (2010) edn., 1998.

Cecchini, M. A., Machado, L. A. T., Andreae, M. O., Martin, S. T., Albrecht, R. I., Artaxo, P., Barbosa, H. M. J., Borrmann, S., Fütterer, D., Jurkat, T., Mahnke, C., Minikin, A., Molleker, S., Pöhlker, M. L., Pöschl, U., Rosenfeld, D., Voigt, C., Weinzierl, B., and Wendisch, M.: Sensitivities of Amazonian clouds to aerosols and updraft speed, Atmospheric Chemistry and Physics, 17, 10 037–10 050, doi:10.5194/acp-17-10037-2017, 2017.

CFDWiki: SST k-omega model, `https://www.cfd-online.com/Wiki/SST_k-omega_model`, accessed: 2019-08-25, 2011.

Chen, W.-H., Liao, C.-Y., and Hung, C.-I.: A numerical study on the performance of miniature thermoelectric cooler affected by Thomson effect, Applied Energy, 89, 464–473, doi:10.1016/j.apenergy.2011.08.022, 2012.

Cirisan, A., Luo, B. P., Engel, I., Wienhold, F. G., Sprenger, M., Krieger, U. K., Weers, U., Romanens, G., Levrat, G., Jeannet, P., Ruffieux, D., Philipona, R., Calpini, B., Spichtinger, P., and Peter, T.: Balloon-borne match measurements of midlatitude cirrus clouds, Atmospheric Chemistry and Physics, 14, 7341–7365, doi:10.5194/acp-14-7341-2014, 2014.

ControlToolbox: Control Toolbox - MathWorks product webpage, `https://ch.mathworks.com/products/control.html`, accessed: 2019-08-18, 2019.

Corti, T., Luo, B. P., de Reus, M., Brunner, D., Cairo, F., Mahoney, M. J., Martucci, G., Matthey, R., Mitev, V., dos Santos, F. H., Schiller, C., Shur, G., Sitnikov, N. M., Spelten, N., Vössing, H. J., Borrmann, S., and Peter, T.: Unprecedented evidence for deep convection hydrating the tropical stratosphere, Geophysical Research Letters, 35, doi:10.1029/2008gl033641, 2008.

Dauhut, T., Chaboureau, J.-P., Escobar, J., and Mascart, P.: Large-eddy simulations of Hector the convector making the stratosphere wetter, Atmospheric Science Letters, 16, 135–140, doi:10.1002/asl2.534, 2015.

DeMott, P. J., Prenni, A. J., Liu, X., Kreidenweis, S. M., Petters, M. D., Twohy, C. H., Richardson, M. S., Eidhammer, T., and Rogers, D. C.: Predicting global atmospheric ice nuclei distributions and their impacts on climate, Proc Natl Acad Sci U S A, 107, 11 217–22, doi:10.1073/pnas.0910818107, URL `https://www.ncbi.nlm.nih.gov/pubmed/20534566`, 2010.

Dirksen, R., Felix, C., Lehmann, V., and Haefele, A.: CIMO-17 Decision related to the 2021 upper-air instrument intercomparison, `https://www.wmo.int/pages/prog/www/IMOP/meetings/Upper-Air/UAI-2021-Planning/CIMO_UAI-Prep_INF.4_CIMO-17-Rec.docx`, accessed:2019-09-10, 2019.

Dirksen, R. J., Sommer, M., Immler, F. J., Hurst, D. F., Kivi, R., and Vömel, H.: Reference quality upper-air measurements: GRUAN data processing for the Vaisala RS92 radiosonde, Atmospheric Measurement Techniques, 7, 4463–4490, doi:10.5194/amt-7-4463-2014, 2014.

DOWSIL: DOWSIL 340 Heat Sink Compound, https://www.dupont.com/content/dam/Dupont2.0/Products/transportation/Literature/Downloaded-TDS/0901b803809b781c.pdf, accessed:2019-08-04, 2019.

ebmpapst: Product data sheet 412 J/2HH Fan, https://www.distrelec.sk/Web/Downloads/45/65/EN_412J_2HH.pdf, accessed:2019-08-07, 2019.

EngineeringToolbox: Dry Air Properties, https://www.engineeringtoolbox.com/dry-air-properties-d_973.html, accessed: 2016-05-04, 2005.

EngineeringToolbox: Metals Specific Heat, https://www.engineeringtoolbox.com/specific-heat-metals-d_152.html, accessed:2019-07-23, 2019a.

EngineeringToolbox: Metals Thermal Conductivity, https://www.engineeringtoolbox.com/thermal-conductivity-metals-d_858.html, accessed:2019-07-23, 2019b.

ENSCI: Cryogenic Frost Point Hygrometer, https://www.en-sci.com/product/cryogenic-frost-point-hygrometer/, accessed:2019-08-04, 2019.

Fahey, D. W., Gao, R. S., Möhler, O., Saathoff, H., Schiller, C., Ebert, V., Krämer, M., Peter, T., Amarouche, N., Avallone, L. M., Bauer, R., Bozóki, Z., Christensen, L. E., Davis, S. M., Durry, G., Dyroff, C., Herman, R. L., Hunsmann, S., Khaykin, S. M., Mackrodt, P., Meyer, J., Smith, J. B., Spelten, N., Troy, R. F., Vömel, H., Wagner, S., and Wienhold, F. G.: The AquaVIT-1 intercomparison of atmospheric water vapor measurement techniques, Atmospheric Measurement Techniques, 7, 3177–3213, doi:10.5194/amt-7-3177-2014, 2014.

Fluke: Fluke Calibration 1502A-156 Tweener Thermometer Readout for RTD, RTD and SPRT Probes, https://datasheet.octopart.com/1502A-156-Fluke-datasheet-33467034.pdf, accessed:2019-07-21, 2019.

Fueglistaler, S., Dessler, A. E., Dunkerton, T. J., Folkins, I., Fu, Q., and Mote, P. W.: Tropical tropopause layer, Reviews of Geophysics, 47, doi:10.1029/2008rg000267, 2009.

Fujiwara, M., Shiotani, M., Hasebe, F., Vömel, H., Oltmans, S. J., Ruppert, P. W., Horinouchi, T., and Tsuda, T.: Performance of the Meteolabor "Snow White" Chilled-Mirror Hygrometer in the Tropical Troposphere: Comparisons with the Vaisala RS80 A/H-Humicap Sensors, Journal of Atmospheric and Oceanic Technology, 20, 1534–1542, doi:10.1175/1520-0426(2003)020<1534:Potmsw>2.0.Co;2, 2003.

Giancoli, D.: Electric Currents and Resistance, book section 25, p. 658, Prentice Hall, Upper Saddle River, New Jersey, 4th ed edn., 2009.

Glanville, A. A. and Birner, T.: Role of vertical and horizontal mixing in the tape recorder signal near the tropical tropopause, Atmospheric Chemistry and Physics, 17, 4337–4353, doi:10.5194/acp-17-4337-2017, 2017.

Goodman, P. and Chleck, D.: Persistent Water Vapour Contamination and Stratospheric Measurement, Nature, 231, 258–260, doi:10.1038/231258b0, 1971.

Hall, E. G., Jordan, A. F., Hurst, D. F., Oltmans, S. J., Vomel, H., Kuhnreich, B., and Ebert, V.: Advancements, measurement uncertainties, and recent comparisons of the NOAA frost point hygrometer, Atmos Meas Tech, 9, 4295–4310, doi:10.5194/amt-9-4295-2016, 2016.

Hanlon, T. and Risk, D.: Using computational fluid dynamics and field experiments to improve vehicle-based wind measurements for environmental monitoring, Atmospheric Measurement Techniques Discussions, pp. 1–18, doi:10.5194/amt-2018-354, 2018.

Hardy, B.: ITS-90 Formulations for Vapor Pressure, Frostpoint Temperature, Dewpoint Temperature, and Enhancement Factors in the Range –100 to +100 °C, The Proceedings of the Third International Symposium on Humidity and Moisture, London, England, 1998.

Hill, G. E. and Woffinden, D. S.: A Balloonborne Instrument for the Measurement of Vertical Profiles of Supercooled Liquid Water Concentration, Journal of Applied Meteorology (1962-1982), 19, 1285–1292, URL https://www.jstor.org/stable/26179462, 1980.

Holton, J. R., Haynes, P. H., McIntyre, M. E., Douglass, A. R., Rood, R. B., and Pfister, L.: Stratosphere-troposphere exchange, Reviews of Geophysics, 33, doi:10.1029/95rg02097, 1995.

Huang, Y., Coggon, M. M., Zhao, R., Lignell, H., Bauer, M. U., Flagan, R. C., and Seinfeld, J. H.: The Caltech Photooxidation Flow Tube reactor: design, fluid dynamics and characterization, Atmospheric Measurement Techniques, 10, 839–867, doi:10.5194/amt-10-839-2017, 2017.

Hurst, D. F., Oltmans, S. J., Vömel, H., Rosenlof, K. H., Davis, S. M., Ray, E. A., Hall, E. G., and Jordan, A. F.: Stratospheric water vapor trends over Boulder, Colorado: Analysis of the 30 year Boulder record, Journal of Geophysical Research, 116, doi:10.1029/2010jd015065, 2011.

iMet 4: iMet-4 Radiosonde 403 MHz GPS Synoptic Technical Data Sheet, https://www.intermetsystems.com/ee/pdf/202084-10_iMet-4_Technical_Data_Sheet.pdf, accessed: 2019-07-24, 2019.

Immler, F. J., Dykema, J., Gardiner, T., Whiteman, D. N., Thorne, P. W., and Vömel, H.: Reference Quality Upper-Air Measurements: guidance for developing GRUAN data products, Atmospheric Measurement Techniques, 3, 1217–1231, doi:10.5194/amt-3-1217-2010, 2010.

IPCC: Climate Change 2013: The Physical Science Basis. Contribution of Working Group I to the Fifth Assessment Report, Report, Intergovernmental Panel on Climate Change, 2013.

Jorge, T.: Simulink - Heat sink loop - optimal paratmeters estimation, URL https://iacweb.ethz.ch/staff/teresap/Thesis/Opt_Tsink/, 2018a.

Jorge, T.: Simulink - Peltier element loop - optimal paratmeters estimation, URL https://iacweb.ethz.ch/staff/teresap/Thesis/Opt_Tmirror+Thot/, 2018b.

Jorge, T.: Simulink: Reference surface loop - optimal paratmeters estimation, URL https://iacweb.ethz.ch/staff/teresap/Thesis/Opt_Trefsurf/, 2018c.

Jorge, T. and Cesbron, G.: Simulink - PCFH Model, URL https://iacweb.ethz.ch/staff/teresap/Thesis/PCFHModel_Simulink/, 2018a.

Jorge, T. and Cesbron, G.: LabView - PCFH Automatic testing, URL https://iacweb.ethz.ch/staff/teresap/Thesis/LabView/, 2018b.

Jorge, T. and Wienhold, F. G.: Peltier Cooled Frost point Hygrometer (PCFH) Telemetry Interface, URL ftp://iacftp.ethz.ch/pub_read/frank/PCFH/, 2019.

Kanai, Y.: Mirror surface state detection device and moisture detection device, uS Patent 7,168,850 B2, 2007.

Kanai, Y.: Moisture detection device, uS Patent 7,393,135 B2, 2008a.

Kanai, Y.: Detector for detecting state on detection surface, uS Patent 7,380,980 B2, 2008b.

Kanai, Y.: Thermoelectric device and mirror surface state detection device, uS Patent 7,736,051 B2, 2010.

Khaykin, S. M., Engel, I., Vömel, H., Formanyuk, I. M., Kivi, R., Korshunov, L. I., Krämer, M., Lykov, A. D., Meier, S., Naebert, T., Pitts, M. C., Santee, M. L., Spelten, N., Wienhold, F. G., Yushkov, V. A., and Peter, T.: Arctic stratospheric dehydration – Part 1: Unprecedented observation of vertical redistribution of water, Atmos. Chem. Phys., 13, 11 503–11 517, doi:10.5194/acp-13-11503-2013, 2013.

Kigali: UN Environment News relating to the Montereal Protocol Ammendments, `https://www.unenvironment.org/news-and-stories/news/kigali-amendment-montreal-protocol-another-global-commitment-stop-climate`, accessed: 2019-07-16, 2016.

Kämpfer, N. e.: Monitoring atmospheric water vapour., vol. 10 of *ISSI Scientific Report Series*, Springer-Verlag New York, doi:10.1007/978-1-4614-3909-7, 2013.

Komhyr, W. D., Barnes, R. A., Brothers, G. B., Lathrop, J. A., and Opperman, D. P.: Electrochemical concentration cell ozonesonde performance evaluation during STOIC 1989, Journal of Geophysical Research, 100, doi:10.1029/94jd02175, 1995.

Korolev, A., McFarquhar, G., Field, P. R., Franklin, C., Lawson, P., Wang, Z., Williams, E., Abel, S. J., Axisa, D., Borrmann, S., Crosier, J., Fugal, J., Krämer, M., Lohmann, U., Schlenczek, O., Schnaiter, M., and Wendisch, M.: Mixed-Phase Clouds: Progress and Challenges, Meteorological Monographs, 58, 5.1–5.50, doi:10.1175/amsmonographs-d-17-0001.1, 2017.

Korolev, A. V., Isaac, G. A., Cober, S. G., Strapp, J. W., and Hallett, J.: Microphysical characterization of mixed-phase clouds, Quarterly Journal of the Royal Meteorological Society, 129, 39–65, doi:10.1256/qj.01.204, 2003a.

Krämer, M., Schiller, C., Afchine, A., Bauer, R., Gensch, I., Mangold, A., Schlicht, S., Spelten, N., Sitnikov, N., Borrmann, S., de Reus, M., and Spichtinger, P.: Ice supersaturations and cirrus cloud crystal numbers, Atmospheric Chemistry and Physics, 9, 3505–3522, doi:10.5194/acp-9-3505-2009, 2009.

Kräuchi, A., Philipona, R., Romanens, G., Hurst, D. F., Hall, E. G., and Jordan, A. F.: Controlled weather balloon ascents and descents for atmospheric research and climate monitoring, Atmos Meas Tech, 9, 929–938, doi:10.5194/amt-9-929-2016, 2016.

Lawson, P., Gurganus, C., Woods, S., and Bruintjes, R.: Aircraft Observations of Cumulus Microphysics Ranging from the Tropics to Midlatitudes: Implications for a "New" Secondary Ice Process, Journal of the Atmospheric Sciences, 74, 2899–2920, doi:10.1175/jas-d-17-0033.1, 2017.

Leblanc, T., Walsh, T. D., McDermid, I. S., Toon, G. C., Blavier, J. F., Haines, B., Read, W. G., Herman, B., Fetzer, E., Sander, S., Pongetti, T., Whiteman, D. N., McGee, T. G., Twigg, L., Sumnicht, G., Venable, D., Calhoun, M., Dirisu, A., Hurst, D., Jordan, A., Hall, E., Miloshevich, L., Vömel, H., Straub, C., Kampfer, N., Nedoluha, G. E., Gomez, R. M., Holub, K., Gutman, S., Braun, J., Vanhove, T., Stiller, G., and Hauchecorne, A.: Measurements of Humidity in the Atmosphere and Validation Experiments (MOHAVE)-2009: overview of campaign operations and results, Atmospheric Measurement Techniques, 4, 2579–2605, doi:10.5194/amt-4-2579-2011, 2011.

Lewis, F. L., Vrabie, D. L., and Syrmos, V. L.: Optimal Control, Jonh Wiley and Sons, Inc., USA, third edition edn., 2012.

Lüönd, F.: Experimental study on immersion freezing of size selected mineral dust particles, PhD dissertation, ETH Zürich, doi:10.3929/ethz-a-005982778, 2009.

Lohmann, U., Luond, F., and Mahrt, F.: An Introduction to Clouds, Cambridge University Press, doi:10.1017/cbo9781139087513, 2016.

Lundquist, J. K., Churchfield, M. J., Lee, S., and Clifton, A.: Quantifying error of lidar and sodar Doppler beam swinging measurements of wind turbine wakes using computational fluid dynamics, Atmospheric Measurement Techniques, 8, 907–920, doi:10.5194/amt-8-907-2015, 2015.

Massie, S. T. and Hunten, D. M.: Stratospheric Eddy Diffusion-Coefficients from Tracer Data, Journal of Geophysical Research-Oceans, 86, 9859–9868, doi:10.1029/JC086iC10p09859, 1981.

Mastenbrook, H. J.: Frost-point hygrometer measurements in the stratosphere and the problem of moisture contamination, Humidity and Moisture Measurement and Control in Science and IndustryVol. II, New York, Reinhold Publishing Co., II, 480–485, 1965.

Mastenbrook, H. J.: A control system for ascent-descent balloon soundings of the atmosphere, J. Appl. Meteor, 5, 737–740, 1966.

Mastenbrook, H. J.: Water Vapor Distribution in the Stratosphere and High Troposphere, Journal of the Atmospheric Sciences, 25, 299–311, doi:10.1175/1520-0469(1968)025<0299:Wvdits>2.0.Co;2, 1968.

Mastenbrook, H. J. and Dinger, J. E.: Distribution of water vapor in the stratosphere, Journal of Geophysical Research, 66, 1437–1444, doi:doi:10.1029/JZ066i005p01437, 1961.

Mastenbrook, H. J. and Oltmans, S. J.: Stratospheric Water Vapor Variability for Washington, DC/Boulder, CO: 1964–82, Journal of the Atmospheric Sciences, 40, 2157–2165, doi:10.1175/1520-0469(1983)040<2157:Swvvfw>2.0.Co;2, 1983.

MathWorksDoc: MathWorks Documentation: lsqnonlin nonlinear least-squares solver, `https://ch.mathworks.com/help/optim/ug/lsqnonlin.html`, accessed: 2019-08-20, 2019a.

MathWorksDoc: MathWorks Documentation: Estimate Model Parameter Values (Code), `https://ch.mathworks.com/help/sldo/examples/estimate-model-parameter-values-code.html#d119e2213`, accessed: 2019-08-20, 2019b.

Matula, R. A.: Electrical resistivity of copper, gold, palladium, and silver, Journal of Physical and Chemical Reference Data, 8, 1147–1298, doi:10.1063/1.555614, 1979.

May, R. D.: Open-path, near-infrared tunable diode laser spectrometer for atmospheric measurements of H2O, Journal of Geophysical Research: Atmospheres, 103, 19 161–19 172, doi:10.1029/98jd01678, 1998.

MeteoSwiss: GAW-CH Plus research projects 2018-2021, `https://www.meteoswiss.admin.ch/home/research-and-cooperation/international-cooperation/gaw/national-activities.html`, accessed:2019-09-05, 2018.

Mote, P. W., Rosenlof, K. H., McIntyre, M. E., Carr, E. S., Gille, J. C., Holton, J. R., Kinnersley, J. S., Pumphrey, H. C., Russell, J. M., and Waters, J. W.: An atmospheric tape recorder: The imprint of tropical tropopause temperatures on stratospheric water vapor, Journal of Geophysical Research: Atmospheres, 101, 3989–4006, doi:10.1029/95jd03422, 1996.

Murphy, D. M. and Koop, T.: Review of the vapour pressures of ice and supercooled water for atmospheric applications, Quarterly Journal of the Royal Meteorological Society, 131, 1539–1565, doi:10.1256/qj.04.94, 2005.

Oelsner, P.: Gruan-Monitor-MW41, URL https://www.gruan.org/data/software/gm41/, 2019.

Oltmans, S. J. and Hofmann, D. J.: Increase in lower-stratospheric water vapour at a mid-latitude Northern Hemisphere site from 1981 to 1994, Nature, 374, 146–149, doi:10.1038/374146a0, 1995.

Oltmans, S. J., Vömel, H., Hofmann, D. J., Rosenlof, K. H., and Kley, D.: The increase in stratospheric water vapor from balloonborne, frostpoint hygrometer measurements at Washington, D.C., and Boulder, Colorado, Geophysical Research Letters, 27, 3453–3456, doi:10.1029/2000gl012133, 2000.

O'Malley, J.: Schaum's outline of theory and problems of basic circuit analysis, McGraw-Hill Professional, 1992.

OptimizationToolbox: Optimization Toolbox - MathWorks product webpage, https://ch.mathworks.com/products/optimization.html, accessed: 2019-08-18, 2019.

Panasonic: AQ1801, Heat sink, https://www3.panasonic.biz/ac/e/search_num/index.jsp?c=detail&part_no=AQ1801, accessed:2019-08-04, 2019.

Peter, T., Marcolli, C., Spichtinger, P., Corti, T., Baker, M. B., and Koop, T.: Atmosphere. When dry air is too humid, Science, 314, 1399–402, doi:10.1126/science.1135199, URL https://www.ncbi.nlm.nih.gov/pubmed/17138887, 2006.

Petzold, A., Kramer, M., Neis, P., Rolf, C., Rohs, S., Berkes, F., Smit, H. G. J., Gallagher, M., Beswick, K., Lloyd, G., Baumgardner, D., Spichtinger, P., Nedelec, P., Ebert, V., Buchholz, B., Riese, M., and Wahner, A.: Upper tropospheric water vapour and its interaction with cirrus clouds as seen from IAGOS long-term routine in situ observations, Faraday Discuss, 200, 229–249, doi:10.1039/c7fd00006e, 2017.

Pitts, M. C., Poole, L. R., and Thomason, L. W.: CALIPSO polar stratospheric cloud observations: second-generation detection algorithm and composition discrimination, Atmospheric Chemistry and Physics, 9, 7577–7589, doi:10.5194/acp-9-7577-2009, 2009.

Pruppacher, H. R. and Klett, J. D.: Microphysics of Clouds and Precipitation., Kluwer Academic Publishers, 1997.

Randel, W. J., Wu, F., Gettelman, A., Russell, J. M., Zawodny, J. M., and Oltmans, S. J.: Seasonal variation of water vapor in the lower stratosphere observed in Halogen Occultation Experiment data, Journal of Geophysical Research: Atmospheres, 106, 14 313–14 325, doi:10.1029/2001jd900048, 2001.

RMT: Thermoelectric cooling solutions, http://www.rmtltd.ru/, accessed: 2019-07-19, 2019.

Rosenlof, K. H., Oltmans, S. J., Kley, D., Russell, J. M., Chiou, E. W., Chu, W. P., Johnson, D. G., Kelly, K. K., Michelsen, H. A., Nedoluha, G. E., Remsberg, E. E., Toon, G. C., and McCormick, M. P.: Stratospheric water vapor increases over the past half-century, Geophysical Research Letters, 28, 1195–1198, doi:10.1029/2000gl012502, 2001.

Roth+Co.Ag: Thermocouples Calibration Certificates, URL https://iacweb.ethz.ch/staff/teresap/Thesis/CalibrationCertificates/, 2016.

Rowe, D.: CRC Handbook of Thermoelectrics, CRC Press, 1995.

Seinfeld, J. H. and Pandis, S. N.: Atmsopheric Chemistry and Physics - From Air Pollution to Climate Change, John Wiley and Sons, Inc., second edition edn., 2006.

Serke, D., Hall, E., Bognar, J., Jordan, A., Abdo, S., Baker, K., Seitel, T., Nelson, M., Ware, R., McDonough, F., and Politovich, M.: Supercooled liquid water content profiling case studies with a new vibrating wire sonde compared to a ground-based microwave radiometer, Atmospheric Research, 149, 77–87, doi:10.1016/j.atmosres.2014.05.026, 2014.

Simulink: Simulink - MathWorks product webpage, https://ch.mathworks.com/products/simulink.html, accessed: 2019-08-18, 2019.

Skogestad, S. and Postlethwaite, I.: Multivariable Feedback Control, Wiley, Chichester, UK, 1996.

Solomon, S., Garcia, R. R., Rowland, F. S., and Wuebbles, D. J.: On the depletion of Antarctic ozone, Nature, 321, 755–758, doi:10.1038/321755a0, 1986.

Solomon, S., Rosenlof, K. H., Portmann, R. W., Daniel, J. S., Davis, S. M., Sanford, T. J., and Plattner, G. K.: Contributions of stratospheric water vapor to decadal changes in the rate of global warming, Science, 327, 1219–23, doi:10.1126/science.1182488, 2010.

SPI: Swiss Polar Institute, Polar Access Fund, https://polar.epfl.ch/page-156316-en-html/page-153176-en-html/, accessed: 2019-09-05, 2019.

Sugidachi, T.: Studies on the tropospheric and stratospheric water vapor measurements for climate monitoring, PhD dissertation, Hokkaido University, URL http://hdl.handle.net/2115/55416, 2014.

Sugidachi, T.: Meisei SKYDEW instrument: analysis of results from Lindenberg campaign, URL https://www.gruan.org/gruan/editor/documents/meetings/icm-11/pres/pres_0803_Sugidachi_SKYDEW.pdf, work presented at GRUAN ICM-11, Singapore, May 23, 2019, 2019.

Sugidachi, T. and Fujiwara, M.: New Peltier-based chilled-mirror hygrometer "SKYDEW", URL https://www.gruan.org/gruan/editor/documents/meetings/icm-10/pres/pres_0712_Sugidachi_SKYDEW.pdf, work presented at GRUAN ICM-10, Potsdam, April 25, 2018, 2018.

Suomi, V. E. and Barrett, E. W.: An Experimental Radiosonde for the Investigation of the Distribution of Water Vapor in the Stratosphere, Review of Scientific Instruments, 23, 272–292, doi:10.1063/1.1746250, 1952.

Survo, P., Leblanc, T., Kivi, R., Jauhiainen, H., and Lehtinen, R.: Comparison of selected in-situ and remote sensing technologies for atmospheric humidity measurements, Manuscript 13B.2 presented at the 95th American Meteorological Society (AMS) Annual Meeting, URL https://ams.confex.com/ams/95Annual/webprogram/Paper255790.html, 2015.

Thermoelectrics, N. M. S. E.: Thermoelectric effect, http://thermoelectrics.matsci.northwestern.edu/thermoelectrics/index.html, accessed: 2019-07-19, 2019.

Trhlíková, L., Zmeskal, O., Psencik, P., and Florian, P.: Study of the thermal properties of filaments for 3D printing, AIP Conference Proceedings, 1752, doi:https://doi.org/10.1063/1.4955258, 2016.

twig: twig Locator, http://2015.twigcom.com/media/en/Data%20sheets/TWIG_Locator_datasheet.pdf, accessed:2019-08-08, 2015.

Vaisala: Vaisala Radiosonde RS41 Measurement Performance White Paper, Ref. B211356EN-A Vaisala, 2013.

Vaisala: Vaisala Radiosonde RS41-SGP, https://www.vaisala.com/sites/default/files/documents/WEA-MET-RS41SGP-Datasheet-B211444EN.pdf, accessed: 2019-08-11, 2017.

Vaughan, G., Cambridge, C., Dean, L., and Phillips, A. W.: Water vapour and ozone profiles in the midlatitude upper troposphere, Atmospheric Chemistry and Physics, 5, 963–971, doi:10.5194/acp-5-963-2005, 2005.

Vaughan, G., Schiller, C., MacKenzie, A. R., Bower, K., Peter, T., Schlager, H., Harris, N. R. P., and May, P. T.: SCOUT-O3/ACTIVE: High-altitude Aircraft Measurements around Deep Tropical Con-

vection, Bulletin of the American Meteorological Society, 89, 647–662, doi:10.1175/bams-89-5-647, 2008.

Vernier, J. P., Fairlie, T. D., Natarajan, M., Wienhold, F. G., Bian, J., Martinsson, B. G., Crumeyrolle, S., Thomason, L. W., and Bedka, K. M.: Increase in upper tropospheric and lower stratospheric aerosol levels and its potential connection with Asian pollution, Journal of Geophysical Research: Atmospheres, 120, 1608–1619, doi:doi:10.1002/2014JD022372, 2015.

Vömel, H., Oltmans, S. J., Hofmann, D. . J., Deshler, T., and Rost, M.: The Evolution of the Dehydration in the Antarctic Stratospheric Vortex, Journal of Geophysical Research, 100, 13 919–13 926, doi:10.1029/95jd01000, 1995.

Vömel, H., Oltmans, S. J., Johnson, B. J., Hasebe, F., Shiotani, M., Fujiwara, M., Nishi, N., Agama, M., Cornejo, J., Paredes, F., and Enriquez, H.: Balloon-borne observations of water vapor and ozone in the tropical upper troposphere and lower stratosphere, Journal of Geophysical Research-Atmospheres, 107, doi:10.1029/2001jd000707, 2002.

Vömel, H., Fujiwara, M., Shiotani, M., Hasebe, F., Oltmans, S. J., and Barnes, J. E.: The Behavior of the Snow White Chilled-Mirror Hygrometer in Extremely Dry Conditions, Journal of Atmospheric and Oceanic Technology, 20, 1560–1567, doi:10.1175/1520-0426(2003)020<1560:Tbotsw>2.0.Co;2, 2003.

Vömel, H., Barnes, J. E., Forno, R. N., Fujiwara, M., Hasebe, F., Iwasaki, S., Kivi, R., Komala, N., Kyrö, E., Leblanc, T., Morel, B., Ogino, S. Y., Read, W. G., Ryan, S. C., Saraspriya, S., Selkirk, H., Shiotani, M., Valverde Canossa, J., and Whiteman, D. N.: Validation of Aura Microwave Limb Sounder water vapor by balloon-borne Cryogenic Frost point Hygrometer measurements, Journal of Geophysical Research, 112, doi:10.1029/2007jd008698, 2007a.

Vömel, H., David, D. E., and Smith, K.: Accuracy of tropospheric and stratospheric water vapor measurements by the cryogenic frost point hygrometer: Instrumental details and observations, Journal of Geophysical Research: Atmospheres, 112, doi:doi:10.1029/2006JD007224, 2007b.

Vömel, H., Yushkov, V., Khaykin, S., Korshunov, L., Kyrö, E., and Kivi, R.: Intercomparisons of Stratospheric Water Vapor Sensors: FLASH-B and NOAA/CMDL Frost-Point Hygrometer, Journal of Atmospheric and Oceanic Technology, 24, 941–952, doi:10.1175/jtech2007.1, 2007c.

Vömel, H., Naebert, T., Dirksen, R., and Sommer, M.: An update on the uncertainties of water vapor measurements using cryogenic frost point hygrometers, Atmospheric Measurement Techniques, 9, 3755–3768, doi:10.5194/amt-9-3755-2016, 2016.

von Hobe, M., Bekki, S., Borrmann, S., Cairo, F., amp, apos, Amato, F., Di Donfrancesco, G., Dörnbrack, A., Ebersoldt, A., Ebert, M., Emde, C., Engel, I., Ern, M., Frey, W., Genco, S., Griessbach, S., Grooß, J. U., Gulde, T., Günther, G., Hösen, E., Hoffmann, L., Homonnai, V., Hoyle, C. R., Isaksen, I. S. A., Jackson, D. R., Jánosi, I. M., Jones, R. L., Kandler, K., Kalicinsky, C., Keil, A., Khaykin, S. M., Khosrawi, F., Kivi, R., Kuttippurath, J., Laube, J. C., Lefèvre, F., Lehmann, R., Ludmann, S., Luo, B. P., Marchand, M., Meyer, J., Mitev, V., Molleker, S., Müller, R., Oelhaf, H., Olschewski, F., Orsolini, Y., Peter, T., Pfeilsticker, K., Piesch, C., Pitts, M. C., Poole, L. R., Pope, F. D., Ravegnani, F., Rex, M., Riese, M., Röckmann, T., Rognerud, B., Roiger, A., Rolf, C., Santee, M. L., Scheibe, M., Schiller, C., Schlager, H., Siciliani de Cumis, M., Sitnikov, N., Søvde, O. A., Spang, R., Spelten, N., Stordal, F., Sumińska-Ebersoldt, O., Ulanovski, A., Ungermann, J., Viciani, S., Volk, C. M., vom Scheidt, M., von der Gathen, P., Walker, K., Wegner, T., Weigel, R., Weinbruch,

S., Wetzel, G., Wienhold, F. G., Wohltmann, I., Woiwode, W., Young, I. A. K., Yushkov, V., Zobrist, B., and Stroh, F.: Reconciliation of essential process parameters for an enhanced predictability of Arctic stratospheric ozone loss and its climate interactions (RECONCILE): activities and results, Atmospheric Chemistry and Physics, 13, 9233–9268, doi:10.5194/acp-13-9233-2013, 2013.

Weiss, K. P., Bagrets, N., Lange, C., Goldacker, W., and Wohlgemuth, J.: Thermal and mechanical properties of selected 3D printed thermoplastics in the cryogenic temperature regime, IOP Conference Series: Materials Science and Engineering, 102, doi:10.1088/1757-899x/102/1/012022, 2015.

Wendell, J. and Jordan, A.: iMet-1-RSB Radiosonde XDATA Protocol & Daisy Chaining, ftp://aftp.cmdl.noaa.gov/user/jordan/iMet-1-RSBRadiosondeXDATADaisyChaining.pdf/82394, accessed: 2019-07-24, 2016.

Wendisch, M., Pöschl, U., Andreae, M. O., Machado, L. A. T., Albrecht, R., Schlager, H., Rosenfeld, D., Martin, S. T., Abdelmonem, A., Afchine, A., Araùjo, A. C., Artaxo, P., Aufmhoff, H., Barbosa, H. M. J., Borrmann, S., Braga, R., Buchholz, B., Cecchini, M. A., Costa, A., Curtius, J., Dollner, M., Dorf, M., Dreiling, V., Ebert, V., Ehrlich, A., Ewald, F., Fisch, G., Fix, A., Frank, F., Fütterer, D., Heckl, C., Heidelberg, F., Hüneke, T., Jäkel, E., Järvinen, E., Jurkat, T., Kanter, S., Kästner, U., Kenntner, M., Kesselmeier, J., Klimach, T., Knecht, M., Kohl, R., Kölling, T., Krämer, M., Krüger, M., Krisna, T. C., Lavric, J. V., Longo, K., Mahnke, C., Manzi, A. O., Mayer, B., Mertes, S., Minikin, A., Molleker, S., Münch, S., Nillius, B., Pfeilsticker, K., Pöhlker, C., Roiger, A., Rose, D., Rosenow, D., Sauer, D., Schnaiter, M., Schneider, J., Schulz, C., de Souza, R. A. F., Spanu, A., Stock, P., Vila, D., Voigt, C., Walser, A., Walter, D., Weigel, R., Weinzierl, B., Werner, F., Yamasoe, M. A., Ziereis, H., Zinner, T., and Zöger, M.: ACRIDICON–CHUVA Campaign: Studying Tropical Deep Convective Clouds and Precipitation over Amazonia Using the New German Research Aircraft HALO, Bulletin of the American Meteorological Society, 97, 1885–1908, doi:10.1175/bams-d-14-00255.1, 2016.

Wikipedia: Geographical Distance, https://en.wikipedia.org/wiki/Geographical_distance, accessed: 2019-06-21, 2018.

Wikipedia: Linear–quadratic regulator, https://en.wikipedia.org/wiki/Linear%E2%80%93quadratic_regulator, accessed: 2019-08-23, 2019a.

Wikipedia: Entrance length and fully developped flow, https://en.wikipedia.org/wiki/Entrance_length, accessed: 2019-08-25, 2019b.

WMO: Meteorology – A three-dimensional science: Second session of the commission for aerology, World Meteorol. Organ. Bull., VI, 134–138, URL https://library.wmo.int/doc_num.php?explnum_id=6961, 1957.

WMO: Guide to Meteorological Instruments and Methods of Observation, World Meteorological Organization, chapter 12.7.4, https://library.wmo.int/pmb_ged/wmo_8_en-2012.pdf, accessed: 2019-06-03, 2008.

Wärmeleitkleber: fischer elektonik WLK 10, https://www.fischerelektronik.de/web_fischer/de_DE/K%C3%BChlk%C3%B6rper/E01.09/W%C3%A4rmeleitkleber/PR/WLK10_/index.xhtml/Geographical_distance, accessed: 2019-07-22, 2019.

Ziegler, J. G. and Nichols, N. B.: Optimum settings for automatic controllers, Transactions of the ASME, 64, 759–768, 1942.